UNIVERSITY OF
LIVERPOOL

COMPUTER SIMULATION OF THE ATMOSPHERIC ARC PLASMAS ENVIRONMENT FOR PRODUCTION OF NANOSCALE MATERIALS

Thesis submitted in accordance with the requirements of the University of Liverpool for the degree of Doctor in Philosophy

by

Kah Meng Tang

March 2008

Department of Electrical Engineering and Electronics

ABSTRACT

The aim of this study is concerned with the development of computational models for two types of atmospheric technological plasmas with background applications in material processing (waste disposal and production of nano-scale powders) and formation of nano-scale carbon structures (formation of carbon nano-tubes and fullerenes).

The twin torch system consists of two electrode assemblies, each of which has a central electrode surrounded by a nozzle to confine the shielding gas. The two electrodes are configured to have an angle between their axes. The arcing environment is truly three dimensional (3D) and thus requires a three dimensional model to simulate the arcing process.

Representation of 3D shape in the computational domain is a challenging issue and needs to be addressed before a sensible solution is obtained. In the present model a novel numerical scheme is developed to conveniently and automatically allocate cells (each cell is a finite volume in the solution procedure) to a 3D shape. This has greatly enhanced the adaptability of the model to cope with complex geometries encountered in arc plasma systems.

One of the key issues in 3D arc modelling is the correct calculation and application of the Lorentz force terms in the momentum equation. For a symmetric arcing case, such as a free burning arc between a conic cathode and a plate anode, slight asymmetry in the distribution of Lorentz force can substantially affect the arc flow hence resulting in a non-symmetric arc column. Validation of the numerical method has been carried out using the free burning arc case by comparing the model predictions with measurements and other available simulation results. It has been shown that the present 3D model produces satisfactory results.

Since the two electrodes of the twin plasma system are water cooled, erosion of the electrode material is minimal and can be neglected. It has been found that the coupling of the two jets is through a thin, tissue like, conducting layer between the two jets. The cross sectional shape of the two jets is deformed by the Lorentz force. The jets are never completely merged. The Lorentz force induced by the arc current and the combined magnetic field of the two jets tends to move the point of separation away from the electrode tips. It is the strong Ohmic heating, resulting from the high temperature (high electrical conductivity) and high electric field in the coupling zone, that heats up the incoming cold gas to a conducting temperature and thus stabilises the electric current path and subsequently the point of separation of the two jets. It is also shown that the change in flow rate does not have significant influence on the parameters of the plasma. The predicted arc voltage is found to be higher than the measurement. The difference is partly attributed to the statistically high frequency

fluctuation of the jet coupling zone. The use of a simple turbulence model brings the prediction closer to the measurement at low current, however results in an excessive reduction in arc voltage at high current. Therefore the use of a conventional turbulence model with a fixed turbulence parameter c to simulate the effect of fluctuations of the jet coupling zone may not be appropriate.

The carbon arc simulated in Chapter 5 is confined by liquid water and burns in the gap between a conic anode and a plate cathode. Such an arrangement aims at maximising the anode erosion rate for the formation of solid carbon structures (carbon nanotubes and fullerenes). A mathematical model has been developed to simulate the dynamics of bubble growth and development of the arc column. A novel numerical scheme is employed to determine the speed of bubble surface expansion. To simulate the removal of gas from within the domain associated with bubble detachment from the discharge zone, an exit is imposed on the bubble surface when its radius reaches 9mm.

Results show that there is large pressure change within the first half millisecond of the discharge. The pressure can be as high as 38bar. Under such a high pressure the water surrounding the bubble is accelerated which leads to an increasing speed of bubble growth. The rapid growth of bubble size under its inertia caused the pressure inside the bubble to rapidly decrease. The arc voltage, which is an indication of the total electrical power input into the domain, settles down in the first millisecond and then maintains a value of 5V.

The arc temperature at initiation is 24000K within a thin hot column. This temperature is quickly reduced to 11000K in 5μs as a result of radiation loss from the arc column. The axis temperature inside the arc column at 30ms is 8500K which is higher than the experimental value measured using a spectroscopic method. The possible reason for this difference could be the instability of the arc column which makes the measured temperature as an average value of the arc column. There exists a relatively large area around the arc core whose temperature is within the range of 4500K to 7000K which is the temperature range from measurement.

A quasi-steady state of arcing is reached within 30ms of arc initiation. The loss of carbon vapour from the computational domain resulting from formation of solid carbon matters is considered by a flux controlled model. Results show that the major loss of the carbon species is at the arc edge which accounts for 99% of the total carbon loss.

The predicted arc column voltage is 5V which is different from the measurement of 16V. The difference is contributed to the cathode voltage fall which is in the order of the ionisation energy of carbon atoms (11.26eV). Taking this aspect into consideration, the prediction falls into the expected range. The biggest difference between the prediction and measurement is the water evaporation rate. The arc model prediction is only a very small fraction of the measurement. However, it is shown that the measured rate of water evaporation may be incorrect since even when the total electrical power

input at the measured arc voltage is used, the amount of water vapour that can be created is only 12.5% of the measured value. This renders the water evaporation rate comparison invalid and further measurements are required.

Future work is discussed at the end of the thesis. Three aspects have been identified that need to be addressed. The instability of the twin torch jet coupling may need to be simulated by a transient model. The cathode sheath is important in determining the whole arc voltage and therefore needs to be simulated using kinetic theory. The effectiveness of three dimensional modelling suffers enormously from the prohibitively long computing time because of the strong relaxation that has to be used to obtain converging results. This naturally requires parallel processing given that high processing power PCs (2.1GHz Pentium Core Duo) have already been used for the present work.

ACKNOWLEDGEMENTS

I would like to express my greatest appreciation to my supervisor Dr. Joseph J. D. Yan for his guidance, encouragement and support throughout my study. Under his guidance, I have learned a lot academically and mentally that has enabled me to deal with the challenging research projects independently. I am deeply grateful to Professor M. T. C. Fang for his stimulating suggestions and discussions, and for his frank and truthful confrontational comments concerning my research and thesis. I wish to thank members of the Arc Research Group, Dr. J. L. Zhang, Dr. K. Kweon, Dr. V. K. Liau and Yiyi Zhan for their valuable discussions and friendships. My thanks are due to Dr. C. Chapman, Dr. David Deegan and Saeed Ismail for their cooperation concerning the arc plasma system. I would like to thank the Lee Foundation of Malaysia, the ORS Awards and the University of Liverpool for financial support. Last but not least, to my fiancée and family, I wish to express my greatest thanks for all their love, endless support and encouragement throughout my study at the University of Liverpool and all over the years.

TABLE OF CONTENTS

CHAPTER 5 CARBON ARC PLASMA CONFINED IN LIQUID WATER

CHAPTER 6 CONCLUSION AND FUTURE WORK

Chapter 1

INTRODUCTION

1.1 Atmospheric Technologic Plasmas and Their Applications

Atmospheric technologic plasmas are an important branch of gas discharges and they are found in many industrial applications in material processing, welding and cutting, waste disposal/energy recovery [1], and more recently, production of small scale materials such as nano-powders [2] and fullerenes and carbon nanotubes [3]. In these systems, the plasma is often generated and maintained either in high frequency electromagnetic fields such as inductively coupled plasma and microwave sustained plasma, or between two electrodes with DC or AC voltage applied. The efficiency and stability of such systems critically depends on the plasma behaviour under specified working conditions and the interaction between the plasma and work piece or the material being processed. For some of the systems, such as the twin torch system (more details in section 1.3) and the carbon arc in water, diagnosis of the plasma parameters is extremely difficult because of the three dimensional, non-symmetric arc shape (the former) or small electrode gap surrounded by water (the latter). However to correlate the working conditions with the yield of the system and to subsequently improve the design, fundamental knowledge on plasma behaviour is essential. This inevitably requires the establishment of good physical models and simulation of the arcing process for detailed information within the plasma environment. For the two systems mentioned above, not many publications and little work has been done to simulate the plasma environment because of the complexity and difficulties involved. The problem is multi-disciplinary (plasma physics, thermodynamics, fluid dynamics) and a number of coupled physical mechanisms have to be considered concurrently and

the highly non-linear governing equations solved in three dimensional domain or in the presence of dynamic evaporating surface.

The present work is aimed at the establishment of appropriate physical models for the plasma environment in the above two systems and carrying out simulation of the arcing processes to obtain detailed information on the plasma behaviour. In this chapter, the fundamentals of thermal plasmas will first be introduced followed by a review of the two areas of applications of thermal plasmas and also the history of arc modelling. The literature review is carried out with the aim to establish a picture on the typical system configuration, range of experimental conditions normally employed and available results and understanding to support the modelling of the plasma environment.

1.2 Fundamentals of Thermal Plasmas

Over 99% of the matter in the universe is in plasma state, which is commonly known as the fourth state of matter. Plasma is an ionised gas containing electrons, ions and neutrals. Plasma can be generated in a variety of ways (e.g. by electric discharges, shock waves, laser induced and by direct heating) under different conditions (different gases and pressures). An ionised gas is called a plasma if its characteristic length is much larger than the electron Debye length so that the ionised gas attains charge quasi-neutrality.

At atmospheric pressure and above, particle collisions are sufficiently frequent to ensure that all species attain the same temperature and that the particle distributions at various energy levels obey the Boltzmann distribution although the radiation field inside the plasma departs from that of black body. For such a plasma its state is characterised by two thermodynamic variables (e.g. pressure and temperature) and its behaviour can be described by a single fluid conservation equations modified to take into account the special processes associated with given plasma conditions and the effects of electromagnetic fields. Such plasma state is commonly known as in local thermal equilibrium (LTE [1]). Plasmas with such characteristics are also known as thermal plasmas. Atmospheric arc discharges (commonly known as arcs or arc

plasmas), a special form of electrical discharge characterised by low voltage drops in electrode regions, are usually in LTE.

The discovery of arc discharges at the turn of 19th century can be regarded as the beginning of the study of man-made plasmas. Up to the Second World War, little was known about the fundamental processes occurring in atmospheric arc discharges. The discovery of nuclear fusion and the subsequent realisation of the potential of controlled thermal nuclear fusion promoted intense research activities in basic plasma physics during and immediately after the war [4]. The basic equations describing the behaviour of plasmas ranging from collisionless to collision dominated plasmas were formulated. In parallel with the development of basic plasma theory, diagnostic techniques, especially after the invention of the lasers, have been developed to such an extent that the measurement of basic plasma parameters has become common.

Arc plasmas are characterised by their high temperature and high energy density/flux, which are ideal for certain technical applications. Thus, arc plasmas are the key element for many industrial applications, such as light sources, material welding and cutting, surface spraying and interrupting fault currents in power systems. More recently thermal plasmas based on electric arc discharge have been used for decomposition (waste disposals), deposition (thermal plasma chemical vapour deposition) and synthesis of fine powders (in the nanometre scale range) through plasma densification [5].

1.3 Twin Torch Arc Plasma for Production of Fine Powders

Arc plasma is a high temperature ionized gas generating intense heat in a safe and controlled manner. Because this heat source is clean, compact and controllable, arc plasmas provide unique opportunities for industrial processing. Arc plasmas have been used for the production of small scale materials. The twin torch plasma system [6,7,8] and carbon arc in water [3,9,10] are two typical examples in this area. In the former, an arc is generated between two electrodes with an included angle (angle between the axis of the two electrode assemblies) of 90 to 120 degrees. The development of the twin torch system originated from the practice of heating non-conducting materials,

especially ceramics. Conventional method of using non-transferred arc [6] has the disadvantage of nozzle blocking by powder agglomerates, and increased nozzle erosion. On the other side, using transferred arc requires preheating the ceramic material to first form a conducting path for the current before an electric arc can be established to deliver high energy flux to the material. An anode is usually required to be submerged into the molten ceramic material to complete the circuit. However, this introduced some side effects. For example, electrolytic reactions lead to increased anode erosion, which subsequently produces more contamination to the molten material. The idea of a twin torch system was developed with the purpose to remove these intrinsic problems associated with transferred arc.

Figure 1.1 shows the twin torch plasma system and figure 1.2 is a typical image of the twin torch DC plasma. Compared with the conventional non-transferred and transferred arc plasma systems, the twin torch system has the advantage of maintaining a plasma coupling zone that is located well away from the two electrode tips with easy access for material feeding while still sustaining a high energy density. This provides the convenience of flexibility for introducing raw material in the form of coarse powders, or wires into the plasma region for adequate vaporization [6]. However, research on this type of plasma system has so far been mainly experimental. However, there is still a scarcity of reproducible experimental results because of the difficulties associated with the measurements on a 3-dimensional arc, often non-steady, and because of the costs of running these systems, usually at very high power level. Thus, experimental results are mainly concerned with the Voltage-Current (V-I) characteristics of the arc and its shape using high speed photography.

Williams [11] first described the operation of a twin torch system in 1992 and 1993, which was later patented for the production of high purity aluminium nitride powders (advanced ceramic material). Pure aluminium ingot was placed in contact with the coupling region of the plasma which evaporate the former. NH_3 gas was fed into the plasma coupling zone and its vicinity via a pipe. Aluminium vapour reacts with nitrogen atoms to form aluminium nitride in regions where the temperature is around 2700K. The typical voltage is 150V for a 460A DC arc with 80 Newton litre per minute (Nl/min) of nitrogen to anode (copper) and cathode (thoriated tungsten) nozzles

[11,12]. However, the included angles and the electrode separation was not given. The influence of the included angles by the electrodes was discussed based on arc voltage measurement. With a large included angle, the arc approaches a conventional transferred arc with a low arc voltage. When the included angle gradually reduces, distinct cathode and anode torches start to form and because of the opposite polarity, the two torches tend to repel each other, which results in an increase in arc voltage [11]. An important observation from the above work is that the torches moves towards an unstable regime for small included angles because of the repelling effect. This can also be seen from a high speed video footage provided by Tetronics.

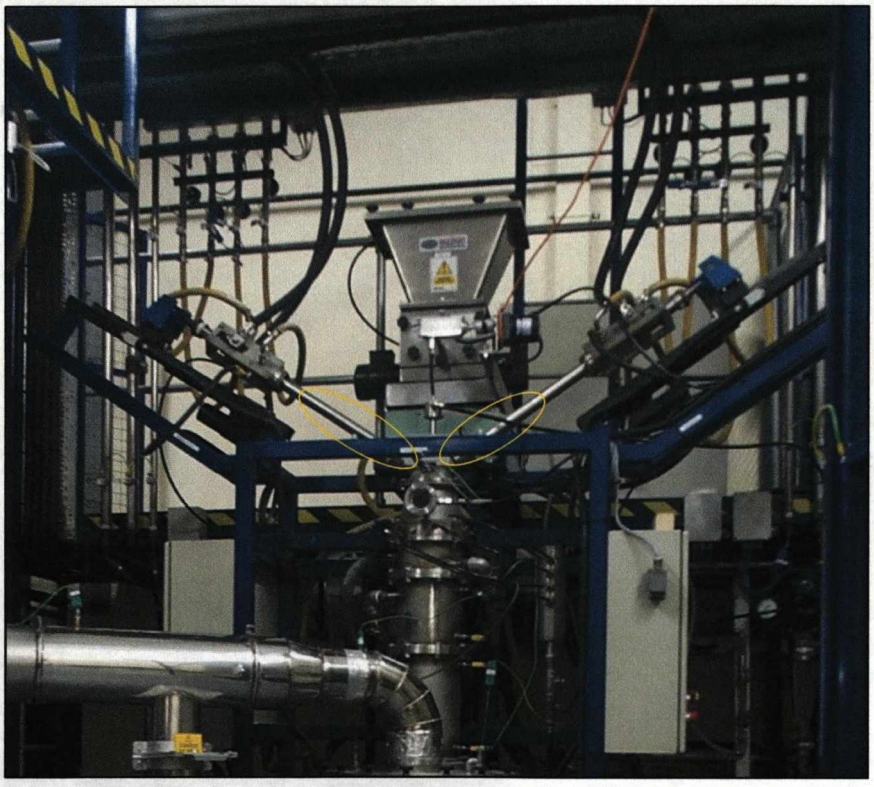

Figure 1.1 The twin torch plasma system used in Tetronics for the production of fine powders (Yellow rings indicate the location of the two torches)

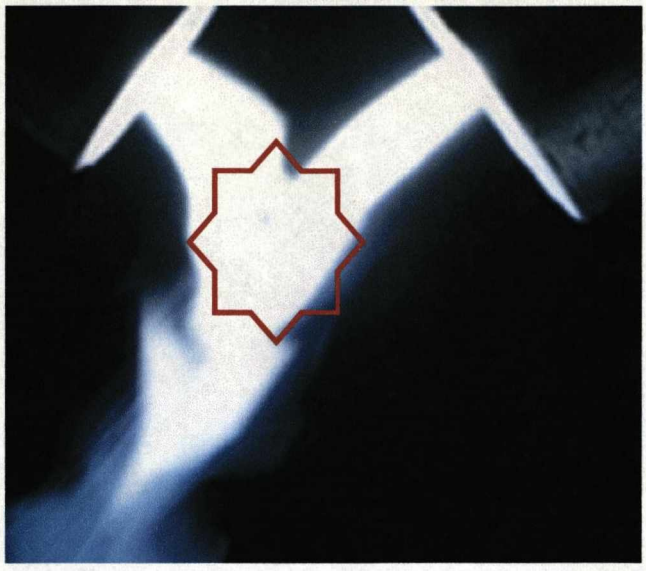

Figure 1.2 Image showing a typical twin torch arc plasma with the coupling zone shown by the red indicator

Limited experimental results on temperature, species concentration and electron number density measurement are available for particular electrode arrangement and working gases (argon and nitrogen) [6,13]. For the measurement of parameters near the electrodes, they assumed axis-symmetry and Abel inversion is used to derive the emission coefficient. For the plasma coupling zone they assumed a plane symmetry (the plane made by the axis of the two electrodes) and used the methods described in [14,15,16] for deriving the plasma temperature and electron number density. The starting point of using this plane symmetry method is that the plasma radiation emission decreases exponentially with decrease in temperature (assuming the total density of the emitting particles is not sensitive to temperature change provided that the plasma temperature is lower than the "norm temperature" at which the emission coefficient reaches a maximum) and observed emission is mainly from a thin layer of plasma around the symmetry plane. The total intensity can then be approximated by assuming a plasma thickness. Thus the measurement is more accurate near the anode and cathode where the arc column is close to axisymmetry. The typical arc temperature near the argon shielded anode is between 11000K to 13000K (temperature on axis) at a discharge current of 200A [6]. Similar temperature range was obtained for the cathode jet shielded by nitrogen. The temperature in the coupling zone is lower (8500K to

10000K) as a result of the broadened conducting area [6,13]. The electron number density has a typical value of $6x10^{22}/m^3$ near the anode, $6x10^{22}/m^3$ near the cathode and decreases to $1x10^{22}/m^3$ in the plasma coupling zone.

Apart from the spectroscopic measurement as mentioned above, Megy et al [6] also presented a comprehensive study of the voltage-current characteristics of the twin torch plasma system over a wide current range. The arcing gas for these measurements was argon for both cathode and anode with a flow rate of 20 and 30Nl/min respectively. V-I characteristics were obtained for a current range of 400A to 1000A, that of included angle from 45 to 175 degrees, and an electrode separation range of 76mm to 178mm. The electrical power input varied from 50kW to 300kW. These results will be used in the present work to compare with the results from the computer simulation.

Despite the many advantages of using twin torch plasmas for a range of industrial applications, the major problem associated with the operation of this type of arc is the stability arising from the coupling and repelling mechanisms of the two electrode jets [7]. The heating efficiency is critically related to the size, temperature, velocity and stability of the coupling zone. Relying on experiments only to understand the plasma behaviour and to optimise the design of such a system is expensive and prohibitively time consuming. Correct modelling of the arcing process would provide valuable information as regards the plasma environment. It also provides the baseline information for future study of plasma-particle interaction in such a high temperature environment. Therefore the establishment of a realistic computer model of the twin torch plasma is one of the objectives of the present study.

1.4 Carbon Arcs for Formation of Carbon Nanotubes (CNT) and Fullerenes

As mentioned in section 1.1, the second part of the present work is to model the carbon arc generated in water. This plasma system is used for the formation of carbon structures including nanotubes and fullerenes. This section presents a review of its application in this emerging field. A brief introduction to carbon nanostructure and a history to the application of this method are given below to provide necessary

background knowledge in this field. This will be followed by a review on the plasma system and its normal operation conditions and available experimental results.

Nanotechnology [17] is a dominant research area in modern engineering because of the potential benefits that humans can take by using the special properties of nanometre scale materials. Materials begin to be dominated by the atoms and molecules at the surfaces if the ordered atomic arrangements of the latter are restricted to nanometre scale. Under such a condition, the material properties start to be strikingly different from the bulk material. Nanomaterials can comprise a range of different morphologies including nanotubes, nanowires, and a range of spherical structures. Carbon nano-scale material is an important branch in nano-technologies.

Carbon nanotubes (CNT) are sheets of graphite rolled up to make a tube. The dimensions are variable (down to 0.4nm in diameter). Nanotubes can be formed within nanotubes leading to a distinction between multi-walled and single-walled carbon nanotubes (MW- and SWCNT). Apart from remarkable tensile strength, nanotubes exhibit varying electrical properties (depending on the way the graphite structure spirals around the tube, and other factors) and so they can be insulating, semi-conducting or conducting. Due to their large surface area CNTs are interesting media for electrical energy storage and they are still under investigation as a hydrogen storage medium [18]. CNTs also show good properties in electron emission which could result in large area display applications [19].

C_{60} fullerenes were first discovered in 1985 by Kroto et al [20]. Nanotubes and fullerenes were first observed in 1991 by Iijima [21] in the carbon soot of graphite electrodes during an arc discharge with a current of 100A. The first macroscopic production of carbon nanotubes was made in 1992 by two researchers at NEC's Fundamental Research Laboratory [22]. In the past 17 years there has been substantial research effort in investigating the formation of CNTs with varying arc discharge configurations and gaseous environment, such as by plasma chemical vapour deposition (CVD) [23,24,25], laser vaporization [26], the use of carbon arc in helium [21, 27,28], in argon [29], in nitrogen [30], in sodium chloride solution [31], and in water maintained gaseous environment [9-10,32-38].

Among all the methods mentioned here, the plasma in water environment is very promising since it has several distinct advantages. Firstly, it does not require vacuum environment that is needed for plasma based CVD and the purity of the product is usually high [9]. Secondly, the production rate can be high as a result of efficient cooling of the reaction region near the cathode and arc edge by water and water vapour [10]. Thirdly, this method does not need any special method to remove the nanomaterials from the reaction surface since the particles can automatically detach from the electrode surface and float to the water surface or sink to the bottom of the container for collection.

In the past 10 years there has been increasing activities worldwide to use carbon arcs generated in water to form CNTs and other nano-scale materials. Most of the research has however focused on the examination of the structure of the product using Transmission Electron Microscopy (TEM) and Scanning Electron Microscopy (SEM). Although there is overall measurement of the erosion rate of electrode (mainly anode, for example 117mg/min at 30A and 20V with a gap length of 1mm), product rate (15% of electrode erosion) and water evaporation rate ($100cm^3/min$), there is a serious lack in understanding the formation of general plasma environment associated with bubble growth and the pattern of transport of carbon particles (ions and atoms) from the erosion surface to the reaction zone. There has also been little knowledge on the mechanisms of formation of carbon structures

Limited spectroscopic diagnosis of the emission characteristics of the water based arc and its plasma parameters is available but the results are obtained with an average sense. Lange et al [39] used a CCD camera to identify the lines and bands emitted from the water plasma. The Swan band from the C_2 radicals are then used to derive the column density (density in conventional meaning integrated over electrode gap length, thus having a unit of $1/m^2$) of C_2 and the temperature. Because of the fluctuations of the plasma zone associated with bubble dispersion and motion of arc root over the electrode surface, the results can only be interpreted on an average sense. For the discharge condition of 40A and 21V, the temperature is within the range of 5500K to 6500K in the electrode gap. It was noted that the same discharge condition in helium results in a plasma temperature that is 1500K lower than that in the water plasma [39].

The C_2 number density is however strongly affected by the material of the electrodes. The measured column density (number density multiplied by the electrode gap) with pure carbon (graphite) electrodes is lower ($1.0x10^{19}/m^2$) than that with C+0.8% Gd doped electrode ($1.4x10^{19}/m^2$). It is proposed that the lower density is a consequence of low erosion rate of pure carbon in comparison with doped electrode material.

The formation and growth of CNTs and fullerenes requires the existence of a region with temperature below the boiling point of carbon which is 4203K. The possible regions that meet this temperature requirement are the water cooled cathode surface and at the edge of the plasma column where steep temperature gradient exists. It is therefore not surprising that all the plasma in water arc systems use a very small electrode gap length between 0.7mm to 1.5mm and a current below 100A to create such a cooled region. Although these parameters are obtained from experience by examining the product rate and morphology of carbon structures, it nevertheless has its physical reasons. As shown in figure 1.3, carbon vapour is commonly produced from a small anode with a diameter of 5mm to 6mm. The use of a small anode tip assured a high and uniform energy flux from the arc column to the electrode surface, thus maintaining stable electrode erosion. On the other hand, a small anode attachment results in a stronger magnetic pinch effect which produces gas flow away from the anode surface. This convective flux helps transport the produced carbon particles towards the cathode surface.

The reasons for the use of a small gap length are not well explained in the literature. There could be two possibilities. Firstly, with a larger gap length, there will be excessive Ohmic heating dumped into the arc column and more energy will be lost through radiation, increasing the system instability and reducing the system efficiency. Secondly, with a longer electrode gap carbon vapour produced at the anode surface may be more easily transported outside the arc column by diffusion and convection, resulting in less carbon particles reaching the cathode surface and reduce the production rate of carbon structures.

It has been proposed by Gamaly [40] that the growth of nanotubes is a result of directed motion of carbon ions from the anode under the action of electric field. However, this view is not shared by some of the other researchers since the latter have

demonstrated that nanotubes can also grow in an environment with isotropic velocity distribution of carbon atoms or ions [26]. However, it is commonly accepted that the presence of high concentration of carbon particles (ions or atoms) and a suitable temperature environment for nucleation and growth of the carbon structures is critical to the production rate of the nanostructures.

A detailed understanding of the plasma environment and the transport of carbon species can only be obtained by appropriately modelling the arcing process. This is the second objective of the present work. Since the formation of carbon structures is far too complicated, therefore the present work is mainly concerned with the establishment of a model to simulate the generation of carbon vapour from anode, the transport of carbon vapour into the arcing environment and the dynamics of gas bubbles. It is hoped that such a model will serve as a platform upon which further advanced investigation into the formation of carbon nanostructure is based.

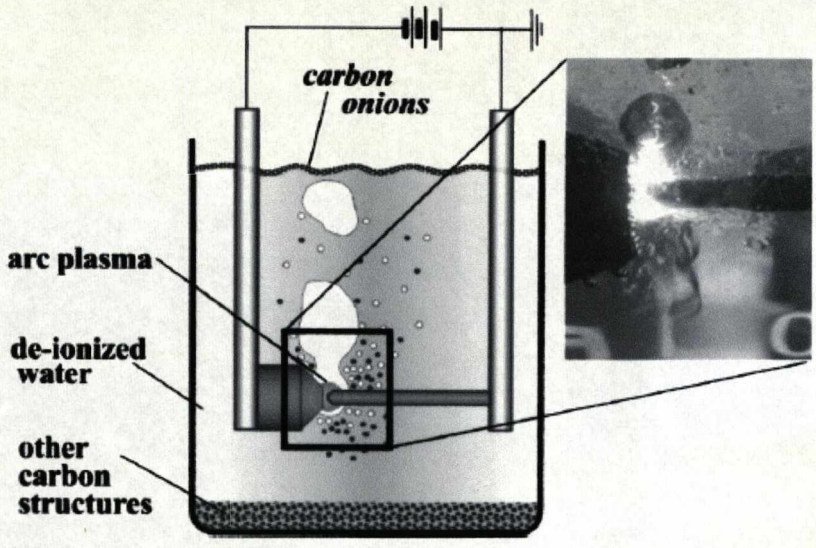

(a)

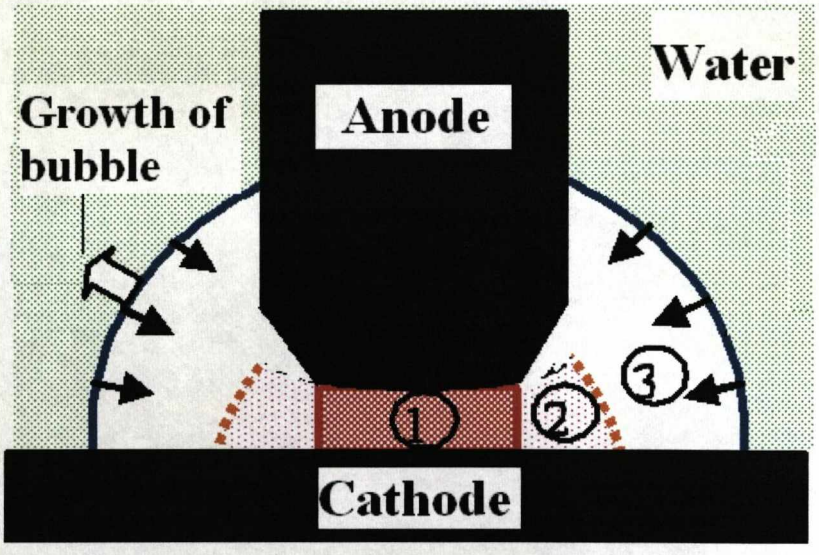

(b)

Figure 1.3 Photograph of the water based carbon arc system (a) [9] and schematic diagram of a carbon arc generated in water (b) with three regions of (1) plasma column, (2) arc edge with steep temperature gradient and (3) ambient region with moving boundary as a result of water evaporation and electrode erosion.

1.5 Review of Arc Models

Since the middle nineteen sixties there have been intense research activities into the field of arc plasma modelling. Extensive efforts have been made to establish a satisfactory arc model, which will ultimately lead to an analytical design method for plasma engineering systems. The essence of arc modelling is to find an adequate mathematical description of important physical processes occurring in a plasma system. The following review on arc modelling in chronological order shows that the ability to model a plasma system is closely related to knowledge and understanding that is available to the modellers, the development of computational numerical schemes and the computing power.

1.5.1 Early "Black Box" models

The first model was probably proposed by Slepian [41] for arcs in high voltage switchgear. The first mathematical description of a dynamic arc was given in 1939 by Cassie [42], who assumed constant and uniform temperature in the arc column. This is virtually an approximation for radiation controlled, optically thin arc at very high current. The diameter of the arc responds proportionally to the variation of the electric current. Since there is no description of the arc's internal structure, this type of model is commonly referred to as the black box model. In 1943, Mayr [43] proposed a model for low current arc. He assumed that the arc radius and the energy loss per unit length remain constant. By relating the resistance of the arc to its heat content through an exponential function, Mayr expressed the energy conservation equation as a simple first order (with respect to time) differential equation. The models of Cassie and Mayr are only for extreme cases in circuit interruption arcs.

Browne [44] in 1948 combined these two models to use them to describe circuit breaker arcs at high current (Cassie's equation) and low current (Mayr). Since these black box models do not take account of the plasma physics, their performance largely depends on the availability of test results and their applicability is restricted to situations for which experimental results are used to derive the model parameters.

Elenbaas [45] in 1946 first started the work to describe the arc's behaviour in terms of its thermal and electrical properties based on energy conservation. He assumed a uniform, cylindrical arc column maintained by a DC current, for which the energy loss is solely due to thermal conduction. The conservation equation (also known as Elenbaas equation) is then given by

$$\frac{1}{r}\frac{d}{dr}(rk\frac{dT}{dr})+\sigma E^2=0 \tag{1.1}$$

where k is the thermal conductivity, σ the electrical conductivity, and E the axial electrical field. Equation (1.1) is obviously oversimplified in that some of the important processes such as radiation and convection are excluded from the energy balance, thus limiting its validity to arcs with negligible axial variation and radiation energy loss. Subsequent applications of Elenbaas' equation by Frind [46] and Phillips [47] to transient wall stabilised arcs established for the first time how the arc's time constant is related to the gas properties and the system dimension.

1.5.2 Integral model

In high voltage circuit breakers arcs usually burn in a strongly accelerating flow. Thus the effect of convection had to be considered. However due to the relatively high computational cost in comparison with that of short-circuit test in the nineteen seventies simplifications of arc conservation equations were necessary. It was assumed that the arcs are axisymmetrical. Arc conservation equations were radially integrated. The resultant radially integrated conservation equations are known as the integral arc conservation equations. The closure of the integral arc conservation equations requires knowledge of the radial temperature and velocity profiles. The differences between various arc integral models lie with the different assumptions on the temperature and velocity profiles. A series of seven papers on integral arc modelling were published by Swanson and Roidt [48-54] between 1970 and 1977, which, together with the work of Topham [55], marked a turning point in arc modelling. The similarity between an arc in an axial flow and a boundary layer was clearly recognised and used to simplify the arc conservation equations. However, their starting conservation equation for energy

[48] is in general not correct, as pointed out by Fang [56]. Their treatment of the terms in the radially integrated energy equation was not physically justified.

An important step in the development of a simplified method of arc analysis, the boundary layer integral method, was taken in 1974 by Cowley [57] in that the arc conservation equations in general form, together with the external flow equations, were rigorously formulated. In a later paper [58], Chan et al extended Cowley's formulation to include an energy integral equation for the arc conducting zone. Thus, the models discussed above are all special cases of this general formulation. The Liverpool-Cambridge arc model has achieved considerable success in elucidating experimental results [59,60,61].

1.5.3 Two dimensional differential method

During the last two decades, the rapid increase in computing power at reduced cost and the availability of reliable numerical method for solving highly nonlinear partial differential flow conservation equations [62] have made arc modelling in full differential form practical. It must be noted that these models are for two dimensional situations. The basic idea of the differential approach is to solve the conservation equations of mass, momentum and energy in full differential form with appropriate initial and boundary conditions of the physical domain. While substantial effort was still directed towards switching arc modelling [62-71], there has been parallel effort on modelling of thermal plasmas for material processing, cutting and welding, and plasma decomposition. Free burning arcs have been used in many industrial applications such as welding, arc lamps, arc furnaces, plasma cutting and plasma heating for mineral processing. Successful simulation of free burning arcs has so far been based on the work of Maecker [72] who first explained the generation of arc flow on the basis of self-magnetic compression on the arc column.

Extensive investigation into free burning arcs in the last twenty five years has been focused on several aspects of the generation of arc plasma. Models differ from each other mainly in two aspects: the arc rooting (current density distribution over the cathode surface) and the calculation of radiation transfer. Predictions based on laminar

flow theory and the assumption of optical thin arc column agreed well with measured temperature field [73-79] for 200A steady state argon arcs.

Arc rooting is a complex phenomenon that involves the interaction between plasma and electrode surface, resulting in a non-equilibrium sheath layer. Most of the models for free burning arcs neglect this sheath layer and assume a distribution of current density over the cathode surface. The current density over the axisymmetrical cathode is usually described by an exponentially decaying function of the distance from the axis of the cathode surface [74,75] or of the square of the distance from the centre [78]. There are also models assuming uniform current density in a circular spot on the cathode surface [73]. The current density distribution and heat conduction at the cathode surface had also been calculated by introducing one dimensional conservation equations of electron number density and energy and a generalised Ohm's law in the cathode sheath layer [76,77]. More recently, there has been considerable effort [80-86] to develop models for the cathode and anode layers by considering mass balance for electrons, ions, neutrals and the change of ions velocity distribution function from Maxwellian to a profile fulfilling the so called Bohm criteria [87].

Since the late nineteen eighties commercial computational fluid packages have been adapted for arc modelling with considerable success. These packages are usually installed on a PC or a laptop. Thus, PC based arc modelling has become a useful tool to engineers and designers.

1.6 Recent Development in Three Dimensional Modelling of Thermal Plasmas

Only very recently we have witnessed an increased activity in modelling three dimensional thermal plasmas. The physical description of three dimensional arcs is similar to that for two dimensional arcs. However, the computational effort required for a three dimensional arc is much greater than that needed for two dimensional (2D) arc modelling. The main difficulty lies with the availability of computational software that can be used to accurately represent the three dimensional geometry of the plasma system under investigation, and with the computing time required to obtain a well

converged solution on a PC. Compared with 2D simulation, it is much more difficult to ensure rapid convergence of the solution procedure.

Most of the three dimensional modelling work is related to free burning arcs and non-transferred arc torch. Kaddani et al [78] is probably the first person to engage a full three dimensional model in the simulation of a free burning arc in argon at 200-300A, between two plane electrodes. The current density on the cathode surface is specified by an exponential distribution, which is similar to that used in [74]. It was shown that the three dimensional (3D) model produces similar results as those from a 2D model for physical quantities within the arc column. It was also pointed out that the boundary conditions at the cathode in the 3D model plays an important role in maintaining the stability of the arc and this problem does not exist in 2D simulations where stability is intrinsically enforced. Various 3D models were later on proposed to study the free burning arc [88-90] with different focuses. Results from all these models were compared with experimental results of Hsu et al [74]. Freton et al [88] modelled an free burning arc with three gas injectors located around the cathode tip, Blais et al [89] studied a magnetically deflected free burning arc, while Ramirez et al [90] used a 3D model to compare two distinct numerical formulations in representing the electromagnetic problem in welding arcs.

Another category of 3D modelling is related to non-transferred plasma torch generated between a pointed cathode and a nozzle anode [91-93]. One of the steady-state simulations of the arc inside a DC torch was performed by Li and Chen initially [91] by relying on an initially guessed solution to iteratively converge to a stable arc configuration with the anode root attached to a position naturally evolved from the numerical process. This was followed by [93] by using Steenbeck's minimum principle (also known as the principle of minimum entropy production applied to thermal plasmas) to fix the position of the anode attachment. Gonzales et al [92], using the commercial software FLUENT, also performed steady-state simulations of the arc. In their initial work they assumed a position of the attachment by arbitrarily imposing a region with high temperature and high electrical conductivity. However, they were not able to obtain a convergent solution with this approach. Imposing a

constant high electrical conductivity over the anode surface allowed them to obtain a steady-state solution.

Schlitz et al [94-95] used a 3D model to study the effects of external magnetic field and arcing gas on the behaviour of an arc in an enclosed box. The description of the model is three dimensional but the authors used a symmetric plane in the domain. Comparison with experimental results was only carried out for the central line temperature in a single plane. Klinger et al [96] performed steady-state simulations of the arc by arbitrarily specifying the position of the attachment by means of imposing a current density profile over the anode and neglecting the magnetic effects.

Modelling work that is directly relevant to twin torch plasma is very rare and so far only one publication is available with limited information [97]. Barthelemy et al [97] used ESTET 3.4 to model an arc drawn between two parallel electrodes. The magnetic field is calculated using vector potential. They indicated that the arc temperature is between 7000K and 15000K. However they neglected radiation from the arc column in their simulation. Results are given in the form of colour contour diagrams without specifying the boundary conditions that were used to produce the results.

There has been no published work on the simulation of carbon arcs in water. The only publication relevant to the production of nano-particles is that by Bilodeau et al [98] to model a low pressure carbon arc in Helium (13.3kPa) between two rod electrodes. The anode erosion rate was obtained from experiments and used as an input parameter for the arc model. They also imposed zero carbon gradient on the confining wall. One of the basic features is that they neglected the ion drift flux towards the cathode surface by comparing the mobilities of ions and electrons in the plasma column, which is in contrast to the view given by Gamaly [40]. The role of ion drift in the transport of carbon particles towards the cathode surface will be further carefully examined in Chapter 5.

1.7 Scope of Present Investigation

The work in this thesis is aimed at developing realistic arc models for the simulation of atmospheric arc plasma environment which is encountered in application for the production of nanometre scale particles. In consideration of the complexity of the process involved in the formation of the particles, our effort is focused on modelling the plasma environment. For the twin torch plasma system, a three dimensional arc model was developed to accurately represent the electrode/nozzle geometries and to provide sufficient spatial resolution for the arc column. To this end a special numerical program is developed to automatically allocate solid cells in the computational domain to represent the axisymmetric electrode structure in view of the fact that the two electrodes can be placed perpendicular to each other. Without such a programme, it would be extremely difficult to define several hundred of solid patches (required by the computational fluid dynamics (CFD) package in order to represent any solid object in the computational domain) for the electrode.

Lorentz forces produced by the interaction between the current density and the magnetic field induced by the arc's current plays a decisive role in shaping the arc column and the coupling zone of the two jets. Because of the long range nature of the magnetic force, an extended domain from the domain occupied by the arc has been used to implement the boundary conditions required for the solution of the vector potential. Sufficient number of grids have been used to resolve the steep temperature and density gradient near the arc edge. The model is verified by comparing the solution of a free burning arc with available experimental results and modelling results from other work. The twin torch plasma is then simulated at different current levels and included angles to study the plasma behaviour and more importantly, the high temperature environment in the coupling zone since it is the coupling zone that is ultimately used in the production process of nano-particles. Detailed results of temperature, velocity and pressure fields will be given and compared with available experimental results. The role of Lorentz force is discussed in depth.

For the carbon plasma in water, efforts are focused first on the formation of the gaseous environment by simulating the effect of anode erosion and growth of the gas /vapour bubble. Numerical schemes have been developed to represent an evaporating

and moving water surface with a spherical shape. Conservation of mass, momentum and energy is ensured in such numerical schemes. Next, the focus is to consider the transport of carbon vapours from the anode surface to the reaction zone where nanotubes or particles are formed. The arcing process is intrinsically transient and results at different instants of the simulation are presented and discussed. Experimental results on anode erosion, water evaporation and formation rate of nano materials were used to set up our model parameters. The formation of carbon particles is not directly simulated in the present work because of the poor understanding that is available so far. However the loss of carbon particles as a result of formation of carbon structures is taken into account. This model will serve as a platform onto which more advanced model can be further developed to consider the plasma surface interaction and the micro environment in the cathode sheath where CNTs are formed.

1.8 Organization of Thesis

Since the present work involves two distinctive methods used for the production of nano scale materials, extensive literature review and introduction to the fundamental of plasma physics is given in Chapter 1 together with the objectives of the present work. Chapter 2 details the applied conservation and governing equations for numerical computational, the material properties, the radiation model and the calculation of electric and magnetic field. The implementation of the conservation equations, materials properties and boundary conditions into the computational fluid dynamics software PHOENICS are described in Chapter 3. Since the electromagnetic field induced Lorentz force plays an important role in shaping the three dimensional flow, verification of the 3D model using a free burning arc is also given in this chapter to make sure for an axisymmetric case symmetric results are produced. Chapter 4 is devoted to the modelling of twin torch plasmas under various conditions while the modelling of the carbon plasma in water is detailed in Chapter 5. Conclusion from the present work is drawn in Chapter 6 where possible future work is also discussed.

1.9 References

[1] Boulos M. I., "Thermal Plasma – Fundamentals and Applications (Volume 1)", Plenum Press, New York, 1994

[2] Kearns M., "Development and Applications of Ultrafine Aluminium Powders", Materials Science and Engineering A, Vol. 375-377, pp. 120-126, 2004

[3] Hsin Y. L., Hwang K. C., Chen F. R. and Kai J. J., "Production and in-situ Metal Filling of Carbon Nanotubes in Water", Adv. Mater. Vol. 13, No. 11, 2001

[4] Simon A., "An Introduction to Thermonuclear Research", Pergamon Press, 1959

[5] Pfender E., "Thermal Plasma Technology: Where Do We Stand and Where Are We Going?", Plasma Chemistry and Plasma Processing, Vol. 19, No.1, 1999

[6] Megy S., Bousrih S., Baronnet J. M., Ershov-Pavlov E. A., Williams J. K., Iddles D. M., "Characterization of a Twin-Torch Transferred dc Arc", Plasma Chemistry and Plasma Processing, Vol. 15, No. 2, 1995

[7] Iwao T., Takizawa H., Inaba T., Yumoto M., "Heating Efficiency of Twin Torch Plasma Arc", ISIJ International, Vol. 45, No. 8, pp. 1084-1087, 2005

[8] Ageorges H., Megy S., Chang K., Baronnet J. M., Williams J. K., Chapman C., "Synthesis of Aluminum Nitride in Transferred Arc Plasma Furnaces", Plasma Chemistry and Plasma Processing, Vol. 13, No. 4, 1993

[9] Sano N., Wang H., Alexandrou I., Chhowalla M., Teo K. B. K. and Amaratunga G. A. J., "Properties of carbon onions produced by an arc discharge in water", Journal of Applied Physics, Vol. 92, No. 5, pp. 2783-2788, 2002

[10] Lange H., Sioda M., Huczko A., Zhu Y. Q., Kroto H. W. and Walton D. R. M., "Nanocarbon production by arc discharge in water", Carbon, Vol. 41, pp. 1617-1623, 2003

[11] Williams J. K., "Twin Torch Transferred Arcs with Remote Coupling for Materials Processing and Synthesis", 2nd European Conference on Thermal Plasma Processes, 1992

[12] Frugier P., Girold C., Megy S., Vandensteendam C., Ershov-Pavlov E. A. and Baronnet J. M., "OES Use and Vaporization Modeling for Fly-Ash Plasma Vitrification", Plasma Chemistry and Plasma Processing, Vol. 20, No. 1, 2000

[13] You H., Yan W. Z., Wu C. K., "Numerical Investigation of Flow Field of a Dual-Jet Plasma Generator", Plasma Science & Technology, Vol. 2, No. 1, 2000

[14] Kurskov A. A., Ershov-Pavlov E. A., Chvyaleva L. V., "Reduction of line radiation of an absorbing plasma to an optically transparent plasma", Proceedings of the 8th Symposium on Plasma Chemistry, Vol. 1, pp. 431, 1987

[15] Chvyaleva L. V., Ershov-Pavlov E. A., Kurskov A. A., "Determination of half-width of spectral lines of radiation of an inhomogeneous plasma", Proceedings of the 9th Symposium on Plasma Chemistry, Vol. 1, pp. 394, 1989

[16] Ershov-Pavlov E. A., Kurskov A. A., Chvyaleva L. V., Krat'ko L. I., Chubrik N. I., "An approximate method for measurement of the spectral distribution of the emissivity in inhomogeneous plasma", Proceedings of the 20th international Conference on Phenomena in Ionized Gas, Vol. 3, pp. 825, 1991

[17] Foster L. E., "Nanotechnology: Science, Innovation, and Opportunity", Prentice Hall, 2005

[18] Dillon A. C., Jones K. M., Bekkedahl T. A., Kiang C. H., Bethune D. S. and Heben M. J., "Storage of hydrogen in single-walled carbon nanotubes", Nature, Vol. 386, pp. 377-379, 1997

[19] Baughman R. H., Zakhidov A. A. and de Heer W. A., "Carbon Nanotubes-the Route Toward Applications", Science, Vol. 297, No. 5582, pp. 787-792, 2002

[20] Kroto H. W., Heath J. R., O'Brien S. C., Curl R. F. and Smalley R. E., "C_{60}: Buckminsterfullerene, Nature, Vol. 318, pp. 162, 1985

[21] Iijima S., "Helical microtubules of graphitic carbon", Nature, Vol. 354, pp. 56-58, 1991

[22] Ebbesen, T. W., Ajayan, P. M., "Large-scale synthesis of carbon nanotubes". Nature, Vol. 358, pp. 220-222, 1992

[23] Li W. Z., Xie S. S., Qian L. X., Chang B. H., Zou B. S., Zhou W. Y. Zhao R. A. and Wang G., "Large-Scale Synthesis of Aligned Carbon Nanotubes", Science, Vol. 274, pp. 1701-1703, 1996

[24] Terrones M., Grobert N., Olivares J., Zhang J. P., Terrones H., Kordatos K., Hsu W. K., Hare J. P., Townsend P. D., Prassides K., Cheetham A. K., Kroto H. W. and Walton D. R. M., "Controlled production of aligned-nanotubes bundles", Nature, Vol. 388, Issue 6637, pp. 52-55, 1997

[25] Ren Z. F., Huang Z. P., Zu J. W., Wang J. H., Bush P., Siegal M. P. and Provencio P. N., "Synthesis of Large Arrays of Well-Aligned Carbon Nanotubes on Glass", Science, Vol. 282, No. 5391, pp. 1105-1107, 1998

[26] Guo T., Nikolaev P., Rinzler A. G., Tomanek D., Colbert D. T. and Smalley R. E, "Self-Assembly of Tubular Fullerenes", J. Phys. Chem., Vol. 99, pp. 10694-10697, 1995

[27] Journet C., Maser W. K., Bernier P., Loiseau A., Lamy de la Chapelle M., Lefrant S., Deniard P., Lee R. and Fischer J. E., "Large-scale production of single-walled carbon nanotubes by the electric-arc technique", Nature, Vol. 388, 756-758, 1997

[28] Nishio M., Akita S., Nakayama Y., "Cooling effect on the growth of carbon nanotubes and optical emission spectroscopy in short-period arc-discharge", Thin Solid Films, 464-465, pp 304-307, 2004

[29] Chen C. K., Perry W. L., Xu H., Jiang Y., Phillips J., "Plasma torch production of macroscopic carbon nanotubes structures", Carbon, Vol. 41, pp. 2555-2560, 2003

[30] Ishigami M., Cumings J., Zettl A. and Chen S., "A simple method for the continuous production of carbon nanotubes", Chem. Phys. Lett., Vol. 319, pp. 457-459, 2000

[31] Wang S. D., Chang M. H., Lan K. M. D., Wu C. C., Cheng J. J. and Chang H. K., "Synthesis of carbon nanotubes by arc discharge in sodium chloride solution", Carbon, Vol. 43, 1778-1814, 2005

[32] Sano N., Wang H., Chhowalla M., Alexandrou I., Amaratunga G. A. J., "Synthesis of carbon 'onions' in water", Nature, Vol. 414, pp. 506, 2001

[33] Antisari M. V., Marazzi R., Krsmanovic R., "Synthesis of multiwall carbon nanotubes by electric arc discharge in liquid environments", Carbon, Vol. 41, pp. 2393-2401, 2003

[34] Sano N., Wang H., Chhowalla M., Alexandrou I., Amaratunga G. A. J., Naito M. and Kanki T., "Fabrication of inorganic molybdenum disulfide fullerenes by arc in water", Chem. Phys. Lett., 368, pp. 331-337, 2003

[35] Zhu H. W., Li X. S., Jiang B., Xu C. L., Zhu Y. F., Wu D. H. and Chen X. H., "Formation of carbon nanotubes in water by the electric-arc technique", Chem. Phys. Lett., 366, pp. 664-669, 2002

[36] Biro L. P., Horvath Z. E., Szalmas L., Kertesz K., Weber F., Juhasz G., Radnoczi G. and Gyulai J., "Continuous carbon nanotube production in underwater AC electric arc", Chemical Physics Letters 372, pp. 399-402, 2003

[37] Alexandrou I., Wang H., Sano N., Amaratunga G. A. J., "Structure of carbon onions and nanotubes formed by arc in liquids", Journal of Chemical Physics, Vol. 120, pp. 1055-1058, 2004

[38] Wang S. D., Chang M. H., Cheng J. J., Chang H. K., Lan K. M. D., "Unusual morphologies of carbon nanoparticles obtained by arc discharges in deionized water", Carbon, Vol. 43, 1317-1339, 2005

[39] Lange H., Saidane K., Razafinimanana M. and Gleizes A., "Temperatures and C_2 column densities in a carbon arc plasma", J. Phys. D: Appl. Phys., 32, pp. 1024-1030, 1999

[40] Gamaly E. G., "Mechanism of carbon nanotube formation in the arc discharge", Physical Review B, Vol. 52, No. 3, pp. 2083-2089, 1995

[41] Slepian J., "Extinction of an a.c. arc", AIEE Trans. Vol. 47, pp. 1398-1402, 1928

[42] Cassie A. M., "Arc rupture and circuit severity: a new theory", CIGRE, Paper 102, pp. 1-14, 1939

[43] Mayr O., "Beitrage zur theorie des statischen und des dynamischen lichtbogens (contribution to the theory of static and dynamic arcs)", Arch. Elect., 37, pp. 588-608, 1943

[44] Browne Jnr T. E., "A study of ac arc behaviour near current zero by means of mathematical models", AIEE Trans., Vol. 67, Pt. 1, pp. 147-153, 1948

[45] Elenbaas W., Phillips Research Report, Vol. 1, No. 5, 1946

[46] Frind G., "Time constant of flat arcs cooled by thermal conduction", IEEE Trans. on Power Apparatus and Systems, Vol. 84, pp. 1125-1131, 1965

[47] Phillips R. L., "The behaviour of dynamic electric arcs", ARL Report 64-150, 1964

[48] Swanson B. W. and Roidt R. M., "Boundary layer analysis of an SF6 circuit breaker arc", IEEE Trans., PAS-90, pp. 1086-1903, 1970

[49] Swanson B. W, Roidt R. M. and Browne T. E., "Arc cooling and short line fault interruption", IEEE Trans. PAS-90, pp. 1094-1102, 1970

[50] Swanson B. W. and Roidt R. M., "Thermal analysis of an SF6 circuit breaker arc", IEEE Trans. PAS-91, pp. 381-389, 1972

[51] Swanson B.W. and Roidt R.M., "Some numerical solutions of the boundary layer equations for an SF6 arc", Proc. IEEE., Vol. 59, pp. 493-501, 1971

[52] Swanson B.W. Roidt R.M, and Browne T.E., "A thermal arc model for short line fault interruption", ET-Z-A, Bd.93, pp. 375-380, 1972

[53] Swanson B.W., "A thermal analysis of short line fault interruption", IEE Winter Power Meeting, Paper C-47, 1974

[54] Swanson B.W., "Nozzle arc interruption in supersonic flow", IEEE Trans., PAS-96, 1977

[55] Topham D.T., "The electric arc in a constant pressure axial gas flow", J. Phys. D., Vol. 4, pp. 114-1125, 1971

[56] Fang M.T.C., "A review of gas-blast circuit breaker arc modelling", ULAP-T75, Dept. of Elec. Eng. And Electronics, University of Liverpool, 1983

[57] Cowley M.D., "Integrated methods of analysing electric arcs: I. formulation", J. Phys. D. , Vol. 7, pp. 2218-2231, 1974

[58] Chan, S.K., Cowley, M.D. and Fang, M.T.C., "Integral methods of analysing electric arcs: III shape factor correlation for low radiation and laminar flow", J. Phys. D., Vol. 9, pp. 1085-1099, 1976

[59] Malghan V.R., Fang M.T.C. and Jones G.R., "Investigation of quasi-steady state high current arcs in an orifice air flow", J. Appl. Phys., Vol. 48, pp. 2331-2337, 1977

[60] Bothwell I.R., Cowley M.D. and Grycz B., IEE Conf. Publication, no. 118, pp. 474-477, 1974

[61] Chapman A. and Jones G.R., "The local electrical properties of gas blast arc near current zero", IEEE Trans. Plasma Science, vol. PS-6, pp. 300-313, 1978

[62] Patankar S.V., "Numerical Heat Transfer and Fluid Flow", Hemisphere, New York, 1984

[63] Ragaller K., Egli W. and Brand K.P., "Dielectric recovery of an axially blown SF_6-arc after current zero, Part II theoretical investigation", IEEE Trans. on Plasma Science, Vol. PS-10, pp. 154-162, 1982

[64] Mitchell R.R., Tuma D.T. and Osterle J.F., "Transient two dimensional calculations of properties of forced convection stabilised electric arcs", IEEE Trans. on Plasma Science, Vol. PS-13, pp. 207-213, 1985

[65] Lowke J.J. and Lee H.E., "A numerical study of a two dimensional circuit breaker arc during current interruption", Proc. of gas discharge and their applications, Oxford, pp. 54-56, 1985

[66] Fang M.T.C. and Lin W.Y., "Current zero behaviour of a gas blast arc, Part I: nitrogen", IEE Proc., Vol. 137, Pt. A, No 4, pp. 175-183, 1990

[67] Fang M.T.C. and Zhuang Q., "Current zero behaviour of an SF_6 gas-blast arc. Part I: Laminar flow". J. Phys. D: Appl. Phys., Vol. 25, pp. 1197-1204, 1992

[68] Fang M.T.C., Kwan S. and Hall W., "Arc-shock interaction inside a supersonic nozzle", IEEE Trans. on Plasma Science, Vol.24, No.1, pp.85-86, 1996

[69] Yan J .D., Fang M .T. C. and Hall W., "The development of PC based CAD tools for auto-expansion circuit breaker design", IEEE Trans. on Power Delivery, Vol.14, pp.176-181, 1999

[70] Zhang J. L., Yan J. D., Murphy A. B., Hall W. and Fang M.T. C., "Computational investigation of arc behaviour in an auto-expansion circuit breaker contaminated by ablated nozzle vapour", IEEE Trans. on Plasma Science, Vol. 30, pp. 706-719, 2002

[71] Claessens M., Moller K. and Thiel HG., "A computational fluid dynamics simulation of high- and low-current arcs in selfblast circuit breakers", J. Phys. D: Appl. Phys. 30, pp. 1899-1907, 1997

[72] Maecker H.Z, Phys H., Z., 141, pp. 198-216, 1955

[73] Kovitya P. and Lowke J. J., "Two-dimensional analysis of free-burning arcs in argon", J. Phys. D: Appl. Phys., 18, pp. 53-70, 1985

[74] Hsu K.C., Etemadi K. and Pfender K., "Study of the free-burning high-intensity argon arc", Appl J., Phys. 54 (3), pp. 1293-1301, 1983

[75] Kovitya J. and Cram L.E., "A two-dimensional model of gas-tungsten welding arcs", Welding Journal, pp. 34-39, 1986

[76] Lowke J.J., Kovitya P. and Schmidt H.P., "Theory of free-burning arc columns including the influence of the cathode", J. Phys. D: Appl. Phys. 25, pp. 1600-1606, 1992

[77] Zhu P. Y., Lowke J.J. and Morrow R., "A unified theory of free burning arcs, cathode sheaths and cathodes", J. Phys. D: Appl. Phys. 25, pp. 1221-1230, 1992

[78] Kaddani A., Zahrai S., Delalondre C. and Simonin O., "Three-dimensional modelling of unsteady high-pressure arcs in argon", J. Phys. D: Appl. Phys. 28, pp. 2294-2305, 1995

[79] Fang M. T. C., Zhang J. L. and Yan J. D., "On the Use of Langmuir Probes for the Diagnosis of Atmospheric Thermal Plasmas", IEEE Transaction on Plasma Science, Vol. 33, No. 4, pp. 1431-1442, 2005

[80] Biehler S., Ecker G. and Riemann K. U., "Theory of the presheath in a weakly ionized plasma with hot neutrals", Phys. Fluids, Vol. 31, Issue 7, 1999

[81] Li H. P. and Benilov M. S., "Effect of near-cathode sheath on heat transfer in high-pressure arc plasmas", J. Phys. D: Appl. Phys., Vol. 40, pp. 2010-2017, 2007

[82] Benilov M. S., "Analysis of thermal non-equilibrium in the near-cathode region of atmospheric-pressure arcs", J. Phys D: Appl. Phys., Vol. 30, pp3353-3359, 1997

[83] Schmitz H. and Riemann K. U., "Analysis of the cathodic region of atmospheric pressure discharges", J. Phys. D: Appl. Phys., Vol. 35, pp. 1727-1735, 2002

[84] Benilov M. S., "Theory and modelling of arc cathodes", Plasma Sources Sci. Technol., Vol. 11, 2002

[85] Benilov M. S. and Cunha M. D., "Heating of refractory cathodes by high-pressure arc plasmas: II", J. Phys. D: Appl. Phys., Vol. 36, pp. 603-614, 2003

[86] Benilov M. S., Cunha M. D. and Naidis G. V., "Modelling interaction of multispecies plasmas with thermionic cathodes", Plasma Sources Sci. Technol., Vol. 14, pp. 517-524, 2005

[87] Rethfeld B., Wendelstorf J., Klein T. and Simon G., "A self-consistent model for the cathode fall region of an electric arc", J. Phys. D: Appl. Phys., Vol. 29, pp. 121-128, 1996

[88] Freton P., Gonzalez J. J. and Gleizes A., "Comparison between a two- and a three-dimensional arc plasma configuration", J. Phys. D: Appl. Phys. 33, pp. 2442-2452, 2000

[89] Blais A., Proulx P. and Boulos M. I., "Three-dimensional numerical modeling of a magnetically deflected dc transferred arcs in argon", J. Phys. D: Appl. Phys. 36, pp. 488-496, 2003

[90] Ramirez M. A., Trapaga G. and McKelliget J., "A comparison between two different numerical formulations of welding arcs simulation", Modelling Simul. Mater. Sci. Eng, 11, pp. 675-695, 2003

[91] Li H. P. and Chen X., "Three-dimensional modelling of a DC non-transferred arc plasma torch", J. Phys. D: Appl. Phys. 34, pp. L99-L102, 2001

[92] Gonzales J. J., Freton P. and Gleizes A. "Comparisons between two- and three-dimensional models: gas injection and arc attachment", J. Phys. D: Appl. Phys. 35, pp. 3181-3191, 2002

[93] Li H. P., Pfender E. and Chen X., "Application of Steenbeck's minimum principle for three-dimensional modeling of DC arc plasma torches", J. Phys. D: Appl. Phys. 36, pp.1084-1096, 2003

[94] Schlitz L. Z., Garimella S. V. and Chan S. H., "Gas dynamics and electromagnetic processes in high-current arc plasmas. Part I. Model formulation and steady state solutions", Journal of Applied Physics, Vol. 85, No. 5, 1999

[95] Schlitz L. Z., Garimella S. V. and Chan S. H., "Gas dynamics and electromagnetic processes in high-current arc plasmas. Part II. Effects of external magnetic fields and gassing materials", Journal of Applied Physics, Vol. 85, No. 5, 1999.

[96] Klinger L., Vos J. B., Appert K., "High-resolution CFD simulation of a plasma torch in 3 dimensions", Centre de Recherches en Physique des Plasmas – Preprint Report, LRP 763, 2003, http://crppwww.epfl.ch

[97] Barthelemy B. Girold C., Delalondre C., Paya B., Baronnet J. M., "Modeling a pilot-scale combustion/vitrification furnace under oxygen plasma arc transferred between twin torches", Proceedings of the 16th Symposium on Plasma Chemistry, 2003

[98] Bilodeau J. F., Pousse J. and Gleizes A., "A Mathematical Model of the Carbon Arc Reactor for Fullerene Synthesis", Plasma Chemistry and Plasma Processing, Vol. 18, No. 2, 1998

Chapter 2

THE ARC MODEL

2.1 Introduction

Computer simulation of an atmospheric plasma system requires the proper formation of governing equations supplemented by material and transport properties and sub-models representing the effect of important processes such as radiation and turbulence. As discussed in Chapter 1, the state of atmospheric arc plasma is often close to LTE as a result of frequent collisions between plasma particles. The plasma flow can also be treated as a continuum medium with a mass averaged velocity. In the present work, two plasma systems were studied, the twin-torch system and the water confined carbon arc. They both operate at atmospheric pressure. The current range in the first system is from 300A to 1000A while in the second system from 30A to 100A. The use of LTE assumption in the first case is well justified because of its high current.

The typical electrode gap in the water confined plasma case is 0.7mm to 1mm. Experimental observations [1,2] have shown that the electrode gap and its vicinity are filled with brightly illuminating substances during the arcing process, suggesting a relatively large region with high temperature. This is in favour of the establishment of LTE condition at the middle of the discharge zone as a result of reduced temperature gradient. Anode erosion is also strong, typically 117mg/min for 30A and sufficient to fill the whole electrode gap in several millisecond (detailed results in Chapter 5). This argument is further supported by spectroscopic diagnosis of the plasma environment [3] where no OH radicals in the radiation emission region were found. It is known that carbon vapour has a higher electrical conductivity than water vapour in the temperature range from 5000K to 10000K (details given in section 2.72). The conducting of 30A through the arc column therefore requires a lower electric field than

that for pure water plasma. This also helps to maintain a smaller temperature difference between the electrons and heavy particles. Recently, Akita et al [4] has used the LTE assumption in the diagnosis of the temperature of an arc generated between two graphite electrodes with He as the background gas at a pressure of 100torr to 300torr. The temperature obtained at the axis is 6000K. In a recent mathematic model developed by Bilodeau et al [5] for carbon arcs in helium at low pressure (13.3kPa), LTE was also assumed for the plasma state of the arc at 80A. Since there is no evidence indicating severe departure from LTE for the carbon arcs, the assumption of LTE will also be used in the present work to describe the carbon arc generated in water. This mean all species attain the same temperature and the plasma state is determined by two parameters, pressure and temperature, for the twin-torch system and with species concentration(s) as additional parameters in case of carbon and water mixture.

The objective of this chapter is therefore to make justified assumptions to the plasma state and to develop governing equations that can be used to describe the plasma flow. Supplementary equations, such as the calculation of the electromagnetic fields will be derived. Material and transport properties of the arcing gas will also be discussed and presented. The specification of boundary conditions and initial conditions (for water confined plasma only) will be deferred to the relevant chapter.

2.2 Basic Governing Equations

Assuming LTE, the electrical and thermodynamic behaviour of arcs can be described by the time averaged Navier-Stokes equations modified to take into account the effects of electromagnetic fields (Ohmic heating and the Lorentz force) and radiation transport. The basic conservation equations in general differential form can be written as:

Continuity equation

$$\frac{\partial \rho}{\partial t} + \nabla \bullet \left(\rho \vec{V}\right) = 0 \tag{2.1}$$

Momentum equation

$$\frac{\partial \rho \vec{V}}{\partial t} + \nabla \bullet \left(\rho \vec{V} \vec{V}\right) - \nabla \bullet \left((\mu_l + \mu_t)\nabla \vec{V}\right) = -\nabla P + \left(\vec{J} \times \vec{B}\right) + viscous\ terms \tag{2.2}$$

Energy equation

$$\frac{\partial \rho h}{\partial t} + \nabla \bullet \left(\rho \vec{V} h\right) - \nabla \bullet \left(\frac{(k_l + k_t)}{c_p} \nabla h\right) = \sigma E^2 + q + viscous\ terms \tag{2.3}$$

Mass concentration equation

$$\frac{\partial \rho c_m}{\partial t} + \nabla \bullet \left(\rho \vec{V} c_m\right) - \nabla \bullet \left(\rho (D_l + D_t)\nabla c_m\right) = 0 \tag{2.4}$$

where ρ, h and P are the total density, enthalpy and pressure respectively. $\vec{V}$ the velocity vector, μ_l and μ_t are the laminar and turbulent molecular viscosity, k_l and k_t are the laminar and turbulent molecular thermal conductivity. c_p is the specific heat at constant pressure, σ the electrical conductivity and c_m the mass concentration of additional species. For laminar flow the values for μ_t and k_t are zero. The discussion of turbulence will be deferred to the relevant chapter.

The closure of equation (2.1) to (2.4) requires the material properties of the arcing gas specifies either as constant or functions of the plasma parameters, the radiation source term q, the equation of state, the current density $\vec{J}$, the magnetic flux density $\vec{B}$, the electric field $\vec{E}$, the laminar diffusivity D_l and turbulent diffusivity D_t.

Equation of state

$$\rho = f(P,T) \tag{2.5}$$

Current continuity

$$\nabla \cdot (\sigma \nabla \varphi) = 0 \tag{2.6}$$

where φ is the electrical potential. In the case where the electrical conductivity, σ, is zero, this equation will result in an incorrect electrical potential distribution. In order to overcome this potential difficulty, the electrical conductivity is limited to a minimum threshold value of 1.0e-3Ohm/m in materials whose electrical conductivity is low.

With the solution of the current continuity equation, the electric field can be computed using equation (2.7) with time varying magnetic potential term omitted. Reason is that the operating currents in the present models are fixed and thus the electric field induced by the varying magnetic field is negligible. The current density is calculated using Ohm's law given by equation (2.8). These values are then used for the calculation of the ohmic heating σE^2 in energy equation (2.3).

Electric field

$$\bar{E} = -\nabla\varphi \tag{2.7}$$

Ohm's law

$$\bar{J} = \sigma\bar{E} \tag{2.8}$$

2.2.1 Governing Equations in 3-dimensional Cartesian Coordinates for the Twin Torch Plasma System

The twin torch plasma system consists of two plasma torches with an included angle from 30 to 175 degrees. It does not have a symmetrical axis, thus requiring a three dimensional arc model. The plasma gas in this case is argon.

The governing equations (2.1–2.3, 2.6-2.8) in Cartesian coordinates can be written as:

Mass
$$\frac{\partial(\rho u)}{\partial x}+\frac{\partial(\rho v)}{\partial y}+\frac{\partial(\rho w)}{\partial z}=0 \tag{2.9}$$

X-momentum
$$\rho\left(u\frac{\partial u}{\partial x}+v\frac{\partial u}{\partial y}+w\frac{\partial u}{\partial z}\right)-\mu\left(\frac{\partial^2 u}{\partial x}+\frac{\partial^2 v}{\partial y}+\frac{\partial^2 w}{\partial z}\right) = -\frac{\partial P}{\partial x}+\left(J_y B_z - J_z B_y\right)+viscous\ terms \tag{2.10}$$

Y-momentum

$$\rho\left(u\frac{\partial v}{\partial x}+v\frac{\partial v}{\partial y}+w\frac{\partial v}{\partial z}\right)-\mu\left(\frac{\partial^2 u}{\partial x}+\frac{\partial^2 v}{\partial y}+\frac{\partial^2 w}{\partial z}\right) = -\frac{\partial P}{\partial y}+\left(J_z B_x - J_x B_z\right)+viscous\ terms \tag{2.11}$$

Z-momentum

$$\rho\left(u\frac{\partial w}{\partial x}+v\frac{\partial w}{\partial y}+w\frac{\partial w}{\partial z}\right)-\mu\left(\frac{\partial^2 u}{\partial x}+\frac{\partial^2 v}{\partial y}+\frac{\partial^2 w}{\partial z}\right) = -\frac{\partial P}{\partial z}+\left(J_x B_y - J_y B_x\right)+viscous\ terms \tag{2.12}$$

Enthalpy

$$\rho\left(u\frac{\partial h}{\partial x}+v\frac{\partial h}{\partial y}+w\frac{\partial h}{\partial z}\right)-\left[\frac{\partial}{\partial x}\left(\frac{k}{c_p}\left(\frac{\partial h}{\partial x}\right)\right)+\frac{\partial}{\partial y}\left(\frac{k}{c_p}\left(\frac{\partial h}{\partial y}\right)\right)+\frac{\partial}{\partial z}\left(\frac{k}{c_p}\left(\frac{\partial h}{\partial z}\right)\right)\right] = \sigma E^2 - q + viscous\ terms \tag{2.13}$$

Current continuity

$$\frac{\partial}{\partial x}\left(\sigma\frac{\partial \varphi}{\partial x}\right)+\frac{\partial}{\partial y}\left(\sigma\frac{\partial \varphi}{\partial y}\right)+\frac{\partial}{\partial z}\left(\sigma\frac{\partial \varphi}{\partial z}\right)=0 \tag{2.14}$$

Electric field

$$\vec{E}=-\left(\frac{\partial \varphi}{\partial x}\hat{x}+\frac{\partial \varphi}{\partial y}\hat{y}+\frac{\partial \varphi}{\partial z}\hat{z}\right) \tag{2.15}$$

Ohm's law

$$J_x=\sigma E_x=-\sigma\frac{\partial \varphi}{\partial x} \qquad J_y=\sigma E_y=-\sigma\frac{\partial \varphi}{\partial y} \qquad J_z=\sigma E_z=-\sigma\frac{\partial \varphi}{\partial z} \tag{2.16}$$

where $\mu=\mu_l+\mu_t$ and $k=k_l+k_t$

2.2.2 Governing Equations in 2-dimensional Polar Cylindrical Coordinates for the Water enclosed Carbon Arc

In reality, because of the irregular bubble growth and burst pattern, the detailed discharge environment deviates from axisymmetry. It has been experimentally observed that large bubbles with dimension of centimetre scale can be generated in the

discharge region and these float up to the liquid's surface. Meanwhile there are also small bubbles generated from the electrolysis process. The electrodes are often arranged in an axisymmetric manner [1-4]. Concentrating on the plasma environment immediately around the electrode gap, Sano et al [1] proposed an axisymmetric description of the bubble shape and the environment enclosed. It is expected that, as long as the plasma environment for the formation of nano-structures is concerned, the use of two dimensional axisymmetric model should be sufficient to predict the natures and characteristics of the carbon environment in which carbon nanostructures are grown.

The governing equations can therefore be written as:

Mass

$$\frac{\partial \rho}{\partial t}+\frac{1}{r}\frac{\partial (r\rho v)}{\partial r}+\frac{\partial (\rho w)}{\partial z}=0 \tag{2.17}$$

Radial-momentum

$$\frac{\partial \rho v}{\partial t}+\frac{1}{r}\frac{\partial \left(r\rho v^2\right)}{\partial r}+\frac{\partial (\rho vw)}{\partial z}-\frac{\partial}{\partial z}\left(\mu\left(\frac{\partial w}{\partial r}+\frac{\partial v}{\partial z}\right)\right) = -\frac{\partial P}{\partial r}-J_z B_\theta + viscous\ terms \tag{2.18}$$

Axial-momentum

$$\frac{\partial \rho w}{\partial t}+\frac{1}{r}\frac{\partial (r\rho wv)}{\partial r}+\frac{\partial \left(\rho w^2\right)}{\partial z}-\frac{1}{r}\frac{\partial}{\partial r}\left(r\mu\left(\frac{\partial w}{\partial r}+\frac{\partial v}{\partial z}\right)\right) = -\frac{\partial P}{\partial z}+J_r B_\theta + viscous\ terms \tag{2.19}$$

Enthalpy

$$\frac{\partial}{\partial t}(\rho h)+\frac{1}{r}\frac{\partial}{\partial r}(r\rho vh)+\frac{\partial}{\partial z}(\rho wh)-\frac{1}{r}\frac{\partial}{\partial r}\left(r\frac{k}{c_p}\frac{\partial h}{\partial r}\right)-\frac{\partial}{\partial z}\left(\frac{k}{c_p}\frac{\partial h}{\partial z}\right) = \sigma E^2 - q + \frac{dP}{dt} + viscous\ terms \tag{2.20}$$

Mass concentration equation

$$\frac{\partial \rho c_m}{\partial t}+\frac{1}{r}\frac{\partial (r\rho vc_m)}{\partial r}+\frac{\partial (\rho wc_m)}{\partial z}-\left(\frac{1}{r}\frac{\partial}{\partial r}\left(r\rho D\frac{\partial c_m}{\partial r}\right)+\frac{\partial}{\partial z}\left(\rho D\frac{\partial c_m}{\partial z}\right)\right)=0 \tag{2.21}$$

Current continuity $$\frac{1}{r}\frac{\partial}{\partial r}\left(r\sigma\frac{\partial\varphi}{\partial r}\right)+\frac{\partial}{\partial z}\left(\sigma\frac{\partial\varphi}{\partial z}\right)=0 \tag{2.22}$$

Electric field $$\vec{E}=-\left[\left(\frac{\partial\varphi}{\partial r}\right)\hat{r}+\left(\frac{\partial\varphi}{\partial z}\right)\hat{z}\right] \tag{2.23}$$

Ohm's law $$J_r=\sigma E_r=-\sigma\frac{\partial\varphi}{\partial r} \qquad J_z=\sigma E_z=-\sigma\frac{\partial\varphi}{\partial z} \tag{2.24}$$

where $\mu=\mu_l+\mu_t$, $k=k_l+k_t$ and $D=D_l+D_t$.

2.3 Magnetic Field Calculation

The self-generated Lorentz force, which results from the interaction between the arc current and the magnetic field induced by the current itself, has to be taken into account when an arc is burning in a stagnant gas environment or for high current. The fundamental Maxwell's equations describing the electromagnetic phenomena in differential forms are

$$\nabla\bullet\vec{D}=0 \tag{2.25a}$$

$$\nabla\bullet\vec{B}=0 \tag{2.25b}$$

$$\nabla\times\vec{H}=\vec{J}+\frac{\partial\vec{D}}{\partial t} \tag{2.25c}$$

$$\nabla\times\vec{E}=-\frac{\partial\vec{B}}{\partial t} \tag{2.25d}$$

where $\vec{D}$ is electric flux density, $\vec{B}$ magnetic flux density, $\vec{H}$ magnetic field, $\vec{E}$ electric field and $\vec{J}$ current density.

For linear, homogeneous (uniform) and isotropic (not aligned along an axis) media,

$$\vec{D}=\varepsilon\vec{E} \tag{2.26a}$$

$$\vec{B} = \mu\vec{H} \tag{2.26b}$$

$$\vec{J} = \sigma\vec{E} \tag{2.26c}$$

where ε is permittivity, μ permeability and σ conductivity.

There exists a curl of a vector $\vec{A}$ or the vector magnetic potential, which satisfy the equation (2.25b), can be defined as

$$\nabla \bullet \nabla \times \vec{A} = 0 \tag{2.27}$$

Thus $$\vec{B} = \nabla \times \vec{A} \tag{2.28}$$

Using equation (2.25c) in steady state and (2.26b), one can write

$$\nabla \times \vec{B} = \mu_0 \vec{J} \tag{2.29}$$

Substituting (2.28) into (2.29),

$$\nabla \times \nabla \times \vec{A} = \mu_0 \vec{J} \tag{2.30}$$

and using vector identity the following equation is obtained

$$\nabla\left(\nabla \bullet \vec{A}\right) - \nabla^2 \vec{A} = \mu_0 \vec{J} \tag{2.31}$$

The solution for $\vec{A}$ is unique only if its curl, divergence and value at one point are specified [6]. The curl is specified by $\vec{B} = \nabla \times \vec{A}$, divergence by letting $\nabla \bullet \vec{A} = 0$ and allowing $\vec{A}$ equal to zero at infinity. Equation (2.31) becomes

$$\nabla^2 \vec{A} = -\mu_0 \vec{J} \tag{2.32}$$

Equation (2.32) is also known as the Poisson's equation and can be decomposed into three separate equations in Cartesian coordinates

$$\nabla^2 A_x = -\mu_0 J_x \qquad \nabla^2 A_y = -\mu_0 J_y \qquad \nabla^2 A_z = -\mu_0 J_z \tag{2.33}$$

The vector magnetic potential $\bar{A}$ can be computed by solving the equations (2.33) with the appropriate boundary condition which will be given in the relevant chapters. The magnetic field $\bar{B}$ is calculated using equation (2.34)

Magnetic field $$B = \left(\frac{\partial A_z}{\partial y} - \frac{\partial A_y}{\partial z}\right)\hat{x} + \left(\frac{\partial A_x}{\partial z} - \frac{\partial A_z}{\partial x}\right)\hat{y} + \left(\frac{\partial A_y}{\partial x} - \frac{\partial A_x}{\partial y}\right)\hat{z} \qquad (2.34)$$

Solution to equation (2.33) is sensitive to the boundary conditions, which is unknown other than being equal to zero at infinity. An extension of the CFD grid system and special treatment of the current density distribution is implemented for the 3-dimensional model in order to obtain accurate solution. This will be discussed in detail in Chapter 3.

For the 2 dimensional case, there are 2 methods of calculating the induced magnetic field, i.e. the solution of the potential vectors equations and Ampere's law. The first method, as explained above, requires the calculation of two scalars, A_r and A_z, the radial and axial potential vector components, using equations

$$B_r = \frac{1}{r}\frac{\partial A_z}{\partial \phi} - \frac{\partial A_\phi}{\partial z} \qquad B_\theta = \frac{\partial A_r}{\partial z} - \frac{\partial A_z}{\partial r} \qquad B_z = \frac{1}{r}\left[\frac{\partial}{\partial r}(rA_\phi) - \frac{\partial A_r}{\partial \phi}\right] \qquad (2.35)$$

The second method applies the equation (2.29) directly to calculate the magnetic field using the plasma current density. In 2-D cylindrical coordinates, the magnetic flux density equations are

$$\frac{1}{r}\frac{\partial B_z}{\partial \phi} - \frac{\partial B_\phi}{\partial z} = -\mu_0 J_r \qquad \frac{\partial B_r}{\partial z} - \frac{\partial B_z}{\partial r} = -\mu_0 J_\phi \qquad \frac{1}{r}\left[\frac{\partial}{\partial r}(rB_\phi) - \frac{\partial B_r}{\partial \phi}\right] = -\mu_0 J_z \qquad (2.36)$$

Since $J_z >> J_r$ and $J_\theta = 0$ in the water confined carbon arc case, only the azimuthal magnetic field B_θ is produced and equation (2.36) becomes

$$\frac{1}{r}\frac{\partial}{\partial r}(rB_\theta) = \mu_0 J_z \qquad (2.37)$$

Although the two approaches represent the same physics, different mathematical and numerical formulations are used, and hence, level of complexities and challenges varies. The second method is used in our 2D model for its simplicity and sufficient accuracy in axisymmetric.

2.4 Radiation Model for 3 Dimensional Twin Torch Argon Plasma

Radiation is an important phenomenon in thermal plasmas. However, an accurate account of radiation transport is very complicated and it involves the solution of the radiation transport equation for the whole spectra range in the volume occupied by the arc [7]. The spectrum to be solved is composed of both the continuous and line spectra, where the lines are determined by the discrete energy levels of the atoms and molecules in the plasma. Work have been done in this area [8] but the data available is very limited and the method is also difficult to implement. Several simplified models have been developed and for argon gas, the most common one is the net emission coefficient (NEC) model. This method is used for our current investigation. The net emission coefficient is only function of the arc temperature with no reabsorption region, based on the assumption of the arc plasma being optically thin [9]. When the temperature is lower than 10000K, the net emission coefficient is set to zero. This assumption has been demonstrated valid for the central regions of arcs and thermal plasmas [10] and successfully used [11,12,13].

The radiation transport model requires the use of net emission coefficients of argon which are given by Menart [14]. In the twin torch plasma system, the arc is burning between a cathode which is made of thoriated tungsten and a copper anode. Both electrodes are water cooled for minimum electrode erosion. Therefore the contamination of metal vapour to the plasma gas is not considered in the present work. Figure 2.1 shows the NEC at 1atm for different path lengths [14]. The net emission coefficient increases by several orders of magnitude over the temperature range shown, which indicates the rate of emission increases faster than absorption when temperature increases. It can be seen that as the path length (L) increases the net emission

coefficient decreases. Often the largest decrease in the net emission coefficient occurs in the first 0.001cm. The reason that the net emission coefficient decreases as the path length increases is the amount of absorption increases while the amount of emission remains the same. Some of the stronger lines are absorbed in very short distances (strong absorption occurs in as short a distance as 1millimetre (mm) for the argon resonance lines), which is why there is a significant change in the net emission coefficients from a path length of 0.000cm to 0.001cm.

Radiation re-absorption will not be considered in the twin torch plasma case. Since optically thin assumption is used for the argon plasma, the NEC of 0mm will be used in the calculation.

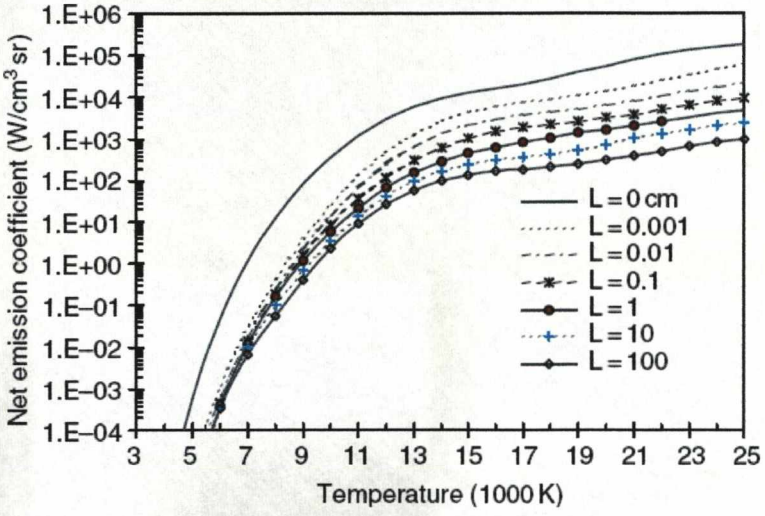

Figure 2.1 Net emission coefficient for Argon plasma at 1atm for different geometrical path lengths (L) for the wavelength range 0.03-2.5 μm [14]

2.5 Radiation Data & Model for Water-Carbon Vapours

In the water confined carbon arc case, the arc is initially burning in water vapour before the carbon vapour produced from anode erosion fills the whole arc column. At a later stage, although the arc is possibly burning in carbon environment, radiation from the arc core can still be absorbed by gas surrounding the arc core. Thus, the radiation characteristics of carbon-water vapour mixture have to be known. However there is no

published net emission coefficient for carbon-water mixture at different concentration of the former. Riad et al [15] calculated the net emission coefficient of carbon and water vapour separately. The net emission coefficient for these two species is shown separately in figures 2.2 and 2.3. It can be seen that carbon has much stronger radiation in the range of temperature interesting to us, 5000K to 10000K. Since there are no detailed investigation and published data available for the net emission coefficient of carbon-water vapour mixture, interpolation is used to calculate the NEC of the mixture with carbon concentration as a parameter.

In a water vapour environment, it was found necessary to consider radiation re-absorption in cold water vapour [16]. Thus to calculate the radiation as energy source in the governing equation, the emission from the arc core which is basically carbon and the re-absorption at the edge with a mixed environment is first calculated. The empirical one dimensional radiation model of Zhang et al [17] is chosen for the present work since it characteristically represent the scenario described here. In the model of [17], an arc radiation radius, which is equivalent to the radius of an isothermal cylinder, is required to calculate the NEC. This radius is normally taken as the radial distance from the symmetric axis to the location of 83% of the axis temperature. The arc that is within this emission radius is called the arc core. A percentage of the radiation from the arc core, which is unknown in the present work, is re-absorbed in the region surrounding the arc. The same approach is used but the re-absorption region is extended to the whole cold vapour region, as suggested in [16]. A schematic diagram of the approximate radiation model is shown in figure 2.4, where T_0 is the maximum temperature at the arc axis, R83 the radius where temperature is equal to 83% of the T_0, R_B is the bubble radius and q_0 is the maximum absorption coefficient located at $0.5(R_B+R83)$. For the carbon arc confined in water, the radial temperature profile is different from an arc in nozzle flow. Numerical difficulty was encountered when using the original definition of the emission radius for the calculation of net emission coefficient. In the present work, a fixed radius of 1mm, which is the typical dimension of the arc core, is used across the whole arc column for this purpose.

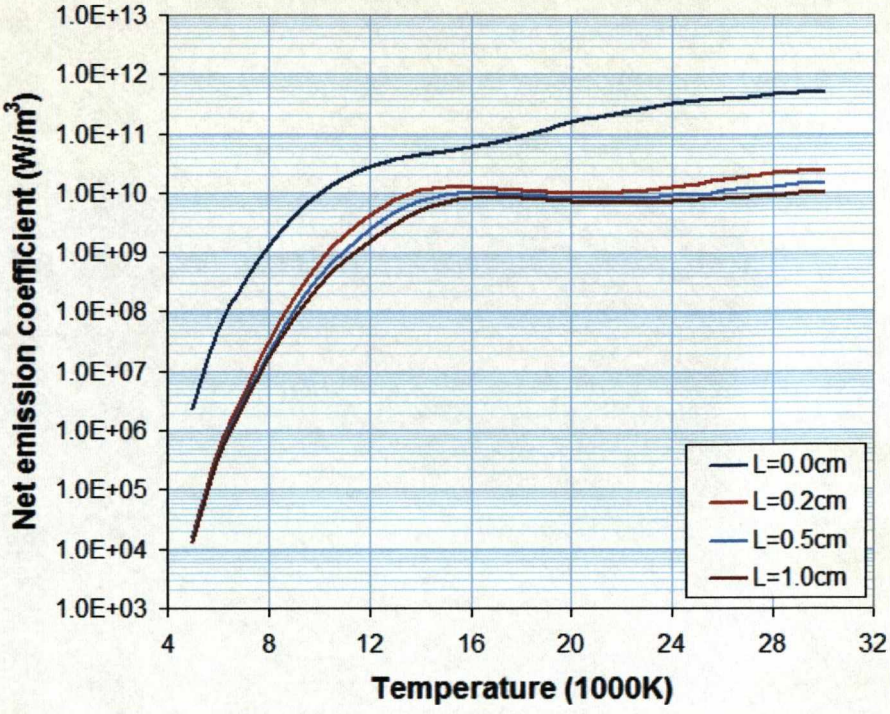

Figure 2.2 Carbon vapour NEC at 1atm for various geometrical path lengths (L)

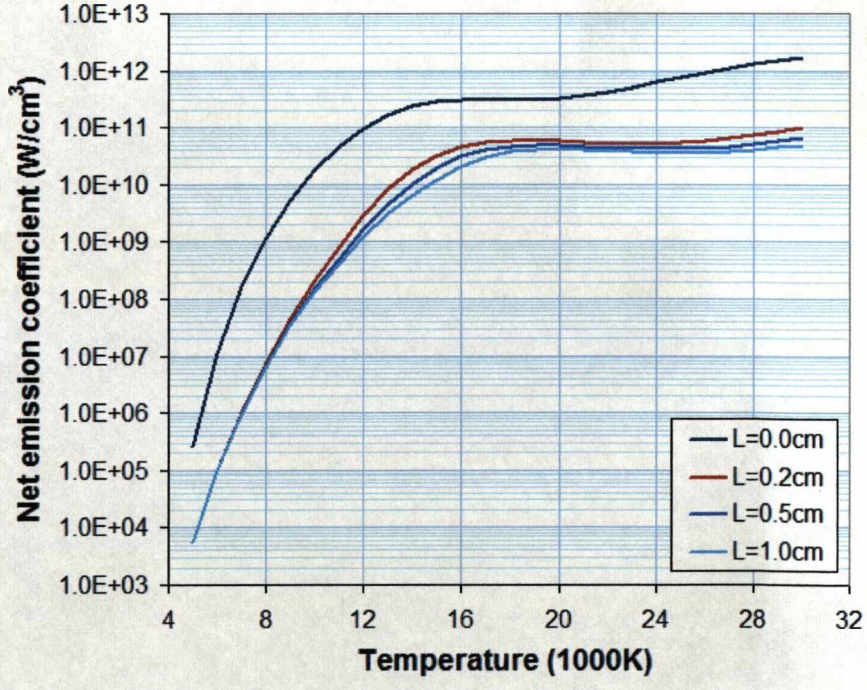

Figure 2.3 Water vapour NEC at 1atm for various geometrical path lengths (L)

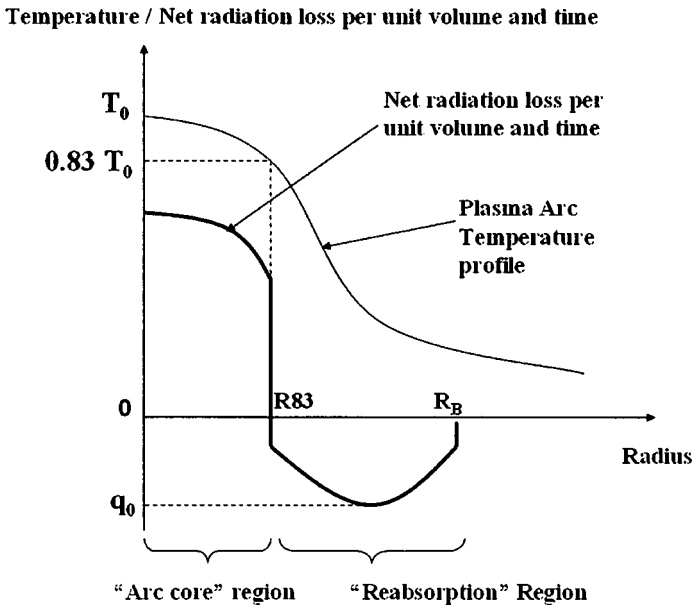

Figure 2.4 Schematic diagram of the approximate radiation model

2.6 Turbulence Model for 3-D Twin Torch Plasma Arc in Argon gas

The argon plasma gas has often been assumed to be laminar in many published papers on free burning arcs [18-23] mostly on 2D models. In principle, turbulence could exists in flows with high Reynolds number or flows of unstable nature. Tetronics has high speed recording of the twin torch DC plasma. It is shown that the illuminating part at the jet coupling zone is not stable. The level of coupling (overlapped part of the two jets) fluctuates. Since a steady state model is used for the simulation, the fluctuation in the level of coupling can be regarded as a way of turbulence mixing. Thus the effect of adding turbulence to the flow and energy transfer needs to be assessed. This will be discussed in detail in Chapter 4.

Due to the uncertainty in the effect of turbulent in the twin torch system, a simple model with minimum computing cost is preferred. In the present work, the simple Prandtl mixing length model is used to represent the effect of turbulence. In a three dimension coordinate system, the turbulence viscosity is related to the velocity through the following equation:

$$\mu_t = (cD)^2\left(\left|\frac{\partial u}{\partial y}\right|+\left|\frac{\partial u}{\partial z}\right|+\left|\frac{\partial v}{\partial x}\right|+\left|\frac{\partial v}{\partial z}\right|+\left|\frac{\partial w}{\partial x}\right|+\left|\frac{\partial w}{\partial y}\right|\right) \tag{2.38}$$

where c is the turbulent parameter and D is the jet width. The value of c will be used as an adjustable parameter in Chapter 4 to assess the influence of turbulence on the predicted arc voltage. The plasma jet has a dimension in the order of 5mm to 10mm. For simplicity, D is given a constant value of 10mm in the present work.

For the water confined carbon plasma, the flow is assumed to be laminar.

2.7 Material Properties

2.7.1 Material Properties of Argon

Argon gas is the inert plasma gas used in the simulation of the twin torch plasma system. In general, argon is preferred as a plasma gas for nano-scale powder production due to its chemical stability. The problem of oxidation, nitriding can be avoided. The plasma temperature is expected to be in the range from 5000K to 15000K. The thermodynamic (specific heat, enthalpy, etc) and transport (viscosity, thermal conductivity, electrical conductivity, etc) properties depend strongly on the composition of the plasma. For argon at atmospheric pressure and temperatures below 35000K, the argon gas consists of Ar, Ar^+, Ar^{++}, Ar^{+++} and e^-. For T < 15000K, Ar atoms and Ar^+ ions are the only heavy species present. Figure 2.5 shows the temperature dependence of the composition (species number densities) of argon plasma at atmospheric pressure (starting from one mole of Ar at room temperature).

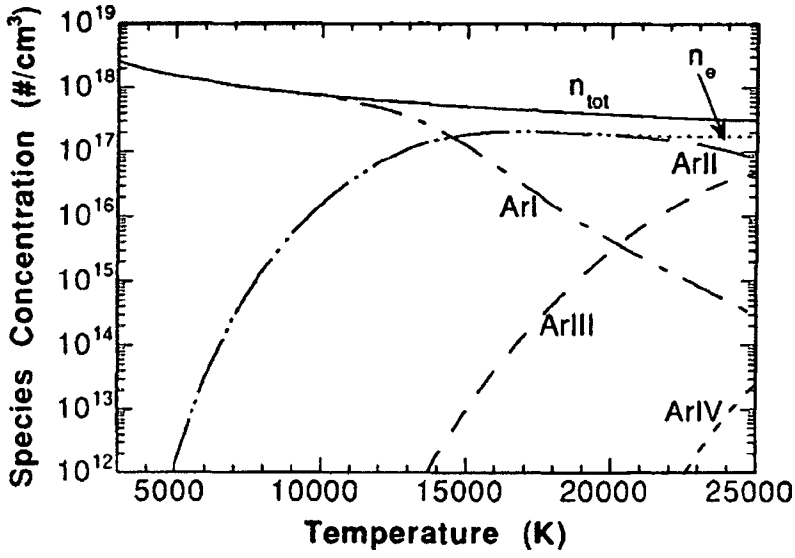

Figure 2.5 Equilibrium composition of a 1atm, pure argon plasma [24]

One of the important characteristics of thermal plasmas is the nonlinearity of the thermodynamic properties with temperature. Figure 2.6 and 2.7 show the variation of enthalpy and specific heat with temperature at atmospheric pressure. The peaks correspond to the first ionization and second ionization of the argon gas at approximately 14500K and 25500K respectively.

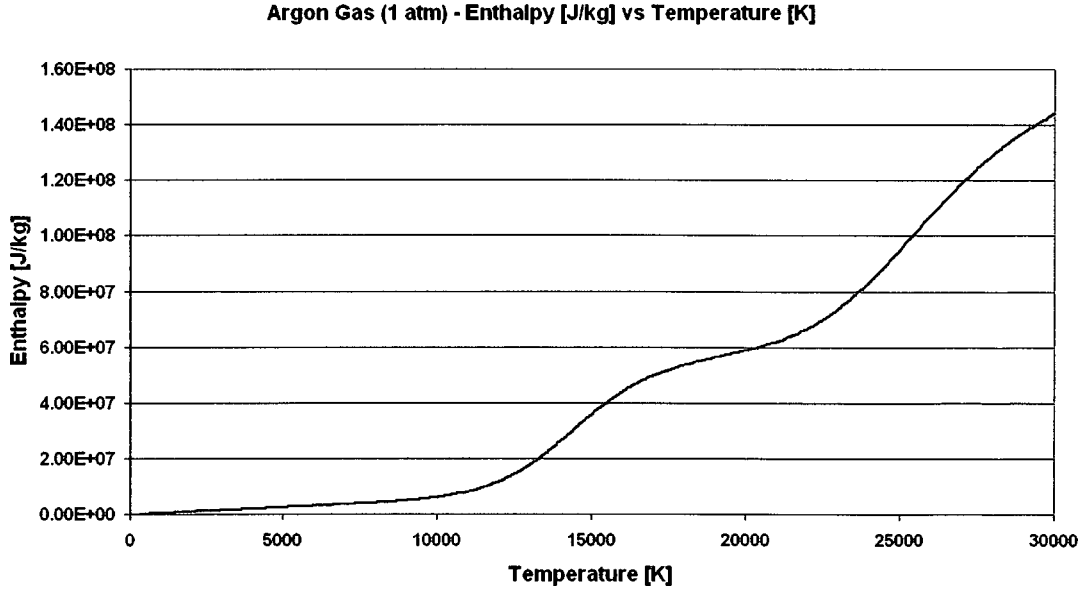

Figure 2.6 Enthalpy of Argon gas at 1atm for temperature range 300K to 30000K

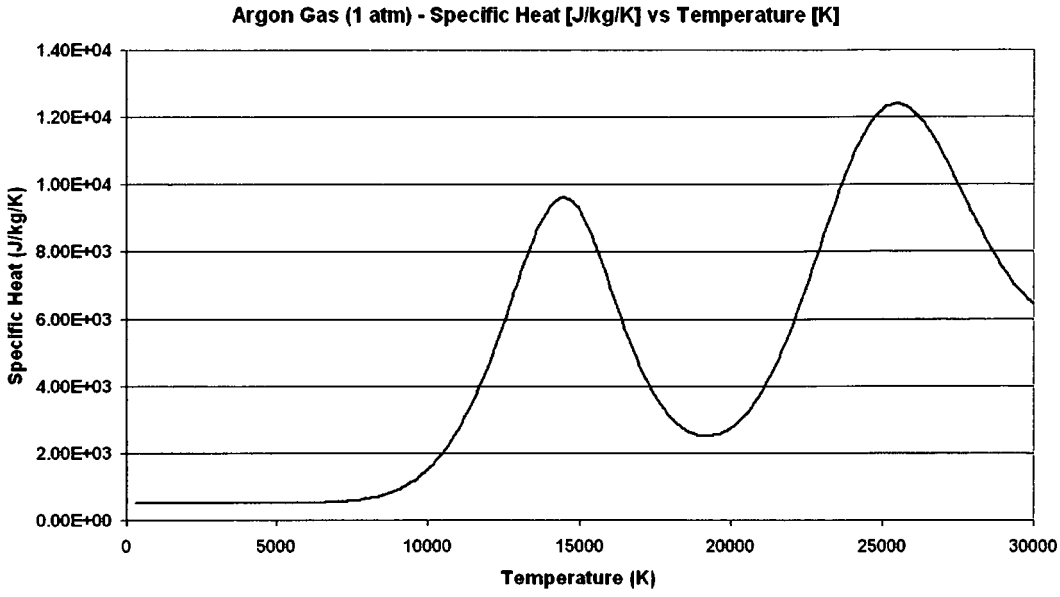

Figure 2.7 Specific heat of Argon gas at 1atm for temperature range 300K to 30000K

Transport properties include the viscosity, thermal conductivity and electrical conductivity. Figure 2.8 shows the variation of viscosity of argon gas with temperature. The values of viscosity increase with temperature at low temperatures. At temperature above 10000K, viscosity decreases with increasing temperatures. This drop in viscosity is due to the ionization of the gas, resulting in Coulomb forces of relatively long range between particles. Figure 2.9 and 2.10 shows the variation of thermal and electrical conductivity with temperature. In the arc model the energy equation is solved in terms of enthalpy. Thus, all material properties are converted into functions of enthalpy in the computation. An extra relation is used to relate plasma temperature to density as shown in figure 2.11. The equation of state for argon at low temperature assumes the form for ideal gas with a gas constant of 208.33J/kg/K. For high temperature, tabulated data is used to calculate density from pressure and enthalpy.

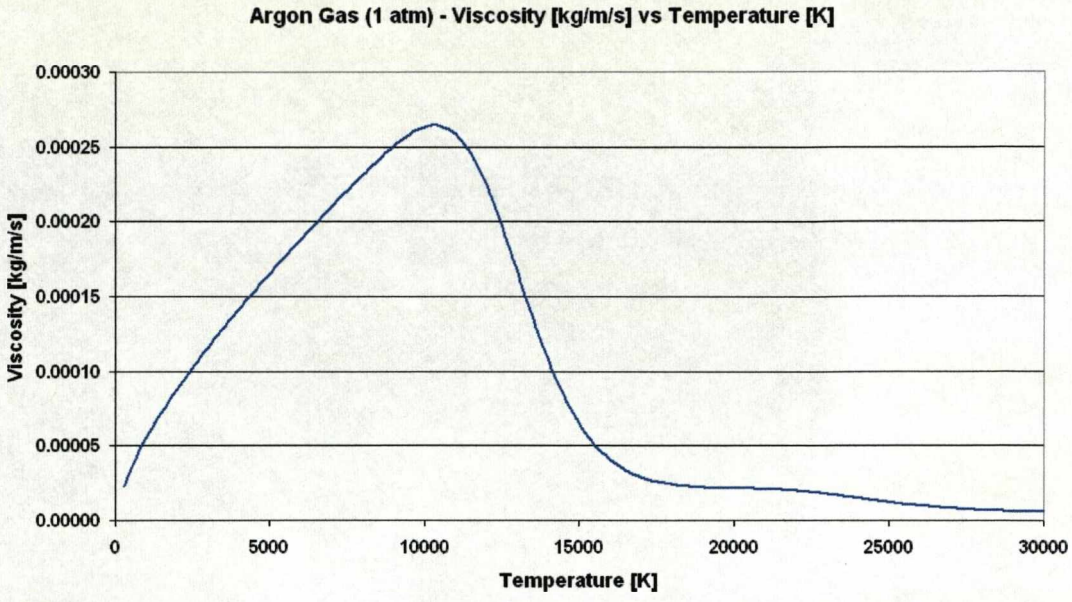

Figure 2.8 Viscosity of Argon gas at 1atm for temperature range 300K to 30000K

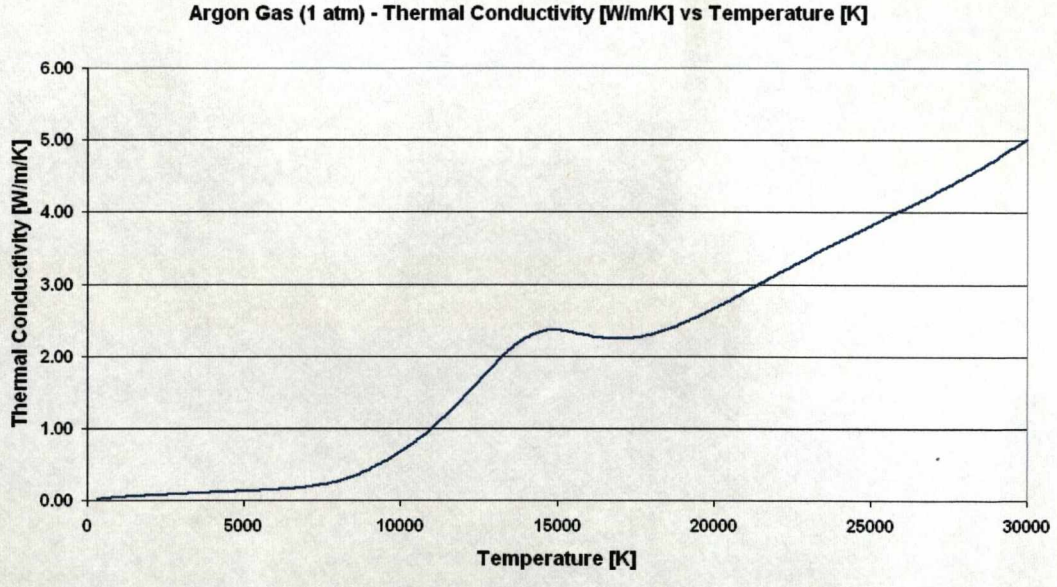

Figure 2.9 Thermal Conductivity of Argon gas at 1atm for temperature range 300K to 30000K

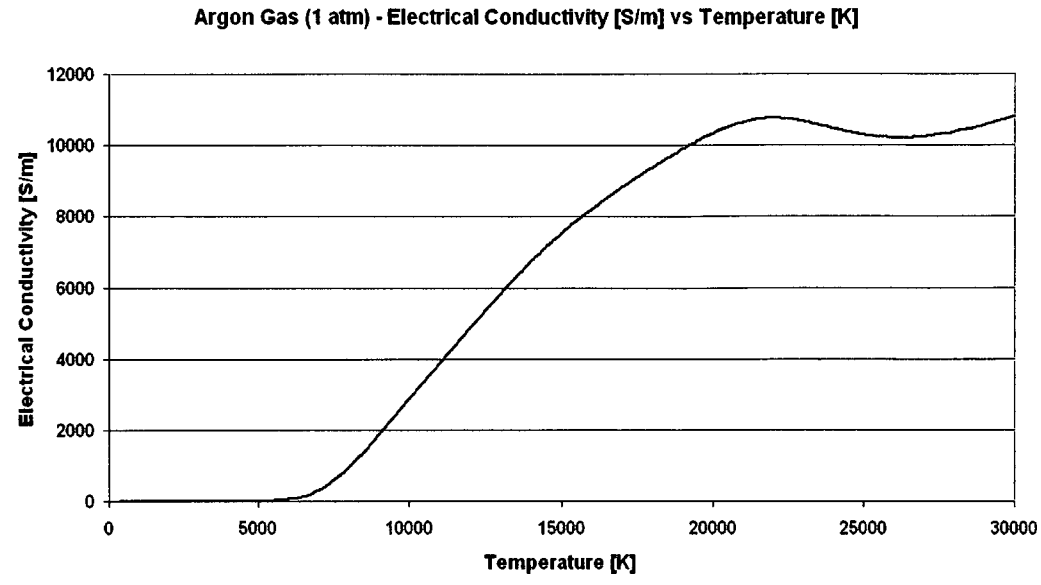

Figure 2.10 Electrical Conductivity of Argon gas at 1atm for temperature range 300K to 30000K

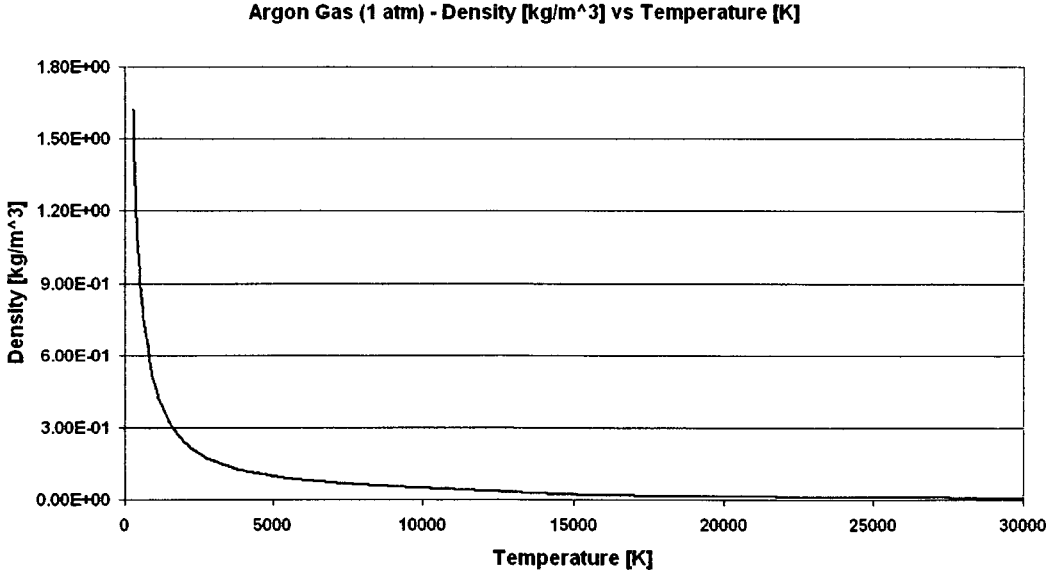

Figure 2.11 Density of Argon gas at 1atm for temperature range 300K to 30000K

2.7.2 Material Properties of Water-Carbon mixture

At present there is no thermodynamic and transport properties available for the mixture of carbon-water vapour. Therefore the properties for pure carbon and pure water vapours are used to calculate the transport properties of the mixture by interpolation with reference to the mass concentration of carbon. The properties are shown in figures 2.12 to 2.18 as a function of the enthalpy.

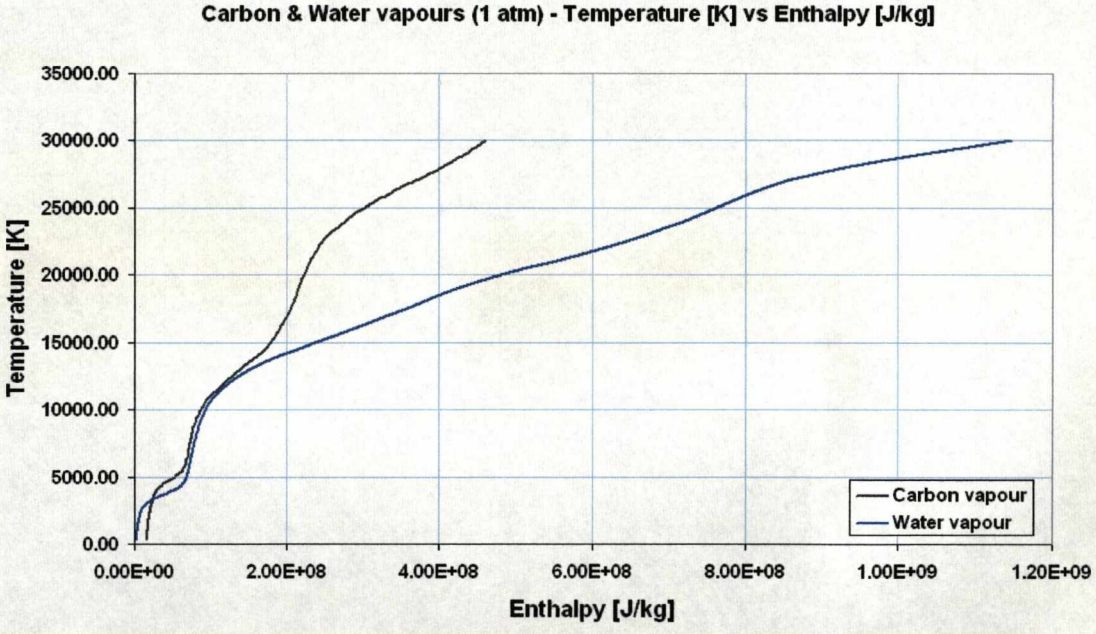

Figure 2.12 Temperature of Carbon and Water vapours as a function of enthalpy at 1atm

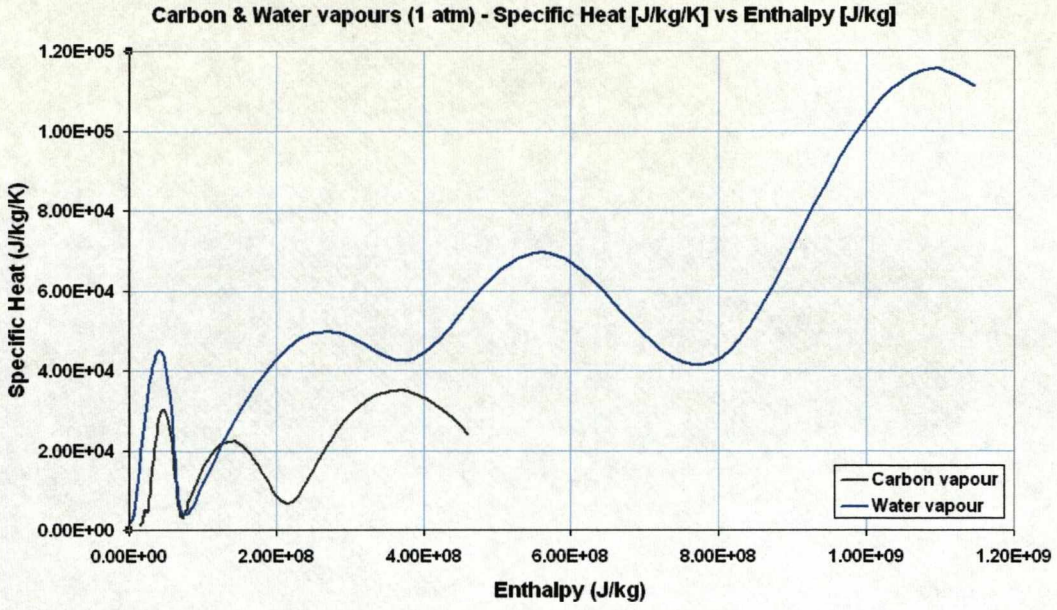

Figure 2.13 Specific Heat of Carbon and Water vapours as a function of enthalpy at 1atm

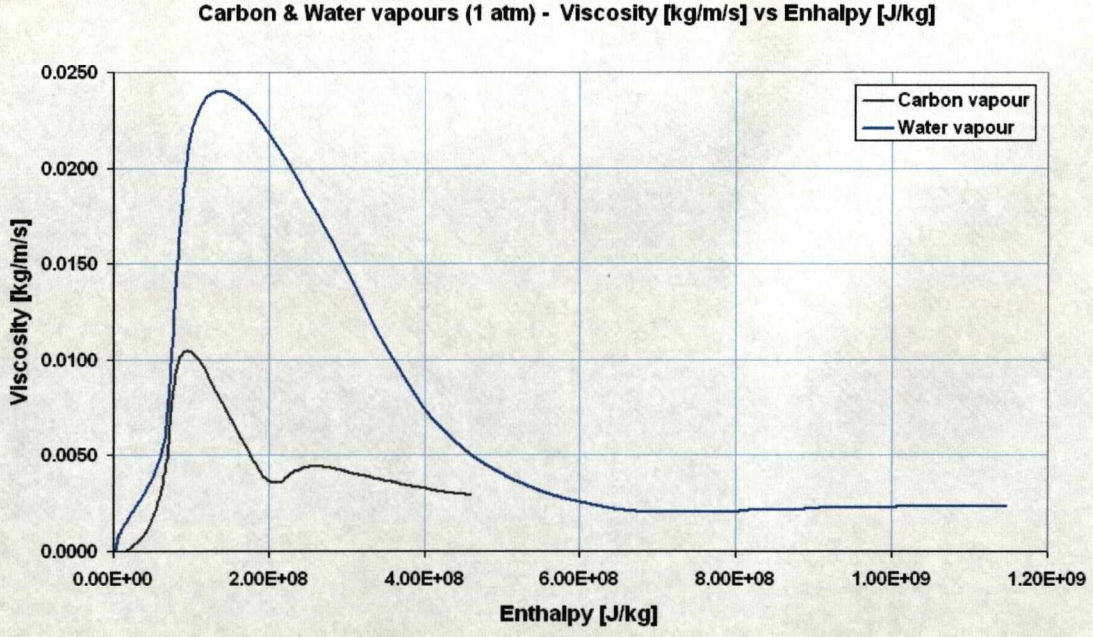

Figure 2.14 Viscosity of Carbon and Water vapours as a function of enthalpy at 1atm

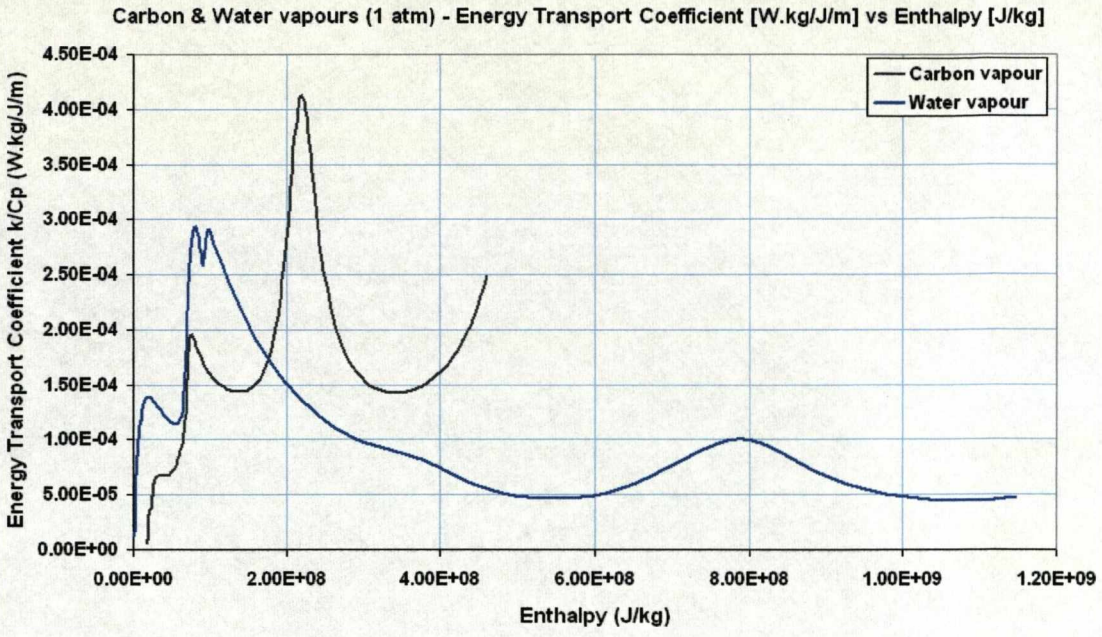

Figure 2.15 Energy Transport Coefficient (*k/cp*) of Carbon and Water vapours as a function of enthalpy at 1atm

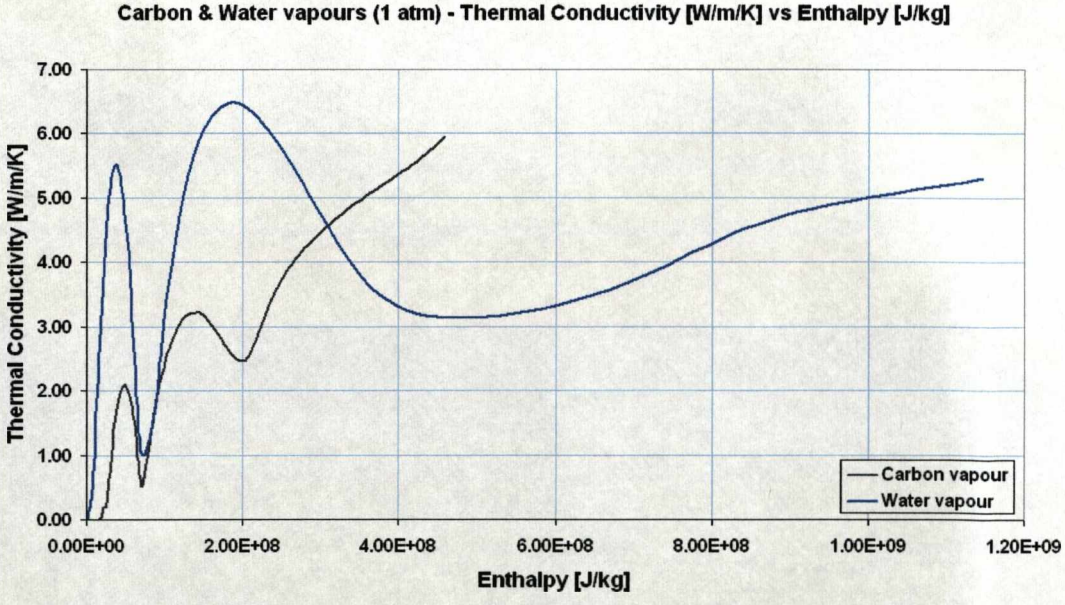

Figure 2.16 Thermal Conductivity of Carbon and Water vapours as a function of enthalpy at 1atm

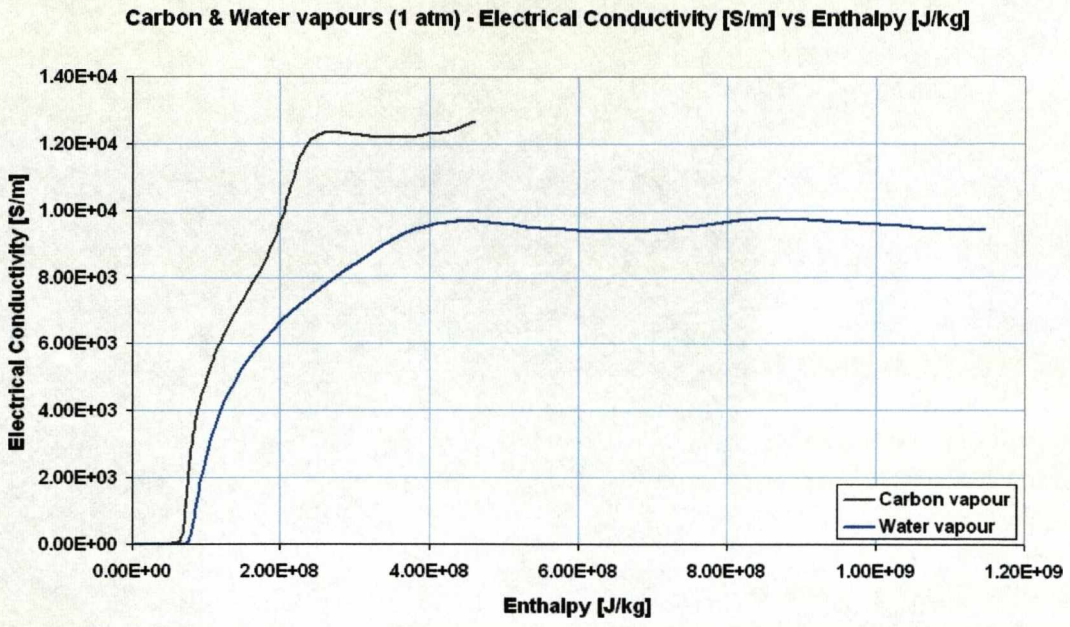

Figure 2.17 Electrical Conductivity of Carbon and Water vapours as a function of enthalpy at 1atm

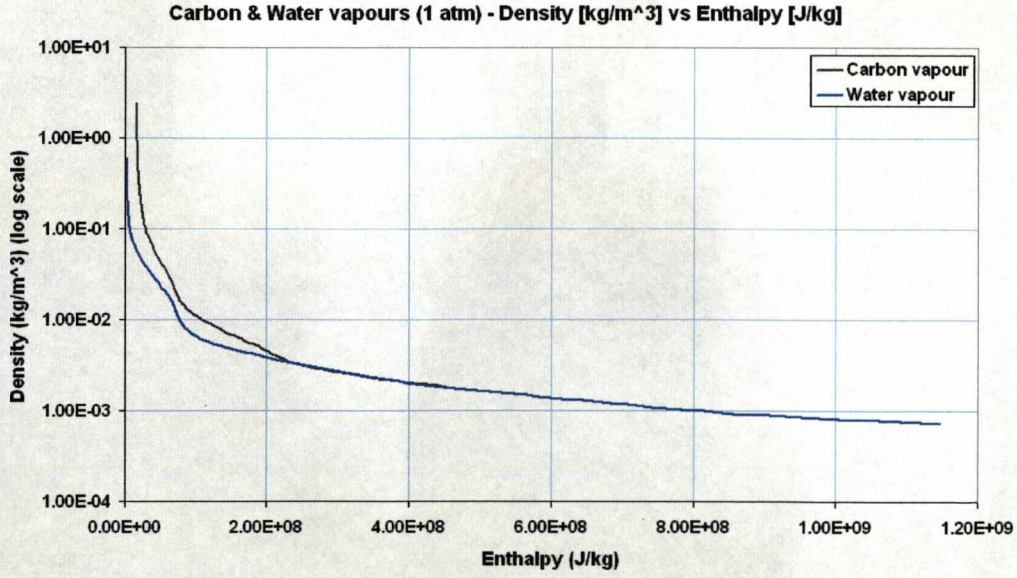

Figure 2.18 Density (log scale at Y-axis) of Carbon and Water vapours as a function of enthalpy at 1atm

It can be seen that the enthalpy corresponding to the lower temperature end is not the same . For example, the enthalpy of water in figure 2.19 at 373K is 2.4471e6J/kg while that for carbon is 1.6620e7J/kg. With a known carbon concentration, the necessary interpolation is performed to obtain the transport properties and also to derive temperature from the calculated enthalpy.

Two interpolation approaches are formulated which make use of the solved variables of enthalpy and mass concentration of additional species to determine the material properties. The first approach (figure 2.19) is suited for two sets of data which have a common data range in the y-axis but a different range in the x-axis, for example the carbon-water vapours temperature-enthalpy relationship as shown in figure 2.12.

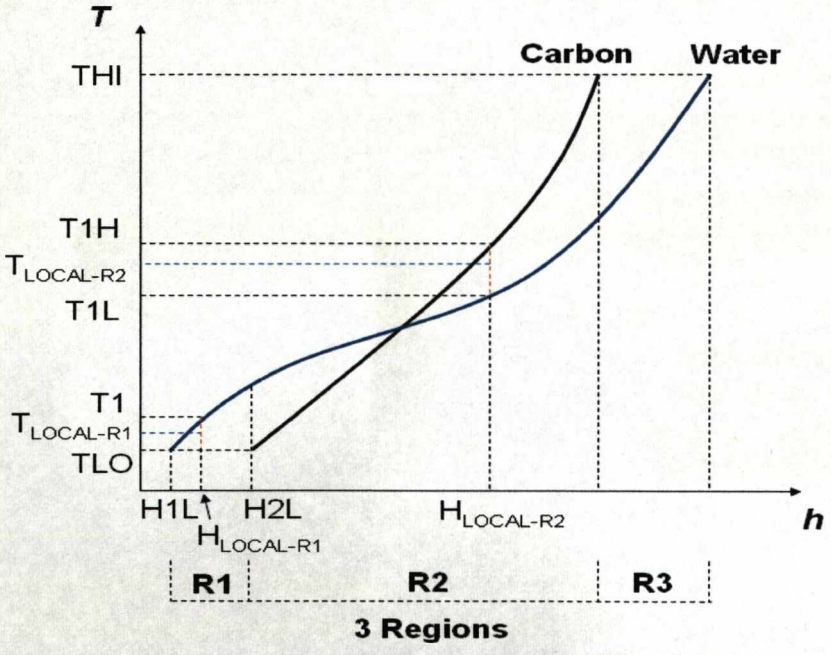

Figure 2.19 Carbon-Water vapours temperature variation with enthalpy

For region 2 where both data is available for carbon and water vapours, a direct interpolation is obtained using the mass concentration of carbon c_m as a weighted factor in the formula

$$T_{LOCAL-R2} = T1L + (T1H - T1L)*c_m \qquad (2.39)$$

where c_m is the mass concentration of additional species.

In region 1, temperature of carbon is assumed a fixed value of TLO for enthalpy range from H1L to H2L. The formula (2.39) is modified accordingly to

$$T_{LOCAL\text{-}R1} = T1 + (T1 - TLO) * c_m \quad (2.40)$$

Region 3 uses the same computation as region 1.

The second interpolation approach is suited for two sets of data which does not have a common range in the x and/or y axis. This approach is used for computing material properties such as specific heat, density, electrical conductivity, etc.

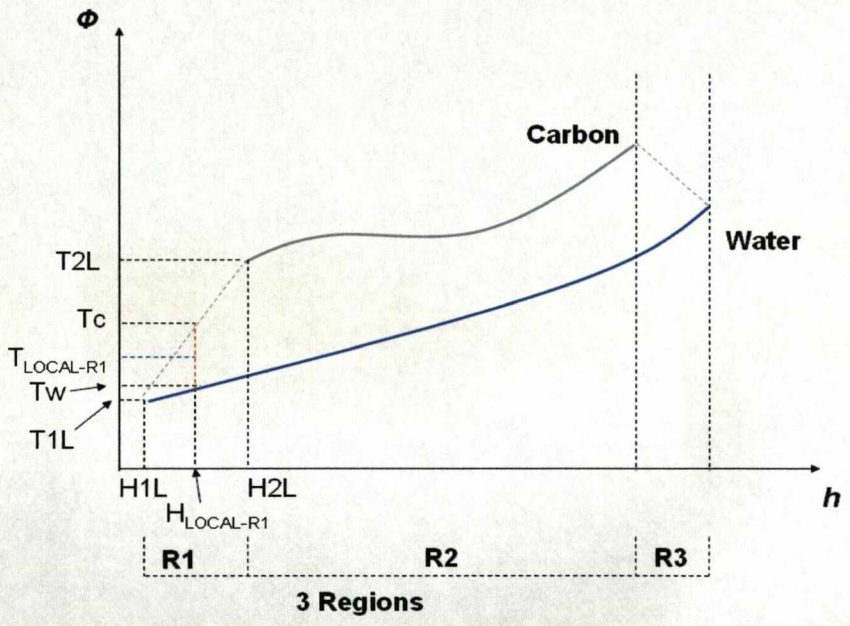

Figure 2.20

For the second approach, region 2 is computed using the same formula (2.39) in the former approach. For region 1, the data is extended in the x-axis. For example of fig 2.20, data for carbon vapour is extended to meet the tip of the water vapour data. At the specified enthalpy, $H_{LOCAL\text{-}R1}$, Tw and Tc is computed. Tc is computed using equation (2.41) and the material properties indicated by $T_{LOCAL\text{-}R1}$ can be determined using equation (2.42). Region 3 uses the same computation as region 1.

$$Tc = T1L + (T2L - T1L) / (H2L - H1L) * (H_{LOCAL\text{-}R1} - H1L) \quad (2.41)$$

$$T_{LOCAL\text{-}R1} = Tw + (Tc - Tw) * c_m \quad (2.42)$$

2.8 Summary

The governing equations for the two plasma systems under investigation are developed in this chapter with consideration of the plasma state in the temperature, current and pressure range. The calculation of electric and magnetic field is also described in detail before a radiation model is presented. The material properties are also given for the different plasma gas or mixture. A suitable method for interpolation of material properties is described for species with different temperature-enthalpy relationship. Consideration of the effect of turbulence for the twin torch plasma will be deferred to Chapter 4 when the measured arc voltage is compared with simulation. The calculation of magnetic field for the twin torch plasma system also required further attention, which will be discussed in Chapter 4. The boundary conditions for the simulation are not given in this chapter since it is more convenient to describe the boundary conditions in each chapter before the results are presented. Simulation of the twin torch is one of the main objectives in the present work. The 3D model should be verified before it is applied to the twin torch system. The next chapter is devoted to the verification of such a model, especially considering the important role of the Lorentz force in shaping the flow pattern and therefore the arc shape.

2.9 References

[1] Sano N., Wang H., Alexandrou I., Chhowalla M., Teo K. B. K and Amaratunga G. A. J., "Properties of carbon onions produced by an arc discharge in water", Journal of Applied Physics, Vol. 92, No. 5, pp. 2783-2788, 2002

[2] Alexandrou I., Wang H., Sano N., Amaratunga G. A. J., "Structure of carbon onions and nanotubes formed by arc in liquids", Journal of Chemical Physics, Vol. 120, pp. 1055-1058, 2004

[3] Lange H., Sioda M., Huczko A., Zhu Y. Q., Kroto H. W. and Walton D. R. M., "Nanocarbon production by arc discharge in water", Carbon, Vol. 41, pp. 1617-1623, 2003

[4] Akita S., Ashihara H. and Nakayama Y., "Optical Emission Spectroscopy of Arc Flame Plasma for Generation of Carbon Nanotubes", Jpn. J. Appl. Phys., Vol. 39, pp. 4939-4944, 2000

[5] Bilodeau J. F., Pousse J. and Gleizes A., "A Mathematical Model of the Carbon Arc Reactor for Fullerene Synthesis", Plasma Chemistry and Plasma Processing, Vol. 18, No. 2, 1998

[6] Hayt H. W., Buck J. A., "Engineering Electromagnetics", McGraw Hill, 2006

[7] Modest M., "Radiative Heat Transfer", McGraw-Hill, New York, 1993

[8] Schnehage S. E., Kock M. and Schulz-Gulde E., "The continuous emission of an argon arc", J. Phys. B: At. Mol. Phys., Vol. 15, pp. 1131-1135, 1982

[9] Bini R., Monno M. and Boulos M. I., "Numerical and experimental study of transferred arcs in argon", J. Phys. D: Appl. Phys., Vol. 39, pp. 3253-3266, 2006

[10] Krenek P. and Hrabovsky M., "Properties of thermal plasma generated by the torch with water stabilized arc", Proc. Of 11th Int. Symp. on Plasma Chem. (ISPC-11), Loughborough, UK, pp. 315-320, 1993

[11] Fang M. T. C., Zhang J. L. and Yan J. D., "On the Use of Langmuir Probes for the Diagnosis of Atmospheric Thermal Plasmas", IEEE Transaction on Plasma Science, Vol. 33, No. 4, pp. 1431-1442, 2005

[12] Jenista J., Heberlein V. R. and Pfender E., "Numerical model of the anode region of high-current electric arcs", IEEE Transaction on Plasma Science, Vol. 25, No. 5, pp. 883-890, 1997

[13] Kovitya P. and Lowke J. J., "Two-dimensional analysis of free-burning arcs in argon", J. Phys. D: Appl. Phys., 18, Pp. 53-70, 1985

[14] Menart J., Malik S., "Net emission coefficients for argon-iron thermal plasmas", J. Phys. D: Appl. Phys. 35, pp. 867-874, 2002

[15] Riad H., Gonzalez J. J. and Gleizes A., "Net emission coefficient for thermal plasmas in H2, O2, H2O, CF4 and CH4", 12th Int. Symp. On Plasma Chem. (ISPC16), 2003

[16] Jenista J., "Water-vortex-stabilized electric arc: III. Radial energy transport, determination of water-vapour-boundary and arc performance", J. Phys. D: Appl. Phys. 36, pp. 2995-3006, 2003

[17] Zhang J. F., Fang M. T. C. and Newland D. B., "Theoretical investigation of a 2kA arc in a supersonic nozzle", J. Phys. D: Appl. Phys., Vol. 20, pp. 368-379, 1987

[18] Lowke J. J., Kovitya P. and Schmidt H. P., "Theory of free-burning arc columns including the influence of the cathode", J. Phys. D: Appl. Phys., Vol. 25, pp. 1600-1606, 1992

[19] Hsu K. C., Etemadi K. and Pfender E., "Study of the free-burning high-intensity arc", J. Appl. Phys., Vol. 54, 1983

[20] Menart J., Malik S. and Lin L., "Coupled radiative, flow and temperature-field analysis of a free-burning arc", J. Phys. D: Appl. Phys., Vol. 33, pp. 257-269, 2000

[21] Blais A., Proulx P. and Boulos M. I., "Three-dimensional numerical modeling of a magnetically deflected dc transferred arc in argon", J. Phys. D: Appl. Phys., Vol. 36, pp. 488-496, 2003

[22] Freton P., Gonzalez J. J. and Gleizes A., "Comparison between a two- and a three-dimensional arc plasma configuration", J. Phys. D: Appl. Phys., Vol. 33, pp. 2442-2452, 2000

[23] Jenista J. Heberlein V. R. and Pfender E., "Numerical model of the anode region of high-current electric arcs", IEEE Transactions on Plasma Science, Vol. 25, Issue 5, pp. 883-890, 1997

[24] Menart J., Heberlein J. and Pfender E., "Theoretical Radiative Emission Results for Argon/Copper Thermal Plasmas", Plasma Chemistry and Plasma Processing, Vol. 16, No. 1, 1996 (Supplement)

Chapter 3

IMPLEMENTATION AND VERIFICATION OF THREE DIMENSIONAL ARC MODEL IN PHOENICS

3.1 Introduction

A commercial computational fluid dynamics (CFD) package, PHOENICS [1], is used in the present work. This package has been used in the University of Liverpool in the past 15 years for modelling circuit breaker arcs [2], free burning arcs [3] and two-temperature microwave induce plasma (MIP) [4].

PHOENICS is a powerful tool with flexible user interface for implementation of physical models. A graphical user interface (GUI) software, Virtual Reality (VR) Editor, enables the grid system and a whole modelling case be set up conveniently. This is certainly true for simulations that only involve flow at relatively low temperature (<3000K) and there are no highly nonlinear sources present in the governing equations. For more complex systems, users can connect their own coding to the numerical solver through the user interface provided to implement their own model. If VR editor is not used, users can then use two programmable files, known as the Q1 and GROUND files, to implement a physical model. One advantage of using PHOENICS is that highly nonlinear material properties or nonlinear source terms can be easily passed to the solver through user-defined FORTRAN subroutines.

In the first part of the present work (Chapter 4), it is necessary to model the twin torch plasma system which has a truly three dimensional configuration. Since the Cartesian coordinate system is used to solve the governing equations for reasons given in Chapter 2, the first issue that needs to be addressed is the representation of the solid parts in the computational domain.

Cells or control volumes are the smallest volumetric unit in finite volume method that is used by PHOENICS to solve the governing equations. In view of the fact that steep temperature and density gradient exists at the edge of the arc column and the coupling zone, very dense grids are necessary in the arc region. With the structured grid system adopted by PHOENICS, a large number of cells will have to be used in the simulation.

PHOENICS uses material index to differentiate between fluid and solid. In PHOENICS, a PATCH is a region defined by a starting cell and an ending cell in each coordinate space. PATCHs are commonly used to define solid regions in the computational domain. However, in the twin torch system, the electrode assemblies have axisymmetry with converging nozzles and rods. It would be very time consuming to use PATCHs to define the electrodes. Further more, in the present work it is necessary to adjust the dimension of the computational domain from time to time. This adds additional difficulties to the use of PATCHs. In the present work, a method has been developed with which the cells in the three dimensional computational domain are automatically allocated for the electrode assembly, thus leads to much improved efficiency in using the PHOENICS package.

This chapter is concerned with the implementation and verification of the three dimensional arc model which will be used in Chapter 4 for the twin torch system. As indicated in Chapter 1, Lorentz force produced by the interaction between the arc current and its magnetic fields plays a decisive role in shaping and subsequently stabilising the geometry of the discharge zone. The gas density in the arc plasma region is usually low and a small asymmetry in the distribution of the current density or magnetic field could lead to an unexpected solution of the arcing process. Thus the calculation of the magnetic field and current density must be sufficiently accurate, not only in its magnitude, but also in its distribution. For example, with a symmetric current density distribution, the magnetic field, thus the Lorentz force, is expected also to be symmetric. In order to meet this requirement, the numerical method used to obtain the magnetic field must be carefully verified. A free burning arc with axisymmetry is then simulated for the verification of the three dimensional arc model.

3.2 Numerical Methods of 3D Object-makeup with Structural Grid

Abstract geometry can be difficult to set up inside a computational domain. The use of Body-Fitted-Coordinates (BFC) simplifies this process in 2D domain but fails to accommodate abstract geometry in 3D domain. The method developed in this section has the capability of generating a geometry which has a symmetrical axis. This method is most applicable for 3D cases with cylindrical object in the domain, which is sufficient for the work in this thesis. The solid or hollow cylindrical shape can be generated by defining the 4 corner points of the cross section of the object that is then rotated 360 degrees around a defined axis to make up the 3D shape.

The procedure of using the method can be defined as:

- Axis and Object Definition – figure 3.1(a)

  - Define an axis using 2 coordinates (AP1 and AP2)

  - Define the 4 points (P1, P2, P3 and P4) to represent the 2 dimensional boundary of the solid. This geometry will be revolved around the axis to produce a cylindrical object.

  - The point AP1 is used as the reference point and the vectors (lines with an arrow) indicated in figure 3.1(a) are computed, along with its magnitude and unit vector.

Radial and Axial Position Definition – figure 3.1(b)

  - Point PD is the intersection point between the axis and the vector from any point at right angle. This point can be found using vector operations.

  - For points P1 to P4, their intersection points (PD1 to PD4) are located. Figure 3.1(b) shows the location of PD2 and PD3.

  - Using the corresponding intersection point (PD) on the axis, the radial and axial position of any point with reference to the axis can be determined. For the example of point P2, the intersection point is PD2 and the axial position on the

axis is equal to the distance between AP1 to PD2, while the radial position is the distance between P2 and PD2.

- Compute the axial and radial position for all the 4 points P1-P4.

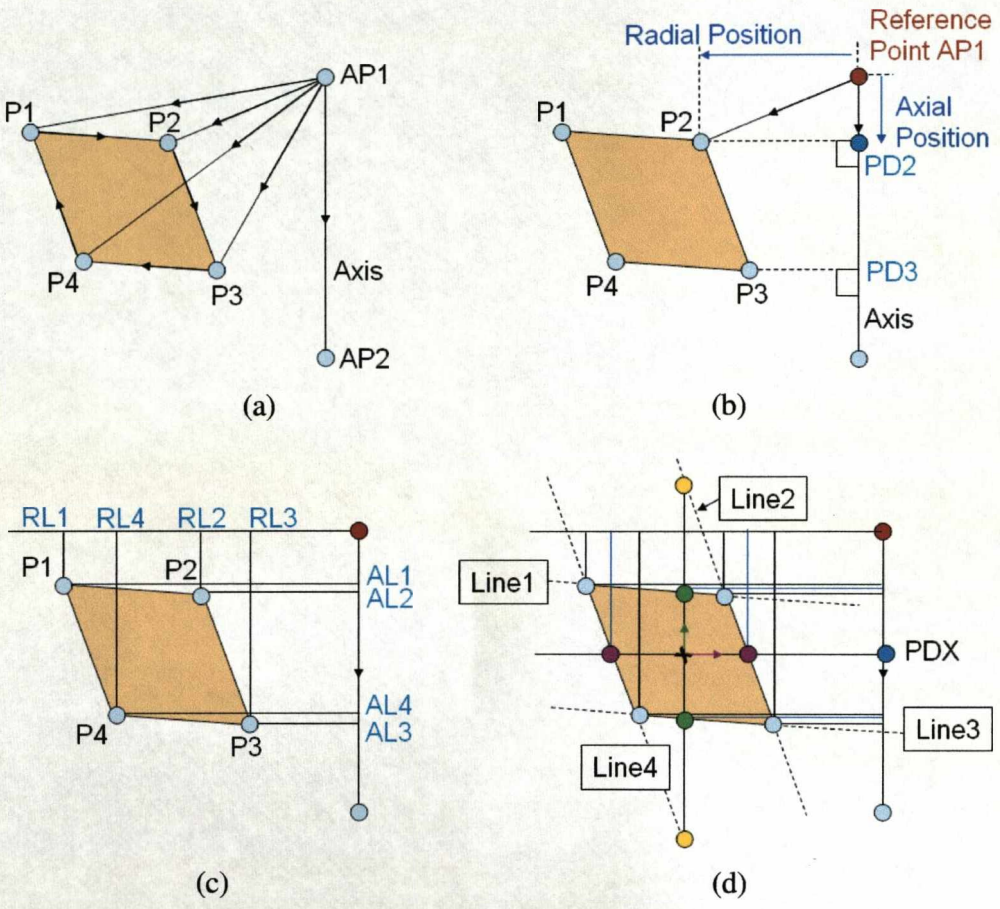

Figure 3.1(a)-(d) Rectangle defined by 4 points P1-P4 is revolved around the axis AP1-AP2 to generate a 3D object

Object Boundary Lines Limits – figure 3.1(c)

- Using the axial and radial positions, the values of AL1 to AL4 and RL1 to RL4 are determined. These values are the axial and radial limits of the object boundary lines of P1-P2, P2-P3, P3-P4 and P4-P1. For example the line P1-P2 is defined by the axial limits of AL1 to AL2 and radial limits of RL2 to RL1.

Cell identification – figure 3.1(d)

- The axis and boundary lines and limits are now defined. To determine if the cell lies within this object boundary, the cell information such as axial position, radial position, the radial and axial vector (indicated by arrows in figure 3.1(d)) are first determined. For any cell to lie within this object boundary, it has to satisfy certain conditions.

- As an example, take the point indicated by 'x'. PDX is the intersection point with the axis.

- Condition 1: the axial vector (green arrow) of point x has to intersect at least 2 boundary lines at 2 valid points (indicated by green dots). The points are valid if it they lies within the axial and radial limits of the object boundary line. In figure 3.1(d), this axial line intersects 4 points, with the valid ones indicated in green and the invalid ones in yellow.

- Condition 2: the radial vector (purple arrow) of point x has to intersects at least 2 boundary lines at 2 valid points (indicated by purple dots).

- However, if the cell is located outside the solid object, the point may still satisfy condition 1 and 2.

- Condition 3: The cell position is located between the two intersection points of the axial vector and between the two intersection points of the radial vector. The cell is identified as a solid object when condition 1, 2 and 3 are satisfied.

Although this method may involve a high number of operations, this procedure is only computed one time at the start of the simulation. The advantage is with its ability to generate solid shapes accurately and applicable to various shapes. In addition, this code enables a quick and easy generation of multiple 3D geometries and applicable to various computational domain of different grid density. Without this code, the concentric cylindrical solid has to be redefined by adjusting many dimensional parameters to make up the required cylindrical shape whenever the grid size or dimensions is changed.

3.3 Grid System and Convergence Control

The number of cells and their distribution in the computational domain need to be adequate so that the local cell size is comparable or smaller than the length scale over which the physical quantities exhibit significant change. This is however not easy to determine for complex arcing situations such as the twin torch plasma. The optimised grid system has to be obtained by tests guided by theoretical consideration. Using a large number of cells can easily solve the problem but it is done with a huge cost in computing time. For 3D simulations, this may lead to a grid number with which the computing time is prohibitively high. A compromise between computing time and grid size has to be set through optimisation. The grid system will be shown in the relevant chapter for information.

In PHOENICS, the solution algorithm proceeds slab by slab for momentum, energy and species concentration equations. A slab is a layer of cells perpendicular to the axial position (z direction). For pressure, electric potential or magnetic vector potential equations, solution is normally obtained using a whole field solver. For each solved-for-variable ϕ_P, in a cell P, the following algebraic equation is iteratively solved

$$a_P\phi_P = \sum_{F\in\{S,N,H,L\}} a_F\phi_F + a_T\phi_T + b \tag{3.1}$$

where the coefficients of a with different subscripts P, F and T represents links between neighbour cells, linearised sources, and solution of previous time step. Because of the highly nonlinear nature of the transport properties and radiation transfer, relaxation is needed to ensure convergence of the solution procedure.

Linear relaxation is normally used for pressure, electrical potential and vector potential. For pressure in atmospheric arc discharges where there is strong axial flow, a linear relaxation factor of 0.3 to 0.5 is necessary. A value of 0.8 is sufficient for electric and magnetic potential equations.

In numerical solution of the governing equations, the iteration process within a time step resembles a "transient process" where the intermediate values continuously changes from the values of the previous time step to the converged value of the present time step. PHOENICS provides a relaxation method called "false-time-step". This method adds the following extra retarding source term to the balance equation (3.2):

$$\frac{\rho V_P}{\Delta t_f}\left(\phi_P - \phi_{P,old}\right) \tag{3.2}$$

where ϕ_P is the cell-value in cell P, $\phi_{P,old}$ is the cell-value resulting from the previous iteration; V_P is the cell volume; and Δt_f is user-set false-time-step. The above expression indicates that if the solution is well converged then the term will be negligibly small. A small value of Δt_f produces a large term thus slows down the change of the concerned variable. Given the value of Δt_f, the relaxation term is then proportional to the difference between the old value and the new value of the variable concerned. This means that if the change during the iteration is too abrupt, then a large retarding "force" is automatically added to slow down the change, thus promoting convergence. It is found that a false time step of 10^{-7}s is necessary for the 3D simulation.

3.4 Free Burning Arc under LTE – Verification of 3D Model

3.4.1 The computational domain

Measurement of plasma parameters in 3D situation is rare and large uncertainties exist in the results. A steady state free burning arc in argon is probably one of the most investigated cases of arc flow for its ease of operation and measurement. Both temperature measurement [5] and numerically predicted temperature and velocity results [6, 7] exist. For the verification of the 3D model, the case studied by Haddad & Farmer [5] was simulated. The current passing through the arc is 200A and the electrode separation is 5mm. the working gas is argon at atmospheric pressure.

The cathode is made of tungsten with a rod diameter of 3.2mm and its tip has a full conical angle of 60 degree. Copper is used as the anode material. At such a moderate current, electrode erosion is not severe and subsequently neglected in most of the modelling work [8,9,10]. For the present 3D simulation, a cubic domain is used where the cathode tip points down with a copper plate placed 5mm away from the tip. The geometry of the computational domain is shown in figure 3.2.

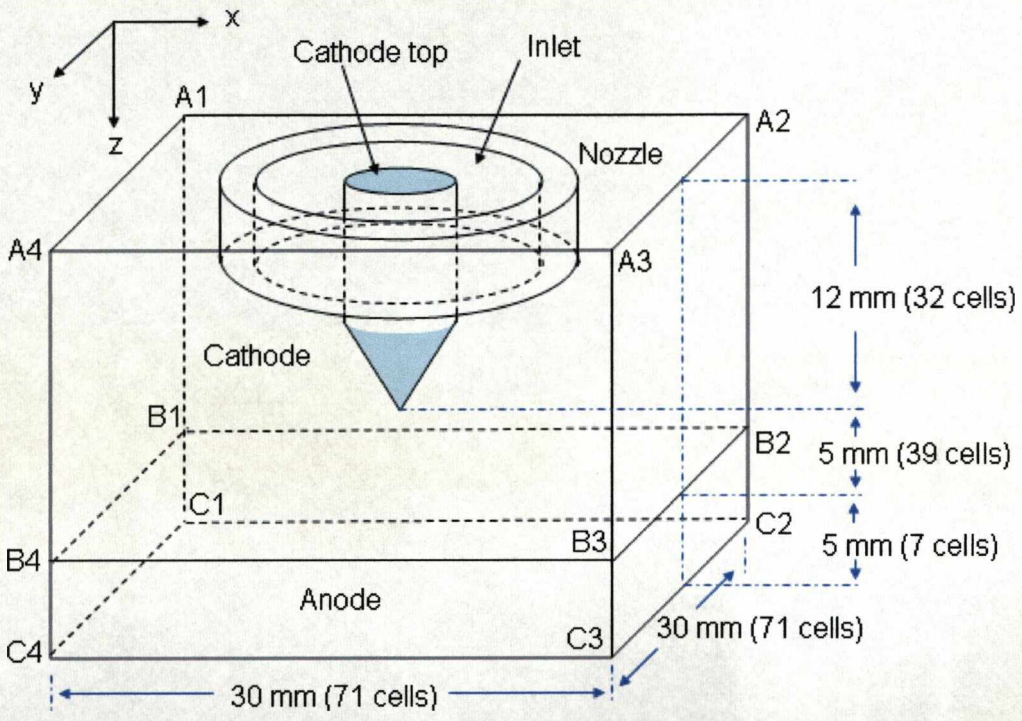

Figure 3.2 Geometry used in the 3D simulation of the free burning arc.

The computational domain size is 30mm, 30mm and 22mm in the x, y and z direction, having 71, 71, 78 cells in the x, y and z direction respectively. Fine grids are used around the cathode tip where magnetic pinch effect is responsible for the generation of the axial velocity. The tungsten cathode has a rod diameter of 3.2mm and cathode flat tip diameter of 0.2mm. The inner and outer radius of the copper nozzle is 5mm and 7mm respectively.

Arc initiation is modelled by placing a hot conducting gas column between the electrodes.

3.4.2 Boundary Conditions

The boundary conditions required for the solution of the governing equations are derived from the real experimental conditions and presented in Table 3.1 where ** means that the gradient of the variable concerned is zero in the normal direction of the boundary face. This implies that there is no diffusive flux across the boundary. For energy equation this is a zero thermal conduction flux condition, for momentum it represents zero friction, and for mass it means zero mass flux. N/A means that boundary condition is not necessary.

Near the cathode surface where the arc resides its root, there is a thin non-LTE layer bridging the arc column and the cathode surface. The physical processes in the sheath layer are not considered in the model. Its main influence on the arc column is in limiting the size of the arc root where strong magnetic pinch exists. In the free burning arc case, the cathode has a conic shape and the arc root is restricted by cold gas entrainment due to magnetic pumping towards the arc axis. This implies that for the free burning arc case the neglect of the cathode sheath has rather limited influence on the solution of the plasma column. In the present work it is assumed that there is no energy loss by thermal conduction from the gas at the boundary near the cathode surface (inside and outside the arc root area, all cathode surface). A non-frictional (slippery) boundary condition is imposed for all momentum equations on all solid surface.

Boundary Group 1: On the cathode top (BG 1 in Table 3.1) , which is a circular area in plane A1-A2-A3-A4, a uniform current density (j_o) is specified for the potential equation where z indicates the axial direction of the cathode rod. The potential equation is solved in both gas and solid regions. The electrical conductivity inside the electrodes is set to a high value of $1x10^6$ S/m. A small value is set in the nozzle which is non-conducting, i.e.$1x10^{-3}$ S/m.

Boundary Group 2: The argon gas enters the arcing space with a temperature of 1123K [11] (BG 2, i.e. boundary group No. 2). The mass flux, $\dot{m}$, through the inlet is calculated from the standard volume flow rate used in the experiment (0.5 Nl/min),

with a density at 300K and 1bar) and the nozzle cross section. The inlet velocity w_{in} is obtained by dividing the mass flow rate by the density corresponding to the inlet conditions.

Boundary Group 3: At the open boundary of BG 3, the pressure is fixed to 1bar and the velocity is adjusted by the solver according to the fixed pressure boundary condition. Since the boundary is sufficiently away from the arc, thermal conduction across the boundary and friction is neglected.

Boundary group 4: On the anode surface B1-B2-B3-B4, the arc has a large anode attachment and the anode is normally cooled for minimum anode erosion. Thus the anode surface temperature should not be higher than the melting temperature which is 1355K. As shown later in the results, the gas temperature near the whole anode surface is much higher than the boiling temperature, the energy loss, FF through thermal conduction into the anode body is calculated by

$$FF = \frac{1}{2}\left[\left(\frac{k}{c_p}\right)_g + \left(\frac{k}{c_p}\right)_s\right]\frac{(H1_g - H1_s)}{0.5(\Delta z)} \tag{3.3}$$

where k is the thermal conductivity, c_p the specific heat at constant pressure, $H1$ the enthalpy, Δz the width of the cell in the z-direction and the subscript g and s indicates the cell occupied by the argon gas and solid respectively. The value of k/c_p for the energy loss is taken as the average of the value at the centre of the cell occupied by argon gas (indicated by the subscript g) and the value at the cell face of the gas and solid boundary (indicated by the subscript s). Corresponding to the temperature of 1355K, their values are found to be $H1_s$ = 7.0502e5J/kg and $(k/cp)_s$ = 1.0094e-4 W.kg/J/m. $0.5(\Delta z)$ is the half-cell width of the cell immediately before the anode with a value of 1.1905e-4m.

Boundary group 5 and 6: On these boundary faces only the condition for the electrical potential equation need to be specified. This is given in the Table 3.1.

Boundary conditions for the calculation of the magnetic flux density will be given in section 3.4.4.

Boundary group No.	Boundary	Pressure, P (bar)	x and y-direction velocity, u and v (m/s)	z-direction velocity, w (m/s)	Temperature, T (K) or Enthalpy, h (J/kg)	Electric Potential, Φ (V)
1	Cathode Top	N/A	N/A	N/A	N/A	$\frac{\partial \Phi}{\partial z} = \frac{j_0}{\sigma}$
2	Inlet	$\dot{m}$	0	w_{in}	1123K	**
3	A1-A2-A3-A4, A1-A2-B2-B1, A2-A3-B3-B2, A3-A4-B4-B3, A1-A4-B4-B1 (Outlets)	1bar	**	**	**	**
4	B1-B2-B3-B4 (Anode)	N/A	**	**	*FF*	N/A
5	B1-B2-C2-C1, B2-B3-C3-C2, B3-B4-C4-C3, B1-B4-C4-C1 (Anode)	N/A	N/A	N/A	N/A	**
6	C1-C2-C3-C4 (Anode)	N/A	N/A	N/A	N/A	$\Phi = 0$

Table 3.1 Boundary conditions for the simulation of free burning arc

3.4.3 The Mesh System

Since Cartesian coordinate system is used for the 3D simulation, fine grids are used in the cathode tip region to accurately represent the geometry of the cathode and provide sufficient spatial resolution to the physical quantities. The mesh is shown in figure 3.3(a)-(d). Diagram 3.3(a) is the rectangular computational domain and the contour is shown at the top plane showing the cylindrical solid, with the middle cross section showing the cathode, anode and nozzle, both with respect to the cell distributions in the domain. The region between the cathode and anode has a denser grid. The denser grid is also vital to model the conic shape of the cathode. The cross sectional dimension of the cell size at the cathode tip is 0.0968mm by 0.0968mm and a height of 0.1238mm.

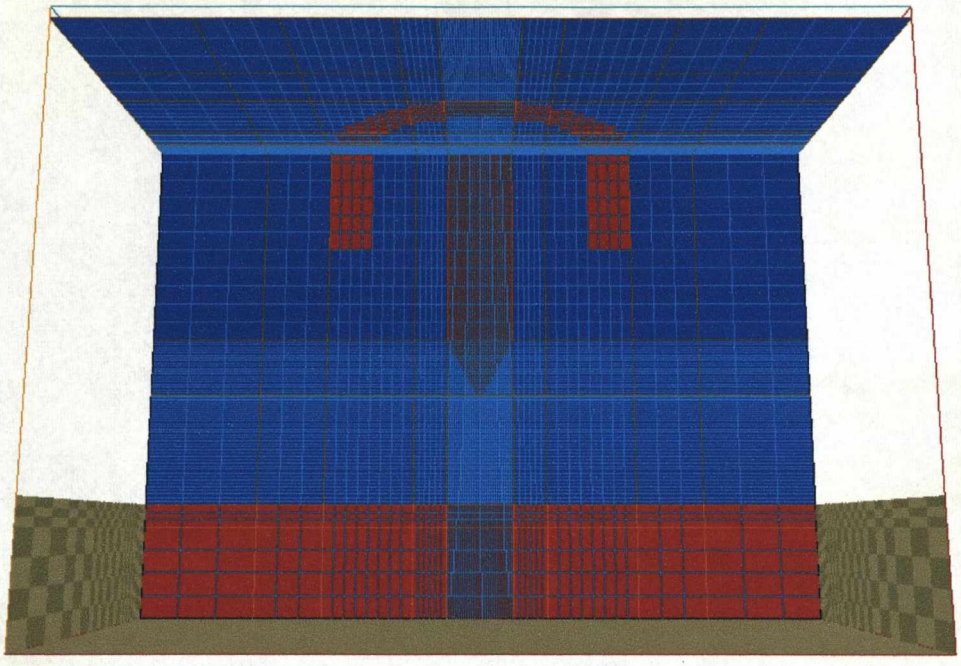

Figure 3.3(a)

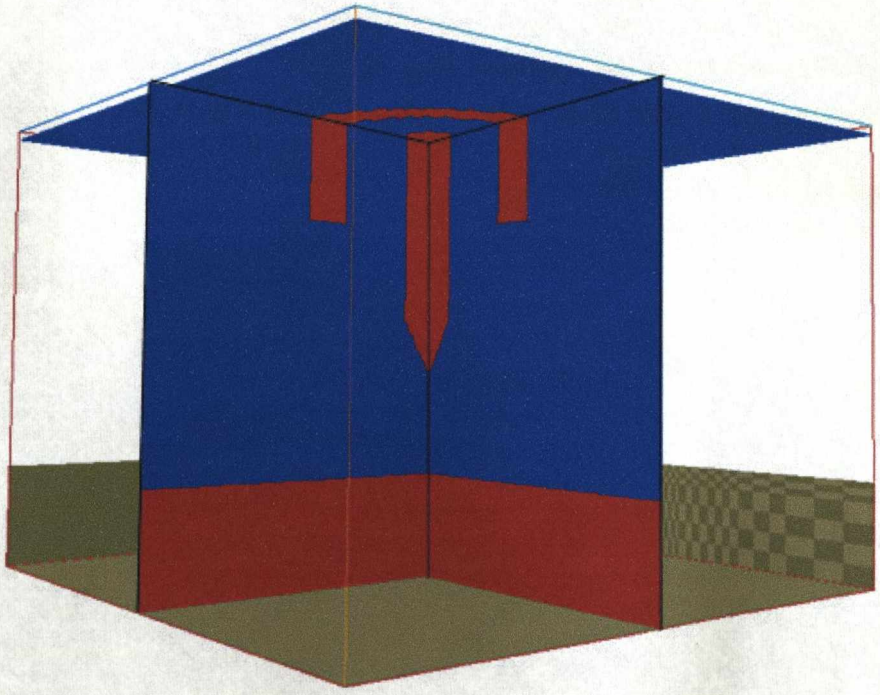

Figure 3.3(b)

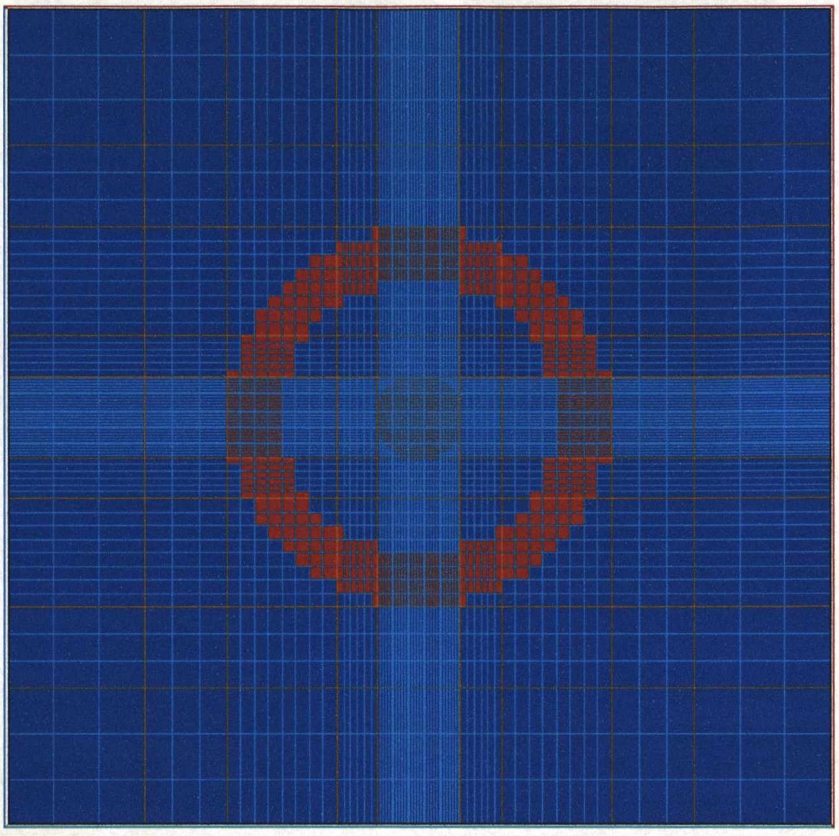

Figure 3.3(c)

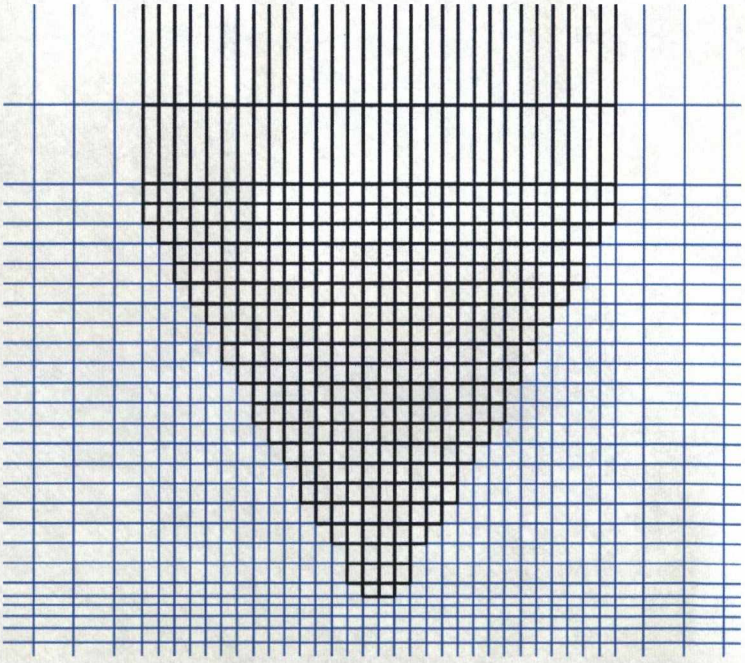

Figure 3.3(d)

Figure 3.3(a)-(d) shows the mesh system and solid region (red) from different view

3.4.4 The Role of Lorentz Force and Magnetic Field Calculation

The vector magnetic potential vector, $\bar{A}$ is obtained by solving the equation (2.31). This allows the magnetic field to be computed using formula (2.28) and eventually the Lorentz force using the equations below.

Lorentz Force, $$\bar{F}_L = \bar{J} \times \bar{B} \tag{3.3}$$

And in Cartesian coordinates it can be expressed as,

$$\bar{F}_L = \hat{x}(J_y B_z - J_z B_y) + \hat{y}(J_z B_x - J_x B_z) + \hat{z}(J_x B_y - J_y B_x) \tag{3.4}$$

The magnetic potential is of long range and the solution to equation (2.31) is sensitive to the boundary conditions as well as the location of these boundaries. It would be inaccurate to use the CFD domain boundary for this purpose. To overcome this difficulty, the method in [12] is used where the CFD computational domain is extended in all six directions to make a larger domain for the vector potential. With the extended domain as shown in figure 3.4 the boundaries are now located sufficiently away from the arc column and the magnetic vector potential is set to zero at all boundaries. In this extended domain, the solution for electric potential is dependent on the current density. For continuity terms, the current density of at the top region of the domain, i.e. the top of the cathode, is extended into the large domain. The current density values at the first slab of the CFD domain is copied to the extended grid.

This solution method is implemented using the free burning arc case.

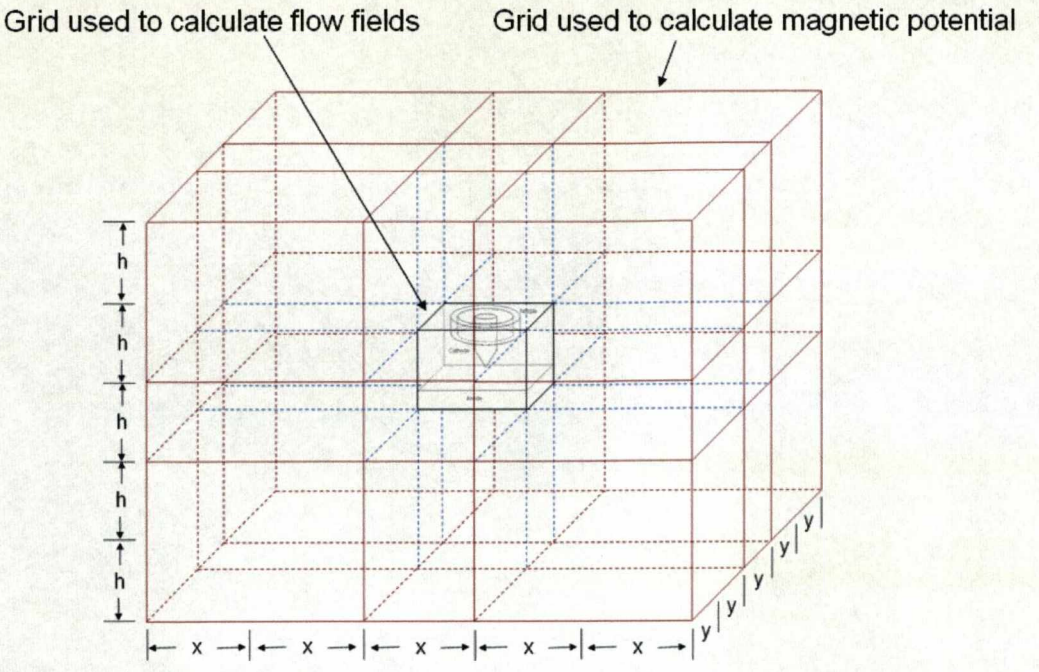

Figure 3.4 The CFD computational domain and extended computational domain used for the solution of magnetic potential

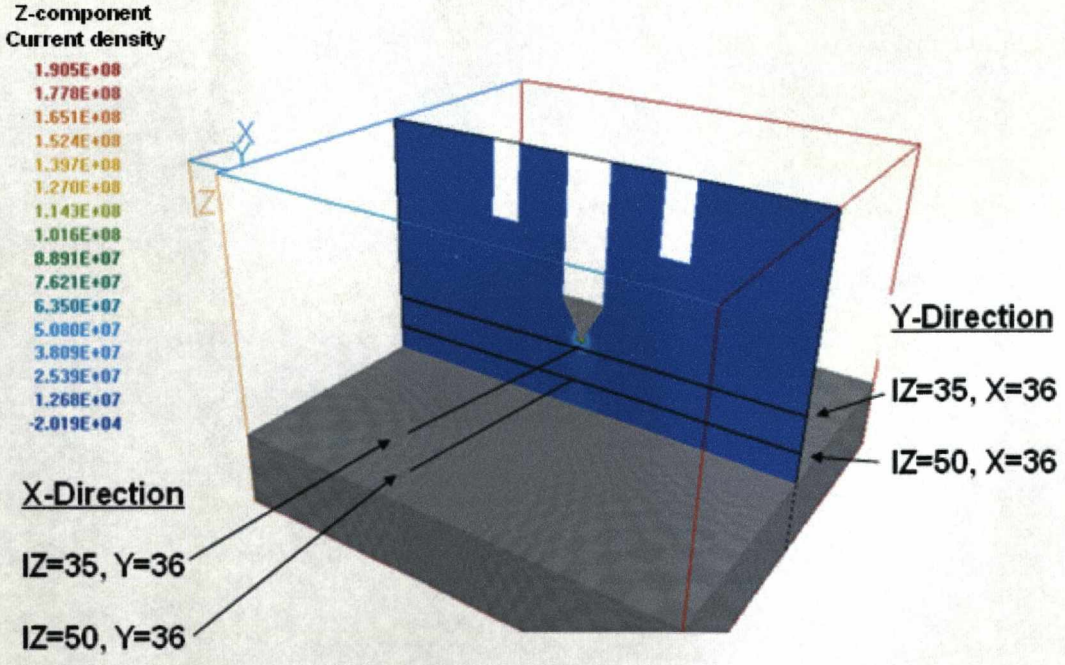

Figure 3.5 Magnetic field monitoring location and data plotting

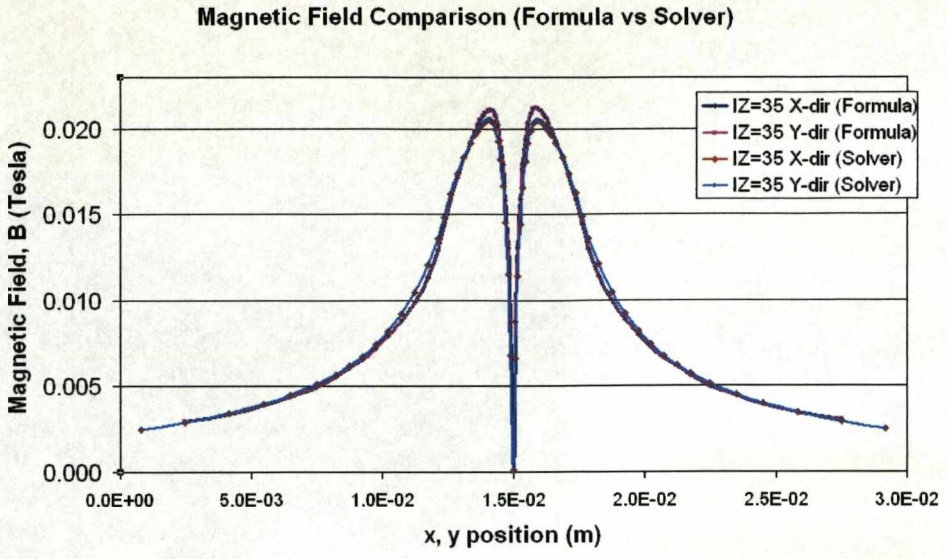

Figure 3.6 Magnetic field values (magnitude) comparison between formula and solver at IZ slab 35

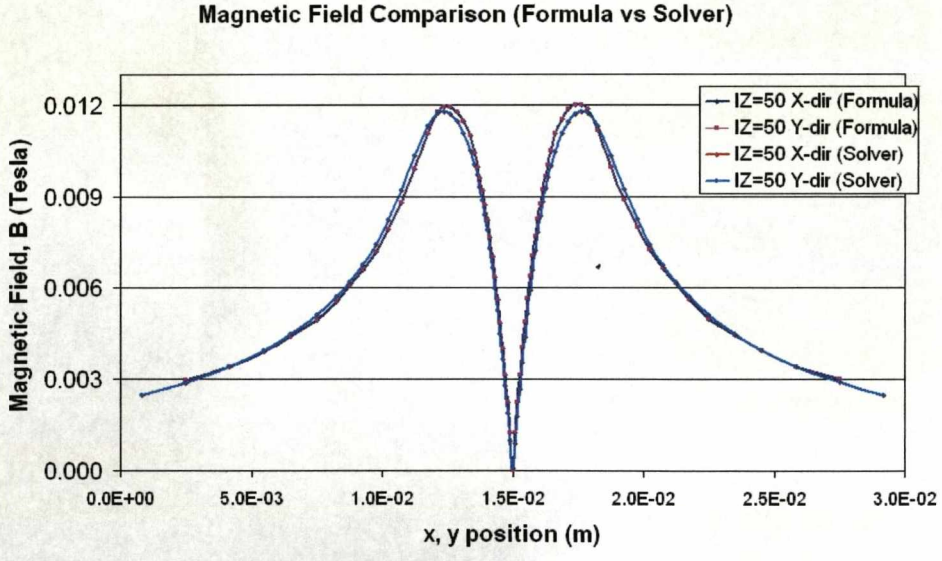

Figure 3.7 Magnetic field values (magnitude) comparison between formula and solver at IZ slab 50

Figure 3.6 and 3.7 show a comparison between the magnetic flux density value computed by the user's solver and that from analytic solution for an infinitely long conductor, $B = \mu I / 2\pi r$, where μ is the permeability of space, I is the current included in the circle with radius of r, and r is the radius where the magnetic flux density is calculated. Data is plotted for IZ at slab 35 which is 1mm from the cathode

tip and IZ slab 50 which is 18mm from the anode (see Figure 3.5) in the x-direction and y-direction. Note that the values below zero are inversed in fig 3.6 and 3.7 to optimise the scale representation of the chart and allows the comparison of the magnitude and distribution of the two sides. At slab 35 (near cathode tip), the magnetic field is stronger due to the higher current density distribution compared to the values at slab 50. Results show good agreement in magnitude. The solver produced a value that is slightly lower than the data computed using the formula above. This difference, for data computed using the formula, could be attributed to the slight discrepancy of the integrated current due to the staggered grid and the fact that the magnetic field formula used for comparison is for an infinitely long conductor. The diagram also shows that the magnetic field is generally symmetrical as the x and y direction data superimposed on each other.

For 2D axisymmetric simulation, axisymmetry is automatically forced by the boundary conditions. This is however not the case in 3D simulation where the electrode symmetry line is at the middle of the computational domain and gas can flow in all three directions. Lorentz force can be very strong yet the plasma density is very low. Thus a small asymmetry present in the distribution of the magnetic field or current density could lead to a significant asymmetry in the plasma solution. This important aspect has been carefully studied in the present work since it occupies a central position in successfully modelling the 3D arc.

In a separate case with identical discharge conditions, the magnetic flux density is calculated at the staggered grid cell centre and then used as the source terms in the momentum equation. Surprisingly a rather asymmetric distribution of the velocity and temperature around the symmetric axis of the electrode arrangement is observed. This is shown in figure 3.8 and 3.9 for magnetic field and temperature/velocity. The peak magnitude difference in the computed magnetic field is only 1.52e-4Tesla or 1.6% of the peak value. However, this difference is magnified when multiplied by the current density, resulting in an asymmetric Lorentz force. The reason for the difference is that solution of the momentum equation in PHOENICS is on the cell surface instead of the cell centre as presented by Patankar [13].

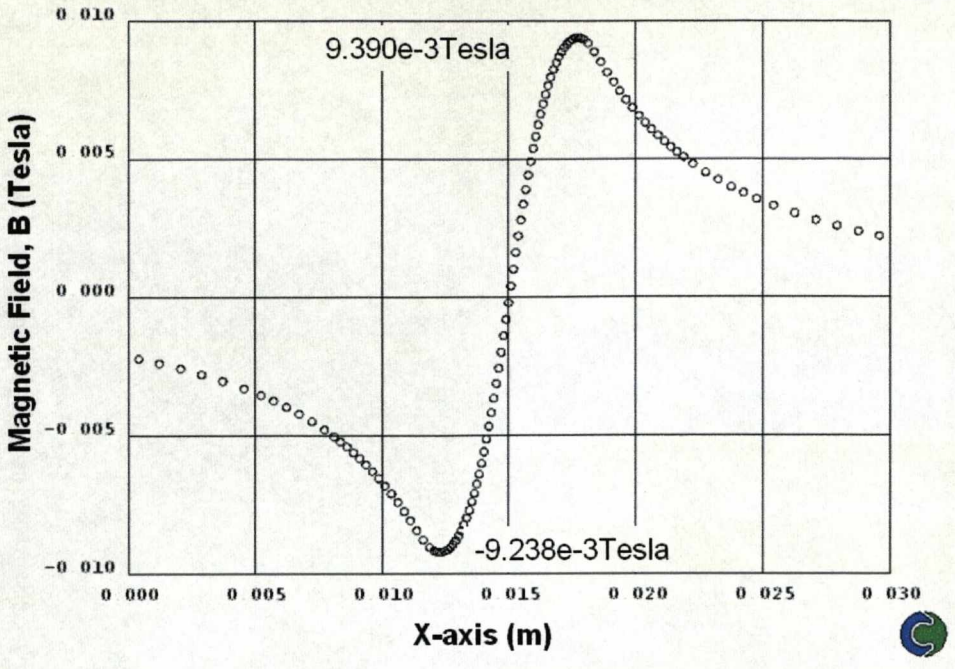

Figure 3.8 Magnetic field in the y-direction (BY) at the line IY=40 and IZ=40 for asymmetry case

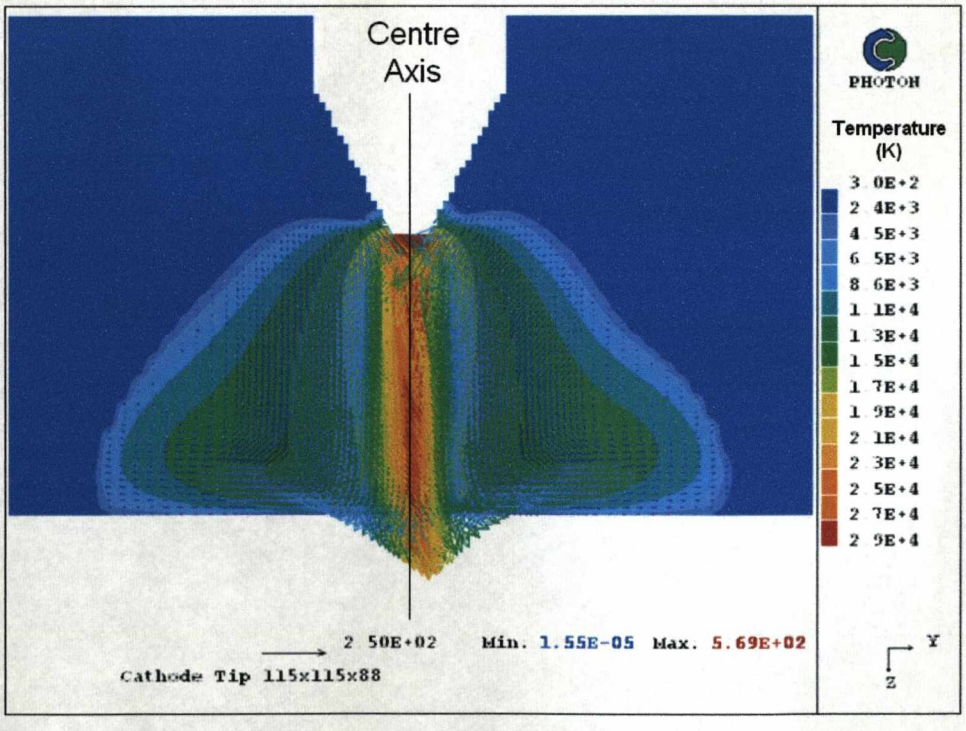

Figure 3.9(a) Asymmetric temperature and velocity contour in the y-direction cross section

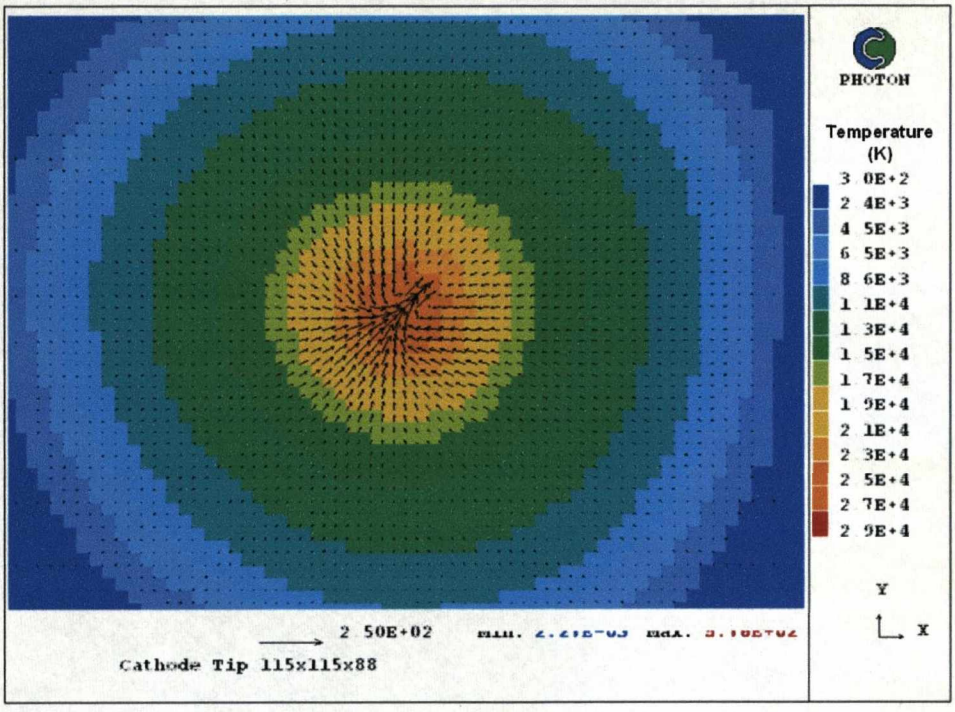

Figure 3.9(b) Asymmetric temperature and velocity contour in the z-direction cross section

3.4.5 Results and comparisons

In figure 3.10 and 3.11, temperature and velocity contours show the typical bell-shape for the free-burning arc due to the impingement on the flat anode and also anode cooling. The maximum temperature reached near the cathode tip (less than 1mm) and the maximum velocity is found approximately 1.5mm away from the tip. This high temperature (approx. 23000K) is caused by the strong Ohmic heating in the restricted arc column. The high velocity (approx. 440m/s) of the fluid is achieved through pumping forces created by the arc self-induced magnetic field.

In the last three decades, the axisymmetric arc model has been widely studied [6,11,14,15]. In general, the difference between those models is the critical boundary condition at the cathode tip; some prefer to input a current density profile as done in [14,15] while others choose to include the cathode in the calculation domain and set Jz=I/Ac at the top cylindrical part of the cathode [6,11]. Nevertheless, these models are all proven to give satisfactory results in regard of the plasma parameters (temperature, velocity, electric potential).

Experimental results on plasma temperature [16] are available for comparison for the case that is simulated in this chapter. There are also results computed by other researchers [11] for the same discharge conditions. The verification of the 3D model focuses on two issues, the axis temperature magnitude, radial temperature distribution and the symmetry of the solution.

Figure 3.12 shows the shape of the arc column at temperatures from 8000K, 10000K and 12000K. Results from measurement and other sources are detailed in Table 3.2 for typical plasma parameters. The distribution of pressure and electric potential is also shown in figure 3.13 and 3.14.

The axis temperature is plotted in figure 3.15 together with the results from [11] and [16]. The radial temperature profiles in several planes with different distance from the cathode tip are given in figures 3.16(a)-(e). In a small region from the cathode tip, prediction from this work is lower than that from [16] possibly because the coordinate system and grid system is different in the two simulations. At 0.5mm our prediction agrees very well with the measurement (figure 3.16(a)). The predicted axis temperature is slightly lower than the measurement in the region 2-3mm for the cathode tip. The axis velocity is also given in figure 3.17. The maximum velocity is well within the values predicted by other [11].

The results show that the 3D model produces symmetry in the plane normal to the axial direction, as shown in figures 3.18(a)-(b).

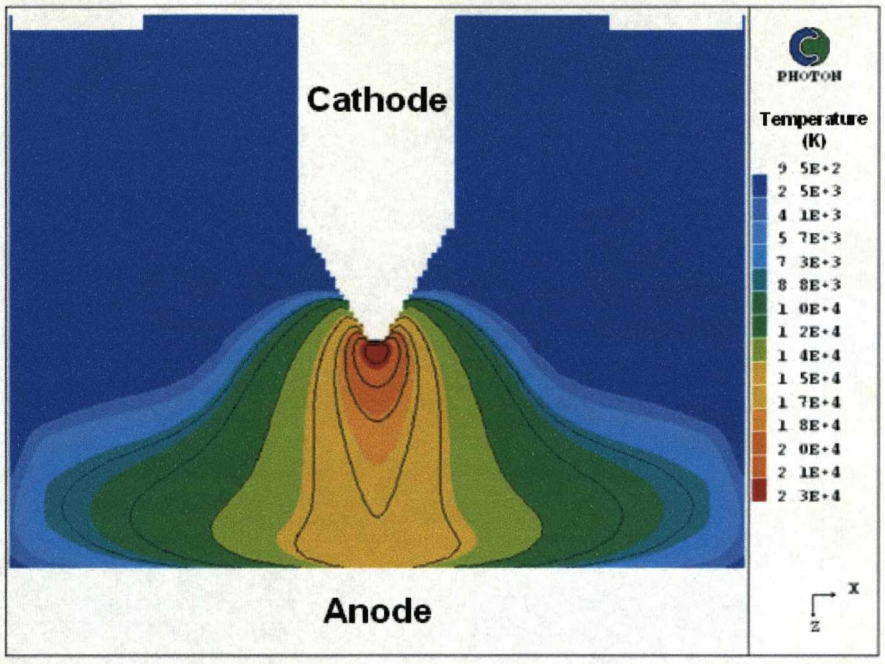

Figure 3.10 Three-dimensional free-burning arc of 5mm and 200A in argon at atmospheric pressure - contours of temperature (8000-22000K, intervals of 2000K)

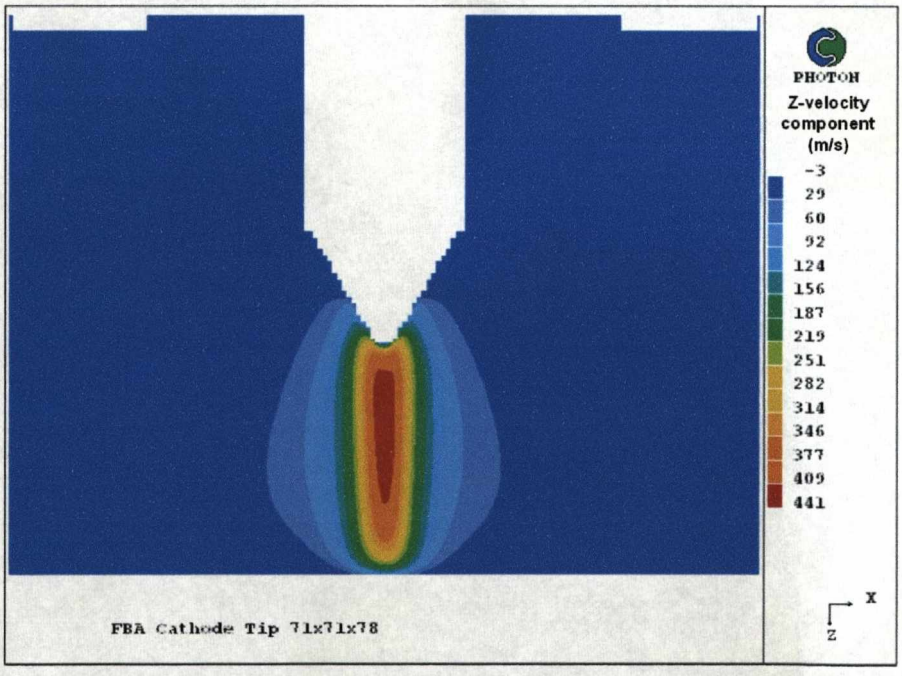

Figure 3.11 Three-dimensional free-burning arc of 5mm and 200A in argon at atmospheric pressure - contours of z-velocity component

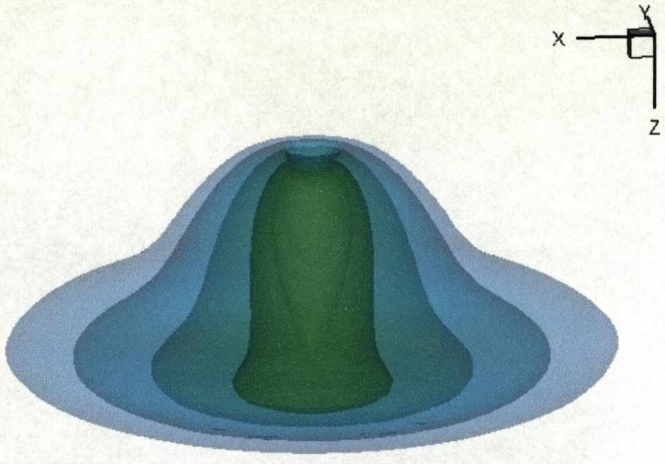

Figure 3.12 Iso-surface temperature at 8000K to 18000K of interval 2000K

Publications	Maximum Temperature (K)	Arc Voltage (V)	Velocity (m/s)
Lowke [17]	24000	12.7	na
Zhu [18]	23700	12.9	na
Lowke [6] (different cathode temperature)	22000, 23900, 24100	11.7, 12.1, 12.1	430, 550, 550
Zhang [11]	26000	na	500
Current simulation result	23800	12.5	530

Table 3.2 Simulation results comparison for temperature, arc voltage and velocity for 5mm argon free burning arc at 200A from various authors

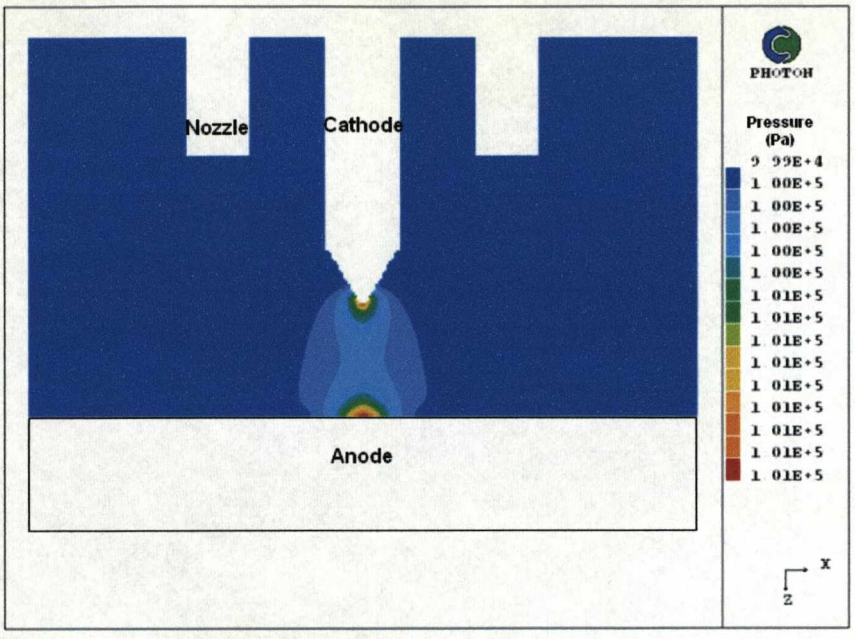

Figure 3.13 Pressure contour for 200A 5mm Argon free burning plasma arc

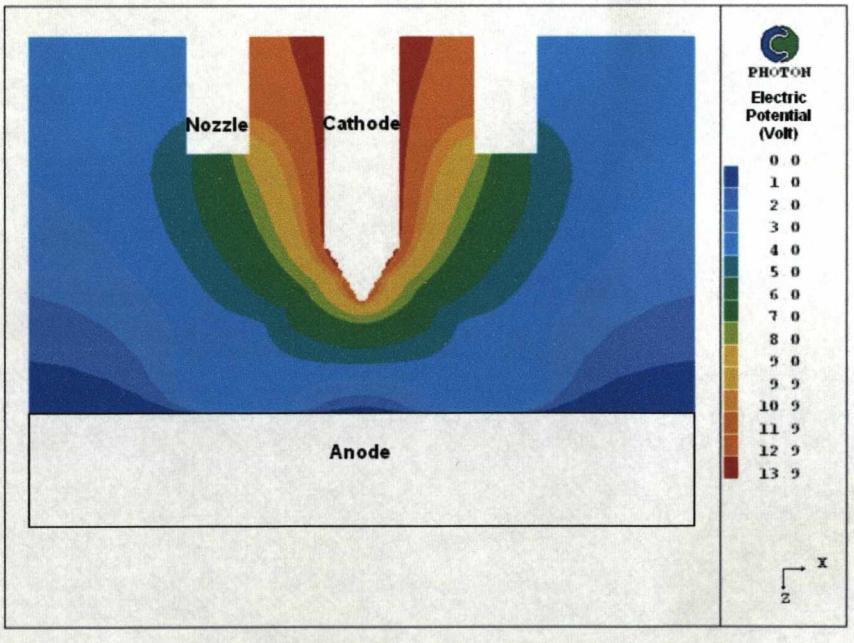

Figure 3.14 Electric potential contour for 200A 5mm Argon free burning plasma arc

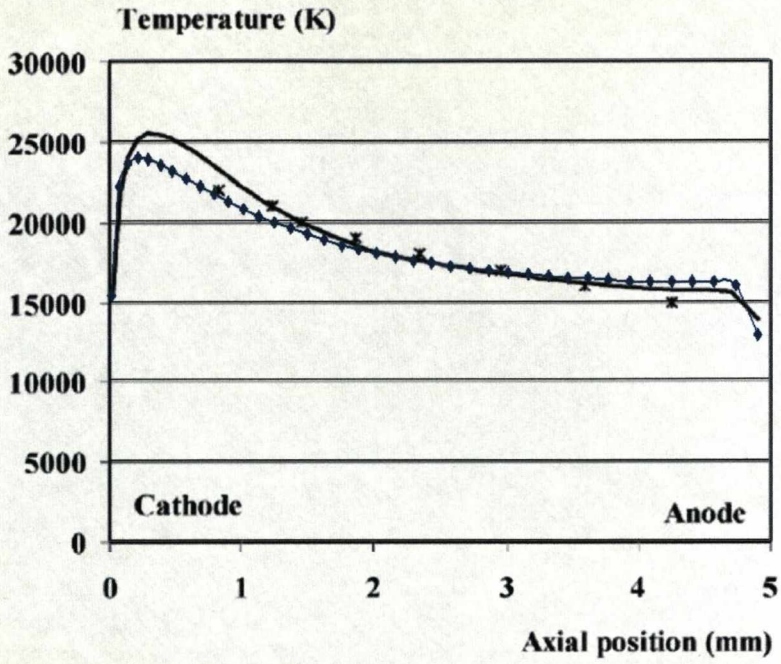

Figure 3.15 Axial temperature comparisons of this work (blue line) with [11] indicated by * and [16] the black solid line. Points read manually from graphs.

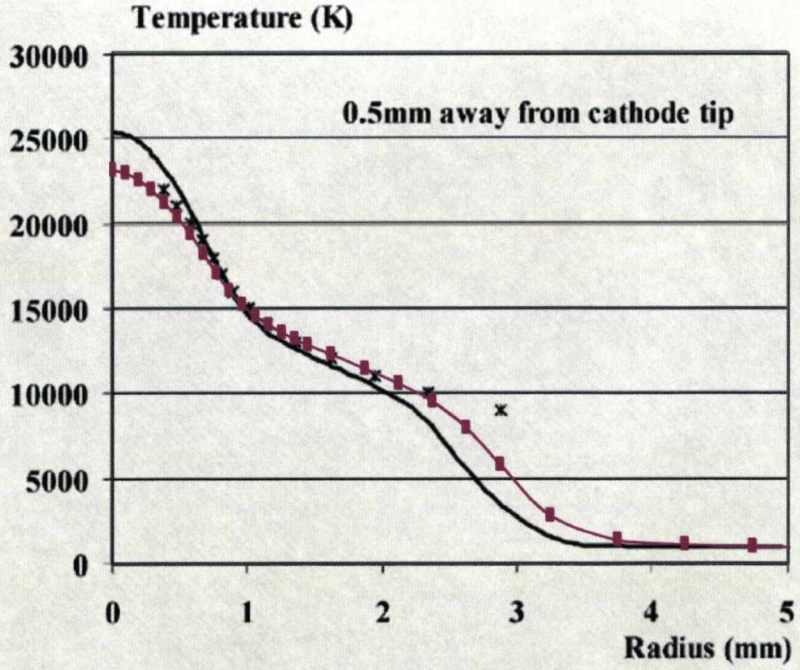

Figure 3.16(a)

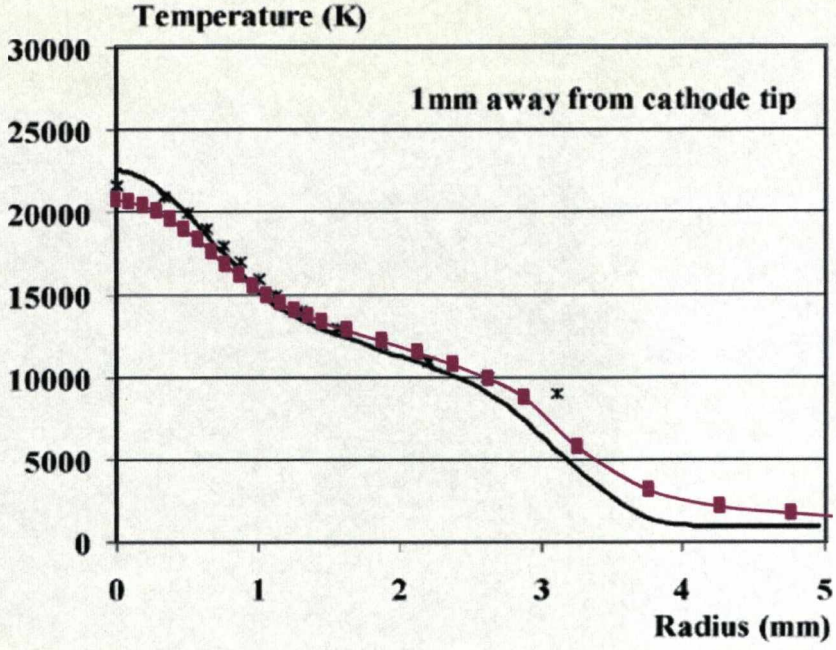

Figure 3.16(b)

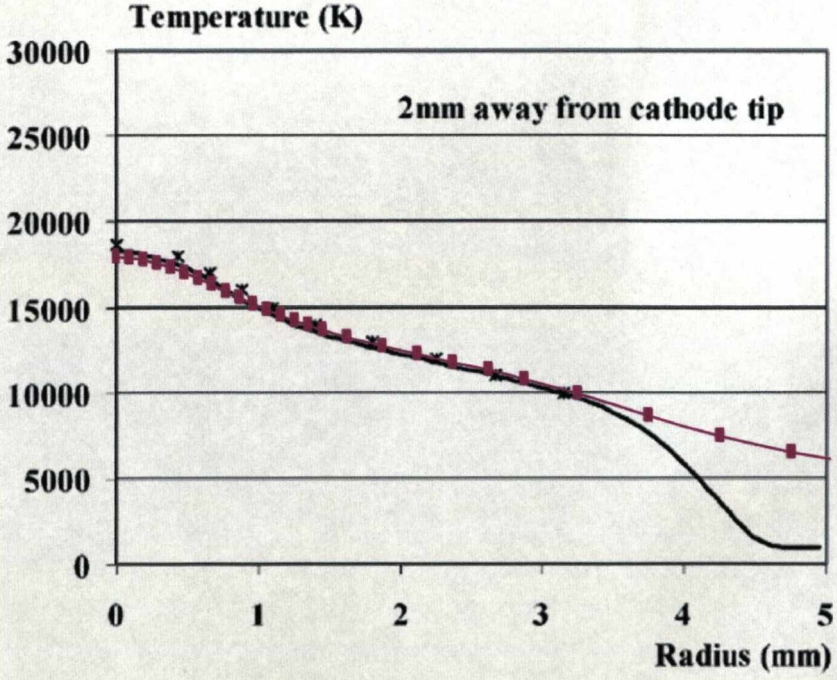

Figure 3.16(c)

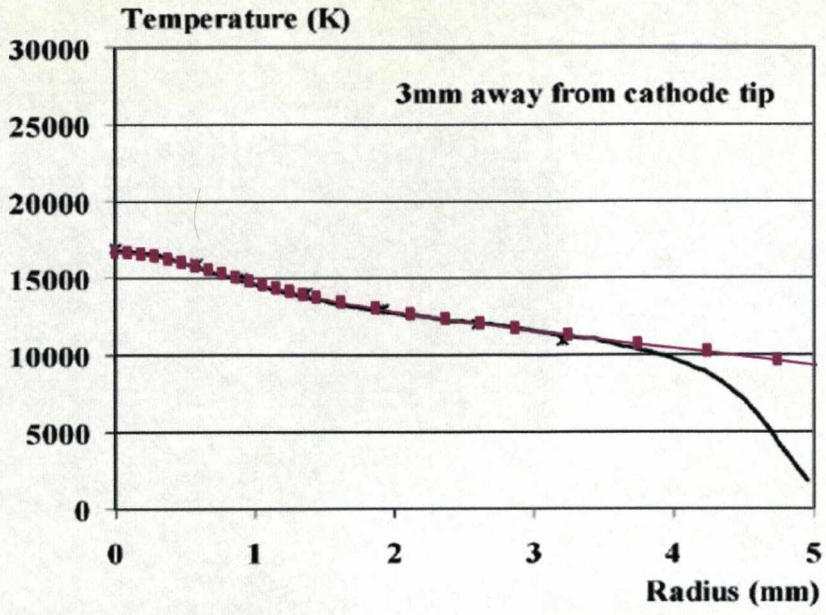

Figure 3.16(d)

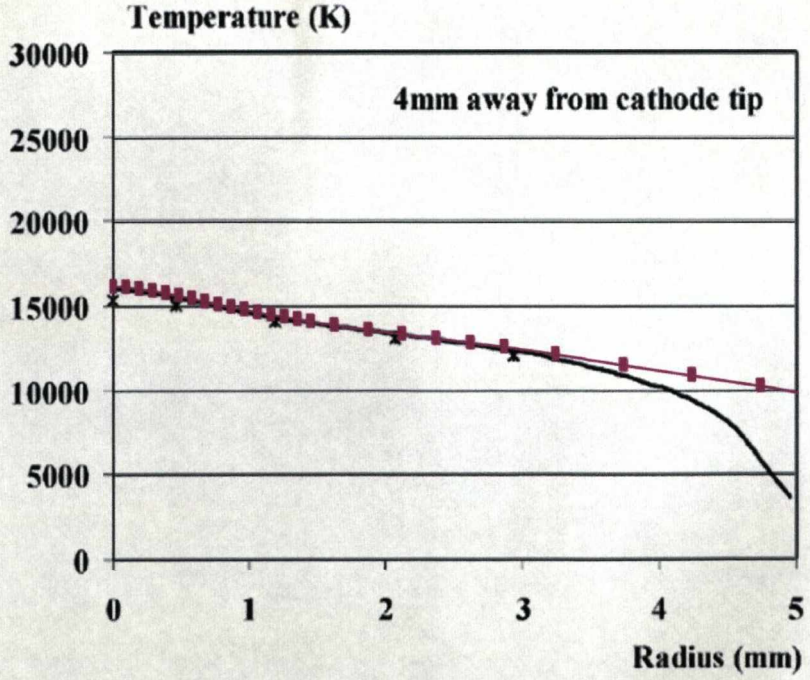

Figure 3.16(e)

Figure 3.16(a)-(e) show the temperature comparison of current simulation (pink line) with Haddad (*) [16] and Zhang (black solid line) [16] at radial locations 0.5, 1.0, 2.0, 3.0 and 4.0mm from the cathode tip

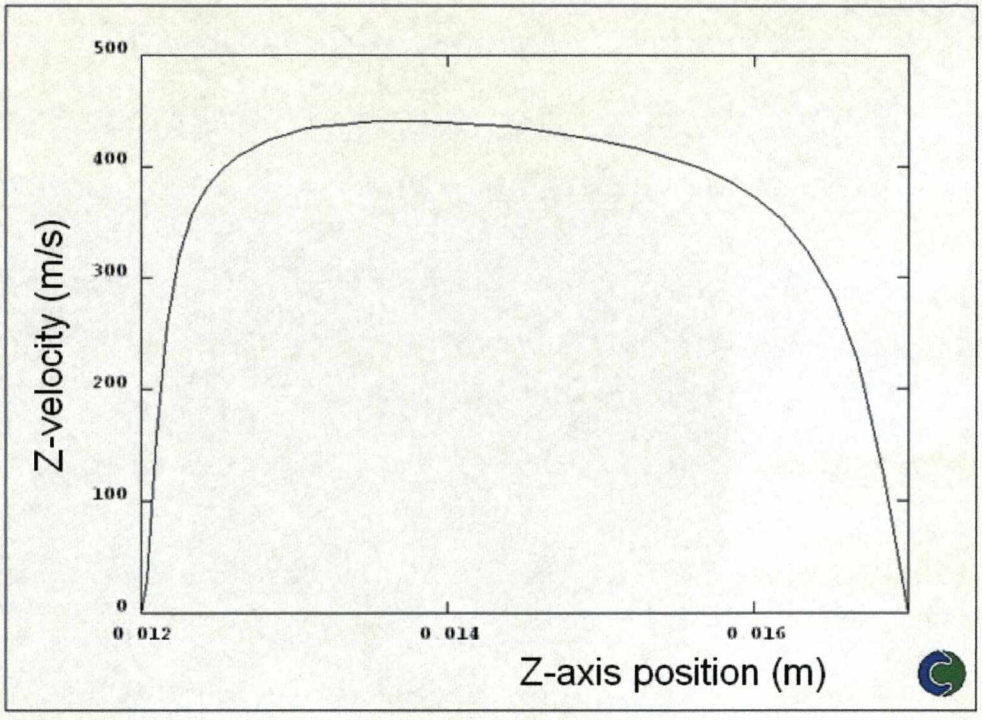

Figure 3.17 Velocity at arc axis

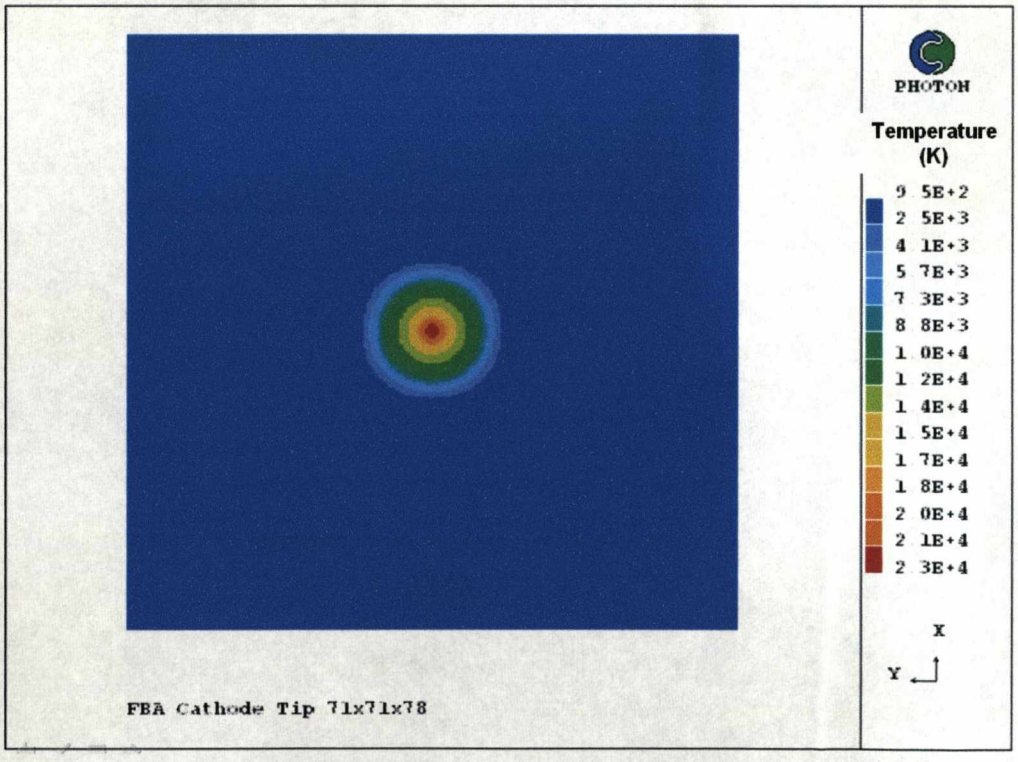

Figure 3.18(a) Temperature contour at IZ=50 (refer fig 3.5) showing symmetrical distribution

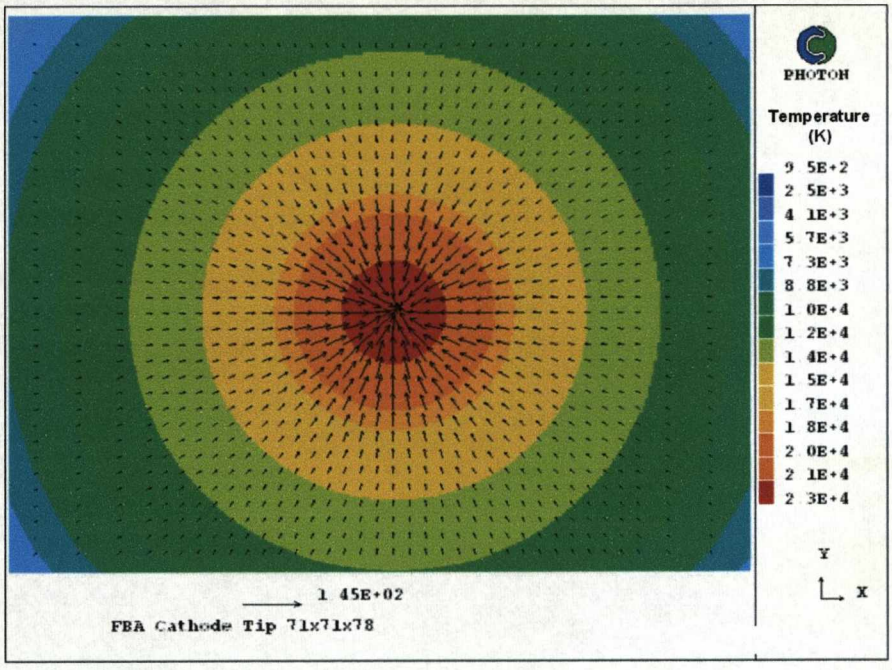

Figure 3.18(b) Temperature contour at IZ=50 (refer fig 3.5) showing a balanced velocity vector distribution

3.5 Summary

Important issues related to the implementation of 3D arc model, such as the representation of 3D objects in the grid system, and the role of Lorentz force in shaping the 3D arc column, is discussed in this chapter. The representation of a 3D object in the computational domain posed a challenge in the process of arc model implementation, especially for orthogonal staggered grid. In the present model, a novel numerical scheme has been developed to conveniently allocate cells within the 3D domain to generate the required solid object. This is a robust numerical scheme which is able to generate complex geometries easily. Special treatment in the computation of the long range magnetic field has been performed and verified. A 3D argon free burning arc model has been developed and the simulation results are compared with available experimental and numerical results. Important parameters of the model such as temperature, velocity, electric potential are compared and show good agreement. The comparison performed in the previous section shows that the a reasonable 3D arc model is achieved. This gives confidence in next chapter to simulate the behaviour of twin torch arc plasmas in a much more complex configuration.

3.6 Reference

[1] PHOENICS Version 3.4, CHAM Ltd, Bakery House, 40 High Street, London SW19 5AU, England

[2] Zhang J. L., Yan J. D., Murphy A. B., Hall W. and Fang M. T. C., "Computational investigation of arc behaviour in an auto-expansion circuit breaker contaminated by ablated nozzle vapor", Trans. on IEEE, Vol. 30, Issue 2, Part 2, pp. 706-719, 2002

[3] Yan J. D., Hall W. B. and Fang M. T. C., "Experimental and theoretical investigation of an enclosed free burning arc in SF6", J. Phys D: Appl. Phys., Vol. 33, pp. 1070-1080, 2000

[4] Liau V. K., Fang M. T. C, Yan J. D and Al-Shamma'a A. I., "A two-temperature model for a microwave generated argon plasma jet at atmospheric pressure", J. Phys. D: Appl. Phys., Vol. 36, pp. 2774-2783, 2003

[5] Haddad G. N. and Farmer A. J. D., "Temperature determinations in a free-burning arc: I. Experimental techniques and results in argon", J. Phys. D: Appl. Phys., Vol. 17, pp. 1189-1196, 1984

[6] Lowke J.J., Kovitya P. and Schmidt H.P., "Theory of free-burning arc columns including the influence of the cathode", J. Phys. D: Appl. Phys. 25, pp. 1600-1606, 1992

[7] Hsu K.C., Etemadi K. and Pfender K., "Study of the free-burning high-intensity argon arc", Appl J., Phys. 54 (3), pp. 1293-1301, 1983

[8] Sansonnens L., Haidar J. and Lowke J. J., "Prediction of properties of free burning arcs including effects of ambipolar diffusion", J. Phys. D: Appl. Phys., Vol. 33, pp. 148-157, 2000

[9] Menart J., Malik S. and Lin L., "Coupled radiative, flow and temperature-field analysis of a free-burning arc", J. Phys. D: Appl. Phys., Vol. 33, pp. 257-269, 2000

[10] Freton P., Gonzalez J. J. and Gleizes A., "Comparison between a two- and a three-dimensional arc plasma configuration", J. Phys. D: Appl. Phys., Vol. 33, pp. 2442-2452, 2000

[11] Fang M. T. C., Zhang J. L. and Yan J. D., "On the Use of Langmuir Probes for the Diagnosis of Atmospheric Thermal Plasmas", IEEE Transaction on Plasma Science, Vol. 33, No. 4, pp. 1431-1442, 2005

[12] Yan J. D., Fang M. T. C. and Jones C., "Electrical and Aerodynamic Behaviour of Arcs Under Shock Conditions", IEEE Transactions on Plasma Science, Vol. 25, No. 5, 1997

[13] Patankar S. V., "Numerical heat transfer and fluid flow", McGraw-Hill, 1980

[14] Gonzalez J. J., Gleizes A., Proulx P. and Boulos M., "Mathematical modeling of a free-burning arc in the presence of metal vapor", J. Appl. Phys., Vol. 74, 1993

[15] Hsu K. C., Etemadi K. and Pfender E., "Study of the free-burning high-intensity argon arc", J. Appl. Phys., Vol. 54, 1983

[16] Haddad G. N. and Farmer A. J. D., "Temperature determinations in a free-burning arc: I. Experimental techniques and results in argon", J. Phys. D: Appl. Phys., Vol. 17, pp. 1189-1196, 1984

[17] Lowke J. J., Morrow R., Haidar J., "A simplified unified theory of arcs and their electrodes", J. Phys. D: Appl. Phys., Vol. 30, pp. 2033-2042, 1997

[18] Zhu P., Lowke J. J., Morrow R, "A unified theory of free burning arcs, cathode sheaths and cathodes", J. Phys. D: Appl. Phys., Vol. 25, pp. 1221-1230, 1992

Chapter 4

TWIN TORCH PLASMA SYSTEM

4.1 Introduction

As discussed in Chapter 1, the twin torch plasma system, with two electrodes oriented at an angle of 90^{o} or above, has unique features when used as a high power source. Because the jet coupling zone is formed at a location well away from the electrode tips, it thus exhibits not only the advantages of a transferred and non-transferred arc, but also some new features. Firstly, similar to a plasma torch created by a non-transferred arc, the generation and maintenance of the high temperature jet does not require the work piece to act as a current emitter or collector. This feature extends its application to treat non-conducting materials such as glass or waste [1]. Secondly, because the jet coupling zone is still part of the electrical current loop, strong Ohmic heating maintains a temperature in the jet coupling zone that is normally higher than that in the torch of a non-transferred arc. Thirdly, the coupling of the two jets produces a hot environment which is remotely located from the electrode tips and its dimension in the transverse direction is larger than both a transferred and non-transferred arc. This special feature allows more flexible ways of feeding solid raw materials or reacting gases into the high temperature zone for product formation, such as the production of nano-scale powders [2]. It circumvents the shortcomings of conventional plasma torches such as nozzle blocking by agglomerates and nozzle erosions.

The efficiency of such a system is closely related to the plasma environment and also the interaction between the plasma and the work piece. To make an informed optimisation of the system performance, understanding the plasma environment and how it responds to the discharge conditions will be the first step. In view of the tremendous difficulties in 3D modelling of arc plasmas, the objective of this chapter is

to, using the model described in Chapter 2, simulate the twin torch plasma system under different working conditions and electrode arrangement, and to study the main features of this system in response to different discharge conditions.

4.2 General Features of the Twin Torch System

The system used in Tetronics has typically two torches placed roughly perpendicular to each, as shown in figure 4.1. The orientation of the torches is described by the included angle, that is the angle between the axes of the two electrodes. In this diagram the included angle is 110° and the shown system is a real twin torch plasma system for nano-scale powder formation. The included angle and the separation from the electrode tips can both be adjusted.

The entire nano-powder production system includes the inert gas injector which is a pipe located between the two electrodes, material feeder, processing reactor of the twin torches or the evaporation chamber, cooling or condensation zone, an optional centrifugal cyclone system, collection zone for collecting processed material. The collection zone is provided downstream of the cooling zone for collecting powders of the condensed vaporised material, which may comprise of a filter cloth. The collected powder product is then sealed, in inert gas, in a container at a pressure above atmospheric pressure. The feed material generally comprise of a metal, for example aluminium or an alloy. Liquid and/or gaseous feeder materials can also be used.

Adjustable parameters of the system enable optimised operations depending on the application requirement. For the arc plasma, its characteristics are determined by the included angle, electrode separation, type of plasma forming gas, mass flow rate at both inlets, and operating current.

As shown in figure 4.2, the bright plasma jets from both electrodes create the coupling zone which is a high temperature environment well suitable for material synthesis and treatment. For low frequency current maintained discharge, the arc root on the cathode surface is much smaller than the anode attachment because of the well known cathode spot phenomenon. The cathode electrode usually has a conic tip to stabilise the arc root

and to allow easy entrainment of gas into the arc column. The thinner arc root leads to stronger magnetic pinch effect generating stronger jet flow in comparison with the anode attachment. The jet from the cathode is thus thinner than that from the anode.

The shape of the coupling zone is affected by a number of factors. The dominant mechanism in shaping the coupling zone is expected to be the Lorentz force generated by the discharge current and its interaction with the magnetic field induced by the current itself. At the same time, the velocity of the jet flow also plays an important role. Argon gas is commonly used in applications where an inert atmosphere is needed to avoid oxidation of the product or work piece. In the present work the twin torch plasma is simulated with argon as its working gas.

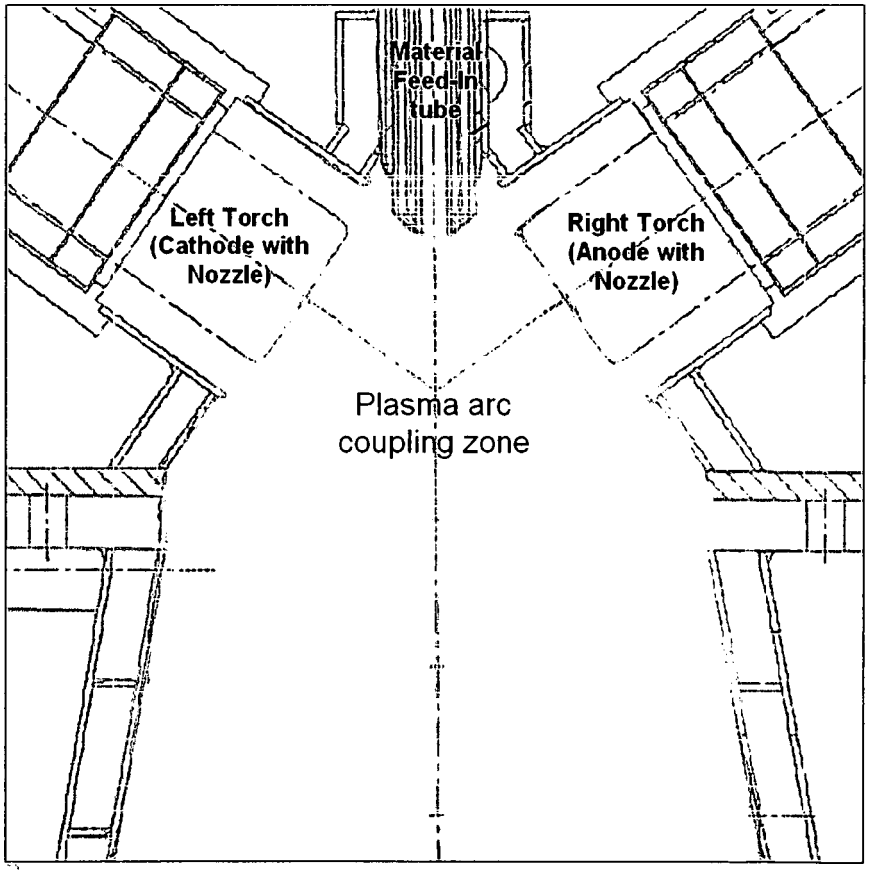

Figure 4.1 Schematic diagram of the a twin torch plasma system

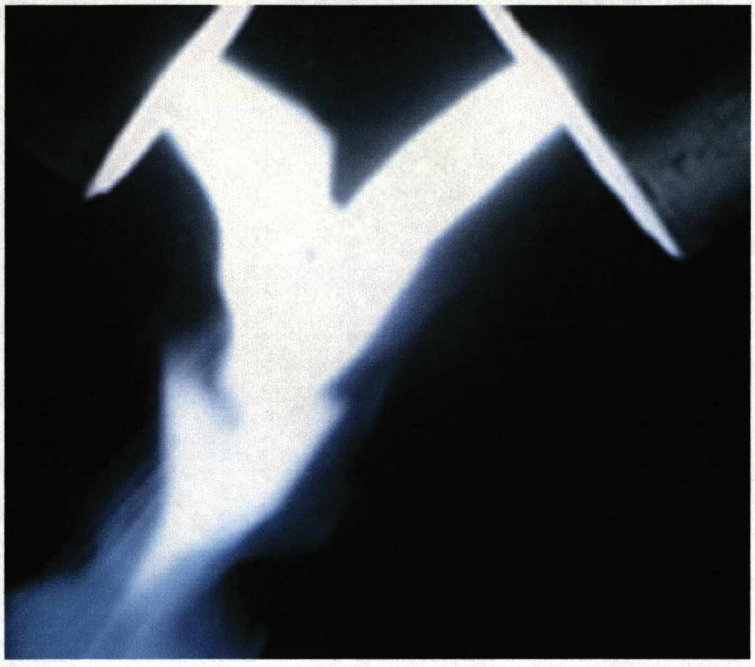

Figure 4.2 Image of the twin torch plasma. The thinner jet originates from the cathode and the bent jet is from the anode.

4.3 Geometry and Dimensions of the Twin Torch System used for Simulation

The cathode torch consists of a thoriated tungsten electrode with a conic tip, as shown in figure 4.3. A copper nozzle provides a shroud of plasma gas around the cathode and also serves as an auxiliary electrode for high frequency plasma ignition. The radius of the cathode tip is 1mm and the full cone angle is 60°. The cathode rod has a radius of 6.5mm and the thickness of the ring-shaped gas inlet is 2mm.

The anode torch is similar to the cathode in structure. The anodic electrode tip is made of a high-purity copper button. The radius of the anode tip is 8mm and the thickness of the ring shaped gas inlet is 2mm. The copper nozzle around the anode is extended from the tip for 10mm in order to minimise anode erosion and confine the anode attachment to the middle of the tip. Both electrode assemblies are water cooled to prolong their life time. The erosion rate of copper and tungsten were both found to be less than 0.01 parts per million (ppm) with argon as the working gas for current range from 200A to 1000A [3]. Erosion of electrode material is negligible.

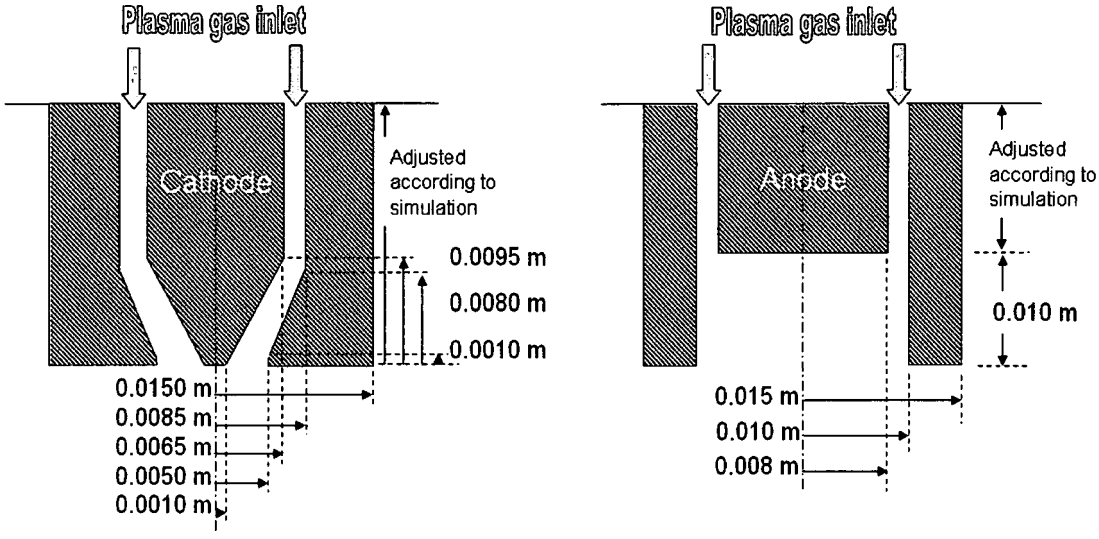

Figure 4.3 Cross section and dimensions of cathode (left) and anode (right) assembly used in the simulation.

Two configurations have been simulated in this chapter at different current levels from 300A to 900A. In the first configuration, the two electrodes have a 90° included angle, as shown in figure 4.4. The torch separation from the cathode tip to the anode tip, is 76mm for which measured V-I characteristics is available for comparison. A cubic computational domain of 130mm x 130mm x 130mm is chosen for the simulation which is sufficiently large to accommodate the plasma jet while limiting the required number of cells to reduce computing time.

Since our focus in the present work is on the plasma environment, the reacting gas feeder pipe and the condensation region in the real device are not included in the computational domain.

In the second configuration, the torches have an 180° included angle, which is basically a transferred arc configuration. The dimensions of the electrodes and electrode separation are the same as in the first system. The computational domain is also the same.

The typical mass flow rates at the cathode and anode inlets are respectively 20 and 30 NL/min.

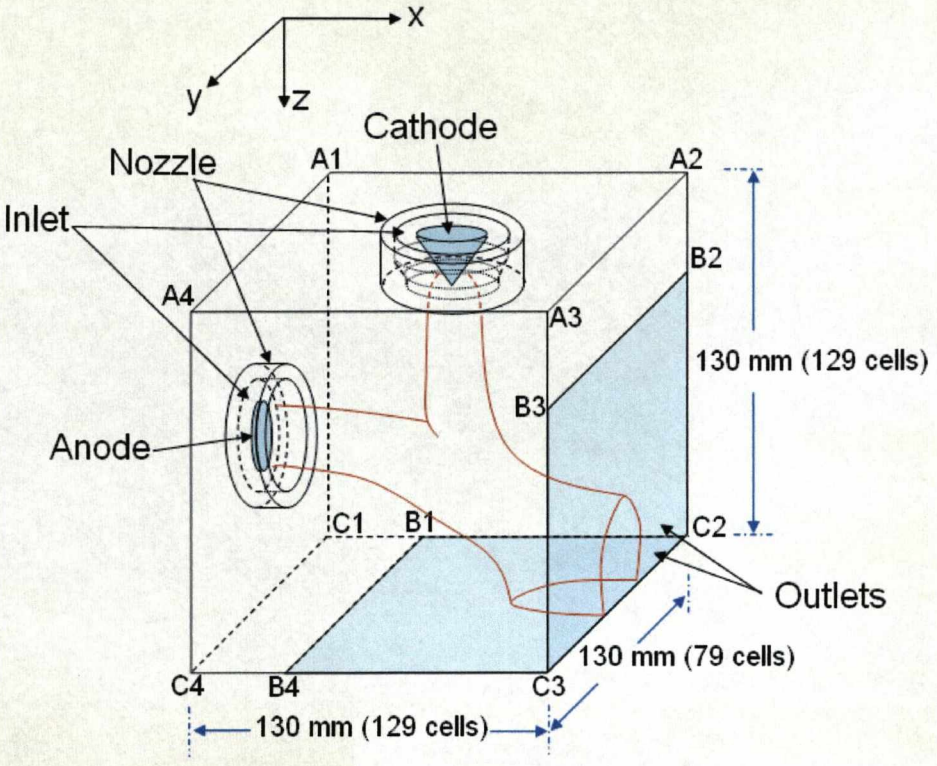

Figure 4.4 Schematic of twin torch plasma system with included angle of 90 degree

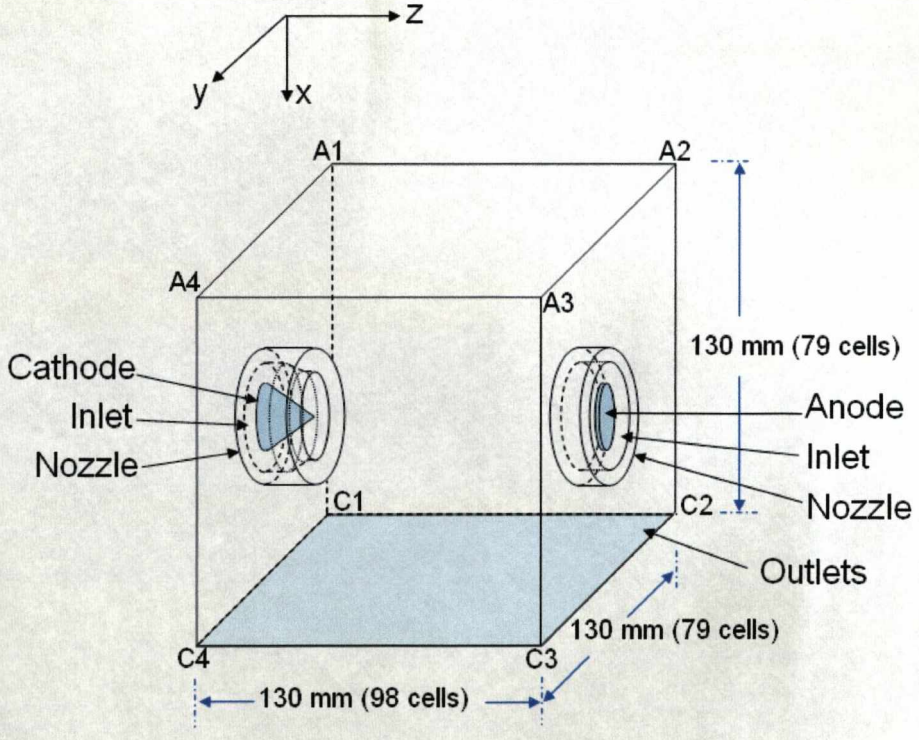

Figure 4.5 Schematic of twin torch plasma system with included angle of 180 degree

The cylindrical shaped geometries of the cathode, anode and nozzles are very difficult to create. This difficulty has been overcame with a user code (detailed in Chapter 3) and successfully generated in the defined computational domain easily.

4.4 Grid System and Boundary Conditions

Due to the large size of the CFD domain, a compromise has to be made between the total number of cells and the computing cost. It would be ideal to have dense grid for the whole CFD domain for best spatial resolution. However, the computation time will be prohibitively long, usually several days on a 2.1 GHz Pentium Core Duo PC with 2GB memory using the serial PHOENICS solver [4]. Thus, the general rule is to set a dense grid is the arc region, especially at the cathode and arc boundary where a high gradient of temperature and density exists, and regions where the flow field undergoes rapid change. Figure 4.6 shows the domain for the case of 90 degree twin torch with 129, 79 and 129 cells in the x, y and z direction respectively, giving a total number of 1.315 million cells. The typical cell size is 0.345mm by 0.345mm in the arc region. The number of cells in the y direction is fewer than that in the other two directions in view of that fact that jet coupling takes place in the x-z plane. For the case of 175 degree twin torch, the number of cells in the x, y and z directions are 79, 79 and 98 cells with the assumption of x and y plane symmetry, and a total number of 0.612 million cells, as shown in figure 4.7. Although the number of cells is reduced, the typical cell size at the arc region remains the same as the former domain.

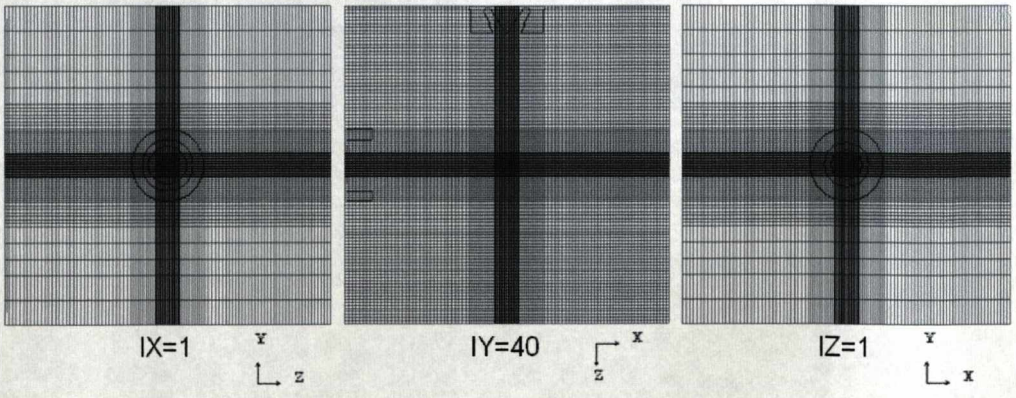

Figure 4.6 Cell distribution for 129 x 79 x 129 grid of case 90 degree twin torch

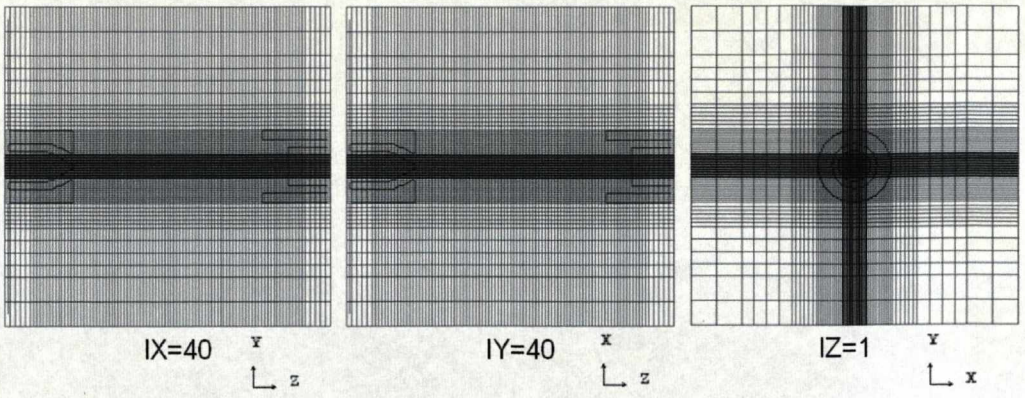

Figure 4.7 Cell distribution for 79 x 79 x 98 grid of case 180 degree twin torch

The boundary conditions for the two systems simulated in this chapter are set in a similar way to those used for the free burning arc in Chapter 3. The only difference is that the argon gas enters the nozzle with a temperature of 300K and there is no energy exchange between the plasma and the anode. The position of the outlet used in the simulation is given in figures 4.4 and 4.5.

4.5 Results and Discussions

4.5.1 Overall Performance of the Arc Model

In order to check the overall accuracy of the 3D arc model, a series of simulations for both configurations were carried out for the current range from 300A to 900A. Because of the time available for this study, only one electrode separation is used. Because a lack of experimental results, only the predicted arc voltage with measurement given in [3] can be compared. The comparison is given in figures 4.8 and 4.9.

It can be seen that in this model, when using the laminar assumption for the plasma flow is able to predict the arc dynamics in terms of its arc voltage variation in response to current change. In this aspect, our model performs very well for both configurations.

However, the predicted arc voltage is on average higher than the measurement by 5V-7V for the 90 degree configuration. It should be lower than the measured arc voltage because in the present work only the arc column is considered with the non-LTE

electrode layers neglected. Morrow and Lowke [6] used a one dimensional model to study the electrode sheaths of a free burning argon arc at 200A and obtained a total electrode voltage fall in the range from 2V to 5V. Benilov [7] used a more advanced model to consider the non-LTE processes in the cathode layer and obtained a cathode fall of about 11V for a tungsten cathode in argon with a current from 300A to 1000A. Taking this into account, the model predicts an arc voltage which is higher than the measurement by about 10% to 15%. It however must be noted that there is no experimental uncertainty given for the measure arc voltage of the twin torch system. Thus the comparison here is only indicative. One possible reason for the higher predicted arc voltage could be due to the arc instability in reality. High speed video has shown that the two jet is not coupled in a stable manner. The position of the two jets are constantly oscillating in the process of coupling and detaching. The rapid fluctuation in the size of the coupling zone produces a statistical effect, that is on average the coupling zone, thus the current conduction area is broadened. This is statistically similar to the effect of the presence of turbulence. Taking this type of oscillation into account a small amount of turbulence is introduced in a separate simulation with a turbulence parameter, which is defined in Chapter 2, of 0.02. As shown in figure 4.8, the arc voltage is reduced by 6V for the two cases simulated. Details on the influence of turbulence will be discussed separately later in section 4.5.6.

In figure 4.9 our predicted arc voltage for the 180 degree is plotted on the same diagram with the measurement for a 175 degree included angle. The difference in the angle of 5 degree is expected to be small therefore it is valid to carry out the comparison. Similar to the 90 degree included angle configuration, our predicted arc voltage is again higher than the measurement by 10% if the electrode sheath fall is taken into consideration. The voltage current slope decreases as the current increases. Again the comparison here is indicative since no measurement uncertainty is given in [3].

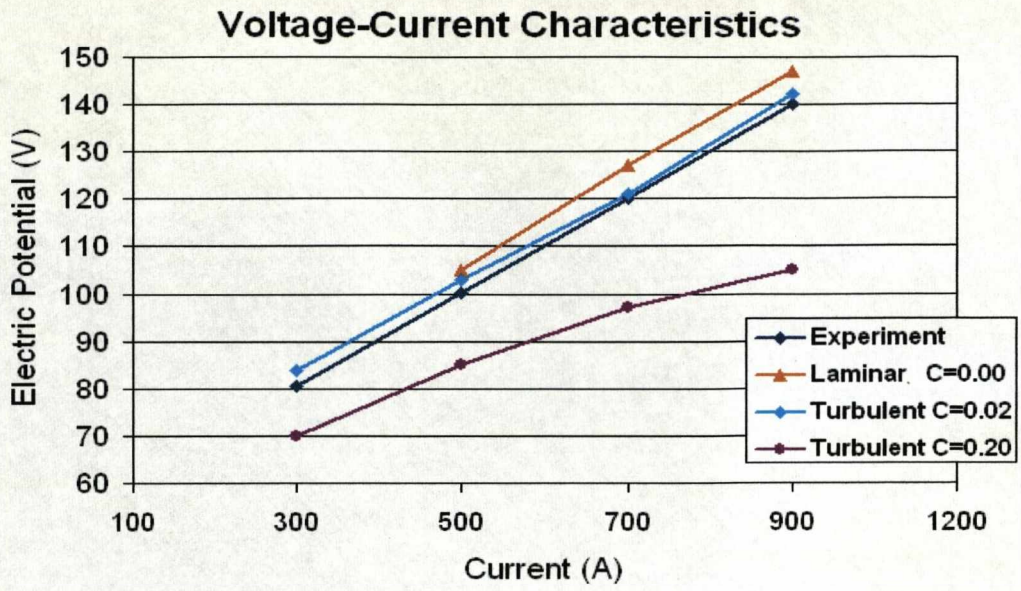

Figure 4.8 Voltage-Current characteristics comparison with experimental data for included angle of 90 degree and torch separation of 76mm. Argon mass flow at inlets are 20Nl/min and 30Nl/min for cathode and anode respectively

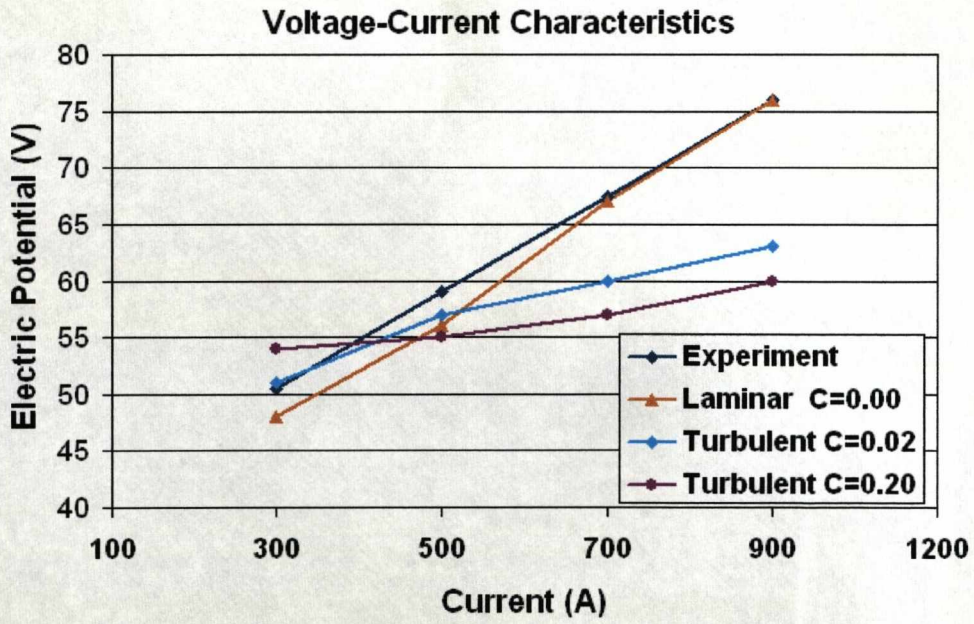

Figure 4.9 Voltage-Current characteristics comparison with experimental data for included angle of 180 degree and torch separation of 76mm. Argon mass flow at inlets are 20Nl/min and 30Nl/min for cathode and anode respectively

4.5.2 Thermal environment of the coupling zone with 90 degree included angle

In this section, the typical plasma behaviour is analysed using the 500A case with laminar flow. Because of the 3D nature of the arc column, it is necessary to define the planes and lines over which the following results are plotted. Without this information it would be very difficult to image the locations.

In figure 4.10(a), the plane IY40 is the middle plane of the domain in the y direction. It passes through the axes of the cathode and anode. Most of the results presented in this section are plotted on this plane. IX63 and IZ63 are the cross section plane on the x and z axis respectively. Figure 4.10(b) shows the horizontal plotting plane where the upper plane contains the plasma profile of the two jets and the lower plane give the cross section of the coupling zone. Figure 4.10(c) shows the line where data are taken for x-y plots.

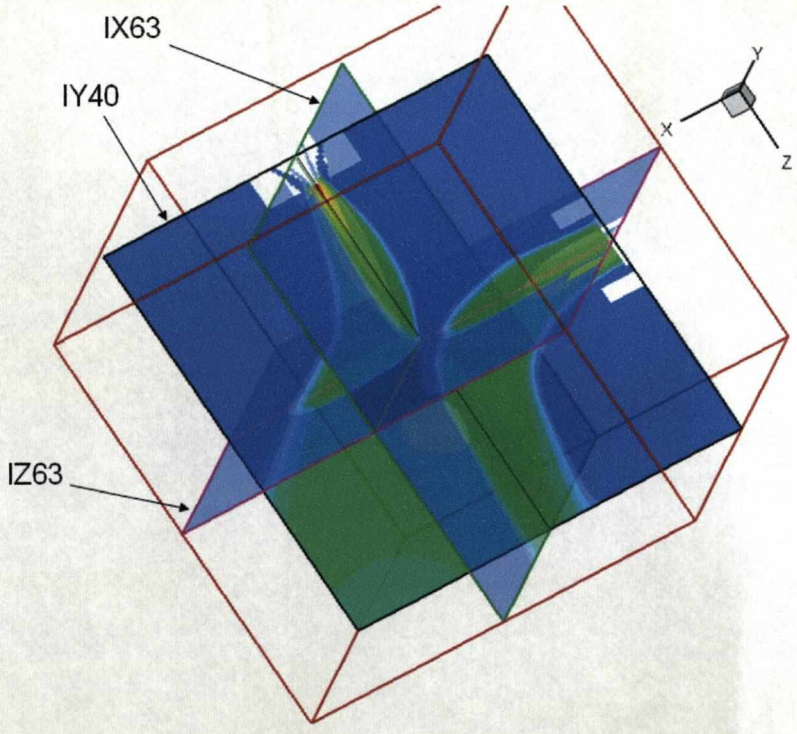

Figure 4.10(a)

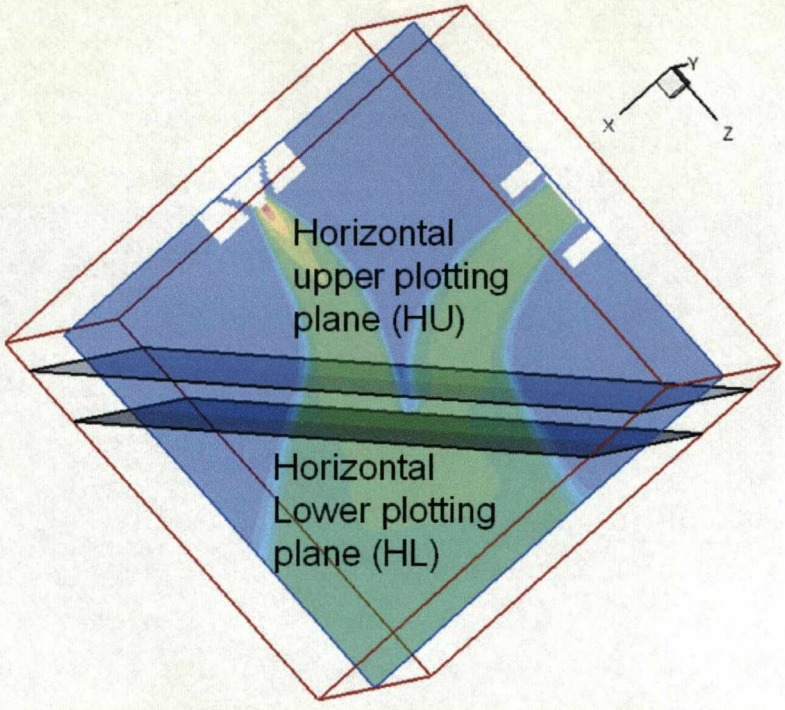

Figure 4.10(b)

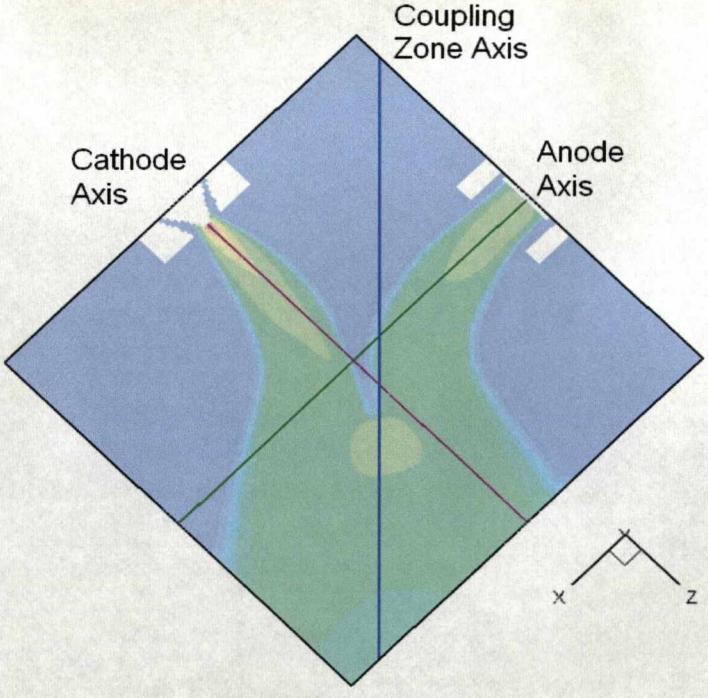

Figure 4.10(c)

Figure 4.10(a)-(c) Contour Plotting planes and line plots (temperature contours are shown for illustration)

Figure 4.11(a) shows the temperature field on the plane IY40, which is the symmetry plane of the coupling zone. The temperature ranges from 300K to 21330K, with the highest temperature at the cathode tip. The two jets serve as the source of hot plasma to sustain the coupling zone where material processing or evaporation of solid materials take place. To give a quantitative description of the temperature distribution, isotherms are given in figure 4.11(b) with a smaller temperature range from 10000K to 21500K for higher temperature resolution. It can been seen that the temperature distribution in the coupling zone is rather uniform from 10500K to 12000K, as shown in figure 4.11(c). The typical width of the coupling zone in the x-z plane is 60mm. There is a sharp edge where temperature drops rapidly from 10000K to 300K in 5mm.

The temperature at the jet separation point is higher with a typical value of 12500K. This high temperature region is essential in maintaining the coupling of the two jets where strong Ohmic heating is present to provide the energy that is convected away and conducted away to the surrounding low temperature area.

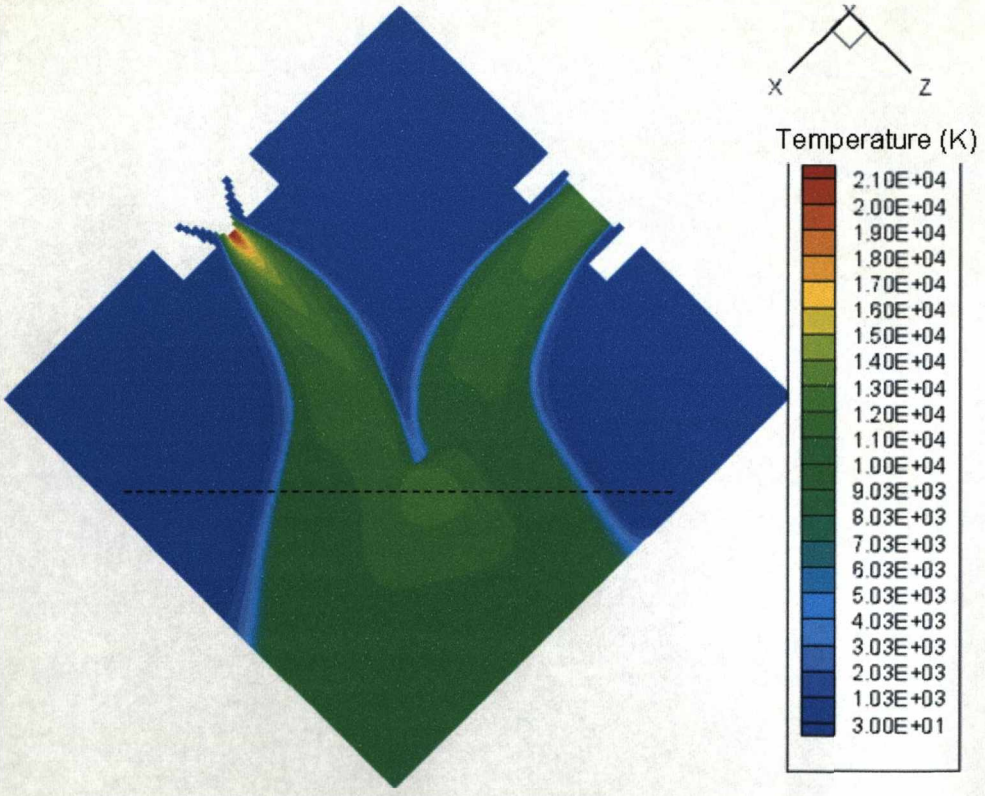

Figure 4.11(a) Temperature contour at IY40 plane, dash line indicates the plotting line for figure 4.11(c)

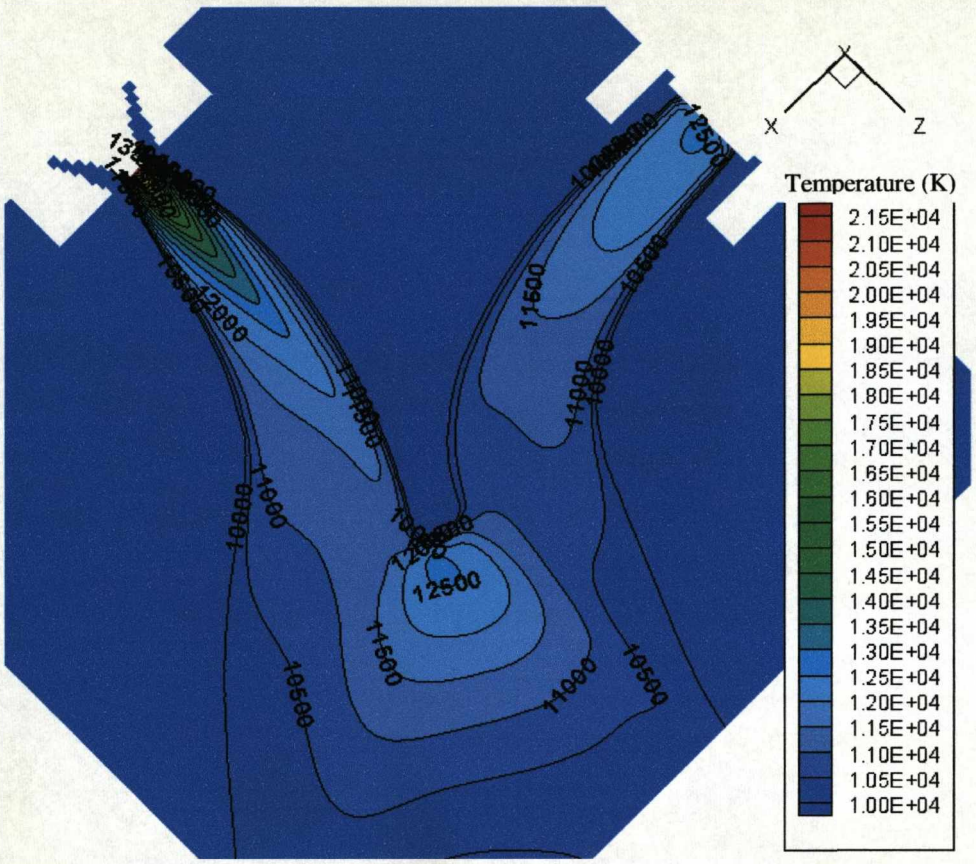

Figure 4.11(b) Temperature field with iso-contour lines

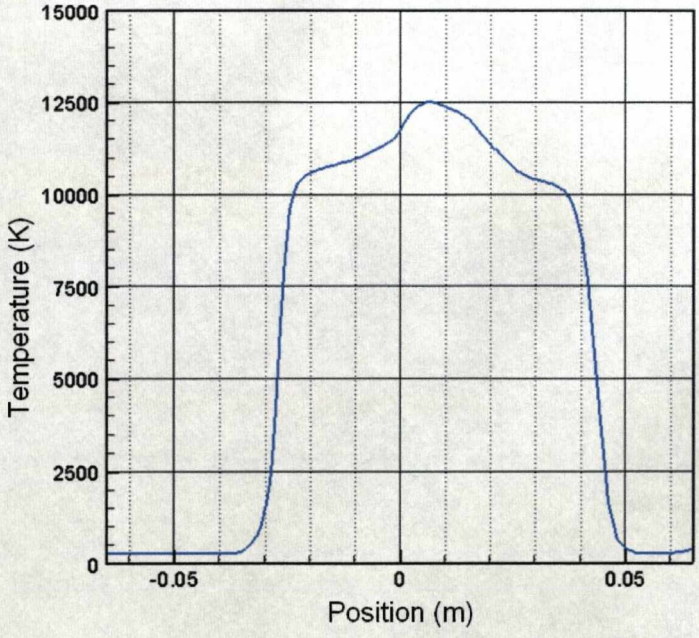

Figure 4.11(c) Temperature plot across the coupling zone

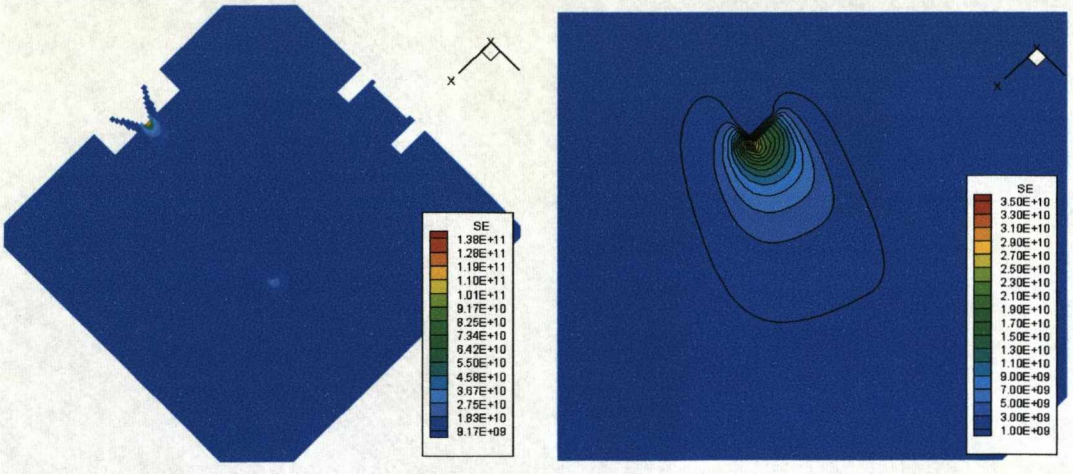

(a) (b)

Figure 4.12 Ohmic heating, SE (W/m^3) (a) for the whole domain and (b) at the coupling zone.

When the work in this chapter started, it was thought that the two jets will merge to form a larger jet. This is however not the case from our simulation. As shown in figure 4.13(a)-(b), the two jets are rather coupled through a thin tissue shaped layer. The current density and temperature in this layer are both high in comparison with those in the two jets before they are coupled ($10^7 A/m^2$, figure 4.15 and 4.16). The electric potential distribution is given in figure 4.17(a). The flow field and streamlines diagram given in figures 4.18 and 4.19 indicate that gas entrainment into the two electrodes mainly in the first 10mm from the electrode tip. Further downstream gas flows within the envelop of the arc column. Gas in the linking tissue between the two jets is from the cold region located at the point of separation.

Results here from the model therefore suggest the question, that how the coupling zone can be most efficiently used for applications where relatively high temperature (over 10000K) is needed, based on its shape and temperature distribution and how the raw materials or reaction gas should be injected into this hot zone. For information the shape of the coupling zone with a minimum temperature of 8000K is also given in figure 4.14.

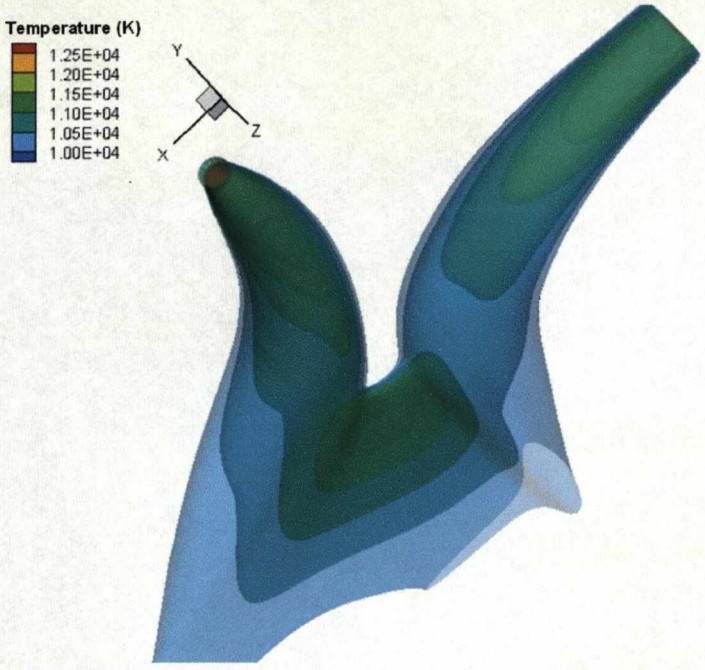

(a) Temperature iso-surface at 10000K to 12500K at 500K intervals

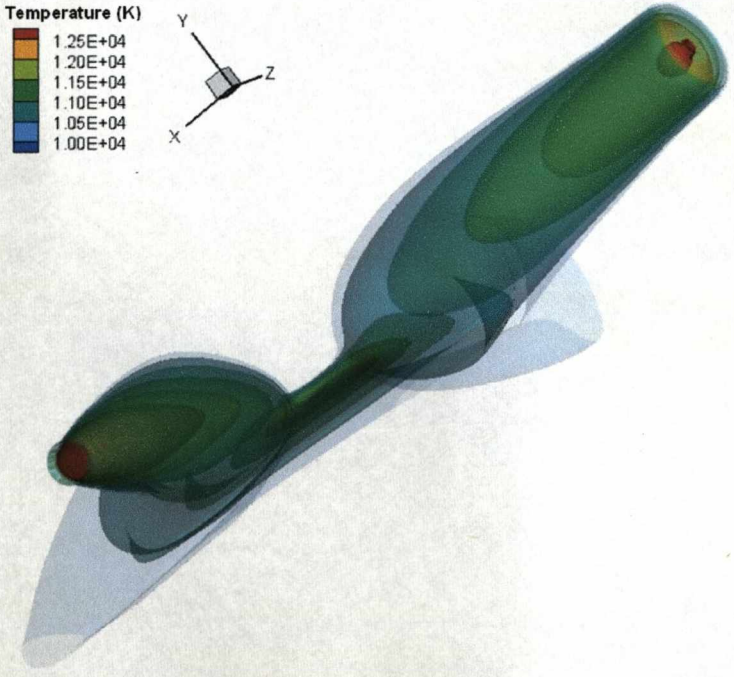

(b) Temperature iso-surface at 10000K to 12500K at 500K intervals (top view)

Figure 4.13(a)-(b) Shape of coupling zone viewed from different directions.

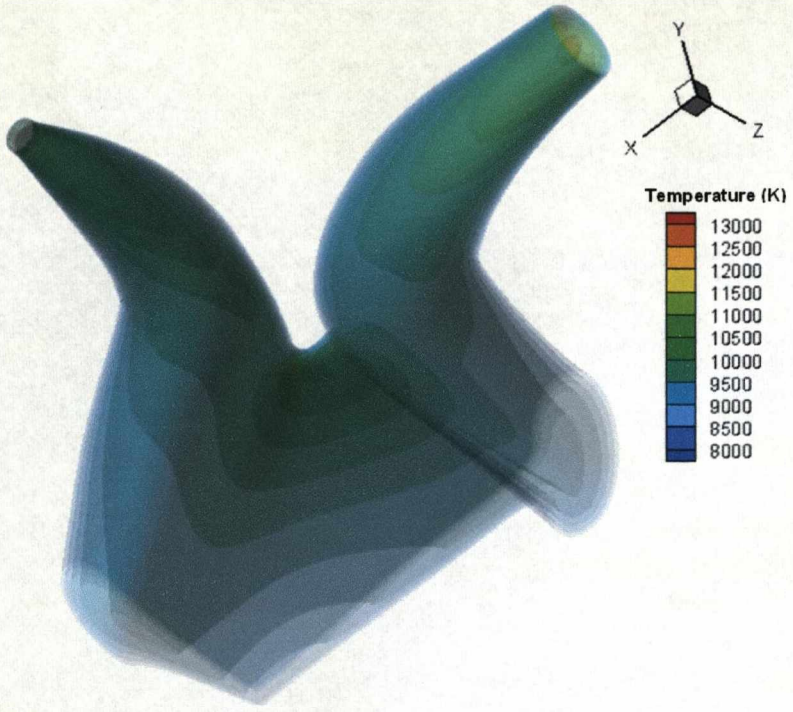

Figure 4.14 Shape of coupling zone with 8000K as its boundary up to 12500K with intervals of 500K

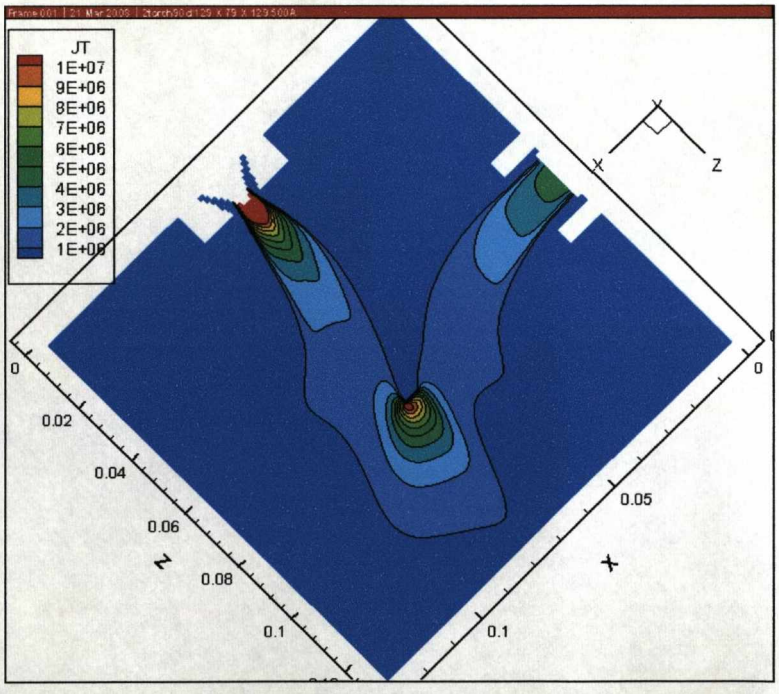

Figure 4.15 Magnitude of Current density, JT (A/m^2). Note that the maximum current density on the cathode tip is around $5e7A/m^2$. The use of a smaller current density range is to visualise the current density in the coupling zone more clearly.

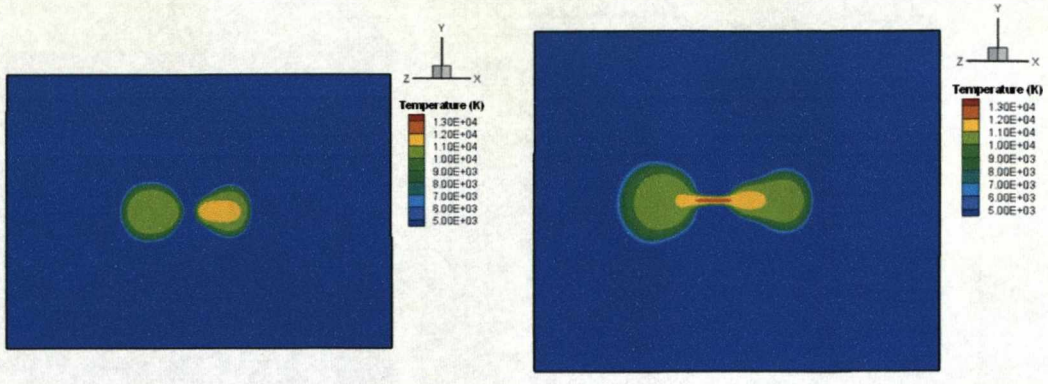

(a) upper plane (b) lower plane

Figure 4.16(a)-(b) Temperature field plotted on upper and lower horizontal planes as indicated in fig 4.10(b)

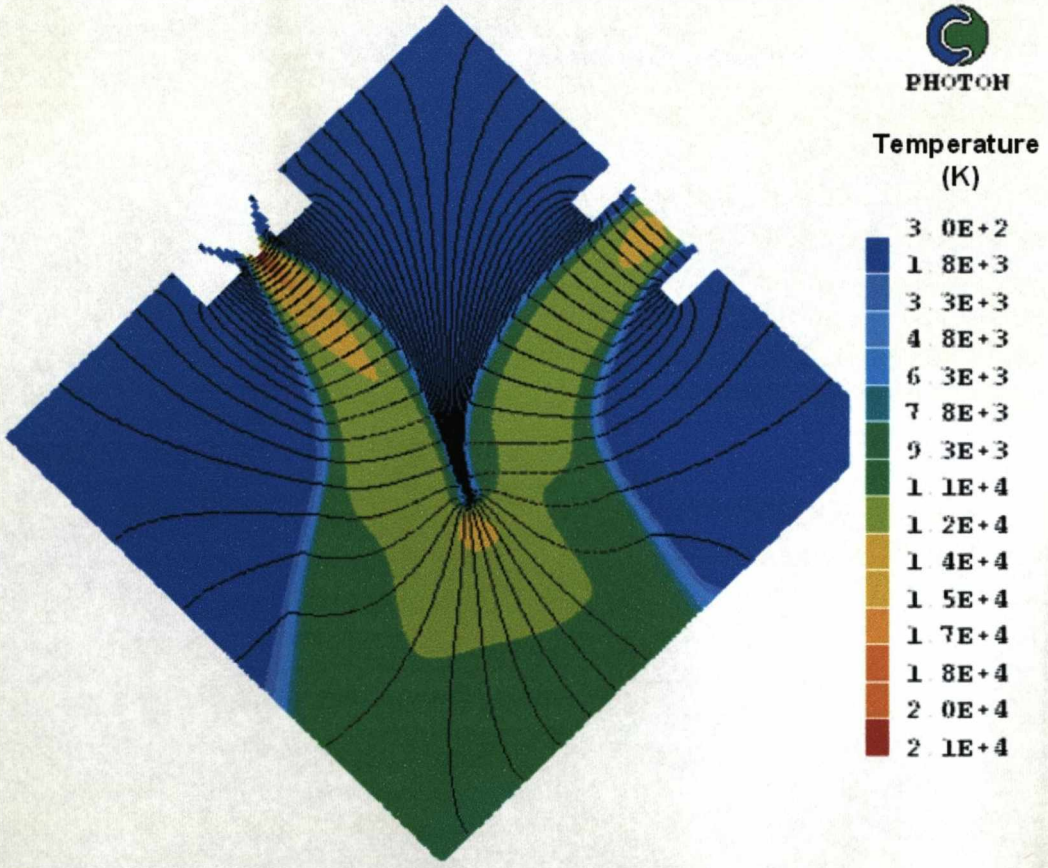

Figure 4.17(a) Electric Potential distribution iso-lines and temperature contour

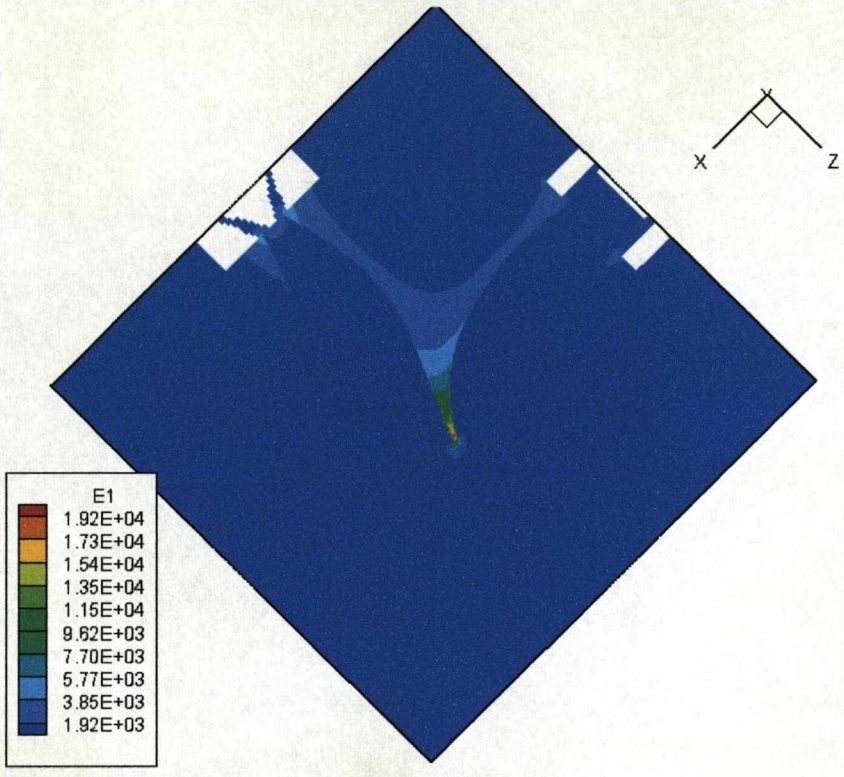

Figure 4.17(b) Magnitude of Electric Field, E1 (V/m)

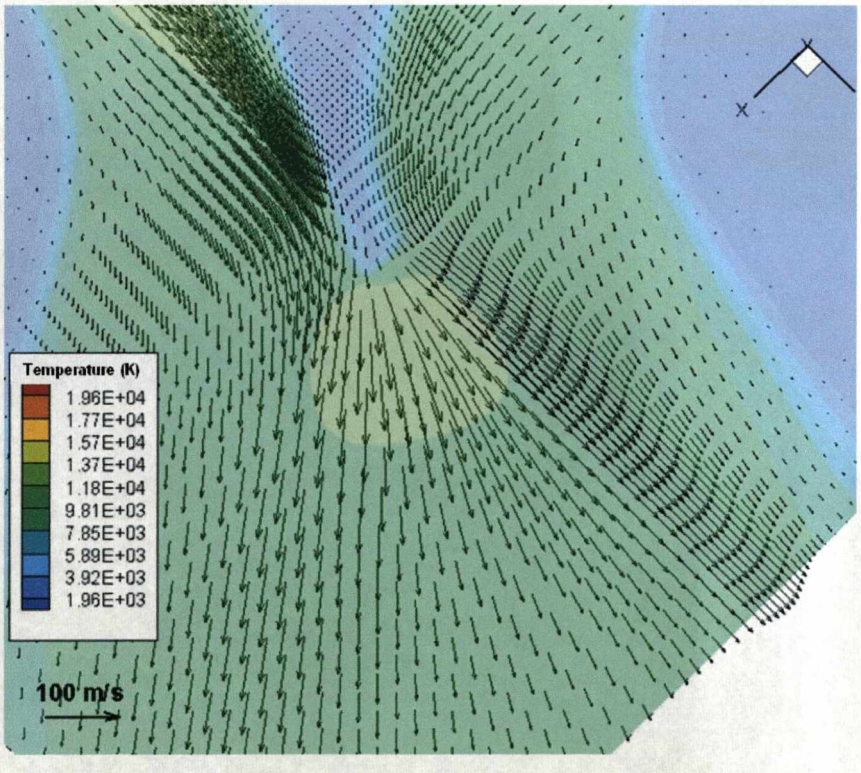

Figure 4.18 Velocity field with temperature contour

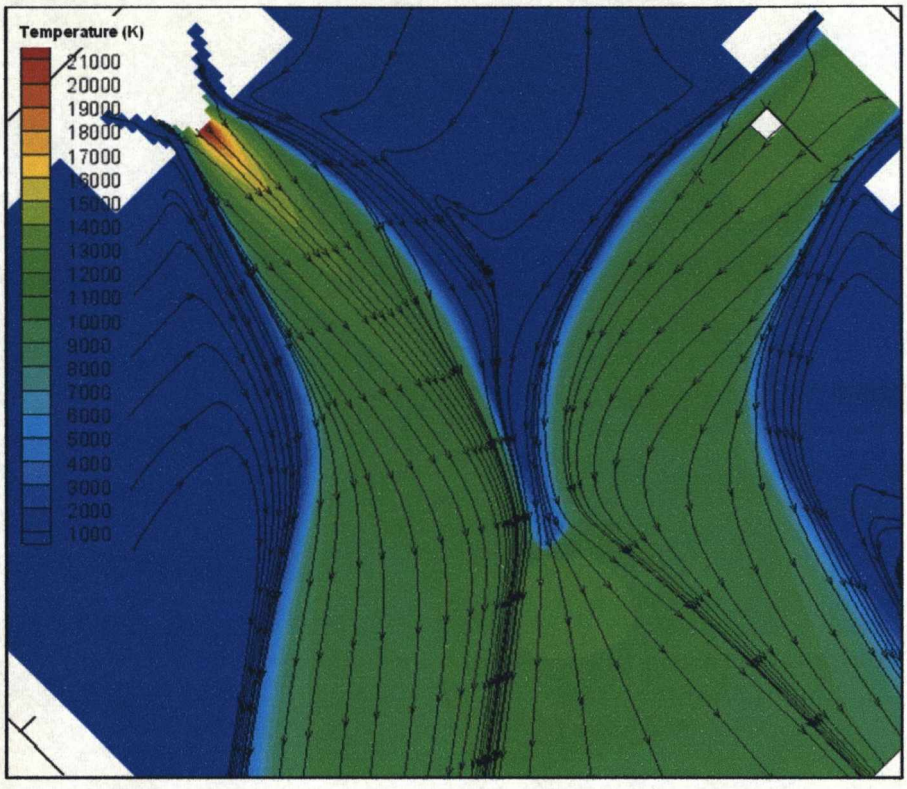

Figure 4.19 Flow Streamlines with temperature contour

4.5.3 Behaviour of the two jets

The cathode jet originates from the cone shaped cathode where strong argon gas is driven out of the shielding nozzle. Because of the argon flow entrainment and the small cathode tip, the arc root is confined mainly on the cathode tip where strong magnetic pinch effect exists. The temperature and pressure distribution in the arc column is given in figure 4.20 and 4.21.

The current density at the cathode tip is the highest in the whole discharge region with a maximum value of 5e7A/m^2. In the first 15mm away from the tip, the cathode jet is axisymmetric, as shown in figure 4.21. The maximum speed of gas near the cathode tip reaches 441m/s (figure 4.22). Because of this high speed of gas flow, the cathode jet is less bent in comparison with the anode jet when both are coupled. This can be seen in figure 4.11.

In contrast to the cathode, the anode jet has a lower speed and its shape is easily affected by the Lorentz interaction between the two jets. As a result, the anode jet exhibits axisymmetry only in the first 10mm from the anode tip despite the extended nozzle to guide the flow (figure 4.23). The velocity vector in the corresponding planes are also shown in figure 4.24 for both anode and cathode jets. The comparison of the velocity component at the anode (x-velocity component) and cathode (z-velocity component) is plotted in figure 4.25.

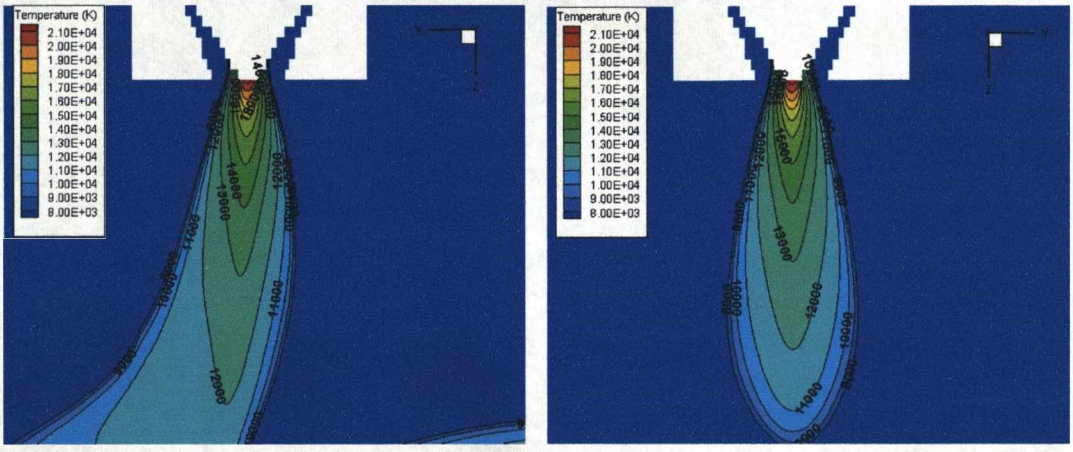

(a) y-view (b) x-view

Figure 4.20(a)-(b) Temperature distribution at the cathode jet for the current of 500A

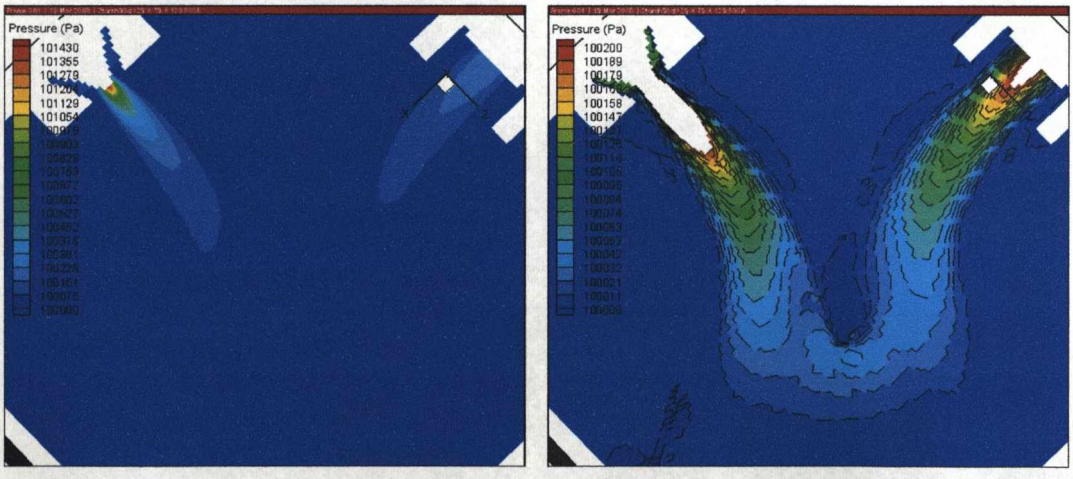

(a) Pressure contour maximum range (b) Pressure contour up to 100.2kPa

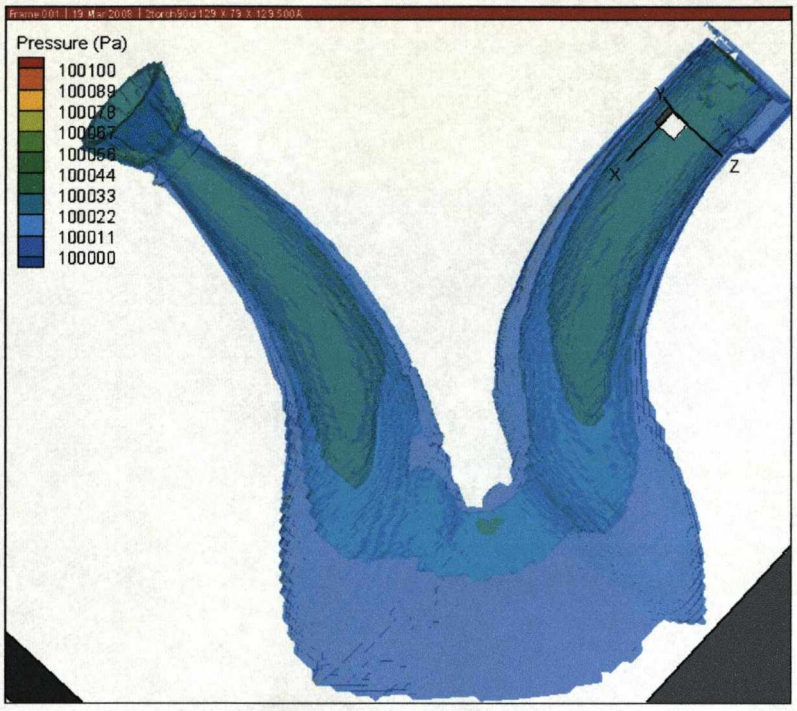

(c) Pressure iso-surface

Figure 4.21(a)-(c) Pressure field

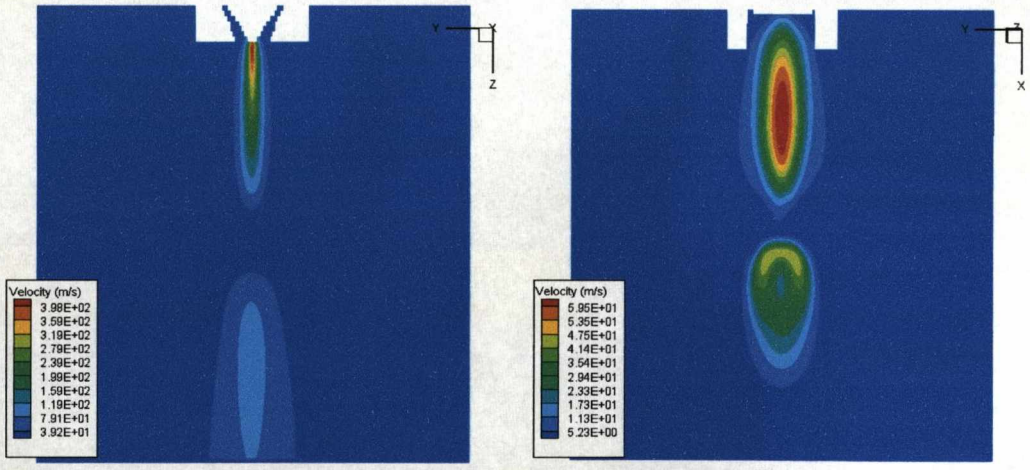

(a) Cathode (b) Anode

Figure 4.22(a)-(b) Velocity of gas flow along the axis of the electrodes

Figure 4.22(a) shows the z- velocity component at the cathode and figure 4.22(b) shows the x-velocity component at the anode. There is a high velocity region at the lower region is due to the contour being plot the plane which passes the other plasma jets as shown in figure 4.10(a) at IX63 and IZ63.

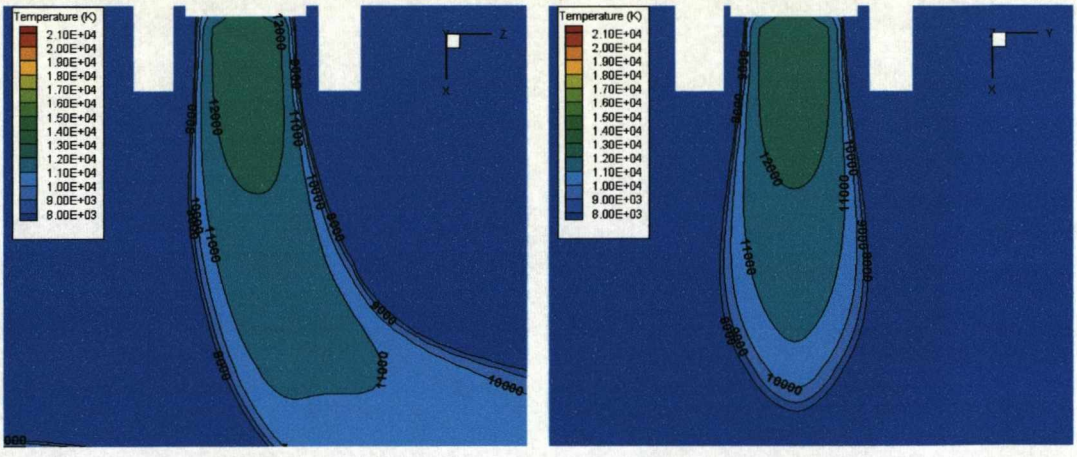

(a) y-view (b) z-view

Figure 4.23(a)-(b) Temperature distribution at the anode jet for the current of 500A

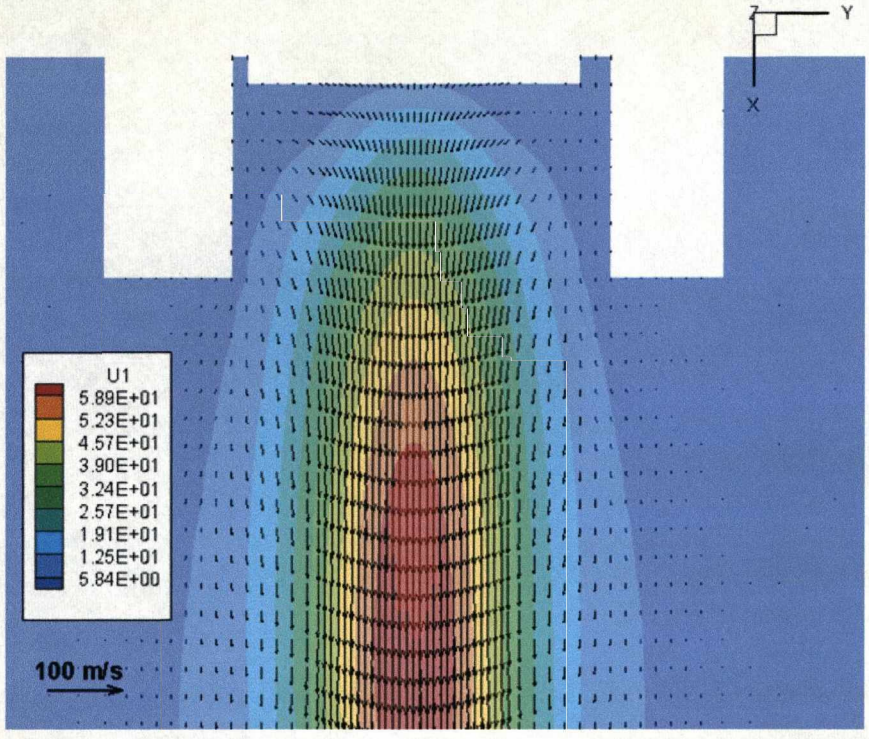

Figure 4.24(a) Velocity vector and x-velocity component U1 magnitude contour (m/s) at anode electrode (z-cross section view)

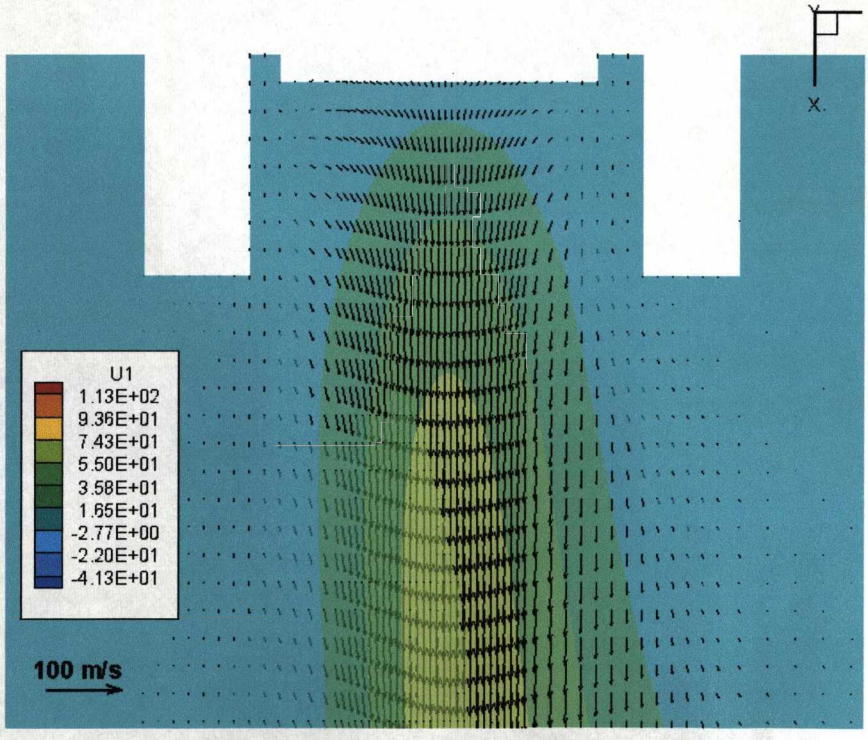

Figure 4.24(b) Velocity vector and x-velocity component U1 magnitude contour (m/s) at the anode (y-cross section view)

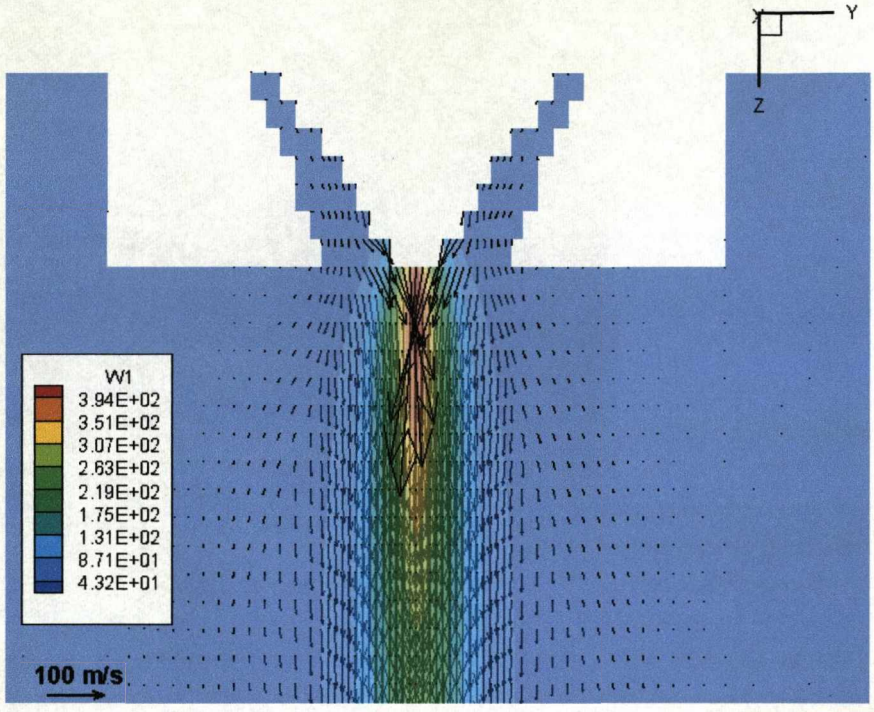

Figure 4.24(c) Velocity vector and z-velocity component W1 magnitude contour (m/s) at the cathode (x-cross section view)

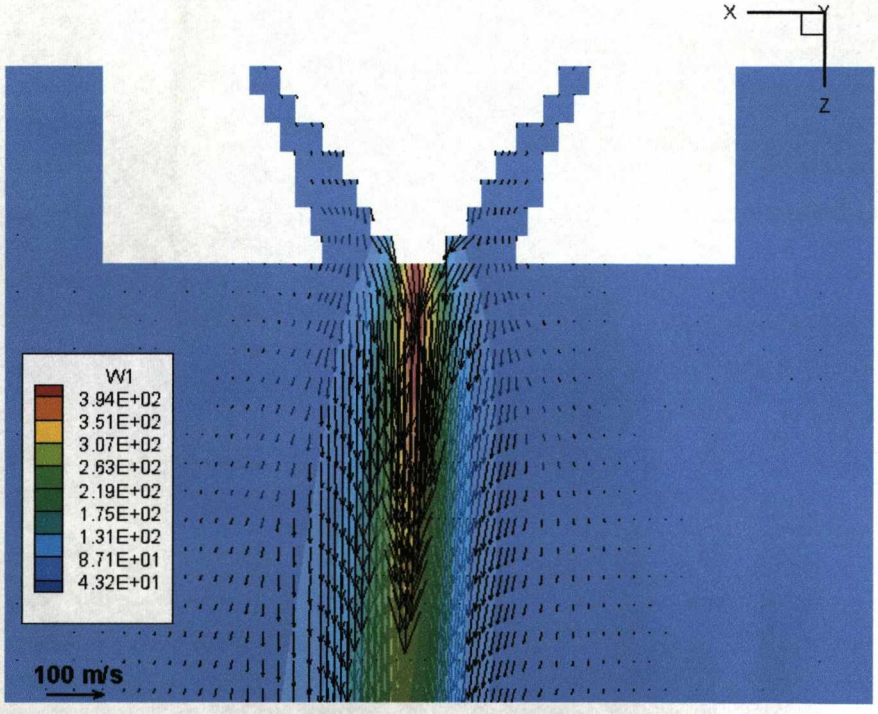

Figure 4.24(d) Velocity vector and z-velocity component W1 magnitude contour (m/s) at the cathode (y-cross section view)

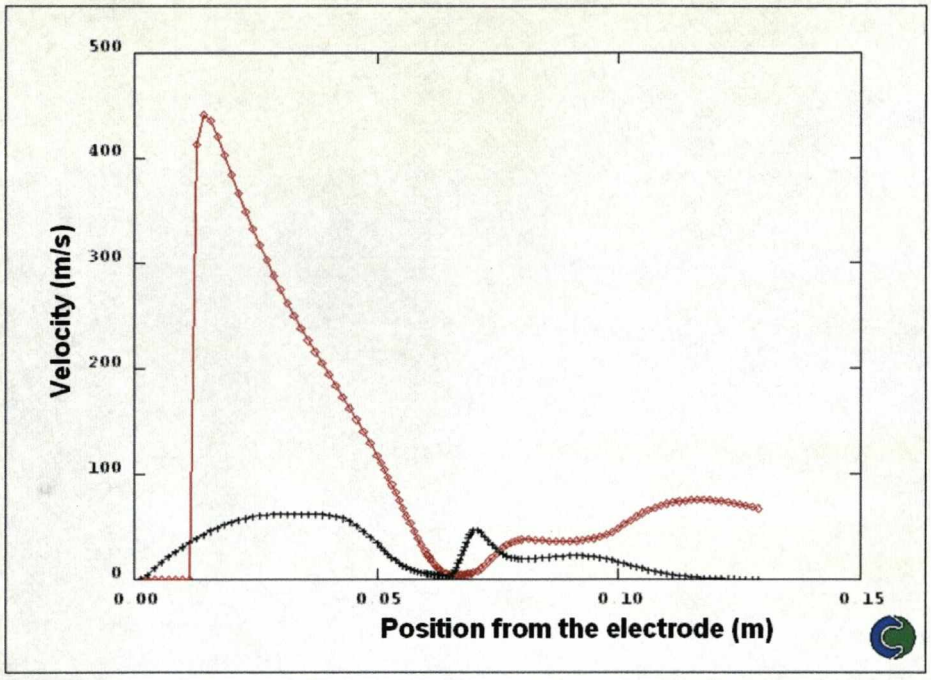

Figure 4.25 Distribution of z-velocity component at the cathode axis (red) and x-velocity component at the anode axis (black), where the axis locations are indicated in figure 4.10(c)

4.5.4 Role of Lorentz Force in shaping the Coupling Zone

As mentioned in the Chapter 3 when the free burning arc is discussed, Lorentz force is an important mechanism in shaping the arc column and the coupling zone. Theoretically, when two thin conductors placed parallel with opposite flow of current, they tend to repel each other. The two jets in the twin torch system, although not parallel, still face an increasing repelling force when they approach each other. However, in this case the distribution of the Lorentz force is more complex and depends on the real shape and conductivity of the arc column.

The magnetic field, Lorentz force due to the current path, and the resulting pinch effect is shown in figure 4.26(a)-(g) and 4.27(a)-(k). As shown in figure 4.27(i), the combined magnetic field between the jets exerts a net force at the point of separation that is directed away from the electrode tip. This force tends to separate the two jets.

Imagine a small cube at this point of separation, several mechanisms contribute to the stabilisation of the current conducting path between the two jets. Firstly, the Lorentz force (with a local value of $8e5N/m^3$) tends to accelerate the hot gas away from the point of separation, which represents a energy flux out of the cube. At the same time, incoming cold gas (figure 4.18) brings little energy into the cube. At the same time, energy is also lost through thermal conduction from the cube since there is strong temperature gradient at the point of separation, as clearly shown in figure 4.11(b). Thus to maintain the gas in the cube conducting, strong Ohmic heating is necessary to provide the energy source that is taken away by the gas pumped out of the cube magnetically. The magnitude of ohmic heating around the point of separation is $2.75e10W/m^3$ (figure 4.12) while radiation loss is $3e9W/m^3$ (figure 4.28). Radiation energy loss is negligible in comparison with Ohmic heating in this region. It is this strong heating that maintains the stable current path in the thin tissue linking the two jets. The strong Ohmic heating can also be seen from figures 4.15 and 4.17(b) showing strong current density and electric field both present at the point of separation.

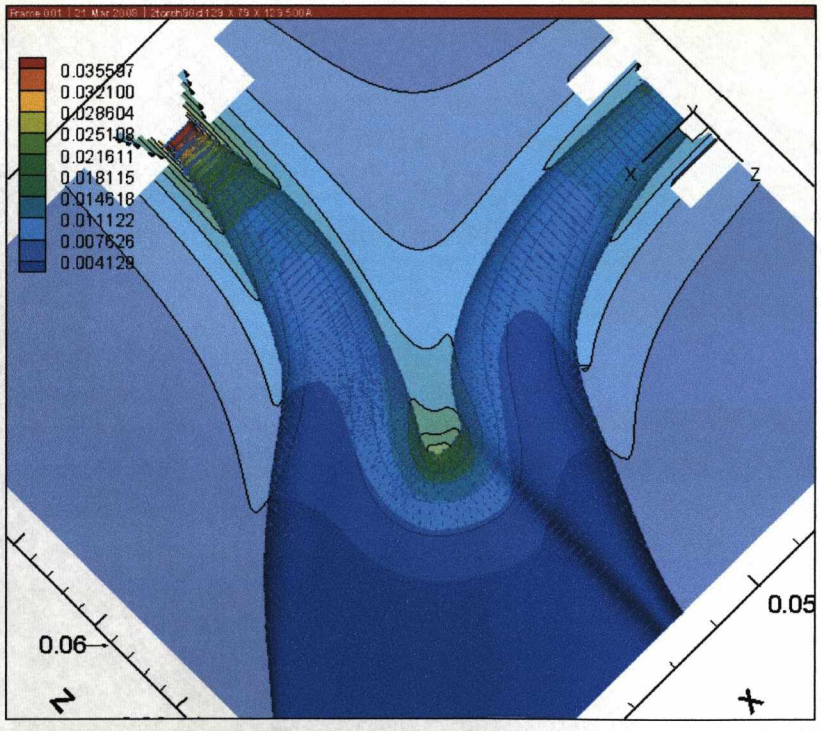

Figure 4.26(a) Magnetic Field Strength and magnetic vectors plotted on a 3D surface (of iso-temperature 10000K), with background contour showing the magnitude.

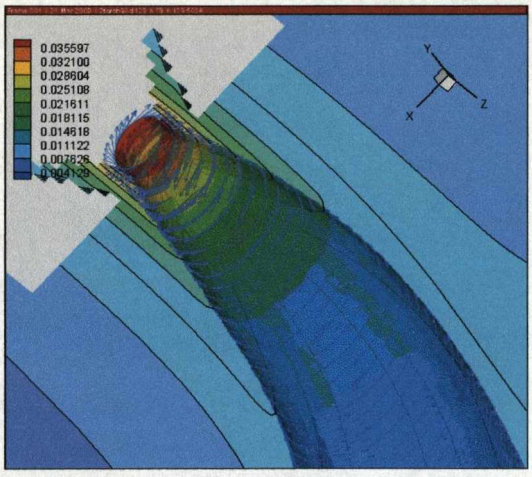

(b) Magnetic Field vector

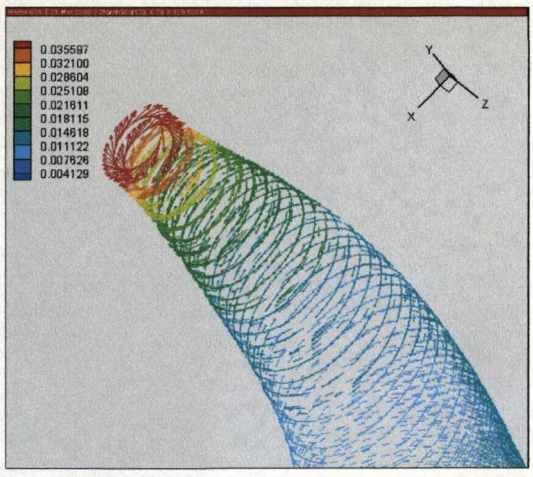

(c) Magnetic Field Vector

(d) Magnetic Field coupling zone

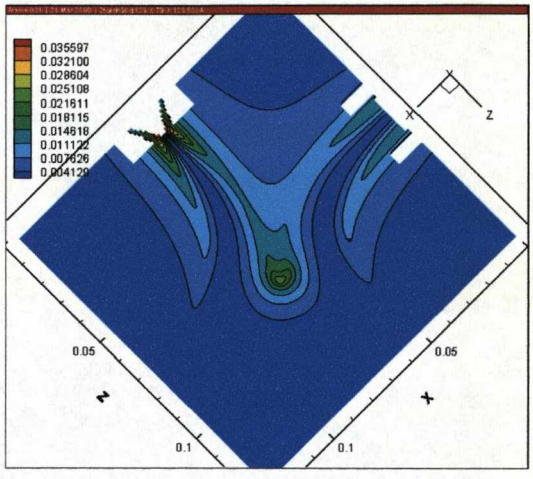

(e) Magnetic Field Strength contour

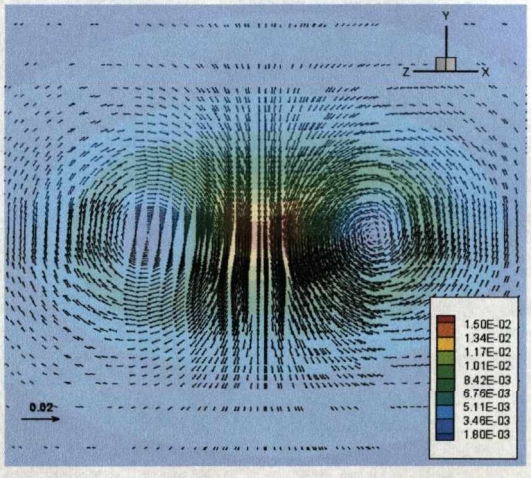

(f) Magnetic Potential vector at HU plane

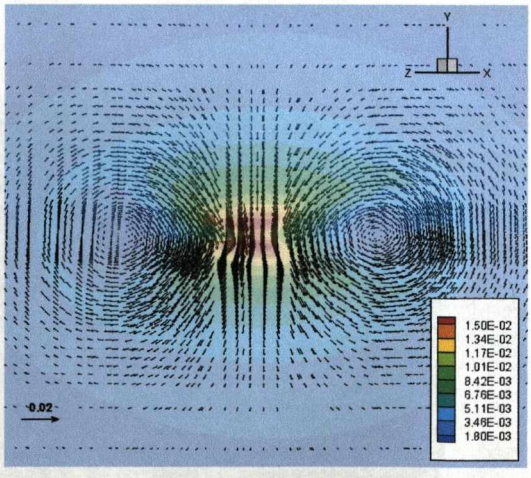

(g) Magnetic Potential vector at HL plane

Figure 4.26(a)-(g) Magnetic field visualised in different planes. All units are in Tesla

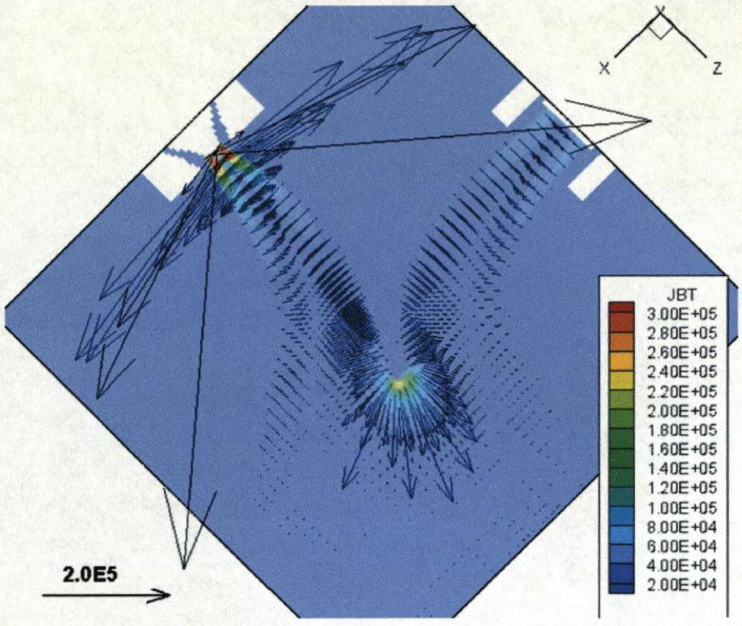

Figure 4.27(a) Lorentz force vector and magnitude, JBT (N/m^3)

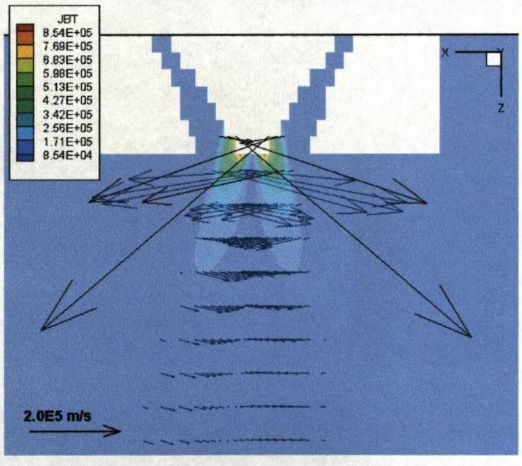

(b) Lorentz force at cathode y-view

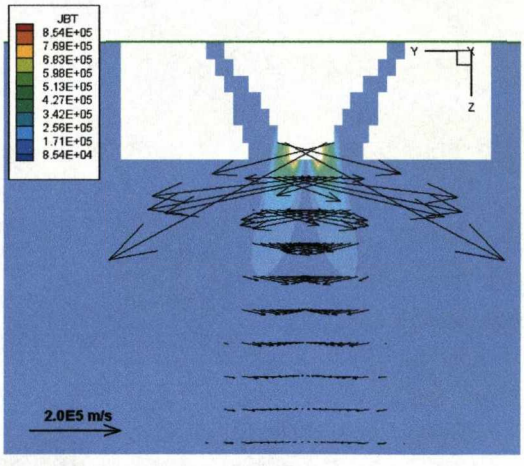

(c) Lorentz force at cathode x-view

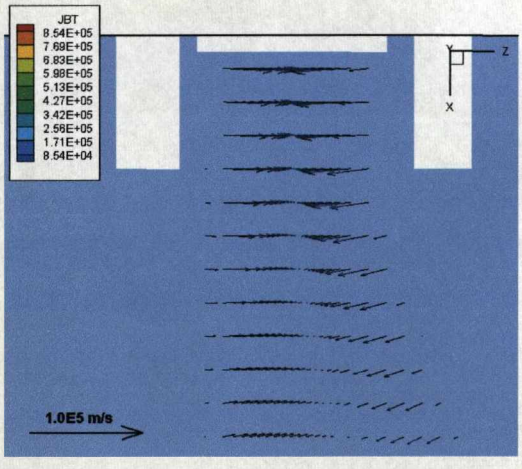

(d) Lorentz force at anode y-view

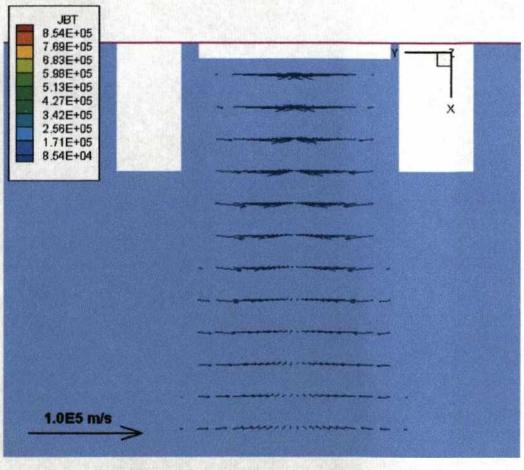

(e) Lorentz force at anode z-view

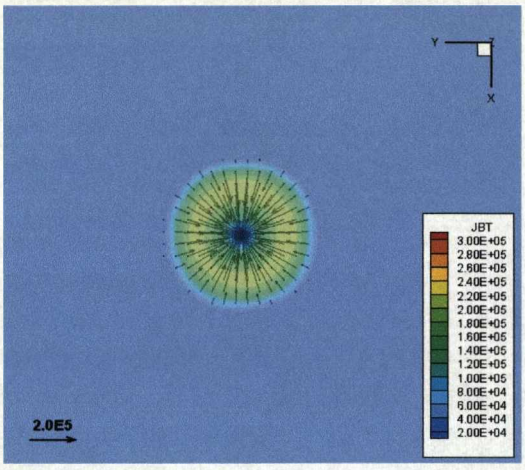

(f) Plasma jet cross section at cathode

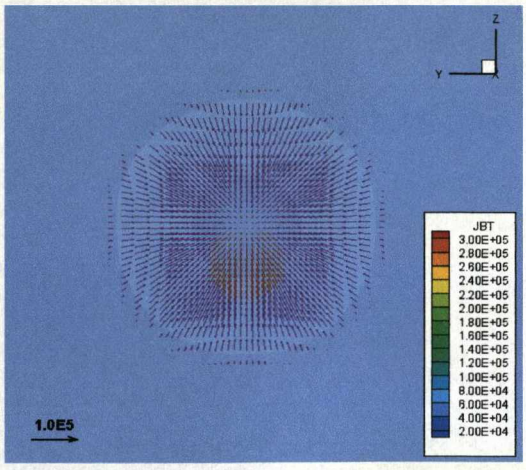

(g) Plasma jet cross section at anode

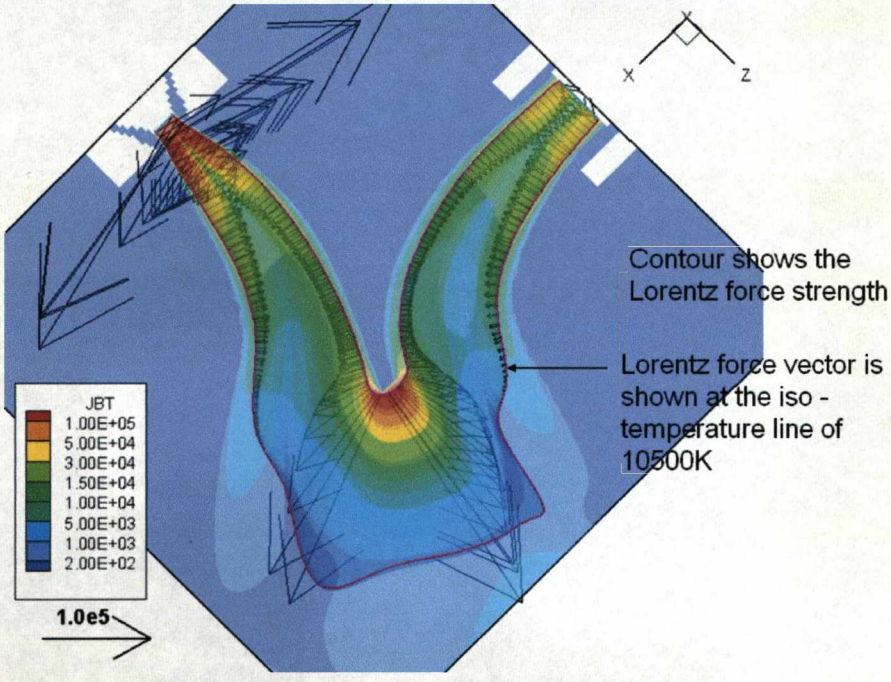

Figure 4.27(h) Lorentz force vector plotted on the iso-surface of temperature at 10000K

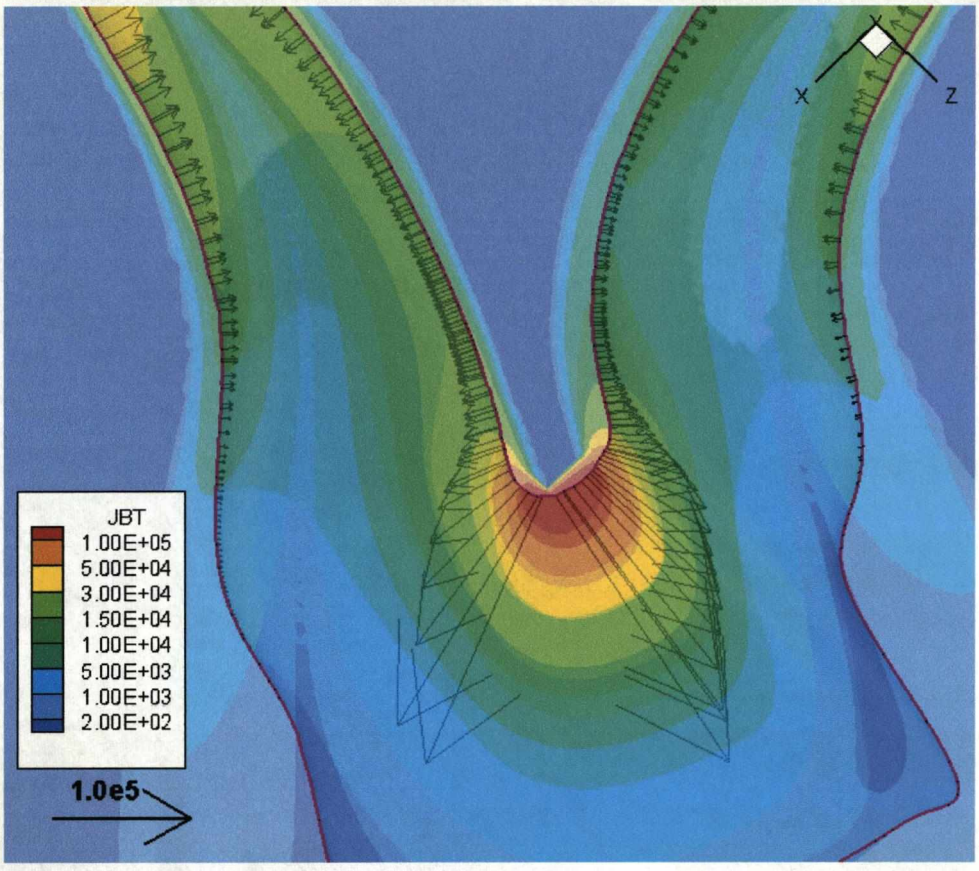

(i) Magnified view of Lorentz force vector plotted on iso-surface of temperature at 10000K

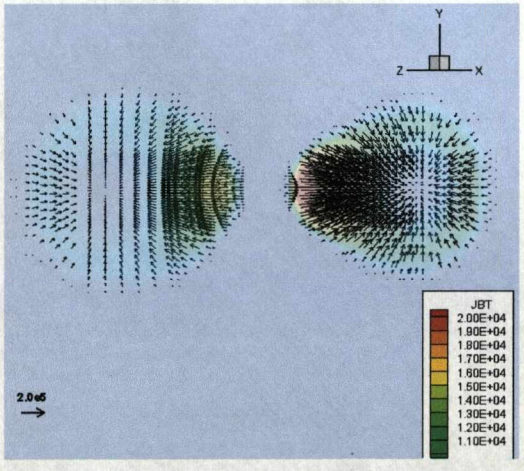

(j) HH plane

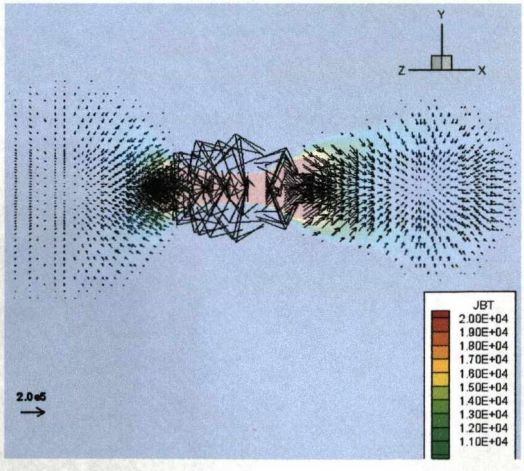

(k) HL plane

Figure 4.27(a)-(k) Lorentz Force Strength, JBT and vector at various cross sections. All units are in N/m^3

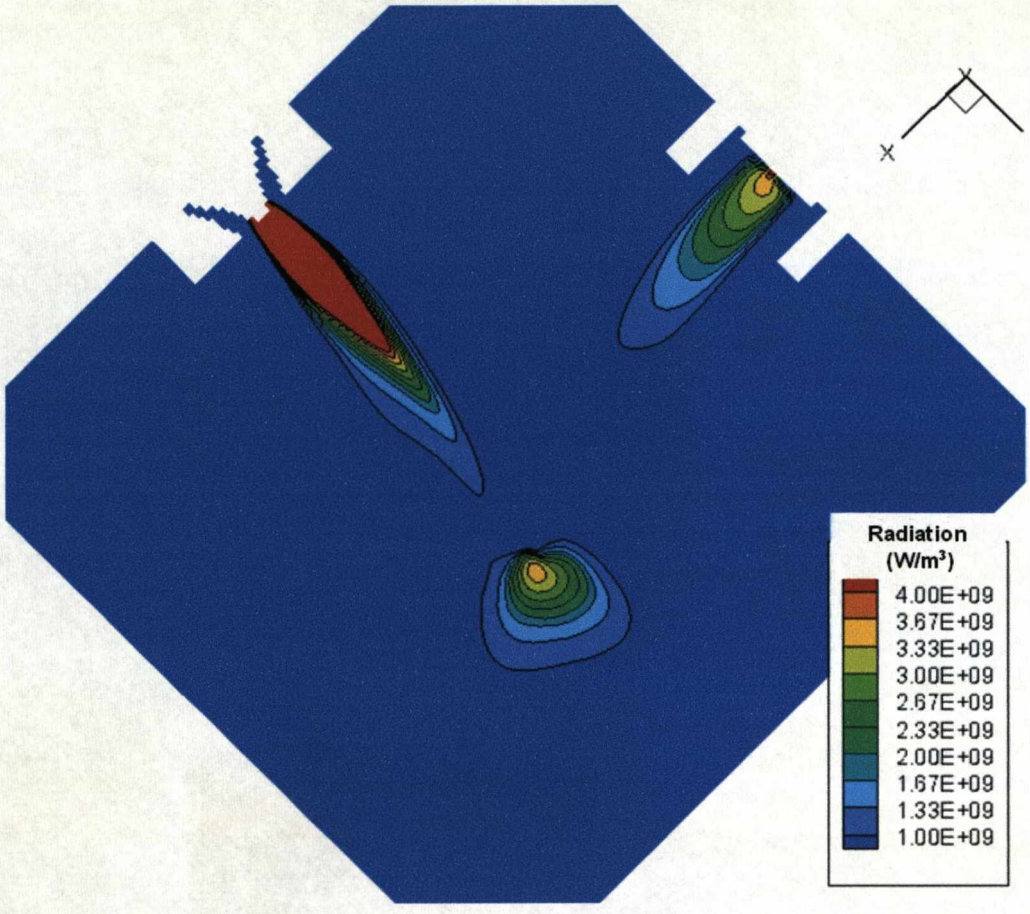

Figure 4.28 Radiation (plotting range up to 4e9W/m^3)

4.5.5 Results for 180 degree Twin Plasma Torches

This configuration resembles a conventional transferred arc used in many applications. Compared with the case of 90 degree included angle, there is no point of separation and there is no distinctive boundary for the two jets. The plasma arc appears as a hot column between the electrodes with temperature of 21000K at the cathode tip and 12000K at the anode tip. Since an argon flow is imposed through the nozzles of both electrodes, the two jets collides and the cathode jet is reflected in a plane located close to the anode. This is clearly seen in figure 4.29 with velocity vectors given in figure 4.31. Despite the fact that only one side of the computational domain is used as exit, the temperature field is rather symmetric as shown in figure 4.29. This is because the arc column is well away from the walls and there is sufficient space for the gas to flow

towards the exit in the surrounding area. The maximum velocity near the cathode is 471m/s. The location of flow reflection is determined by the relative strength of the flow in the two colliding jets. In this particular case, the jet from the cathode is much stronger than that from the anode, which leads to a reflection plane near the anode.

As can be seen in figure 4.32, there is substantial voltage drop near the cathode and anode. The electric field is weaker in the middle section of the arc column in comparison with that near the two electrodes.

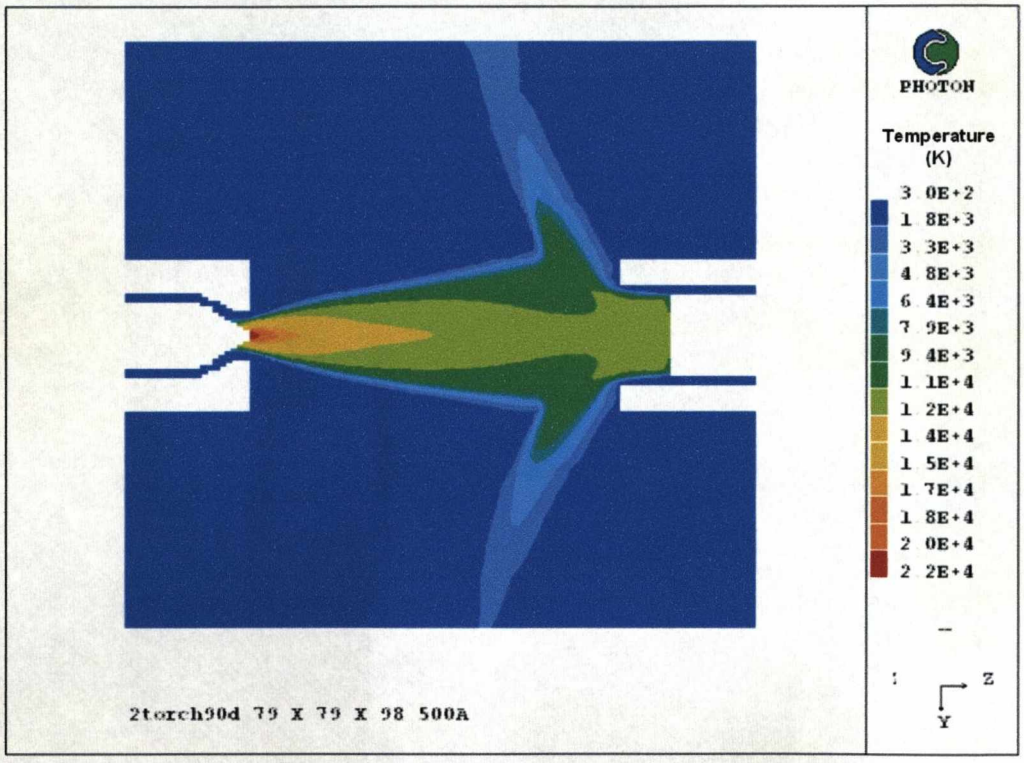

Figure 4.29(a) Temperature contour for 180 degree twin torch in x cross section view

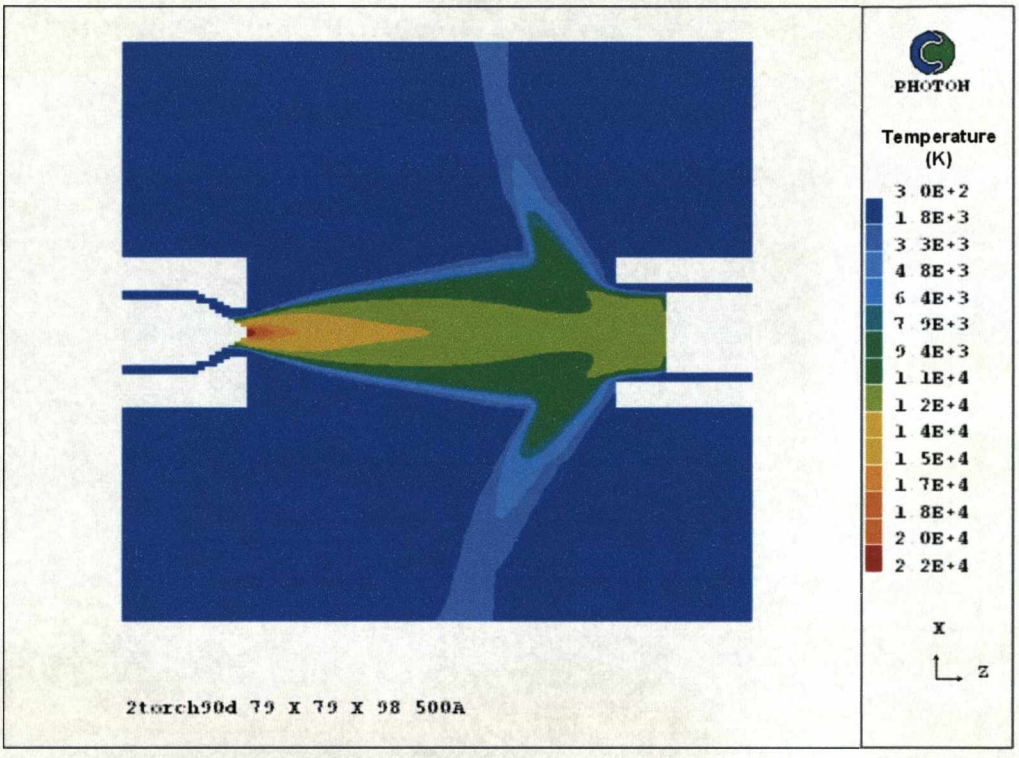

Figure 4.29(b) Temperature contour for 180 degree twin torch in y-cross section view

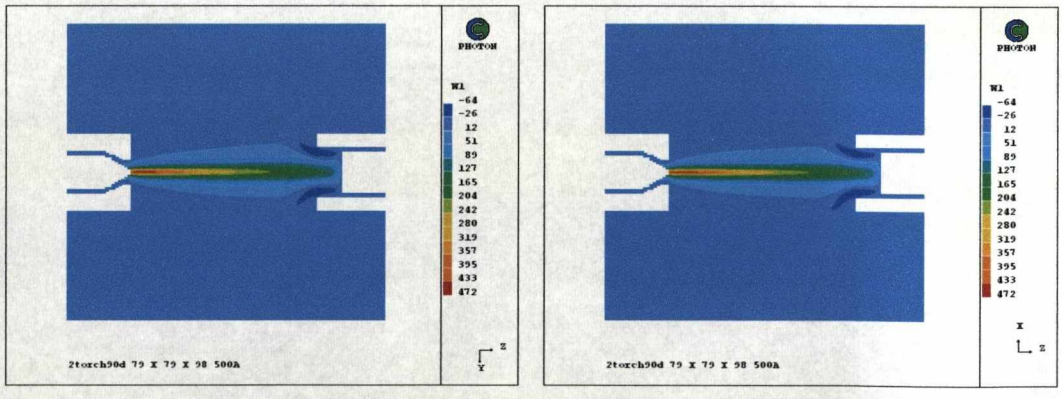

Figure 4.30 Z-velocity contour W1 (m/s) for 180 degree twin torch in the (a) x-cross section view and (b) y-cross section view

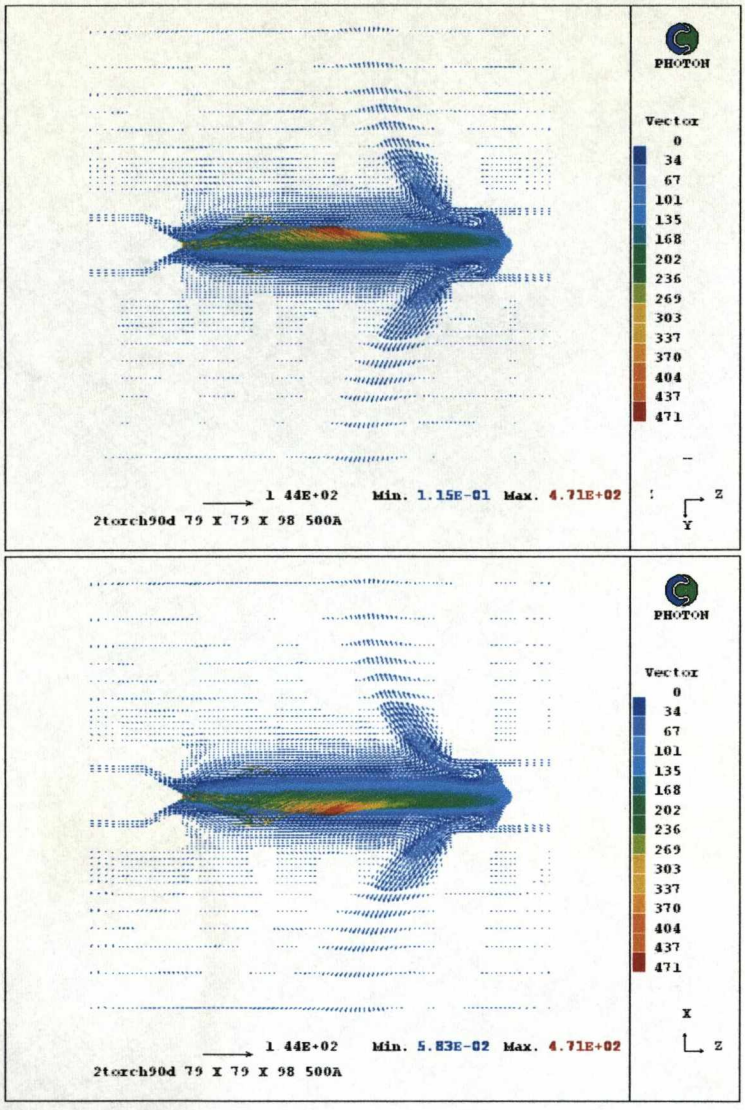

Figure 4.31 Velocity vector (m/s) in the x-cross section view (top) and y-cross section view (bottom)

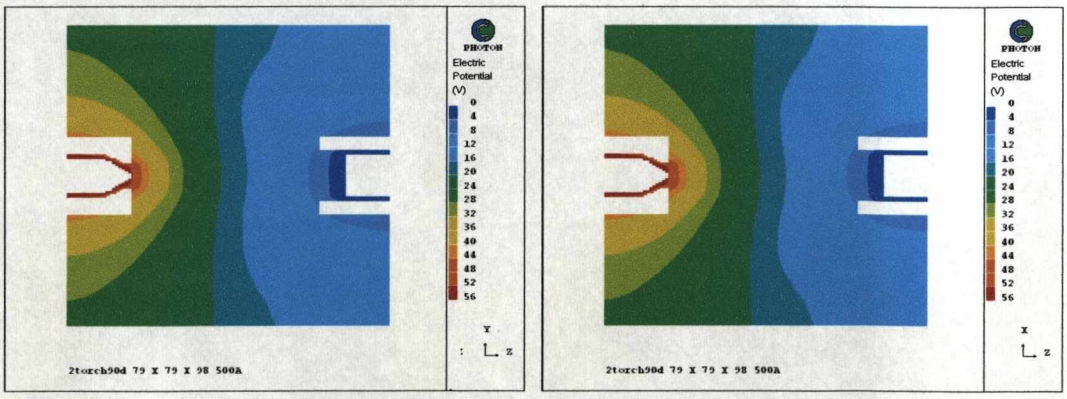

(a) (b)

Figure 4.32(a)-(b) Electric potential contour in the x and y direction

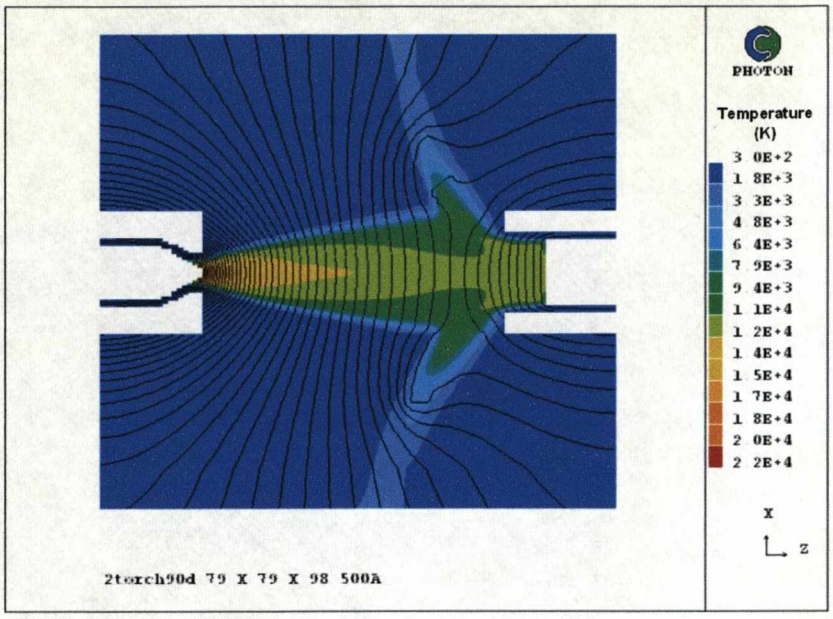

Figure 4.32(c) Electric potential distribution with the temperature contour

4.5.6 Discussion on the Influence of Turbulence

As discussed in section 4.5.1, jet coupling in reality is not a stable phenomenon. The fluctuation of the coupling zone in many ways bears the characteristics of turbulent flow. It is therefore proposed that a turbulence model (Chapter 2) that is commonly used for switching arc should also be used here to model the energy and momentum exchange as a result of the fluctuation of the coupling zone.

Results in figures 4.8 and 4.9 show a similar feature on the role of turbulence. For higher current, the addition of strong turbulence (c=0.2) results in an arc voltage that is far lower than the measurement, even when the possible effect of cathode and anode voltage fall are taken into consideration. The influence of lower arcing voltage is substantially weaker. This comparison implies that turbulence effect is stronger at lower current, thus requires consideration in the model. For the perpendicular electrode arrangement, a turbulence parameter higher than 0.02 but lower than 0.1 should be used despite the arcing gas is argon. For the nearly coaxial case, the application of turbulence may not be appropriate because of the stable arc flow. Results in this chapter also show that the application of a conventional turbulence model may not be appropriate for modelling the effect due to fluctuation of the coupling zone. Future work is necessary to address this issue.

4.5.7 Influence of Discharge Conditions on Size of Coupling Zone

Given a fixed configuration of the electrodes, the working conditions that affect the arc column are the gas flow rate and the current. In section 4.5.2, a case of 500A is presented. When the arc current increases, the size of the coupling zone slightly increases, as shown in figure 4.33. The size of the two jets near their electrode does not change substantially.

Simulation for different volumetric flow rate at the torch inlets is also carried out. The flow rate ratio of argon gas at the cathode to the anode are 15:25, 20:30 and 25:35 Nl/min, which are referred to as cases R1, R2 and R3 respectively. Figure 4.34 shows the comparison of the temperature iso-lines of the plasma arcs. The location of the coupling zone is moved away from the electrode tips as the mass flow rate in both nozzles increases. The size of the jets and the isotherm region of 12000K at the point of separation has very little change with the flow rate. The increase flow rate from 15:25Nl/min to 25:35Nl/min produces a temperature and velocity increase of only 720K (figure 4.36) and 28m/s (figure 4.37) respectively at the cathode tip. So in this sense the increase in argon flow rate cannot be used to change the plasma parameters.

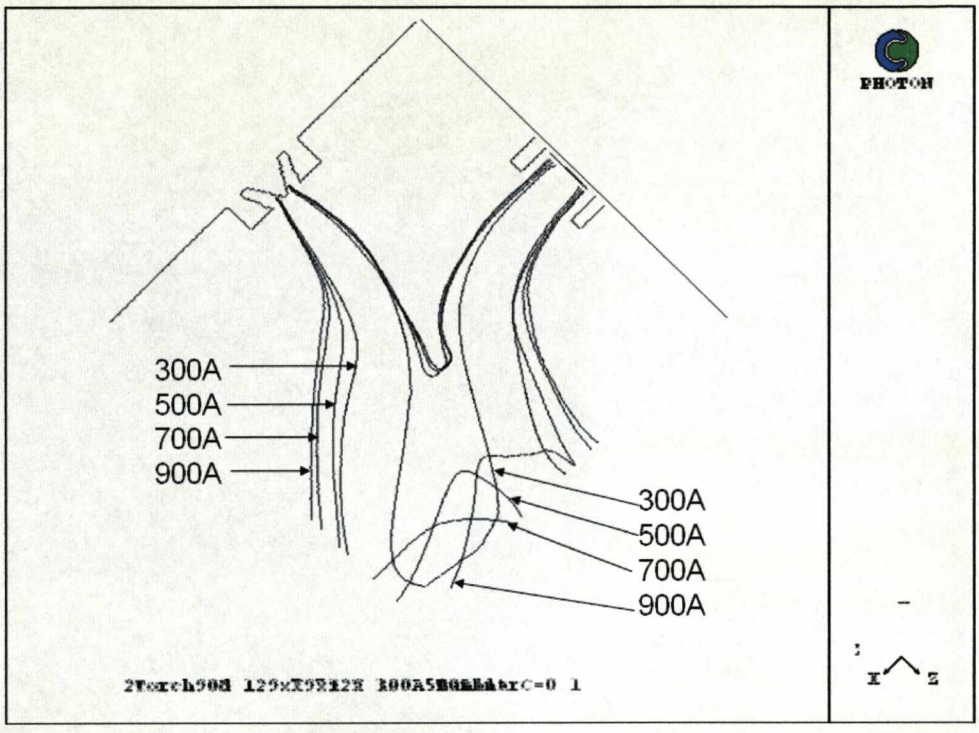

Figure 4.33 Temperature iso-lines of 10000K for turbulence parameter c=0.0 at current 300A, 500A, 700A and 900A

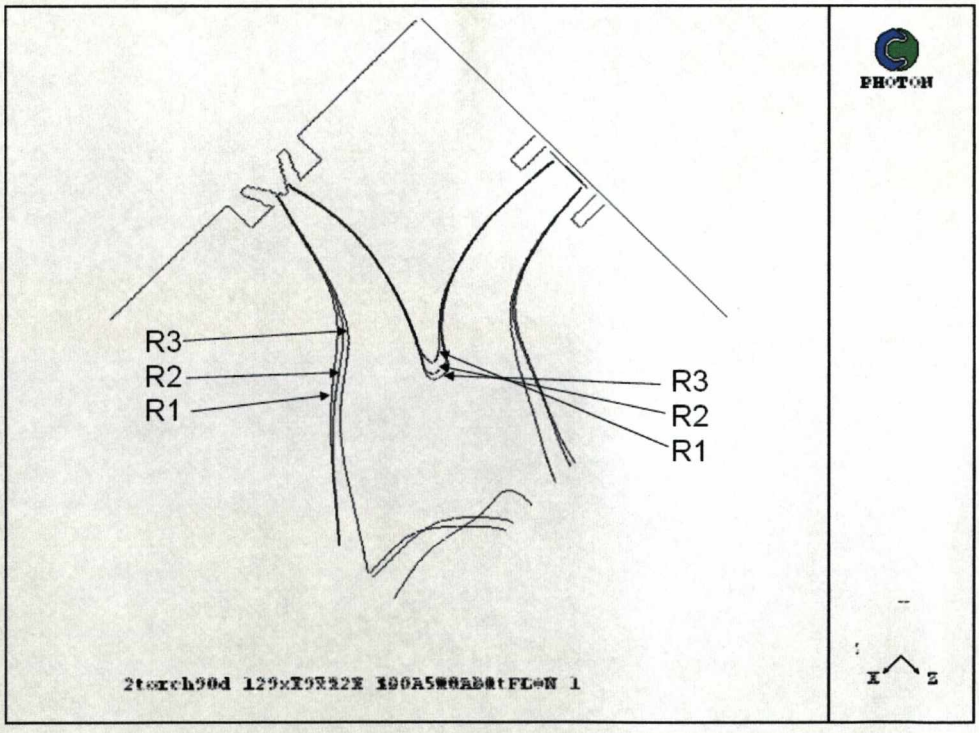

Figure 4.34 Temperature iso-lines at10000K for different volumetric flow rate with cathode to anode ratios of R1 (15:25Nl/min), R2 (20:30Nl/min) and R3 (25:35Nl/min)

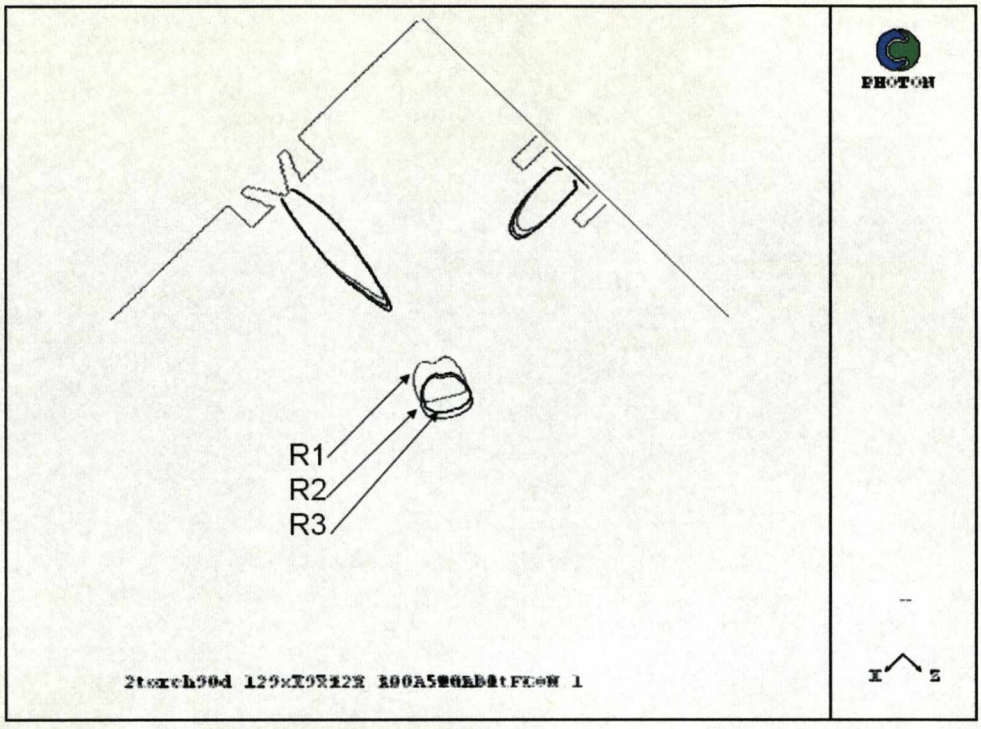

Figure 4.35 Temperature profile of 12000K for different volumetric flow rate with cathode to anode ratios of R1 (15:25Nl/min), R2 (20:30Nl/min) and R3 (25:35Nl/min)

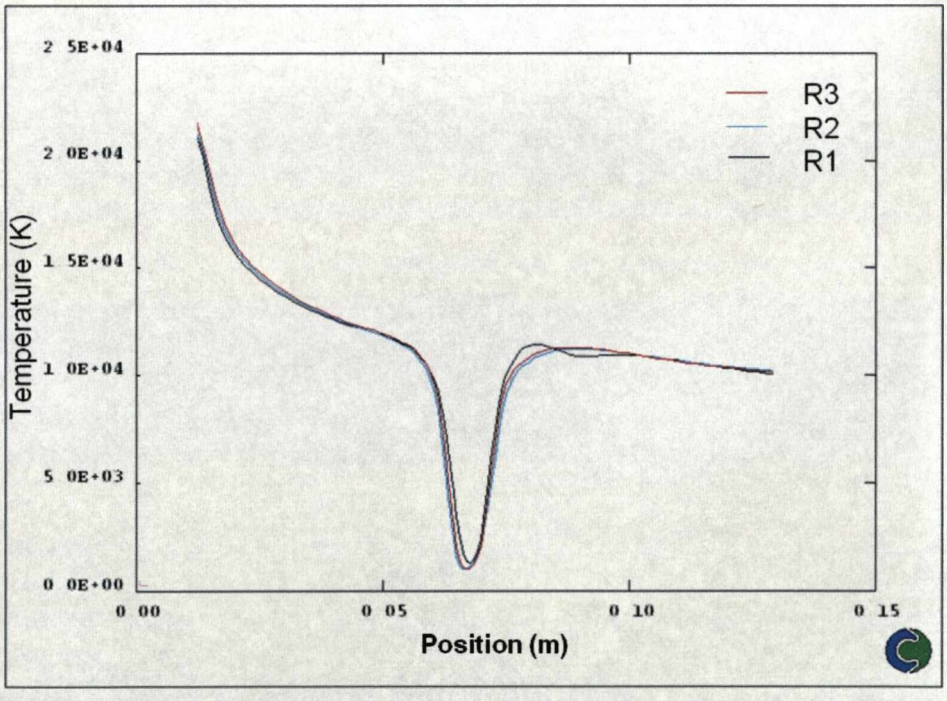

Figure 4.36 Temperature at cathode axis for different volumetric flow rate tip with cathode to anode ratios of R1 (15:25Nl/min), R2 (20:30Nl/min) and R3 (25:35Nl/min)

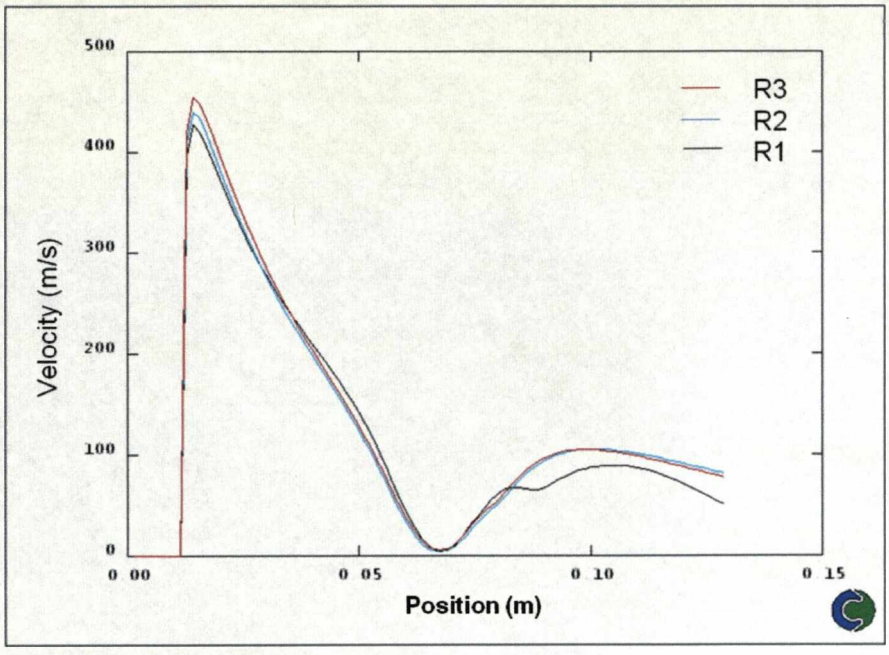

Figure 4.37 Velocity at cathode axis for different volumetric flow rate with cathode to anode ratios of R1 (15:25Nl/min), R2 (20:30Nl/min) and R3 (25:35Nl/min)

4.6 Summary

The behaviour of twin torch plasma system is studied in this chapter for two electrode configurations, using the 3D model proposed in Chapter 2. It has been shown that the coupling of the two jets is through a thin, tissue like conducting layer between the two jets. The jets are never completely merged. The Lorentz force induced by the arc current and the combined magnetic field of the two jets tends to move the point of separation away from the electrode tips. It is the strong Ohmic heating, resulting from the high temperature and high electric field in the tissue layer, that heats up the incoming cold gas and thus stabilises the point of separation of the two jets. Detailed temperature, velocity and magnetic field are given with appropriate discussion. The influence of the argon flow rate is also assesses and it is shown that the change in flow rate does not have significant influence on the parameters of the plasma. Although the 3D model can predict the dynamic change of the arc voltage in response to the change in arc current, the predicted arc voltage is in general higher than the measurement of which no experimental uncertainty is given in the reference. The high predicted arc

voltage is partly attributed to the statistic high frequency fluctuation of the jet coupling zone. The use of a simple turbulence model brings the prediction closer to the measurement at low current, but results in an excessive reduction in arc voltage at high current. Therefore the use of a conventional turbulence model to simulate the effect of fluctuation of the jet coupling zone may not be appropriate.

4.7 References

[1] Frugier P., Girold C., Megy S., Vandensteendam C., Ershov-Pavlov E. A. and Baronnet J. M., "OES Use and Vaporization Modeling for Fly-Ash Plasma Vitrification", Plasma Chemistry and Plasma Processing, Vol. 20, No. 1, 2000

[2] Williams J. K., "Twin Torch Transferred Arcs with Remote Coupling for Materials Processing and Synthesis", 2nd European Conference on Thermal Plasma Processes, 1992

[3] Megy S., Bousrih S., Baronnet J. M., Ershov-Pavlov E. A., Williams J. K., Iddles D. M., "Characterization of a Twin-Torch Transferred dc Arc", Plasma Chemistry and Plasma Processing, Vol. 15, No. 2, 1995

[4] PHOENICS Version 3.4, CHAM Ltd, Bakery House, 40 High Street, London SW19 5AU, England

[5] Megy S., Bousrih S., Baronnet J. M., Ershov-Pavlov E. A., Williams J. K., Iddles D. M., "Characterization of a Twin-Torch Transferred dc Arc", Plasma Chemistry and Plasma Processing, Vol. 15, No. 2, 1995

[6] Lowke J. J., Morrow R. and Haidar J., "A simplified unified theory of arcs and their electrodes", J. Phys. D: Appl. Phys., Vol. 30, pp. 2033-2042, 1997

[7] Benilov M. S. and Cunha M. D., "Heating of refractory cathodes by high-pressure arc plasmas: II", J. Phys. D: Appl. Phys., Vol. 36, pp. 603-614, 2003

Chapter 5

CARBON ARC PLASMA CONFINED IN LIQUID WATER

5.1 Introduction

The application background of the carbon arc plasma confined in liquid water has been presented in Chapter 1. This type of arc discharge environment is also commonly referred to as "arc in water" in publications describing the production of carbon nano-scale structures such as CNTs or fullerenes [1-5]. This type of arc is usually generated between two graphite electrodes immersed in deionised water [1]. The arc is started by short-circuiting the two electrodes with a current source (30A to 100A), usually in DC, applied. One of the electrodes is then withdrawn from the other to a form a gap length of 0.7mm to 1.0mm. For most applications used to form carbon nano-scale structures, literature review shows that the arc voltage, measured from the two electrodes, is all within the range of 16V [1] to 30V [3]. In the experiments, carbon structures (nanotubes, fullerenes) can be seen floating on the water surface or sank to the bottom of the container. CNTs were also formed in the deposit attached to the cathode surface. Available measurements on the plasma system include the erosion rate of the anode, production rate of carbon nanostructures, water evaporation rate, and arc voltage. Despite these general observations and measurements from various groups, there still is uncertainty as regarding the formation region of these nano-scale structures in the discharge zone. One of the major obstacle in understanding the physical processes related to the formation of the carbon nano-scale structures is the lack of knowledge of the plasma environment, especially the transport and distribution of the carbon plasma species in the discharge zone. Although spectroscopic diagnosis of the plasma parameters has

been attempted and some results are reported [4,6,7], measurement of plasma temperature is generally unreliable and no experimental uncertainty in the results can be determined. This is a result of the hostile environment (contamination of water by condensed carbon matters) and the intrinsically unstable nature of the discharge (creation and destruction of bubbles, arc root movement on cathode surface).

Understanding the formation and sustainability of the plasma environment is essential in the process of gaining more advanced knowledge of the production process of carbon structures. Relying purely on experiments will not be able to provide the required detailed information on the plasma environment. Thus computer modelling with a distributed nature, i.e. using differential governing equations, is desired to obtain detailed information as regard the arc dynamics, the establishment of the arcing environment and the transport of carbon species. Apart from the work in [8], which is concerned with a steady state carbon arc in helium and argon, there has been so far no work published on the modelling of a dynamic arc, such as the arc produced in water.

This chapter is therefore concerned with the development of an arc model for the plasma in water application. Because of the complexity in the arcing environment and a lack of understanding of some of the processes involved, approximations will be made to simplify the model. In the following sections, the initial and boundary conditions will be first discussed before the typical behaviour of the arcing process is analysed in detail. The improvement that is needed will be discussed at the end of the chapter.

5.2 Water Evaporation and Bubble Growth

5.2.1 Water Displacement due to Pressure Difference

The breakdown of the electrode gap is not simulated in the model. It is assumed that when the arc starts, a small spherical bubble of 1mm radius already exists. In reality, the atmosphere surrounding the arc may not be in a spherical shape and the modelling of such an irregular atmosphere is at present almost impossible. The

images of the carbon arc reported in [2] show that the atmosphere has an envelope similar to a sphere, as shown in figure 5.1. It is noted that the image in figure 5.1 is from a carbon arc with the axis of the two electrodes positioned horizontally. This is why the upper part of the bright region is slightly bigger than the lower half. When the electrodes are positioned vertically, the shape of the atmosphere will become more asymmetric. To study the evolution of the change of the arcing environment in a statistical manner, approximations have to be made. In this chapter, it is assumed that a spherical bubble, with its centre located on the middle point of the axis in the electrode gap, is developed and grows in the course of discharge.

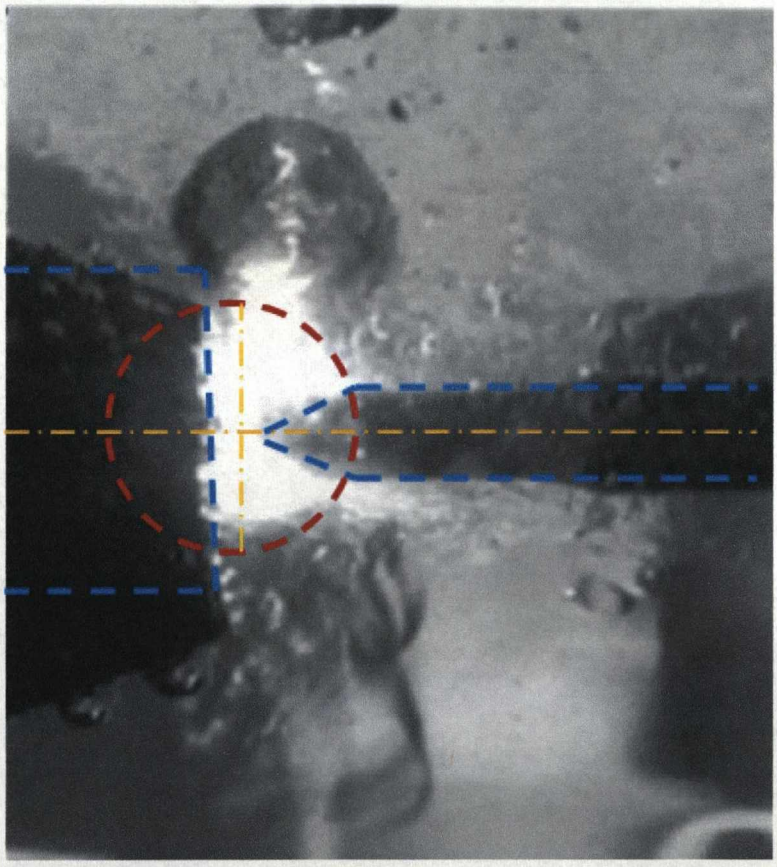

Figure 5.1 Image from a real carbon arc confined in liquid water [1] fitted with the spherical bubble model that is to be used in this chapter. In experiment the electrodes were positioned horizontally.

The growth of the bubble is governed by a number of processes which will be described below. The first factor that contributes to the growth of the bubble is the pressure acting on the bubble surface. In the present work, a conic anode and a cylindrical cathode are used, as shown in figure 5.2. Shortly after the arc is initiated, strong Ohmic heating will heat up the gas in the discharge zone and thus increases its pressure. A force is thus acted on the bubble surface. For fixed discharge geometry and dimensions of the electrode assembly, the area of the bubble surface is a function of the bubble radius. Mathematically this area can be calculated using the integral method. For our case, the area as a function of bubble radius is given in figure 5.3 for the dimensions shown in figure 5.2. The area used in the computation is in terms of the bubble surface area percentage of a complete sphere with respect to their radius.

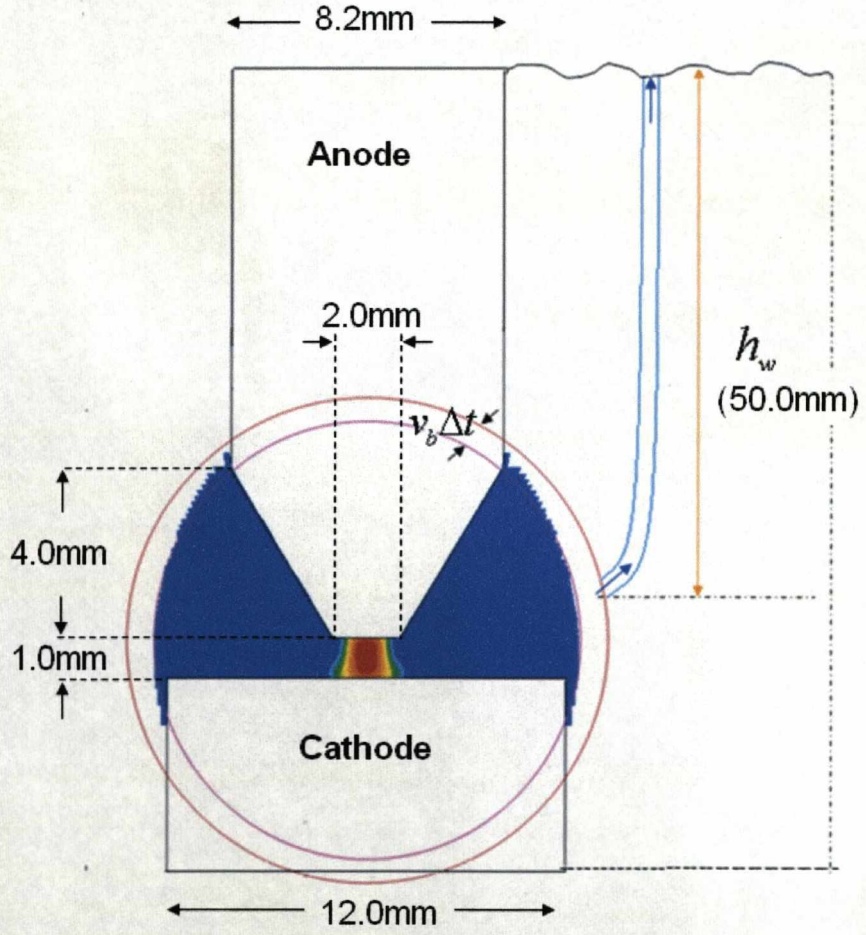

Figure 5.2 Diagram showing calculation of water displacement due to pressure difference

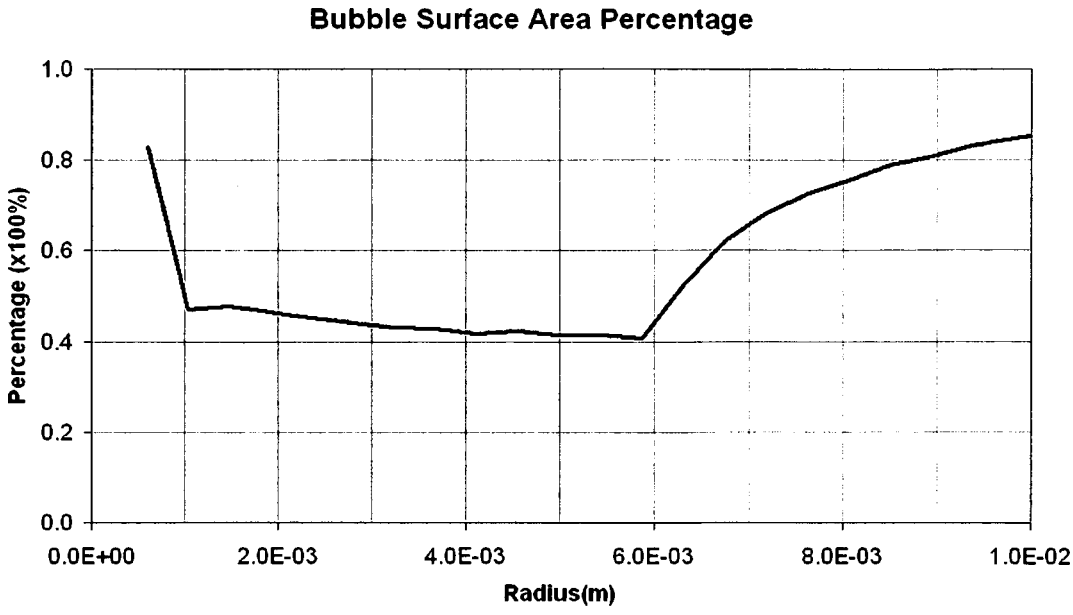

Figure 5.3 Actual bubble surface area as percentage of sphere surface area as a function of bubble radius

Flow in the bubble is generally stagnant except the strong gas flow near anode due to electrode erosion. Thus the pressure inside the bubble is expected to be uniform. Using P_A as the average pressure near the bubble surface, the force acting in the normal direction of a small area of the bubble surface is

$$F_{\delta A} = P_A \cdot \delta_A \tag{5.1}$$

where δ_A is the surface element. The displacement of water in the vessel by bubble growth is a complex fluid dynamics phenomenon and is out of the scope of the present research. A simple one dimensional model is thus employed to simulate the dynamic of the bubble. As shown in figure 5.2, the water adjacent to the bubble surface is assumed to be displaced in a virtual pipe (similar to a streamline pipe) with a length equal to the water level h_w as indicated in the diagram. With this assumption, the total normal force acting on the inlet of the virtual pipe can be summed up by

$$F_A = P_A \cdot A(r_b) \tag{5.2}$$

On the other end of the virtual pipe the total force acting by the atmosphere on the water in the virtual pipe is

$$F_{air} = 10^5 A(r_b) \tag{5.3}$$

where the virtual pipe is assumed to have a constant cross section across its length. Neglecting the pressure due to the height of the water (20mm to 100mm in practice), the net force acting on the water that is to be displaced is

$$F = (P_A - 10^5) \cdot A(r_b) \tag{5.4}$$

With the mass of water in the virtual pipe being $\rho_w A(r_b) h_w$ where ρ_w is density of water, the instantaneous displacement speed of the water due to pressure difference is

$$V_{bp} = V_{bp0} + \int_0^t \frac{(P_A - 10^5) A(r_b)}{\rho_w A(r_b) \cdot h_w} dt = V_{bp0} + \int_0^t \frac{(P_A - 10^5)}{\rho_w h_w} dt \tag{5.5}$$

where the bubble area has been cancelled. V_{bp0} is the initial speed of the bubble. It is assumed to be zero in the simulation.

Equation (5.5) is a simple and ideal representation of the bubble displacement process. It has been noticed in the simulation to be presented in this chapter that once the water is accelerated at the initial stage of arcing with a high pressure in the bubble, the dimension of the bubble will continue to grow at a high speed due to its inertia, leading to a very low pressure in the bubble. In practice there is viscous effect in the body of water which will help prevent this type of overshot of the bubble size. To take this factor into account, the bubble displacement speed due to pressure difference is simply being reset to zero when the pressure in the bubble is lower than the atmospheric pressure. The effect of this setting will be discussed in the results section.

5.2.2 Bubble Growth due to Water Evaporation.

The growth of the bubble size is also affected by the evaporation of water at the bubble surface. Excluding the effect of bubble surface movement due to pressure difference, the bubble surface can still move according to the evaporation rate. Since a spherical shape is used to represent the bubble in the present model, this implies that the amount of water evaporated is uniformly taken from the whole bubble surface. The amount of vapour produced is assumed to be proportional to the amount of radiation reaching the bubble surface. Assuming the total amount of radiation emitted from the arc core for a unit length of arc column (a hot region where net radiation is emitted out) is Q_e, the amount of radiation re-absorption in the cold surrounding is Q_a, then the amount of radiation reaching the bubble surface is

$$Q_s = Q_e - Q_a \tag{5.6}$$

The energy required to evaporate unit mass of liquid water to vapour at its boiling point is designated by h_{ev}, which includes the enthalpy change from room temperature to the boiling temperature of water and the latent energy of water which is 2.27×10^6J/kg, the amount of water evaporated $\dot{m}$ is then

$$\dot{m} = \frac{Q_s}{h_{ev}} \tag{5.7}$$

This amount of water divided by its density ρ_w will give the volume of liquid water that is evaporated:

$$\dot{v} = \frac{\dot{m}}{\rho_w} \tag{5.8}$$

Integrating over the bubble surface, the total amount of water evaporated in unit time can be obtained. Equating the total evaporation rate of water to the volume of liquid water contained in the layer between the two spheres shown in figure 5.2, the formula becomes

$$\int \dot{m} dz = A(r) \cdot V_{be} \cdot \rho_w \tag{5.9}$$

where V_{be} is the speed of bubble surface movement due to evaporation. The combined speed of bubble growth is therefore

$$V_b = V_{bp} + V_{be} \tag{5.10}$$

5.2.3 Numerical scheme for bubble movement

In the simulation the movement of bubble surface is implemented by changing the liquid cells immediately outside of the bubble into gas according to the bubble radius. The criterion is that all cells whose distance (from the cell centre) to the origin of the bubble is smaller than the bubble radius will be set as gas cells at the beginning of each time step in a transient simulation. However, simply changing a cell from liquid into gas does not guarantee the conservation of mass, momentum and energy, therefore is incorrect.

In reality, the flow of gas just by the bubble surface is determined by two processes. Firstly, for an evaporating surface, the water vapour generated from the bubble surface adds mass, momentum and energy to the cells by the bubble surface. These sources tend to force the gas to flow towards the interior of the bubble. At the same time, the continuous expansion of the bubble has the effect of taking gas away from the cells by the bubble surface. With small size of cells, the conservation of mass requires that the reduction of mass per unit time in the boundary gas cells as a result of bubble expansion should be equal to the total volume of cells that are changed from liquid to gas in unit time. Mathematically this can be expressed by

$$\delta A s_s dt = -\delta A V_b dt \rho_{gas} \tag{5.11}$$

where δA is the surface element, s_s the surface mass source, and ρ_{gas} is the gas density of the cell adjacent to the bubble surface. Equation (5.11) can be further simplified as

$$s_s = -V_b \rho_{gas} \tag{5.12}$$

To implement this numerical scheme in the CFD package, it is necessary to convert the negative surface mass source given by equation (5.12) into a volume source. This is achieved by decomposing the bubble growth speed into two velocity components

as shown in figure 5.4 for a grid system that is close to orthogonal. The negative volume source obtained for the boundary cells is

$$S_{bv} = \frac{S_{sr}\Delta A}{\Delta V} + \frac{S_{sz}\Delta A}{\Delta V} = \frac{-2\pi r\Delta z\rho_{gas}V_{br}}{2\pi r\Delta r\Delta z} + \frac{-2\pi r\Delta r\rho_{gas}|V_{bz}|}{2\pi r\Delta r\Delta z} = \frac{-\rho_{gas}V_{br}}{\Delta r} + \frac{-\rho_{gas}|V_{bz}|}{\Delta z} \quad (5.13)$$

where S_{sr} and S_{sz} represent the decomposed surface mass source given in (equation 5.14 and 5.15). Note that a modulus V_{bz} is used as the bubble is able to expand in both the positive and negative axial directions, while V_{br} can only expand in the positive radial direction for a 2D model. It is found that, due to the solution process of PHOENICS, the density in the liquid cells needs to be set in a particular manner to make sure the computed results are correct. Since this is package dependent, the details will be neglected despite it required much substantial coding effort.

$$V_{br} = \frac{(y-y_0)V_b}{\sqrt{(z-z_0)^2+(y-y_0)^2}} \quad (5.14)$$

$$V_{bz} = \frac{(z-z_0)V_b}{\sqrt{(z-z_0)^2+(y-y_0)^2}} \quad (5.15)$$

where y and z are the coordinates of the cell centre, and y_0 and z_0 are the coordinates of the bubble centre.

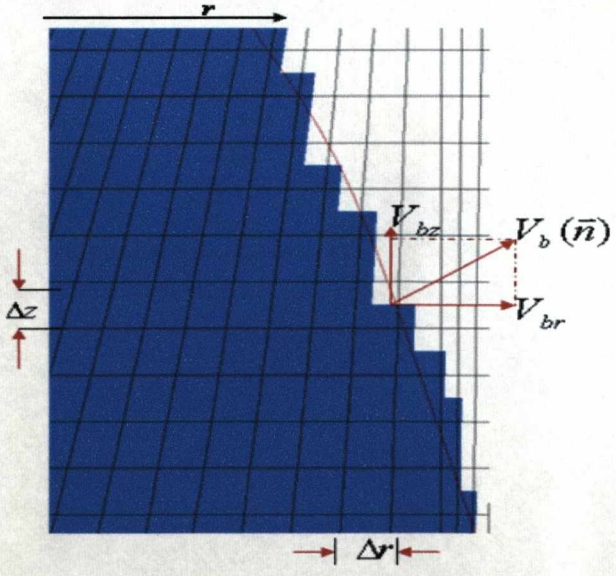

Figure 5.4 Implementation of bubble growth in BFC grids

5.3 Grid System, Initial and Boundary Conditions

The electrode gap in the present work is 1mm and axially divided into 20 cells with an axial width of 50μm. The typical radial width of the cells in the arc region is 25μm. The cell size away from the electrodes is typically 0.5mm since the physical quantities in this region has low gradient.

No friction between gas and solid or liquid surface is present in the model. Thus there is no momentum source for the momentum equations as a result of surface friction. There is no thermal conduction between the bubble gas and the liquid water. Thus only the boundary conditions on the two electrodes need to be specified.

On the anode surface, an axial influx of carbon vapour into the computational domain is imposed. Since the arc-electrode interaction via the thin non-LTE layer is not considered, apart from the vapour flux, the arc does not transfer energy with the anode. An erosion rate of 117mg/min is used in the simulation following the measurement in [1] whose experimental conditions are close to those used in the present work. The measurement in [1] was derived from the mass change of electrode over the whole arcing process. In the model, the erosion rate is assumed a constant of 2.0e-6kg/s which is measured in [1]. Since the size of the anode arc root changes with time, it is assumed that the erosion only takes place over the anode attachment where the gas temperature is higher than 4500K. The mass flux is then calculated by

$$\dot{m}_{carbon} = \frac{2\times10^{-6}}{\int_0^{r_{4500K}} 2\pi r dr} \tag{5.16}$$

where r_{4500K} is the radius over the anode surface where the gas temperature is 4500K. The carbon vapour enters the domain at a temperature of 4500K.

On the cathode surface, the thermal conduction between the plasma gas and the electrode is approximately considered by adding a volumetric energy loss source of

$$\dot{h} = -\frac{T_{gas} - 6000}{10^{-4}(\Delta z)} \cdot k_{ave} \tag{5.17}$$

where k_{ave} = 0.7J/m/s/K and Δz = 1.0e-4m which is chosen for a typical layer thickness over which the gas temperature drops to a low value. The use of 6000K as the low temperature end is based on the consideration that in the cathode sheath layer CNTs are formed in the deposit of the cathode surface and the temperature near the CNTs should be slightly higher than the boiling temperature of carbon which can be as high as 5800K.

It is well accepted that atmospheric arcing normally involves a cathode spot for current emission. The detailed discussion is beyond the scope of the present work. To consider its effect, a conducting circular area is imposed on the cathode surface only over which current is allowed to pass. This implies that the electrical conductivity at the other part of the cathode surface is set to a low value of 1e-3S/m to prevent current from flowing through it. The dimension of this conducting circular area is calculated by dividing the arc current by a current density of 6e6A/m^2.

In practice the bubble will detach from the discharge region when its size is over a limit. As displayed schematically in figure 1.3(a), a gas channel may be formed when the bubble develops into a certain size for gas to escape from the liquid environment. This is simulated in the present model by attaching a channel to the anode as shown in figure 5.5.

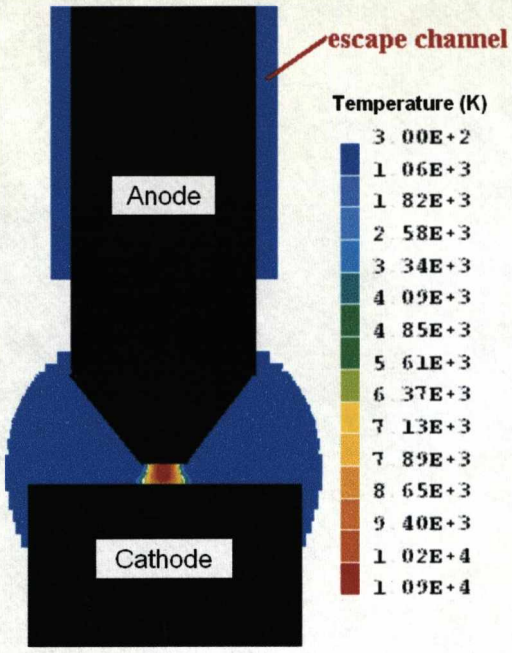

Figure 5.5 The addition of an escape channel for gas to escape from the arcing environment when the bubble radius is greater than 9mm. The upper end of the channel is maintained at a pressure of 1bar.

The arc is initiated by placing a thin hot column of conducting temperature on the axis. The radius of this hot column is 0.2mm and its temperature is 24000K (figure 5.6). It is also assumed that the bubble at time zero is filled with water vapour at 1bar and 300K. The discharge current is 30A DC.

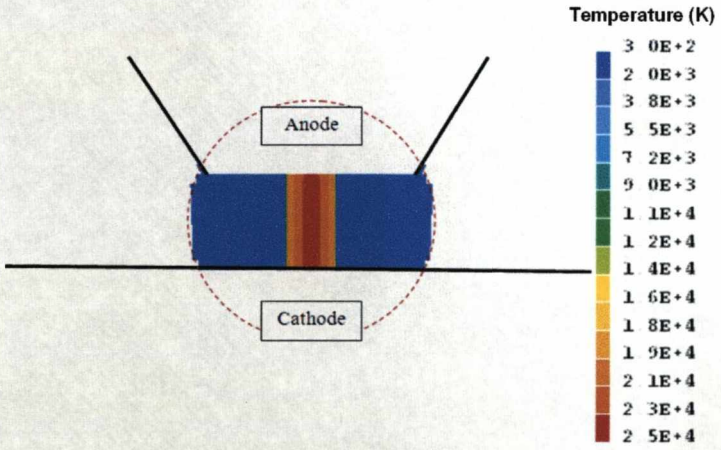

Figure 5.6 Initial state of arc and bubble environment. The bubble at time zero is filled with water vapour at 1bar and 300K

5.4 Results and Discussion

5.4.1 Bubble Dynamics at the Initial Stage of Arc

In the results presented in this chapter, radiation from the arc core reaches the bubble surface without any absorption. This setting will be discussed in section 5.5.

Since the arc is initiated in a small bubble of water vapour, there is strong Ohmic heating inside the arc column shortly after the initiation of the arc. This strong radiation flux (figure 5.7) reaches the small bubble surface, causes rapid evaporation of the water surface and thus an increase in the bubble radius (figure 5.8). This effect reaches its maximum at 30μs with a water surface recession rate of 19m/s. After this time, with the continuous growth of the bubble size as given in figure 5.9, the area to volume ratio of the bubble decreases, and the acceleration effect due to evaporation slows down.

At the same time, the pressure inside the bubble increases rapidly (figure 5.10(a)) due to arc heating and pressurisation of water vapour due to evaporation. The increase in pressure exerts an increasing force on the bubble surface, thus the acceleration due to pressure difference overtakes the surface recession due to evaporation at 100μs.

Figure 5.8 also shows a very interesting point. Initially the pressure in the bubble increases rapidly up until 0.07ms (figure 5.10(a)), and according to equation (5.5) the acceleration also increases with time. When the pressure passes its peak at 0.07ms, the acceleration also slows down. It is rather surprising that the overall speed of expansion of the bubble radius keeps a more or less constant value, which gives the straight line section in figure 5.9.

At 0.5ms after arc initiation, the continuous acceleration of the bubble leads to rapid expansion. When the pressure inside the bubble decreases after 0.1ms, the bubble continues grow. On the other hand because of the growth of the arc size, total emission from the arc column also decreases. This produces less and less water vapour. The combined effect results in a rapid decease in bubble pressure. At 0.5ms, the pressure in the bubble is already lower than the atmospheric pressure. As

discussed in section 5.2, in view of the fact that viscous effect also participated in the growth of the bubble, the bubble speed due to pressure difference is reset to zero if the pressure inside the bubble is lower than the atmospheric pressure. Immediately after this time, the growth of the bubble is mainly controlled by the water surface evaporation which is negligible. At 2ms, the pressure inside the bubble slowly increases, which drives the bubble to grow very slowly.

From the above discussion it can be seen that the initial pressure transient process inside the bubble lasts for about 0.5ms with a bubble radius of 8mm.

After 0.5ms, the bubble grows at a very slow speed due to the low pressure inside the bubble. It takes the bubble almost 5ms to increase its radius to 9mm when it joins the escape channel. Because of the exchange of mass with the atmosphere, there is virtually no pressure difference and the bubble size remains constant afterward. Further arcing process will drive the arc to approach a steady state.

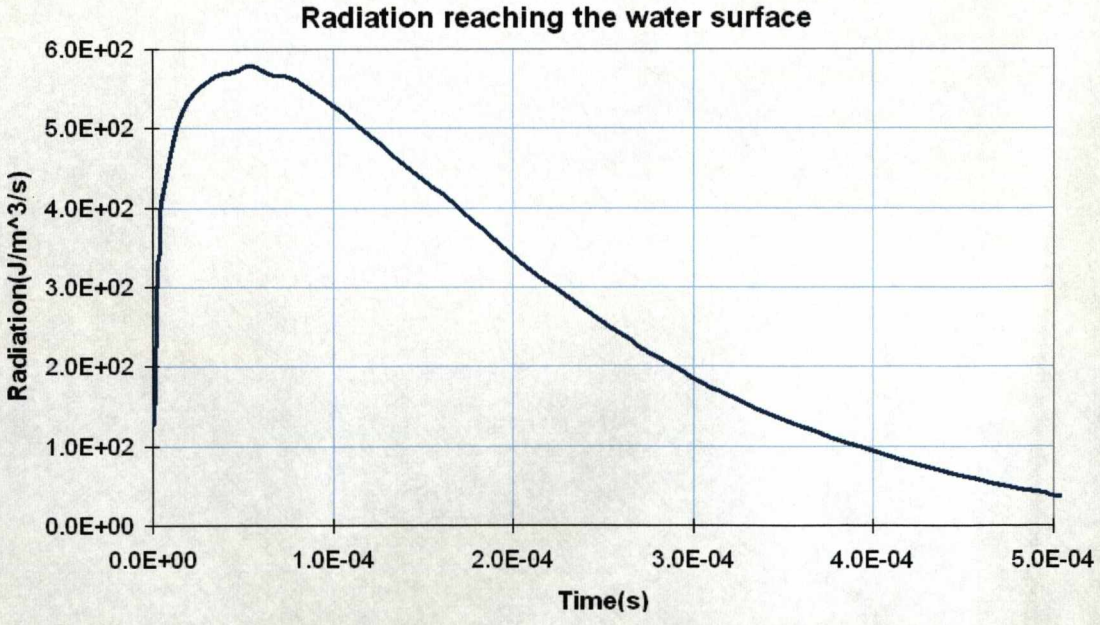

Figure 5.7 Total radiation reaching the water surface as a function of time

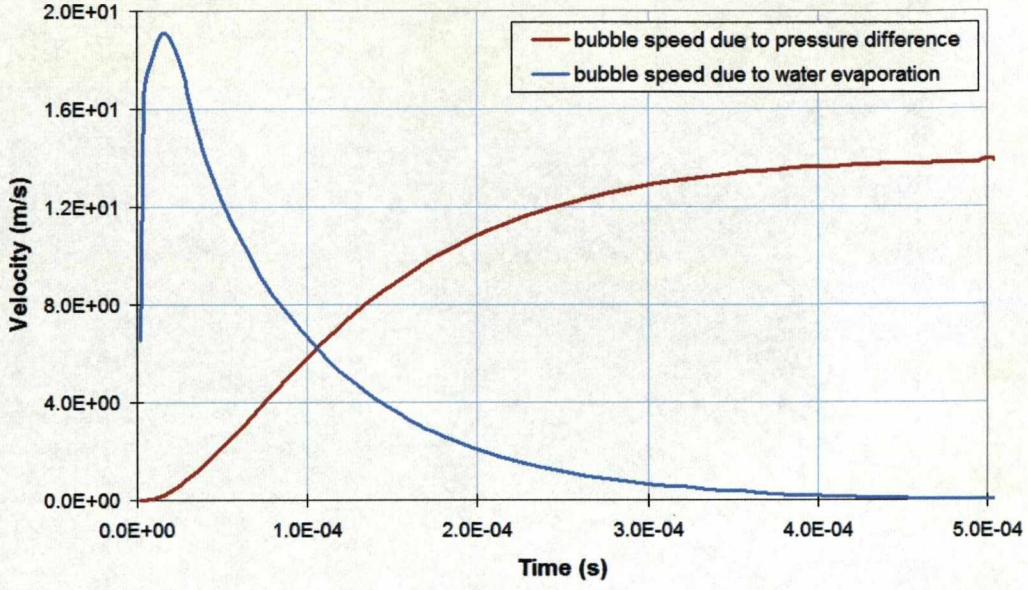

Figure 5.8 Contributions to bubble radius expansion speed by pressure difference (red) and water evaporation (blue)

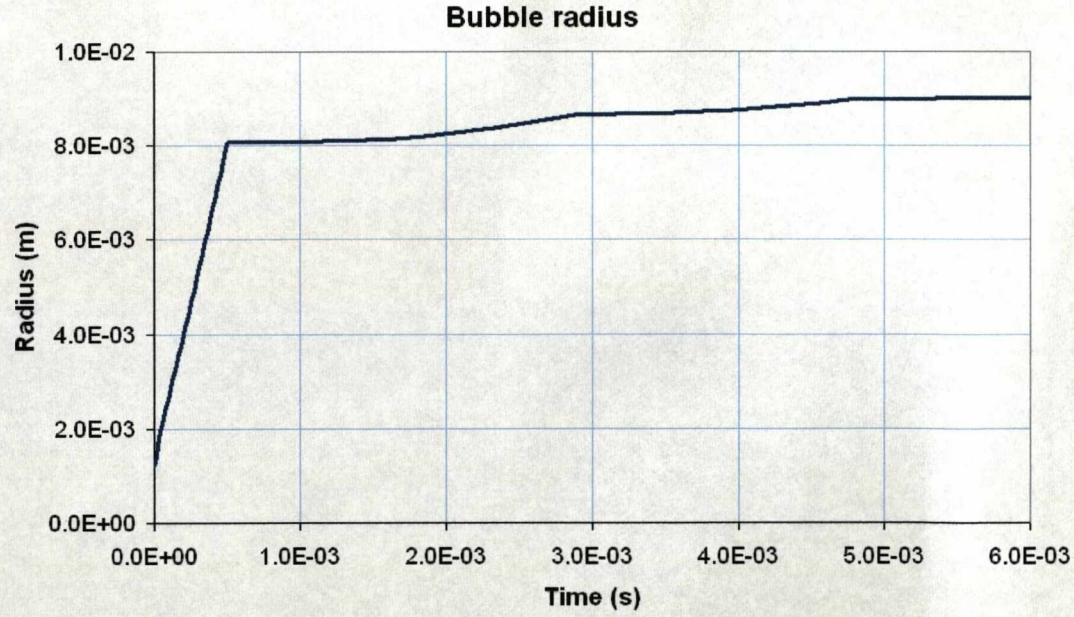

Figure 5.9 Bubble radius as a function of time

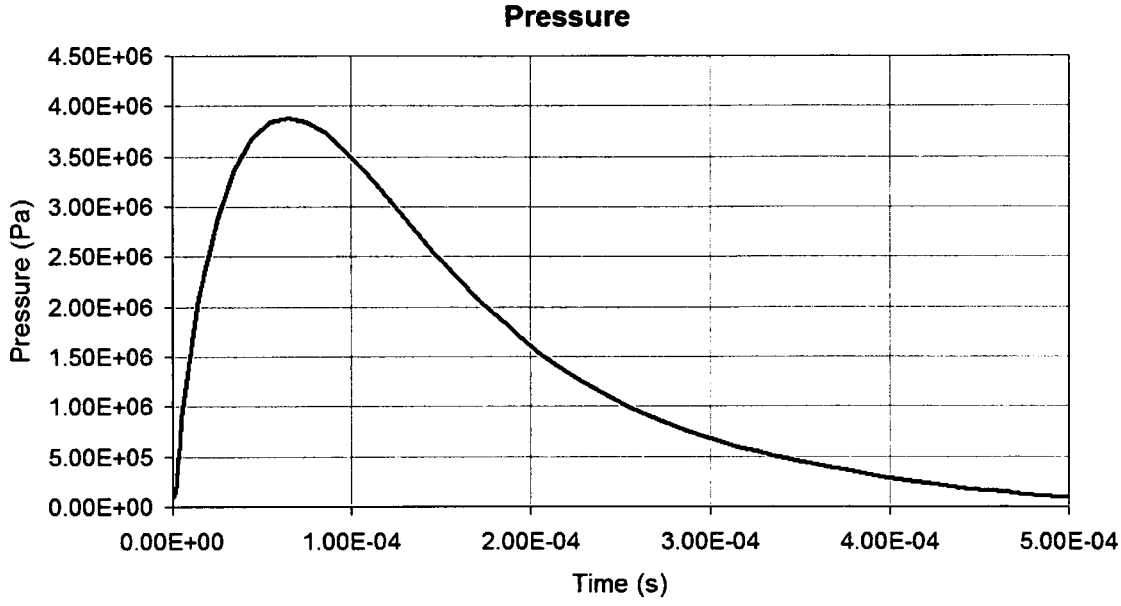

Figure 5.10 (a) Pressure in the bubble as a function of time

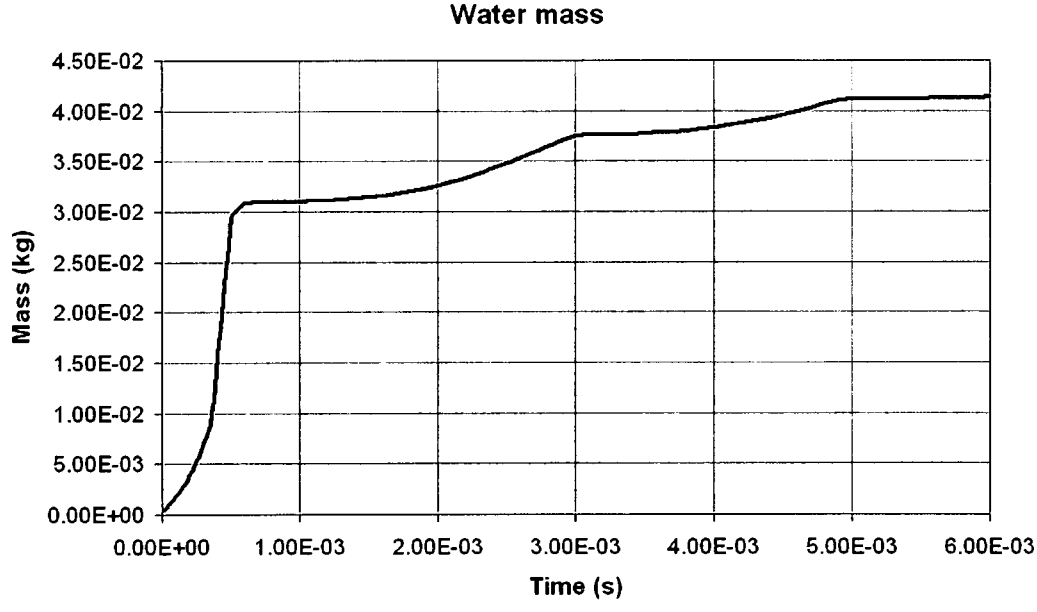

Figure 5.10 (b) Water mass that is to be displaced as a function of time

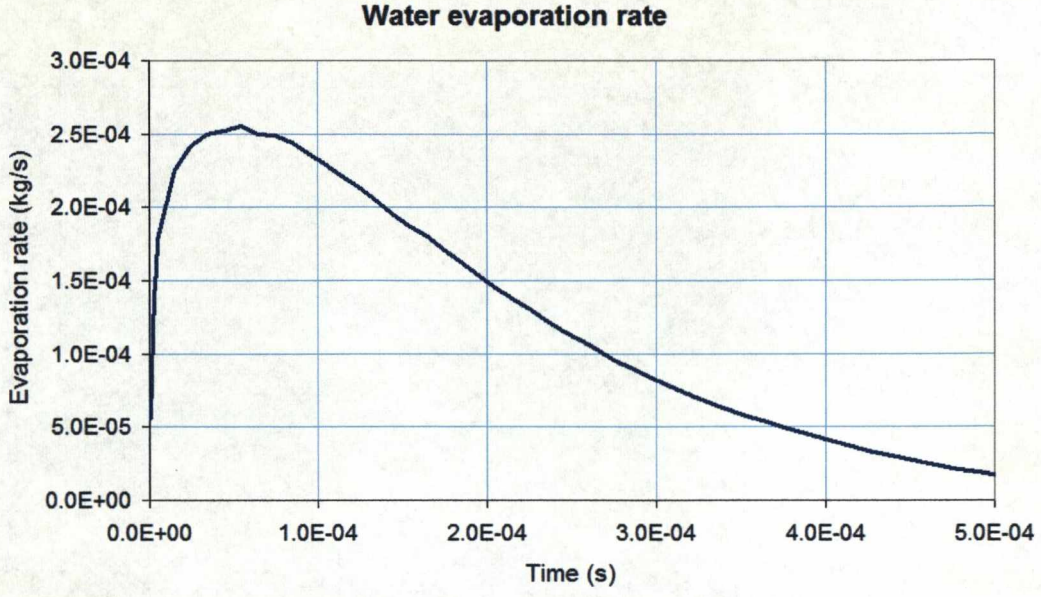

Figure 5.11 Evaporation rate of water as a function time

5.4.2 Development of Arc Column and Transport of Carbon Species

In the present work the arc is initiated with a hot column in water vapour as shown in figure 5.12(a). The maximum temperature in the arc is 24000K. Since the anode vapour comes into the domain at a high speed (200m/s), carbon species is rapidly convected towards the cathode. At 5μs, most of the arc column is filled with carbon (figure 5.12(c)). The arc column at this time is also expanded with an adjusted temperature distribution (figure 5.12(b)). The axial velocity reduces at the cathode surface the impingement of the carbon jet results in reverse flow also near the cathode. At the same time, water vapour is evaporated at the bubble surface and generates an inwards flow. As a consequence, a swirling flow pattern is formed around the anode root (figure 5.12(b)).

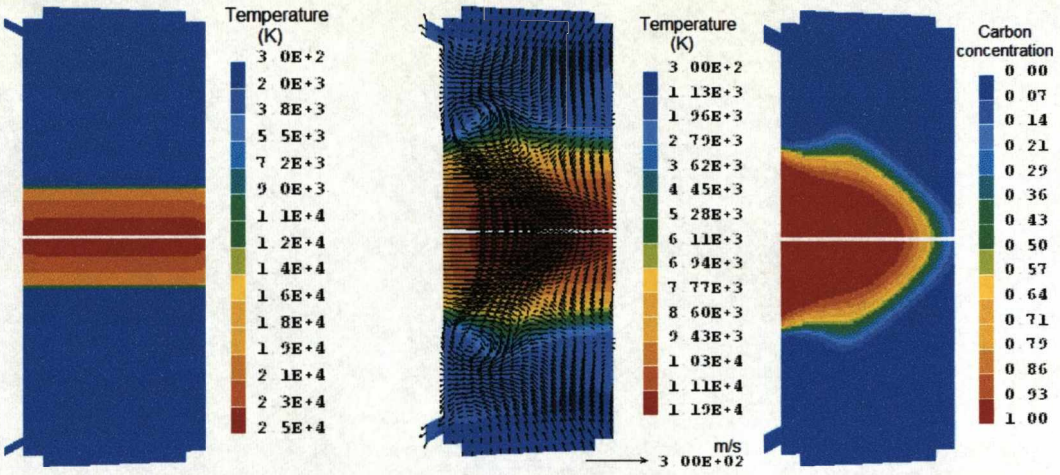

(a) (b) (c)

Figure 5.12 Comparison of (a) the temperature at initiation, with (b) arc temperature and velocity field at 5μs, and (c) carbon concentration at 5μs

The transient arcing process is shown in figure 5.13 where a sequence of the arc temperature is given at different instants. The arc temperature adjusts itself quickly based on Ohmic heating and radiation. As given in figure 5.14, it takes only about 2μs for the axis temperature to decrease from the initial 24000K to 10000k. This is a result of rapid radiation energy transfer. At 30ms, most of the cathode surface is covered by carbon species (figure 5.15). The input of electric energy is controlled by the arc voltage. At the very beginning of arc initiation, the hot column has a small radius and a high column voltage is imposed to force the current of 30A (figure 5.16(a)). Because carbon has a higher electrical conductivity than water vapour, with the spread of carbon species in the arc column, the column voltage drops immediately. However, the pressure in the bubble during this period rises quickly from atmospheric pressure to 38bar in just 70μs (figure 5.10(a)). More radiation is emitted because it has been assumed that the net emission coefficient of carbon species is proportional to pressure. With the decrease in bubble pressure, the arc voltage also decreases, and slowly settles down to 5.0V at 30ms.

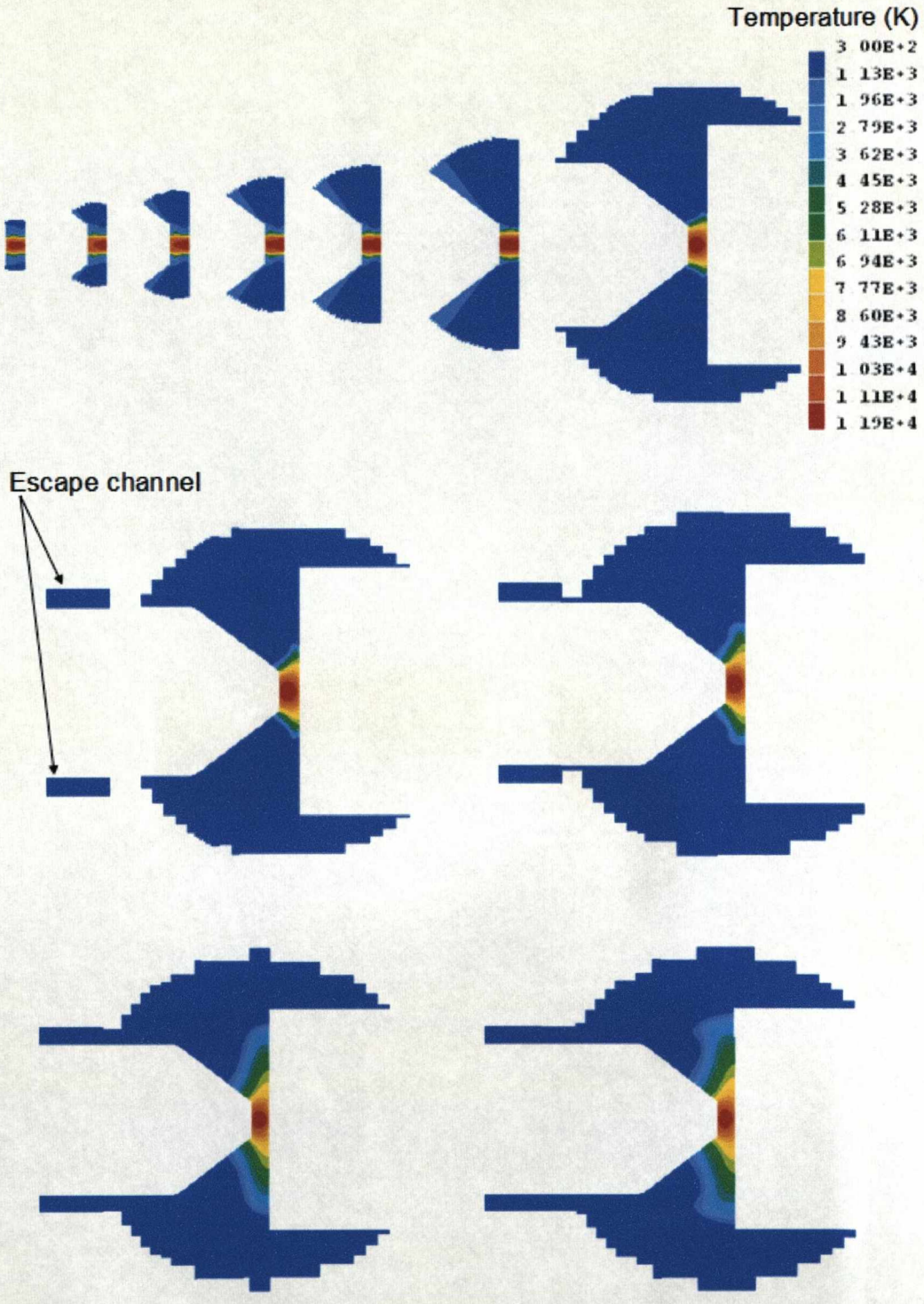

Figure 5.13 Arc shape and different instants (from top left to bottom right): 5µs, 55µs, 105µs, 155µs, 205µs, 305µs, 505µs, 2ms, 5.5ms, 25ms, 30ms. Temperature scale is only indicative here.

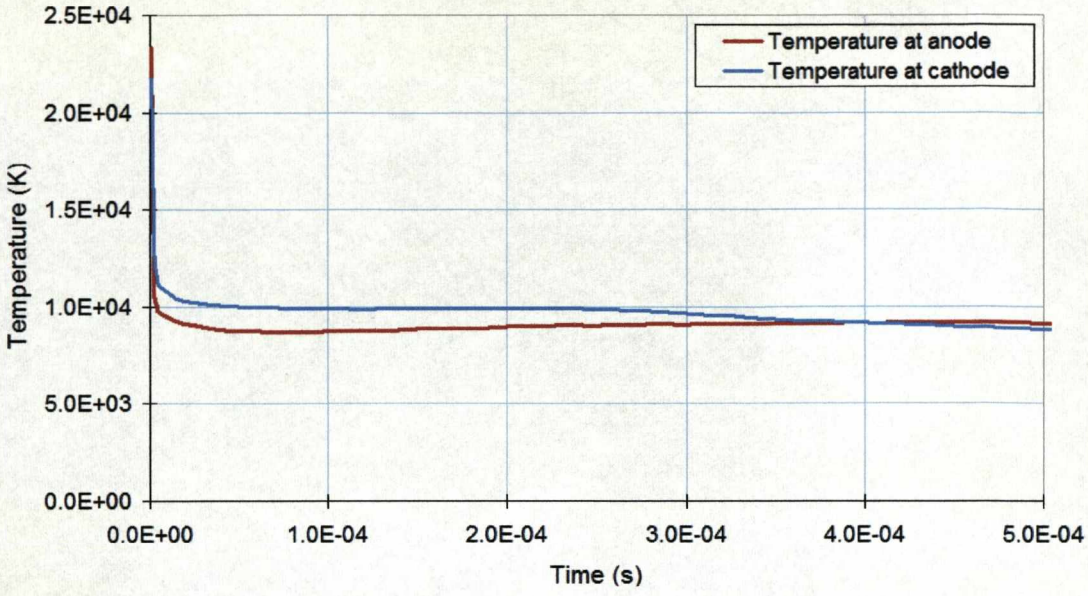

Figure 5.14 Temperature near anode and cathode as a function of time

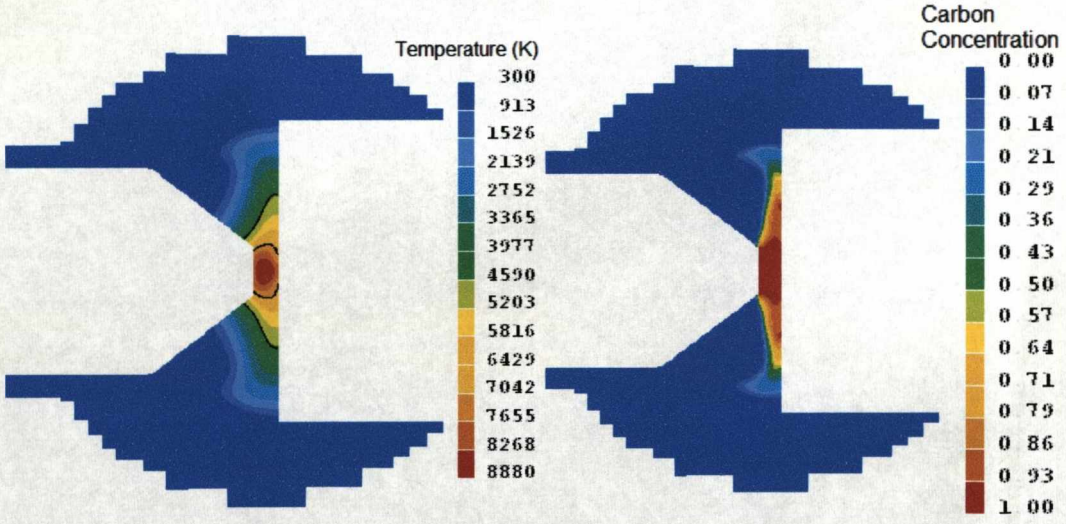

(a) (b)

Figure 5.15(a) Temperature contour with lines indicating temperature of 4500K and 7000K, and (b) distribution of carbon species at 30ms from arc initiation

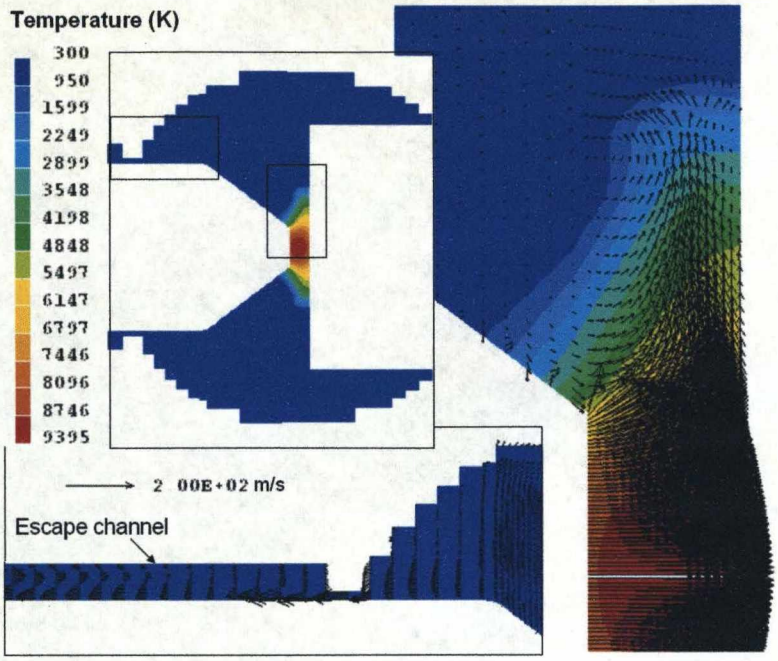

Figure 5.17 Gas flowing to atmospheric environment from within the bubble when the bubble is linked to the escape channel.

5.4.3 Consideration of Loss of Carbon Species and Water Evaporation

The main purpose of this carbon arc confined in liquid water is to form carbon nano-scale structures. Carbon vapour is lost from the arc column through several mechanisms. The first mechanism is the carbon vapour loss near the cathode surface where CNTs are formed and also solid carbon deposits are formed. The second mechanism for carbon vapour loss is by the arc edge (figure 5.18), according to [1] where the steep temperature gradient turns carbon vapour into fullerene-like structures. For an anode evaporation rate of 117.0mg/min, 19.5mg/min is collected as solid matters. This gives a carbon vapour loss percentage of about 15%. Other experiment produces similar results [9]. Because the mechanisms for the formation of carbon structures and the relationship between production rate and plasma environment are poorly understood so far, a flux controlled model is adopted in considering the carbon vapour loss. The axial velocity at 0.1mm away from the cathode surface is used to calculate the carbon vapour flux towards the cathode surface.

This flux Γ_{cc} is

$$\Gamma_{cc} = \rho_c w c \tag{5.18}$$

where ρ_c is the density of carbon vapour, w is the axial velocity and c is the carbon concentration. 15% of this carbon flux is assumed to be lost from the computational domain in the cells immediately adjacent to the cathode surface. A similar approach is taken at the arc edge, where in a plane perpendicular the axis, in the first cell from the symmetric axis where the local temperature is lower than 4500K, 15% of the positive flux in the radial direction is lost from the domain. This can be expressed as

$$\Gamma_{ce} = \rho_c v c \tag{5.19}$$

where v is the radial velocity. The carbon vapour enters the domain at a rate of 2e-6kg/s. Figure 5.19 shows the simulation results for the total loss of carbon at the cathode surface and at the arc edge. The loss at the arc edge in the quasi-steady stage of arcing is 2.9e-7kg/s and that at the cathode is 1.2e-8kg/s. This means nearly all of the carbon vapour loss is at the arc edge which is consistent with the flow field given in figure 5.20.

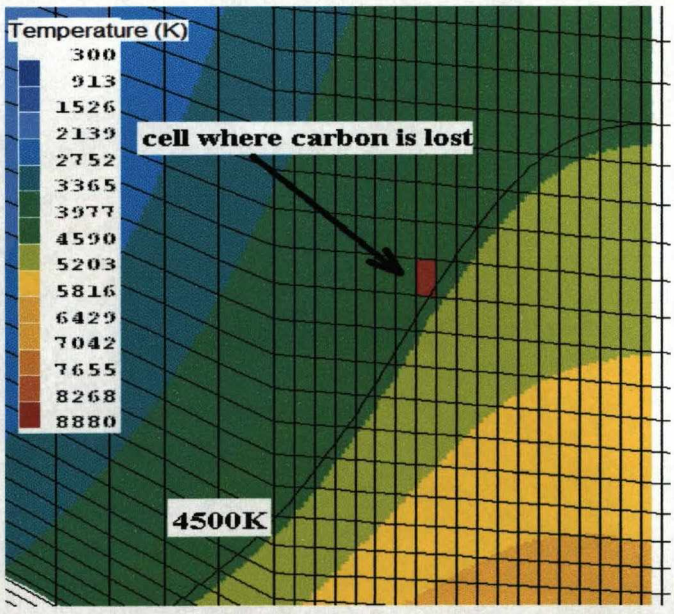

Figure 5.18 Diagram showing carbon vapour is lost from the domain at the arc edge

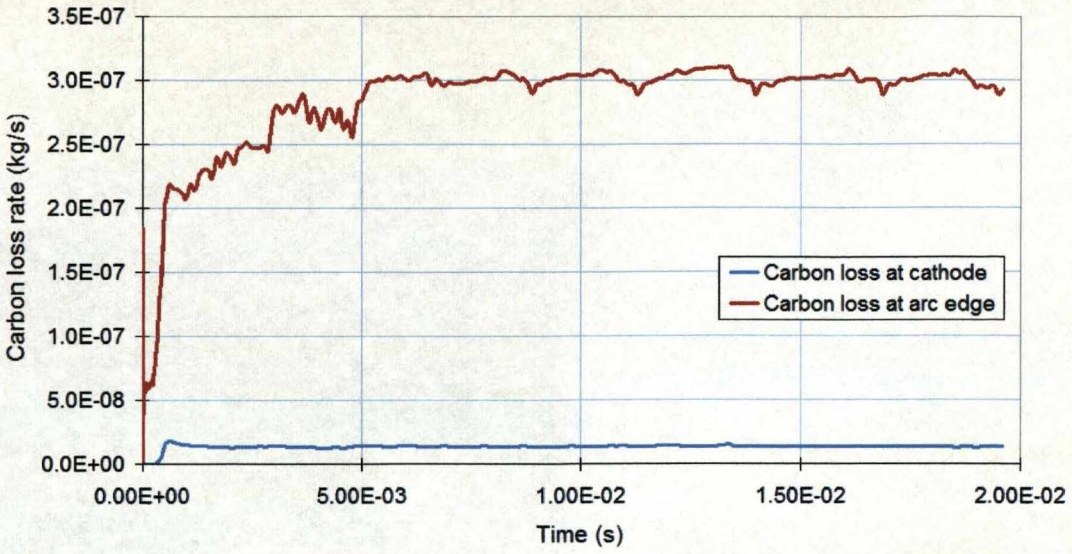

Figure 5.19 Carbon loss rate (kg/s) near cathode (blue) and at arc edge (red)

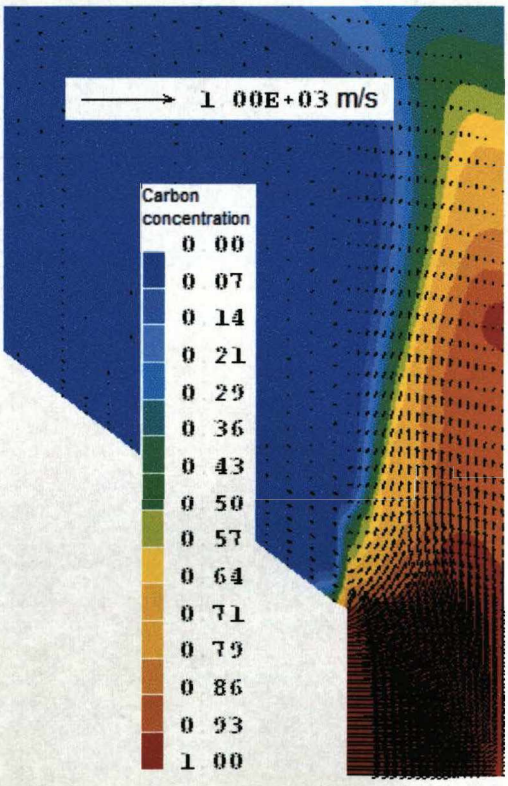

Figure 5.20 Velocity field at 30ms with carbon mass concentration distribution. Maximum axial velocity is 370m/s

5.5 Limitations of the Model and Future Improvement

As indicated by mass spectrometer analysis in [2], water vapour reacts with carbon atoms to form carbon monoxide and hydrogen gas. This reaction is not taken into account, because the total volume of reactant and product has the same value before and after the reaction. It thus does not affect the bubble dynamics substantially. The effect of the reaction energy also not considered. This reaction is probably endothermic (ΔH° = +131.3kJ/mol for reaction of H_2O with solid carbon). Assuming 85% of carbon vapour released from the anode reacts with water, then the energy involved in this reaction is 22J/s. The electric power input is 150J/s. Radiation loss from the whole arc column is 21J/s at 30ms, which means nearly 130J/s of power is convected away from the arc column. Therefore, reaction energy does have an influence on the temperature distribution at the arc edge. It tends to cool down the arc edge, therefore results in a smaller area of the hot region and increases the temperature gradient at the arc edge. This will need to be considered in the future work.

The measured arc voltage is 16V to 17V [1]. Our prediction only gives a value of 5V. Thus there is a gap of 11V to 12V between the experiment and prediction. In the present model, the cathode and anode sheaths are not taken into consideration. It is well known that electrons emitted by the cathode spot need to be accelerated by strong electric field to ionise the neutrals thus providing ion flux towards the cathode surface [10]. The cathode voltage fall provides the energy that is transported to the cathode surface by ion drift flux. Depending on the ratio of ion current to electron current in the sheath layer, the cathode sheath voltage fall can be as high as the first ionisation energy of the carbon atoms, which is 11.26eV. The electron flux towards the anode surface brings an energy flux that equal to the current multiplied by the work function of carbon which is 4.4eV for graphite. With a current of 30A, this energy flux is about 130J/s, which is higher than the energy that is needed to erode the anode material. The energy needed to produce 117mg/min of carbon is 60J/s for a heat of evaporation of 355.8kJ/mol for carbon. Thus, the remaining 70J/s is probably lost to the water cooled anode. Therefore a negligible voltage fall at the anode can be assumed.

Considering the cathode voltage fall, the total arc voltage would be in the range around 16.26V, which agrees with the measured arc voltage. It must be noted that this is only an estimation. A more accurate account of the cathode sheath process will need to follow a self consistent approach adopted by Schmitz and Riemann [10]. However, such an approach will be complicated by the presence of CNTs and carbon deposit.

Another large discrepancy between experiment and prediction is the water evaporation rate. Sano et al [1] gives a value of 99cm^3/min, which is equal to 1.6g/s. Our prediction however only gives a value of 0.01g/s. Taking the total power input corresponding to an arc voltage of 16V, the electrical power is 480J/s. With a latent heat of evaporation of 2.26e6J/kg, the maximum water that can be evaporated is 0.2g, which is only 12% of the measurement. In reality, the power of 480J/s includes the energy used to erode the anode and to provide energy for the reaction discussed at the beginning of this section. Therefore, the accuracy of the measurement in the experiment is questionable.

The present model is mainly aimed at the bubble dynamics and the development of the arc column and the transport of carbon species in the bubble area. Although the carbon loss process is taken into consideration by the flux controlled model, a link between the formation of the carbon structures and the plasma environment is far more complicated and is beyond the scope of the present work.

5.6 Summary

An arc model is developed in this chapter that take account of the bubble dynamics due to water evaporation and pressure difference between the bubble interior and the atmosphere. The arcing gas is provided by flux of carbon vapour from anode erosion. Results show that the model predicts a growth time of in the order of 1ms with a diameter of 1.6cm. This is also the time constant for the arc voltage to stabilise. At 30ms from arc initiation, carbon vapour covers most of the anode surface. The radial dimension of the hot zone around the electrode gap is comparable to that in the image taken from the experiment. Considering the cathode potential drop, our predicted arc column voltage falls within the expected range. Further improvement to the model is needed to consider the reaction between carbon and water vapour which is detected in experiments.

5.7 References

[1] Sano N., Wang H., Alexandrou I., Chhowalla M., Teo K. B. K. and Amaratunga G. A. J., "Properties of carbon onions produced by an arc discharge in water", Journal of Applied Physics, Vol. 92, No. 5, pp. 2783-2788, 2002

[2] Hsin Y. L., Hwang K. C., Chen F. R. and Kai J. J., "Production and in-situ Metal Filling of Carbon Nanotubes in Water", Adv. Mater. Vol. 13, No. 11, 2001

[3] Zhu H. W., Li X. S., Jiang B., Xu C. L., Zhu Y. F., Wu D. H. and Chen X. H., "Formation of carbon nanotubes in water by the electric-arc technique", Chem. Phys. Lett., 366, pp. 664-669, 2002

[4] Nishio M., Akita S. and Nakayama Y., "Cooling effect on the growth of carbon nanotubes and optical emission spectroscopy in short-period arc-discharge", Thin Solid Films, 464 – 465, pp. 304-307, 2004

[5] Antisari M. V., Marazzi R., Krsmanovic R., "Synthesis of multiwall carbon nanotubes by electric arc discharge in liquid environments", Carbon, Vol. 41, pp. 2393-2401, 2003

[6] Akita S., Ashihara H. and Nakayama Y., "Optical Emission Spectroscopy of Arc Flame Plasma for Generation of Carbon Nanotubes", Jpn. J. Appl. Phys., Vol. 39, pp. 4939-4944, 2000

[7] Lange H., Saidane K., Razafinimanana M. and Gleizes A., "Temperatures and C_2 column densities in a carbon arc plasma", J. Phys. D: Appl. Phys., 32, pp. 1024-1030, 1999

[8] Bilodeau J. F., Pousse J. and Gleizes A., "A Mathematical Model of the Carbon Arc Reactor for Fullerene Synthesis", Plasma Chemistry and Plasma Processing, Vol. 18, No. 2, 1998

[9] Lange H., Sioda M., Huczko A., Zhu Y. Q., Kroto H. W. and Walton D. R. M., "Nanocarbon production by arc discharge in water", Carbon, Vol. 41, pp. 1617-1623, 2003

[10] Schmitz H. and Riemann K. U., "Analysis of the cathodic region of atmospheric pressure discharges", J. Phys. D: Appl. Phys., Vol. 35, pp. 1727-1735, 2002

Chapter 6

CONCLUSION AND FUTURE WORK

The work in this thesis is concerned with the development of computer models for two types of atmospheric technological plasma with background applications in material processing (waste disposal, production of nano-scale powders) and formation of nano-scale carbon structures (carbon nano-tubes and fullerenes).

6.1 Three Dimensional Modelling of Twin Torch Plasma System

The twin torch system consists of two electrode assemblies, each of which has a central electrode surrounded by a nozzle to confine the shielding gas. The included angle by the two electrodes and their separation between the electrode tips can be adjusted according to application requirement. The arcing environment is truly three dimensional thus requires a three dimensional model to simulate the arcing process.

In the present work Cartesian coordinate system has been chosen to formulate the three dimensional governing flow and electromagnetic equations which, when solved by the commercial CFD package PHOENICS, gives easier convergence control in comparison with the other coordinate systems such as the body fitted coordinate system. Argon gas emits strong radiation at temperatures above 10000K and its radiation transfer is accounted for by using the so-called net emission coefficient. Radiation re-absorption at the arc edge is negligible and is not considered in the present work. The material and transport properties of argon are highly non-linear functions of temperature and the solution of the governing equations requires careful convergence control.

Representation of 3D shape in the computational domain is a challenging issue and needs to be addressed before sensible solution is obtained. In the present model a novel numerical scheme is developed to conveniently and automatically allocate

cells (each cell is a finite volume in the solution procedure) to a 3D shape. This greatly enhances the ability of the model to cope with complex geometries encountered in the plasma system.

One of the key issues in 3D arc modelling is the correct calculation and application of the Lorentz force terms in the momentum equation. The density in the arc column is low. For a symmetric arcing case, such as the well studied free burning arc between a conic cathode and a plate anode, slight asymmetry in the distribution of Lorentz force can substantially affect the arc flow hence result in a non-symmetric arc column. A validation of our method of calculation has been carried out for the free burning arc case by comparing our prediction with measurement and other available simulation results. It has been shown that the present 3D model produces satisfactory results.

Since the two electrodes are water cooled, erosion of the electrode material is minimal and can be neglected. The working gas is argon which is used to produce an inert environment for material processing. The behaviour of the twin torch plasma system is studied for two electrode configurations using the 3D model proposed in Chapter 2 and validated in Chapter 3. It has been found that the coupling of the two jets is through a thin, tissue like, conducting layer between the two jets. The cross sectional shapes of the two jets are deformed by the Lorentz force. The jets are never completely merged. The Lorentz force induced by the arc current and the combined magnetic field of the two jets tends to move the point of separation away from the electrode tips. It is the strong Ohmic heating, resulting from the high temperature (high electrical conductivity) and high electric field in the tissue layer, that heats up the incoming cold gas to a conducting temperature and thus stabilises the electric current path and subsequently the point of separation of the two jets. It is also shown that the change in flow rate does not have significant influence on the parameters of the plasma. Although the 3D model can predict the dynamic change of the arc voltage in response to the change in arc current, the predicted arc voltage is in general higher than the measurement of which no experimental uncertainty is given in the reference. The high predicted arc voltage is partly attributed to the statistic high frequency fluctuation of the jet coupling zone. The use of a simple turbulence

model brings the prediction closer to the measurement at low current, but results in an excessive reduction in arc voltage at high current. Therefore the use of a conventional turbulence model with a fixed turbulence parameter, c, to simulate the effect of fluctuation of the jet coupling zone may not be appropriate.

6.2 Carbon Arc confined in liquid water

The carbon arc simulated in Chapter 5 is confined by liquid water and burns in the gap between a conic anode and a plate cathode. This is the opposite of a conventional free burning arc where the cathode is normally made into a conic shape. Such an arrangement aims at maximising the anode erosion rate for the formation of solid carbon structures (carbon nanotubes and fullerenes).

A mathematical model is developed in Chapter 5 to simulate the dynamics of bubble growth and development of arc column. A novel numerical scheme is employed to determine the speed of bubble surface expansion, which includes the acceleration of surrounding water by pressure difference and also recession of bubble surface due to water evaporation. The erosion rate of anode is obtained by experiment and used as a boundary condition in the model. The carbon vapour enters the domain at a temperature of 4500K. To simulate the removal of gas from within the domain associated with bubble detachment from the discharge zone, an exit is imposed on the bubble surface when its radius reaches 9mm.

Results show that there is large pressure change within the first half millisecond of the discharge. The pressure can be as high as 38bar. Under such a high pressure the water surrounding the bubble is accelerated which leads to an increasing speed of bubble growth. The fast growth of bubble size under its inertia causes the pressure inside the bubble to rapidly decrease. The arc voltage, which is an indication of the total electrical power input into the domain, settles down in the first millisecond and then maintains a value of 5V.

The arc temperature at initiation is 24000K within a thin hot column. This temperature is quickly reduced to 11000K in 5μs as a result of radiation loss from the arc column. During this time the shape of the arc column is also adjusted by the incoming carbon vapour from the anode and the flow field is developed. In this sense, the initial conditions, especially the arc temperature, does not have strong influence on the results as a whole. The axis temperature inside the arc column at 30ms is 8500K which is higher than the experimental value using spectroscopic method. The possible reason for this difference could be the experimental instability of the arc column which makes the measured temperature as an average value of the arc column. From the simulation result, there exists a relatively large area around the arc core whose temperature is within the range from 4500K to 7000K which is the temperature range from measurement.

A quasi-steady state of arcing is reached within 30ms of arc initiation, according to our prediction. The loss of carbon vapour from the computational domain resulting from formation of solid carbon matters is considered by a flux controlled model. Results show that the major loss of the carbon species is at the arc edge which accounts for 99% of the total carbon loss.

The predicted arc column voltage is 5V which is different from the measurement of 16V. The difference is contributed to the cathode voltage fall which is in the order of the ionisation energy of carbon atoms (11.26eV). Taking this aspect into consideration, our prediction falls into the expected range.

The biggest difference between our prediction and measurement is the water evaporation rate. Our prediction is only a very small fraction of the measurement. However, it is shown that the measured rate of water evaporation may be wrong since even using the total electrical power input at the measured arc voltage, the amount of water vapour that can be created is only 12.5% of the measured value. Therefore the accuracy of the measurement in the experiment is questionable.

6.3 Future Work

In modelling the twin torch plasma system, a major assumption has been made, which is the arc is in a steady state. High speed video has however shown that the two jets in the jet coupling zone is constantly oscillating, resulting in a non-steady arc. This effect has been partly accounted for in an attempt by the use of a turbulence model but the effectiveness of such a simple turbulence model with a fixed model parameter is unsatisfactory. Thus the arcing process may need to be treated as a transient case to see if the oscillating phenomenon can be obtained as observed by high speed photograph. In this aspect, a more reliable experimental data is needed for comparison since the only available data for comparison in this thesis is the arc voltage measurement that, according to one of the authors, was obtained with uncertainty.

For atmospheric pressure plasmas, especially for the two types of plasma system studied in this thesis, the plasma is burning in a relatively stagnant environment. This is different from the case in plasma torch or high voltage switchgear where the arc is confined by high speed axial flow. In the former circumstance, the arc root plays an important role in shaping the flow field within and around the arc root. Recent research effort has made progress in modelling the arc column and cathode sheath layer in a self-consistent manner by considering the non-equilibrium processes in the cathode sheath. To further improve the accuracy of the model and reduce the difference between experiment and prediction, conjugate heat transfer within the electrode body and the cathode sheath processes will have to be considered.

For the arc in liquid case, the model developed in this work can be extended to other applications such as fault arcing in high voltage transformer, where an electric arc burns in liquid insulation oil.

The effectiveness of three dimensional modelling suffers enormously from the prohibitively long computing time because of the strong relaxation that has to be used to obtain converging results. This also forces us to use as small as possible a computational domain. To fully investigate the jet coupling zone, a much larger

domain with fine grids for sufficient resolution will be required. This naturally requires parallel processing given that very fast PCs (2.1GHz Pentium Core Duo) has already been used for the present work.